

Electronic Thesis and Dissertation Repository

9-3-2020 1:30 PM

Ultimate and serviceability limit states of large shallow foundations under combined loading

Pengpeng He, *The University of Western Ontario*

Supervisor: Timothy, Newson A., *The University of Western Ontario*

A thesis submitted in partial fulfillment of the requirements for the Doctor of Philosophy degree in Civil and Environmental Engineering

© Pengpeng He 2020

Follow this and additional works at: <https://ir.lib.uwo.ca/etd>



Part of the [Geotechnical Engineering Commons](#)

Recommended Citation

He, Pengpeng, "Ultimate and serviceability limit states of large shallow foundations under combined loading" (2020). *Electronic Thesis and Dissertation Repository*. 7334.
<https://ir.lib.uwo.ca/etd/7334>

This Dissertation/Thesis is brought to you for free and open access by Scholarship@Western. It has been accepted for inclusion in Electronic Thesis and Dissertation Repository by an authorized administrator of Scholarship@Western. For more information, please contact wlsadmin@uwo.ca.

Abstract

Estimation of the bearing capacity and deformations of large shallow foundations under combined loadings can be of great significance. Classical bearing capacity theories, which have been widely used in current geotechnical practice, may not be accurate enough and may not be conservative for some cases. Some geotechnical design guidelines recommend the failure load envelope method as an alternative to conventional theories for ultimate limit state analysis. Although many investigations of this method can be found in the literature, these studies focus primarily on undrained failure envelopes using unlimited-tension interfaces. However, zero-tension interfaces that are more appropriate for onshore foundations have not been well investigated. In addition, less work is available on drained failure envelopes. For serviceability limit states, the majority of approaches used are based on uncoupled, isotropic assumptions. Further work needs to be done on more appropriate elastic solutions for combined loadings. As the wind industry develops, the geotechnical challenges for larger wind turbines and less strong soils will increase. New tools for optimizing foundation design are required for economic construction of these facilities.

General VHMT (combined vertical, horizontal, moment and torsional loading) failure envelopes for circular foundations under undrained and drained soil conditions have been investigated using finite element analysis. The effects of soil strength heterogeneity, foundation embedment and surficial crustal layer have been examined for undrained soil conditions. The results showed that torsional loads can reduce the VHM capacity for circular foundations and foundation embedment can significantly increase the VHMT capacity. Moreover, neglecting the contribution of the crustal soil layer may significantly underestimate the bearing capacity for large shallow foundations. In addition, cohesive-frictional soils have been considered for drained soil conditions. The results showed that drained failure envelopes gradually expand with the soil weight parameter and exponentially expand with the soil friction angle. In comparison, classical bearing capacity theories appear to be rather conservative for combined loadings.

To estimate the deformations of large shallow foundations under complex climate and environmental loads, researchers have proposed many analytical isotropic elastic solutions based on idealized soil conditions, which are often adopted in existing design guidelines. However, many natural soils will be anisotropic or at least transversely isotropic (cross-anisotropic) due to their deposition and complex stress history. This research has investigated the coupled elastic stiffnesses for circular foundations founded in cross-anisotropic soils.

The elastic analyses showed that the coupling between the horizontal and moment responses is minimally affected by the soil anisotropic parameter. In addition, Gibson and embedment correction factors have been derived to account for the effects of soil stiffness non-homogeneity and foundation embedment. The results indicated that a higher Gibson modulus can increase the vertical, horizontal and moment stiffnesses, while it does not affect the coupling stiffness.

Keywords

Circular foundations, finite element analysis, failure envelope, zero-tension interface, torsional load, soil strength heterogeneity, foundation embedment, surficial crust, undrained and drained conditions, foundation stiffness, cross-anisotropic soil, Gibson soil

Summary for Lay Audience

Large onshore and offshore foundations are often subjected to complex environmental and climate loadings. To ensure the safety of structures, these foundations are designed to satisfy various criteria, but two of the most critical are: (1) the foundation capacity is larger than the possible maximum loading and (2) the foundation deformations under working loads are within given tolerances. This thesis has developed new methods for estimating the capacity and deformations of large circular foundations.

To estimate the capacity for circular foundations, the failure load envelope, which defines the failure load surface for combined vertical, horizontal, moment and torsional loading, have been investigated. Practical foundations are often designed to be embedded and many soils exhibit increasing strength with depth and have a thin layer of stiff crust; the effects of foundation embedment, increasing soil strength and surficial crust on the foundation capacity have been examined. This method should aid the capacity assessment for large shallow circular foundations and lead to cost savings.

To assess foundation deformations, the foundation stiffness, which is defined as the ratio of load and resulting displacement, is often adopted. This research has investigated the stiffness for circular foundations. Many natural soil deposits exhibit some degree of directionally dependent stiffness anisotropy due to their complex deposition history, where the soil has different mechanical properties in the vertical and horizontal planes. The developed approach should aid the deformation assessment for large shallow circular foundations and lead to more economic foundation construction.

Co-Authorship Statement

This work was carried out by Pengpeng He under the supervision of Dr. Timothy A. Newson. The finite element modelling and the literature review were carried out by Pengpeng He, and Dr. Newson assisted with the design of the finite element modelling, data interpretation and preparation of the final papers. Jesús González-Hurtado assisted with the parametric study of Chapter 5. Publications from this thesis are detailed as follows:

Chapter 2: Undrained capacity of circular shallow foundations under combined VHMT loading

He, P. and Newson, T.A.

A version of Chapter 2 has been submitted to “*Acta Geotechnica*”.

Chapter 3: Undrained capacity of circular shallow foundations on two-layer clays under combined VHMT loading

He, P. and Newson, T.A.

A version of Chapter 3 has been submitted to “*Canadian Geotechnical Journal*”.

Chapter 4: Drained bearing capacity of circular surface foundations under combined VHMT loading

He, P. and Newson, T.A.

A version of Chapter 4 has been submitted to “*Journal of Geotechnical and Geoenvironmental Engineering*”.

Chapter 5: Effects of soil stiffness anisotropy on elastic solutions of circular foundations under combined loading

He, P., González-Hurtado, J. and Newson, T.A.

A version of Chapter 5 has been submitted to “*Canadian Geotechnical Journal*”.

Acknowledgments

I would like to thank my supervisor Dr. Timothy A. Newson for his unconditional support and patient advice over the years. I can truly say that, without his willingness and endless patience to review this thesis, none of this would have been possible. I am greatly indebted to him for his guidance and providing me with opportunity to grow in his group. He has provided me with a wealth of knowledge and experience that will continue to shape me throughout my academic career. I would also like to thank Dr. Hanping Hong for the encouragement, support and experiences he provided.

I would like to thank the Natural Sciences and Engineering Research Council (NSERC) of Canada, Western University, and China Scholarship Council (CSC) for providing financial support. Sincere appreciation is also expressed to the faculty and staff in the Department of Civil and Environmental Engineering at Western University for providing a dynamic and collaborative research environment.

Special thanks to all of my friends and colleagues who helped with my research and teaching. They always have a positive attitude and a great perspective on life. They set the example and have taught me great life experiences. Their continued support helped me keep moving forward in work and life.

To my parents and my sister, who have been a foundation of any success that I have made. They have taught me that hard work is the key to success. Thank you all for your endless love and support.

Table of Contents

Abstract.....	ii
Summary for Lay Audience.....	iv
Co-Authorship Statement	v
Acknowledgments.....	vii
Table of Contents.....	viii
List of Tables.....	xiii
List of Figures.....	xiv
Nomenclature.....	xxi
1 Introduction.....	1
1.1 Background.....	1
1.1.1 Bearing capacity of shallow foundations.....	2
1.1.2 Elastic behavior of shallow foundations.....	12
1.2 Objectives of the research.....	14
1.3 Thesis outline	15
1.4 References.....	16
2 Undrained capacity of circular shallow foundations under combined VHMT loading	21
2.1 Introduction.....	21
2.2 Method – finite element analysis	22
2.2.1 Material models and interface conditions.....	22
2.2.2 Geometry and mesh.....	23
2.2.3 Sign conventions and loading paths.....	25
2.3 Surface foundations on non-homogeneous soils	26
2.3.1 Pure uniaxial capacity.....	27

2.3.2	Torsion-Vertical loading	28
2.3.3	Horizontal-Torsion loading	29
2.3.4	Moment-Torsion loading.....	31
2.4	Embedded foundations in a homogeneous soil	32
2.4.1	Pure uniaxial capacity	32
2.4.2	Horizontal-Vertical loading.....	34
2.4.3	Moment-Vertical loading	35
2.4.4	Torsion-Vertical loading	37
2.4.5	Moment-Horizontal loading	38
2.4.6	Horizontal-Torsional loading.....	40
2.4.7	Moment-Torsional loading.....	42
2.5	Full 4-D failure envelope in VHMT loading space	43
2.6	Conclusions.....	48
2.7	References.....	48
3	Undrained capacity of circular surface foundations on two-layer clays under combined VHMT loading	51
3.1	Introduction.....	51
3.2	Method – finite element analysis	53
3.2.1	Material models and interface conditions.....	53
3.2.2	Geometry and mesh	55
3.2.3	Sign conventions and loading paths	56
3.3	Finite element results	57
3.3.1	Pure uniaxial capacities.....	57
3.3.2	Horizontal-Vertical loading.....	60
3.3.3	Moment-Vertical loading	62
3.3.4	Torsion-Vertical loading.....	64

3.3.5	Moment-Horizontal loading	66
3.3.6	Horizontal-Torsional loading.....	68
3.3.7	Moment-Torsional loading.....	70
3.4	Full 4-D failure envelope in VHMT loading space	72
3.5	Conclusions.....	75
3.6	References.....	76
4	Drained bearing capacity of circular surface foundations under combined VHMT loading.....	79
4.1	Introduction.....	79
4.2	Method – finite element analysis	81
4.2.1	Material models and interface conditions.....	81
4.2.2	Geometry and mesh.....	82
4.2.3	Sign conventions and loading paths.....	83
4.3	Finite element results	84
4.3.1	Validation.....	84
4.3.2	Pure uniaxial capacities.....	85
4.3.3	Horizontal-Vertical loading.....	88
4.3.4	Moment-Vertical loading	90
4.3.5	Torsion-Vertical loading.....	91
4.3.6	Moment-Horizontal loading.....	93
4.3.7	Horizontal-Torsional loading.....	96
4.3.8	Moment-Torsional loading.....	98
4.4	Full 4-D VHMT failure envelope in VHMT loading space	100
4.5	Conclusions.....	103
4.6	References.....	104

5	Effects of soil stiffness anisotropy on elastic solutions of circular foundations under combined VHMT loading	107
5.1	Introduction.....	107
5.2	Method – finite element analysis	111
5.2.1	Material models and sign conventions	111
5.2.2	Geometry and mesh.....	113
5.3	Finite element results	114
5.3.1	Model calibration.....	114
5.3.2	Stiffness equations for surface foundations on homogeneous soils.....	116
5.3.3	Correction factors for Gibson soils	119
5.3.4	Correction factors for foundation embedment	123
5.4	Conclusions.....	128
5.5	References.....	128
6	Discussions, conclusions and recommendations.....	131
6.1	Discussions.....	131
6.1.1	Ultimate limit state design.....	131
6.1.2	Serviceability limit state design	135
6.2	Summary and conclusions.....	137
6.2.1	Undrained capacity of circular shallow foundations under combined VHMT loading	138
6.2.2	Undrained capacity of circular surface foundations on two-layer clays under combined VHMT loading.....	139
6.2.3	Drained bearing capacity of circular surface foundations under combined VHMT loading	139
6.2.4	Effects of soil stiffness anisotropy on elastic solutions of circular foundations under combined VHMT loading.....	140
6.3	Limitations and recommendations for future work.....	140

6.3.1	Limitations of current research	140
6.3.2	Recommendations for future work.....	141
6.4	References.....	142
	Curriculum Vitae.....	145

List of Tables

Table 2.1: Uniaxial bearing capacity factors for soils with various soil strength heterogeneity ratios.....	27
Table 2.2: Summary of FE-calculated failure envelopes.....	44
Table 2.3: Failure envelopes for a surface foundation on non-homogeneous soils.....	46
Table 3.1: FE cases for crusted soils under undrained conditions.....	54
Table 3.2: Summary of FE-calculated failure envelopes.....	73
Table 4.1: Values of v_0 resulting from FE analyses and the method of characteristics....	85
Table 4.2: Summary of FE-calculated failure envelopes.....	101
Table 5.1: Mesh convergence study (surface foundations on a homogeneous soil with $\mu = 0.3$).....	114
Table 6.1: Soil parameters and ultimate design loads.....	132
Table 6.2: Ultimate limit state design of the foundation.....	133
Table 6.3: Foundation and soil parameters.....	135
Table 6.4: Foundation responses for $G_R/G_{\max} = 0.3$	136

List of Figures

Figure 1.1: Effective area principle (DNV, 2016)	3
Figure 1.2: <i>M-H</i> failure envelopes for shallow foundations at $V/V_{ult} = 0.50$ (after Tapper, 2013): (a) Undrained soil conditions (Martin, 1994) and (b) Drained soil conditions (Cassidy, 1999).....	5
Figure 1.3: Effect of foundation shape on undrained <i>MH</i> failure envelopes under unlimited-tension interface conditions (Gourvenec, 2007)	6
Figure 1.4: Effect of foundation interface conditions on undrained VHM failure envelopes (Taiebat and Carter, 2010): (a) Unlimited-tension interface and (b) Zero-tension interface	7
Figure 1.5: Effects of foundation embedment and soil strength heterogeneity on undrained <i>M-H</i> failure envelopes (Vulpe et al., 2014): (a) Effect of foundation embedment and (b) Effect of soil strength heterogeneity	8
Figure 1.6: Drained VHM failure envelope (Tapper, 2013).....	8
Figure 1.7: Drained <i>M-H</i> failure envelope (Loukidis et al., 2008).....	9
Figure 1.8: Schematics of failure envelopes: (a) Undrained soil conditions & zero-tension interface; (b) Undrained soil conditions & unlimited-tension interface and (c) Drained soil conditions	11
Figure 1.9: Sign conventions for loads and deformations (Osman et al., 2007).....	13
Figure 2.1: Sign conventions and soil strength profile	23
Figure 2.2: Mesh convergence study for a homogeneous soil	24
Figure 2.3: Half-view of the FE mesh: (a) Surface foundation and (b) Embedded foundation ($d/D = 0.50$).....	24

Figure 2.4: VHM failure envelopes of a surface foundation for $\kappa = 0$: (a) H - V ; (b) M - V and (c) M - H at $V/V_{ult} = 0.50$	26
Figure 2.5: T - V failure envelopes: (a) Dimensionless and (b) Normalized.....	28
Figure 2.6: H - T failure envelopes: (a) $V/V_{ult} = 0.75$; (b) $V/V_{ult} = 0.50$ and (c) $V/V_{ult} = 0.25$	30
Figure 2.7: M - T failure envelopes: (a) Dimensionless, $V/V_{ult} = 0.50$; (b) Normalized, $V/V_{ult} = 0.75$; (c) Normalized, $V/V_{ult} = 0.50$ and (d) Normalized, $V/V_{ult} = 0.25$	32
Figure 2.8: Depth correction factors of uniaxial capacities for embedded foundations: (a) V_{ult} ; (b) H_{ult} and (c) M_{ult}	34
Figure 2.9: H - V failure envelopes: (a) Dimensionless and (b) Normalized.....	35
Figure 2.10: M - V failure envelopes: (a) Dimensionless; (b) Normalized; (c) Dimensionless, modified and (d) Normalized, modified.....	37
Figure 2.11: T - V failure envelopes: (a) Dimensionless and (b) Normalized.....	38
Figure 2.12: M - H failure envelopes: (a) Dimensionless, $V/V_{ult} = 0.50$; (b) Normalized, $V/V_{ult} = 0.75$; (c) Normalized, $V/V_{ult} = 0.50$ and (d) Normalized, $V/V_{ult} = 0.25$	40
Figure 2.13: Fitting of the probe values of M - H failure envelopes	40
Figure 2.14: H - T failure envelopes: (a) Dimensionless, $V/V_{ult} = 0.50$; (b) Normalized, $V/V_{ult} = 0.75$; (c) Normalized, $V/V_{ult} = 0.50$ and (d) Normalized, $V/V_{ult} = 0.25$	42
Figure 2.15: M - T failure envelopes: (a) Dimensionless, $V/V_{ult} = 0.50$; (b) Normalized, $V/V_{ult} = 0.75$; (c) Normalized, $V/V_{ult} = 0.50$ and (d) Normalized, $V/V_{ult} = 0.25$	43
Figure 2.16: M - H envelope for a circular surface foundation on a homogeneous soil at $V/V_{ult} = 0.50$ for $T \neq 0$	45

Figure 2.17: 3-D failure surfaces for a circular surface foundation on non-homogeneous soils: (a) VHM at $T = 0$; (b) VHT at $M = 0$ and (c) VMT at $H = 0$	47
Figure 3.1: Soil profile with a surficial crust.....	53
Figure 3.2: Mesh convergence study of Case C31.....	55
Figure 3.3: Half-view of the FE mesh.....	55
Figure 3.4: Sign conventions.....	56
Figure 3.5: M - H and H - T failure envelopes for a uniform soil at $V/V_{ult} = 0.50$: (a) M - H and (b) H - T	57
Figure 3.6: Crust correction factors of uniaxial capacities: (a) V_{ult} and (b) M_{ult}	58
Figure 3.7: Collapse mechanisms under purely vertical loads.....	60
Figure 3.8: H - V failure envelopes for $s_{u0}/s_{ut} = 0.2 \sim 1.0$ & $t_c/D = 0.2$: (a) Dimensionless and (b) Normalized.....	61
Figure 3.9: H - V failure envelopes for $s_{u0}/s_{ut} = 0.6$ & $t_c/D = 0.1 \sim 0.3$: (a) Dimensionless and (b) Normalized.....	62
Figure 3.10: M - V failure envelopes: (a) Dimensionless, $s_{u0}/s_{ut} = 0.2 \sim 1.0$ & $t_c/D = 0.2$; (b) Normalized, $s_{u0}/s_{ut} = 0.2 \sim 1.0$ & $t_c/D = 0.2$; (c) Dimensionless, $s_{u0}/s_{ut} = 0.6$ & $t_c/D = 0.1 \sim 0.3$ and (d) Normalized, $s_{u0}/s_{ut} = 0.6$ & $t_c/D = 0.1 \sim 0.3$	63
Figure 3.11: Collapse mechanisms at M_{ult}	64
Figure 3.12: T - V failure envelopes: (a) Dimensionless, $s_{u0}/s_{ut} = 0.2 \sim 1.0$ & $t_c/D = 0.2$; (b) Normalized, $s_{u0}/s_{ut} = 0.2 \sim 1.0$ & $t_c/D = 0.2$; (c) Dimensionless, $s_{u0}/s_{ut} = 0.6$ & $t_c/D = 0.1 \sim 0.3$ and (d) Normalized, $s_{u0}/s_{ut} = 0.6$ & $t_c/D = 0.1 \sim 0.3$	65
Figure 3.13: M - H failure envelopes for $s_{u0}/s_{ut} = 0.3 \sim 1.0$ & $t_c/D = 0.2$: (a) Dimensionless, $V/V_{ult} = 0.50$; (b) Normalized, $V/V_{ult} = 0.75$; (c) Normalized, $V/V_{ult} = 0.50$ and (d) Normalized, $V/V_{ult} = 0.25$	67

Figure 3.14: *M-H* failure envelopes for $s_{u0}/s_{ut} = 0.6$ & $t_c/D = 0.1 \sim 0.3$: (a) Dimensionless, $V/V_{ult} = 0.50$; (b) Normalized, $V/V_{ult} = 0.75$; (c) Normalized, $V/V_{ult} = 0.50$ and (d) Normalized, $V/V_{ult} = 0.25$ 68

Figure 3.15: *H-T* failure envelopes for $s_{u0}/s_{ut} = 0.2 \sim 1.0$ & $t_c/D = 0.2$: (a) Dimensionless, $V/V_{ult} = 0.50$; (b) Normalized, $V/V_{ult} = 0.75$; (c) Normalized, $V/V_{ult} = 0.50$ and (d) Normalized, $V/V_{ult} = 0.25$ 69

Figure 3.16: *H-T* failure envelopes for $s_{u0}/s_{ut} = 0.6$ & $t_c/D = 0.1 \sim 0.3$: (a) Dimensionless, $V/V_{ult} = 0.50$; (b) Normalized, $V/V_{ult} = 0.75$; (c) Normalized, $V/V_{ult} = 0.50$ and (d) Normalized, $V/V_{ult} = 0.25$ 70

Figure 3.17: *M-T* failure envelopes for $s_{u0}/s_{ut} = 0.2 \sim 1.0$ & $t_c/D = 0.2$: (a) Dimensionless, $V/V_{ult} = 0.50$; (b) Normalized, $V/V_{ult} = 0.75$; (c) Normalized, $V/V_{ult} = 0.50$ and (d) Normalized, $V/V_{ult} = 0.25$ 71

Figure 3.18: *M-T* failure envelopes for $s_{u0}/s_{ut} = 0.6$ & $t_c/D = 0.1 \sim 0.3$: (a) Dimensionless, $V/V_{ult} = 0.50$; (b) Normalized, $V/V_{ult} = 0.75$; (c) Normalized, $V/V_{ult} = 0.50$ and (d) Normalized, $V/V_{ult} = 0.25$ 72

Figure 3.19: 3-D failure surfaces for Case C24 (i.e. $s_{u0}/s_{ut} = 0.6$ and $t_c/D = 0.2$): (a) VHM at $T = 0$; (b) VHT at $M = 0$ and (c) VMT at $H = 0$ 75

Figure 4.1: Mesh convergence study for the case of $G = 2$ & $\varphi' = 20^\circ$ 83

Figure 4.2: Sign conventions..... 83

Figure 4.3: *M-V* and *M-H* failure envelopes for the case of $G = 2$ & $\varphi' = 20^\circ$: (a) *M-V* and (b) *M-H* at $V/V_{ult} = 0.50$ 84

Figure 4.4: Ultimate capacity factors: (a) V_{ult} ; $G = 2$ & $\varphi' = 0 \sim 40^\circ$; (b) H_{ult} ; $G = 2$ & $\varphi' = 0 \sim 40^\circ$; (c) M_{ult} ; $G = 2$ & $\varphi' = 0 \sim 40^\circ$; (d) T_{ult} ; $G = 2$ & $\varphi' = 0 \sim 40^\circ$; (e) V_{ult} ; $G = 0.5 \sim 3$ & $\varphi' = 20^\circ$; (f) H_{ult} ; $G = 0.5 \sim 3$ & $\varphi' = 20^\circ$; (g) M_{ult} ; $G = 0.5 \sim 3$ & $\varphi' = 20^\circ$ and (h) T_{ult} ; $G = 0.5 \sim 3$ & $\varphi' = 20^\circ$ 88

Figure 4.5: *H-V* failure envelopes: (a) Dimensionless; $G=2$ & $\varphi' = 0 \sim 40^\circ$; (b) Normalized; $G = 2$ & $\varphi' = 0 \sim 40^\circ$; (c) Dimensionless; $G = 0.5 \sim 3$ & $\varphi' = 20^\circ$ and (d) Normalized; $G = 0.5 \sim 3$ & $\varphi' = 20^\circ$ 89

Figure 4.6: *M-V* failure envelopes: (a) Dimensionless; $G = 2$ & $\varphi' = 0 \sim 40^\circ$; (b) Normalized; $G = 2$ & $\varphi' = 0 \sim 40^\circ$; (c) Dimensionless; $G = 0.5 \sim 3$ & $\varphi' = 20^\circ$ and (d) Normalized; $G = 0.5 \sim 3$ & $\varphi' = 20^\circ$ 91

Figure 4.7: *T-V* failure envelopes: (a) Dimensionless; $G=2$ & $\varphi' = 0 \sim 40^\circ$; (b) Normalized; $G = 2$ & $\varphi' = 0 \sim 40^\circ$; (c) Dimensionless; $G = 0.5 \sim 3$ & $\varphi' = 20^\circ$ and (d) Normalized; $G = 0.5 \sim 3$ & $\varphi' = 20^\circ$ 92

Figure 4.8: *M-H* failure envelopes at $V/V_{ult} = 0.50$: (a) Dimensionless; $G = 2$ & $\varphi' = 0 \sim 40^\circ$; (b) Normalized; $G = 2$ & $\varphi' = 0 \sim 40^\circ$; (c) Dimensionless; $G = 0.5 \sim 3$ & $\varphi' = 20^\circ$; and (d) Normalized; $G = 0.5 \sim 3$ & $\varphi' = 20^\circ$ 94

Figure 4.9: Fitting of *M-H* envelopes: (a) $G = 2$ & $\varphi' = 0 \sim 40^\circ$ and (b) $G = 0.5 \sim 3$ & $\varphi' = 20^\circ$ 95

Figure 4.10: *H-T* failure envelopes for $G = 2$ & $\varphi' = 0 \sim 40^\circ$: (a) Dimensionless, $V/V_{ult} = 0.50$; (b) Normalized, $V/V_{ult} = 0.75$; (c) Normalized, $V/V_{ult} = 0.50$ and (d) Normalized, $V/V_{ult} = 0.25$ 97

Figure 4.11: *H-T* failure envelopes for $G = 0.5 \sim 3$ & $\varphi' = 20^\circ$: (a) Dimensionless, $V/V_{ult} = 0.50$; (b) Normalized, $V/V_{ult} = 0.75$; (c) Normalized, $V/V_{ult} = 0.50$ and (d) Normalized, $V/V_{ult} = 0.25$ 98

Figure 4.12: *M-T* failure envelopes for $G = 2$ & $\varphi' = 0 \sim 40^\circ$: (a) Dimensionless, $V/V_{ult} = 0.50$; (b) Normalized, $V/V_{ult} = 0.75$; (c) Normalized, $V/V_{ult} = 0.50$ and (d) Normalized, $V/V_{ult} = 0.25$ 99

Figure 4.13: *M-T* failure envelopes for $G = 0.5 \sim 3$ & $\varphi' = 20^\circ$: (a) Dimensionless, $V/V_{ult} = 0.50$; (b) Normalized, $V/V_{ult} = 0.75$; (c) Normalized, $V/V_{ult} = 0.50$ and (d) Normalized, $V/V_{ult} = 0.25$ 100

Figure 4.14: 3-D failure surfaces for a circular surface foundation with $G = 2$ & $\varphi' = 20^\circ$ under drained soil conditions: (a) VHM at $T = 0$; (b) VHT at $M = 0$ and (c) VMT at $H = 0$	103
Figure 5.1: Sign conventions & soil profiles (Osman et al., 2007)	112
Figure 5.2: Effect of model dimensions on the stiffness coefficients for a surface foundation on a homogeneous isotropic soil: (a) K_V and (b) K_{HH}	113
Figure 5.3: Mesh representation.....	114
Figure 5.4: Stiffness coefficients for a surface circular foundation on a homogeneous isotropic soil: (a) K_V ; (b) K_{HH} ; (c) K_{MH} ; (d) K_{MM} and (e) K_T	116
Figure 5.5: Vertical stiffness coefficient for surface foundations on homogeneous soils: (a) $K_V \sim \alpha^2$ and (b) $K_V(1.1-\mu^*) \sim \alpha^2$	117
Figure 5.6: Horizontal and rotational stiffness coefficients for surface foundations on homogeneous soils: (a) $K_{HH}(2.4-\mu^*) \sim \alpha^2$ and (b) $K_{MM}(1.2-\mu^*) \sim \alpha^2$	118
Figure 5.7: Coupling and torsional stiffness coefficients for surface foundations on homogeneous soils: (a) $K_{MH} \sim \mu^*$ and (b) $K_T \sim \alpha^2$	119
Figure 5.8: Gibson correction factor for vertical stiffness: (a) $(C_{\beta,V} - 1) \sim \beta$ and (b) $(C_{\beta,V} - 1)/f_{1,V}(\mu^*)/f_{2,V}(\alpha^2) \sim \beta$	121
Figure 5.9: Gibson correction factors for horizontal, rotational and torsional stiffness: (a) K_{HH} ; (b) K_{MM} and (c) K_T	122
Figure 5.10: Coupling stiffness coefficient for surface foundations on Gibson soils	123
Figure 5.11: Embedment correction factor for vertical stiffness: (a) $(C_{d,V} - 1) \sim d/D$ and (b) $(C_{d,V} - 1)/g_{1,V}(\mu^*)/g_{2,V}(\alpha^2) \sim d/D$	124
Figure 5.12: Embedment correction factors for horizontal, rotational and torsional stiffness: (a) K_{HH} ; (b) K_{MM} and (c) K_T	125

Figure 5.13: Embedment correction factor for coupling stiffness: (a) $K_{MH} \sim d/D$ and (b) $C_{d,MH}/g_{1,MH}(\mu^*)/g_{2,MH}(\alpha^2) \sim d/D$ 127

Figure 6.1: Undrained shear strength profile..... 132

Figure 6.2: Design loads compared with the undrained $M-H$ failure envelopes..... 134

Figure 6.3: Design loads compared with the drained $M-H$ failure envelope..... 135

Nomenclature

Nomenclature used in this thesis, excluding those which only appear once:

μ	Poisson's ratio
A	Soil-foundation contact area (m ²)
B'	Effective foundation width (m)
c'	Effective soil cohesion (kPa)
C_e	Embedment correction factor
C_β	Gibson correction factor
D	Foundation diameter (m)
d	Foundation embedment depth (m)
E_h	Young's modulus in the horizontal direction (MPa)
E_u	Undrained Young's modulus (MPa)
E_v	Young's modulus in the vertical direction (MPa)
G	Weight parameter of soil
G_{hh}	Shear modulus in the horizontal plane (MPa)
G_{hv}, G_{vh}	Shear modulus in the vertical plane (MPa)
H'_{\max}	Reduced horizontal capacity at a given level of vertical load with a non-zero torsional load (kN)
H	Horizontal load (kN)

H_{\max}	Horizontal capacity at a given level of vertical load (kN)
H_{ult}	Pure uniaxial horizontal capacity (kN)
k	Undrained shear strength increase per depth (kPa/m)
K_{HH}	Horizontal stiffness coefficient
K_{MH}, K_{HM}	Coupling stiffness coefficient
K_{MM}	Rotational stiffness coefficient
K_T	Torsional stiffness coefficient
K_V	Vertical stiffness coefficient
LRP	Load reference point
M'_{\max}	Reduced moment capacity at a given level of vertical load with a non-zero torsional load (kN·m)
M	Moment (kN·m)
M_{\max}	Moment capacity at a given level of vertical load (kN·m)
M_{ult}	Pure uniaxial moment capacity (kN·m)
N_c, N_γ, N_q	Bearing capacity factors
s_{cr}	Crust correction factor
s_u	Undrained shear strength (kPa)
s_{u0}	Undrained shear strength at foundation level (kPa)
s_{ut}	Averaged undrained shear strength of the surficial crust layer (kPa)
t	Foundation thickness (m)

T	Torsional load (kN·m)
t_c	Crust thickness (m)
T_{\max}	Torsional capacity at a given level of vertical load (kN·m)
T_{ult}	Pure uniaxial torsional capacity (kN·m)
u_H	Horizontal displacement (mm)
u_V	Vertical displacement (mm)
V	Vertical load (kN)
v_0, h_0, m_0, t_0	Uniaxial bearing capacity factors
V_{ult}	Pure uniaxial vertical capacity (kN)
α	Soil stiffness anisotropy factor
β	Normalized Gibson factor
γ'	Effective unit weight of soil, $\gamma - \gamma_w$ (kN/m ³)
γ_m	Partial safety factor for materials
θ_M	Rotational displacement (deg.)
θ_T	Torsional displacement (deg.)
κ	Shear strength heterogeneity ratio
μ_{hh}	Poisson's ratio for horizontal strain due to horizontal strain
μ_{vh}	Poisson's ratio for horizontal strain due to vertical strain
φ'	Friction angle of soil

1 Introduction

1.1 Background

Estimation of the bearing capacity and deformations of large shallow foundations under combined loadings is of great significance, particularly for onshore and offshore structures, such as oil and gas platforms, wind turbines, transmission towers, masts and other tall structures, due to their significant climate and environmental loadings. Apart from the vertical load due to the self-weight of the superstructure (V), horizontal loads (H) caused by wind, wave and ice can be substantial and a large structural height can lead to significant moment loading (M) of the foundation. In addition, other causes (e.g. accidental ‘snag’ occurrences) can add torsional loads (T) to the load combination.

This chapter briefly reviews the methods for bearing capacity and deformation assessments of large shallow foundations for onshore and offshore structures under combined loadings. The emphasis is on shallow foundations for onshore wind turbines, which are the primary focus of this thesis. In common with other cyclically loaded structures, onshore wind turbine foundations are designed based on ultimate, serviceability and fatigue limit states. Since wind turbine foundations are subjected to considerable moment loading due to large horizontal loading and structural height, the rocking behavior of wind turbine foundations is considered to be a critical design parameter (Lang, 2012). In addition, the ultimate limit state of wind turbine foundations is also significant, and an accurate assessment of bearing capacity is required. Commonly-used geotechnical design guidelines for wind turbine foundations in North America include DNV (2016), API (2011) and ISO (2016). Given the relatively immature nature of the wind industry, optimization of the design methods for these structures is still required and this thesis aims to address some of these gaps.

The assessments of bearing capacity and deformation for shallow foundations are generally separately considered. The bearing capacity calculation often treats the soil as an elastoplastic material and can directly provide the bearing pressure without considering load-displacement behavior. The deformation estimation normally considers the elastic behavior of a soil-foundation system. However, some more advanced methods, for

example, the macro-element approach (e.g. Houlsby and Cassidy, 2002; Cremer et al., 2001) and the nonlinear Winkler approach (e.g. Allotey and El Naggar, 2003, 2008a, 2008b), are able to capture the complete foundation response. The macro-element approach is based on foundation action bounding/yield surfaces and can account for the coupling between responses in different directions. The nonlinear Winkler model idealizes the soil as a system of springs and can be used for the analysis of soil-foundation interaction problems, including horizontal, vertical and rotational responses. These advanced models can also predict the cyclic foundation behaviors and have significant potential for the future. In this chapter, the commonly-used methods for separately assessing the bearing capacity and deformation of large shallow foundations are discussed.

1.1.1 Bearing capacity of shallow foundations

1.1.1.1 Classical bearing capacity theory

The ultimate bearing capacity is referred to the average bearing pressure that can be provided by a geostucture without failure occurring. Traditionally, foundation capacity based on classical solutions for the uniaxial vertical bearing capacity of shallow strip foundations is often adopted (Terzaghi, 1951). The contributions of soil cohesion, soil unit weight and surcharge to the bearing capacity are taken into consideration in an uncoupled manner. The effects of load inclination and eccentricity are considered by introducing a load inclination factor and the effective foundation area. To account for the effects of foundation shape and embedment, shape and embedment factors are also used. Large onshore shallow wind turbine foundations are typically circular (or have forms that can be approximated as circular) and have dimensions of 15-20 m diameter and 2-3 m thickness.

The classical bearing capacity approach has been widely used by geotechnical design guidelines for wind turbine foundations, such as DNV (2016), API (2011) and ISO (2016). The effective area principle for circular and octagonal foundations provided by DNV (2016) is schematically illustrated in Figure 1.1. An equivalent inscribed circular foundation is recommended to accommodate for the octagonal shape. The effective area shaded with stripes (i.e. double circle segment area) is determined based on load

eccentricity ($e = M/V$), and is represented by a rectangle (with dimensions $L' \times B'$) for capacity assessment.

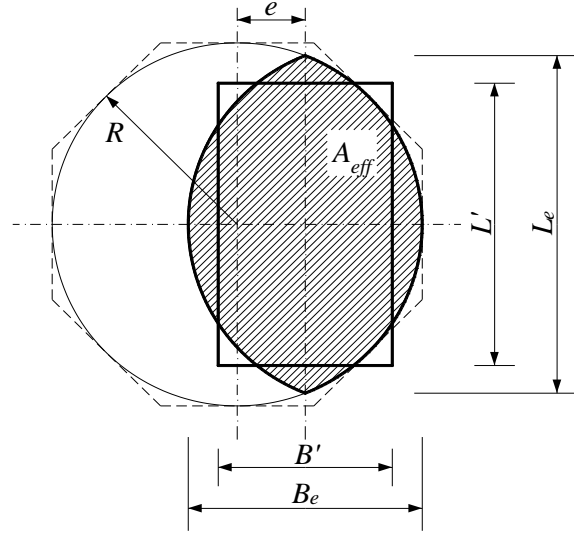


Figure 1.1: Effective area principle (DNV, 2016)

The general form of the bearing capacity equation (BCE) is given by (Meyerhof, 1963):

$$q_u = c' N_c \cdot s_c i_c d_c + 0.5 \gamma' B' N_\gamma \cdot s_\gamma i_\gamma d_\gamma + q N_q \cdot s_q i_q d_q \quad (1.1)$$

where N_c , N_γ and N_q are dimensionless bearing capacity factors accounting for soil cohesion, c' , soil effective unit weight below foundation level, γ' , and surcharge pressure at foundation level, q , respectively; s_c , s_γ and s_q are dimensionless shape factors; i_c , i_γ and i_q are dimensionless inclination factors; d_c , d_γ and d_q are dimensionless embedment factors; and B' is the effective foundation width accounting for load eccentricity. For undrained soil conditions with $\varphi = 0$, the general BCE reduces to:

$$q_u = s_u N_c \cdot s_c i_c d_c + q \quad (1.2)$$

Analytical expressions of the bearing capacity factors are often functions of the soil friction angle, φ' . For example, exact formulae for N_c and N_q (pertain to weightless soils) for a rough strip foundation were provided by Prandtl (1920):

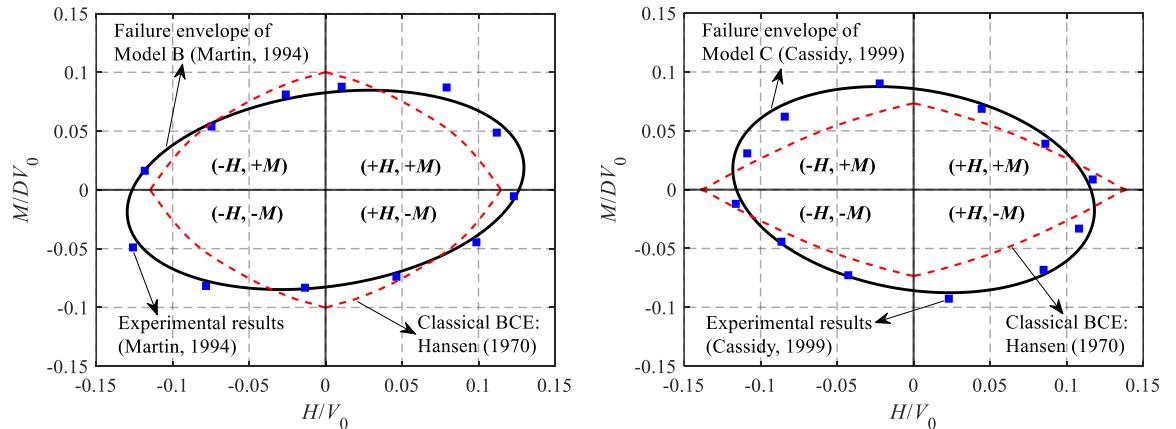
$$\begin{aligned} N_c &= (N_q - 1) \cot \varphi' \\ N_q &= e^{\pi \tan \varphi'} \cdot \tan^2 \left(\frac{\pi}{4} + \frac{\varphi'}{2} \right) \end{aligned} \quad (1.3)$$

Eq. (1.3) reduces to $N_c = \pi + 2$ and $N_q = 1$ under undrained soil conditions. However, there is no consensus on the expression of N_γ due to the complexities introduced by the inclusion of soil self-weight. A variety of solutions for N_γ can be found in the literature (Chen, 2013). The expression recommended by DNV (2016) is shown by Eq. (1.4). Recent studies (e.g. Perkins and Madson, 2000; Cerato and Lutenecker, 2007; Kumar and Khatri, 2008; Loukidis and Salgado, 2011; Conte et al., 2013) also indicate that the effects of foundation size, relative density and stress levels of sands also influence the bearing capacity factors due to strain softening and progressive failure.

$$N_\gamma = 1.5(N_q - 1) \tan \varphi' \quad (1.4)$$

Many empirical and semi-empirical expressions for the modification factors (i.e. shape, inclination and embedment factors) under undrained and drained soil conditions have been proposed. Some of the expressions are summarized by Hansen (1970) and Zadroga (1994).

Since the effects of load inclination and eccentricity are separately considered, this semi-empirical modification of the conventional theories may sometimes be insufficiently accurate (Gourvenec, 2007). Figure 1.2 shows typical experimental results of the failure load combinations (horizontal and moment loads) for shallow foundations under undrained and drained soil conditions, along with the failure envelopes fitted by experimental results. It is apparent that the classical BCE does not provide satisfactory predictions against the experimental results in certain cases and this simple approach is not conservative for all the possible load combinations.



(a) Undrained soil conditions (Martin, 1994) (b) Drained soil conditions (Cassidy, 1999)

Figure 1.2: *M-H* failure envelopes for shallow foundations at $V/V_{ult} = 0.50$ (after Tapper, 2013): (a) Undrained soil conditions (Martin, 1994) and (b) Drained soil conditions (Cassidy, 1999)

Moreover, variations in soil strength with depth are difficult to include in the BCE and non-standard foundation shapes (e.g. octagons) cannot easily be incorporated into this method; an approximate inscribed circle of a double symmetrical polygon is recommended by DNV (2016). The effective area method also does not consider the tensile stress at the soil-foundation interface, which is of great significance for offshore foundations, such as suction caissons. In addition, this approach cannot incorporate the effects of torsional loads, which can be significant for onshore and offshore foundations (Bienen et al., 2007). DNV (2016) introduces an equivalent horizontal load to account for torsional loading, but this form of approximation is not straightforward.

1.1.1.2 Failure envelope approach

The failure envelope approach is a more recently introduced method, which can explicitly incorporate the load interaction effects of the various load components (Shen et al., 2017). It has been recommended as an alternative to conventional theories in API (2011) and ISO (2016). For a given three-dimensional VHM failure envelope, VHM load combinations within this failure envelope have a safe design capacity, whilst load combinations located on or outside this failure envelope are considered to be unsafe.

The shape and size of failure envelopes depends on many factors, such as foundation shape, foundation embedment, soil strength heterogeneity, soil drainage conditions, soil-foundation interface conditions. A number of studies have been undertaken to investigate the failure envelope for strip, rectangular and circular foundations. The VHM failure envelopes for hybrid monopile-footing foundations have also been investigated by El-Marassi et al. (2008), El-Marassi (2011) and Stone et al. (2010). Undrained failure envelopes have mostly determined using numerical and theoretical methods (e.g. Taiebat and Carter, 2002; Gourvenec and Randolph, 2003; Gourvenec, 2007; Feng et al., 2014;

Shen et al., 2016), while drained failure envelopes are relatively sparse and primarily derived based on experimental approaches (e.g. Nova and Montrasio, 1991; Butterfield and Gottardi, 1994; Bienen et al., 2006).

Gourvenec (2007) investigated foundation shape effects on undrained failure envelopes under combined VHM loading. The results show that the shape of foundations considerably affects the size of the failure envelope, while the shapes of the failure envelopes remain generally similar, as shown in Figure 1.3.

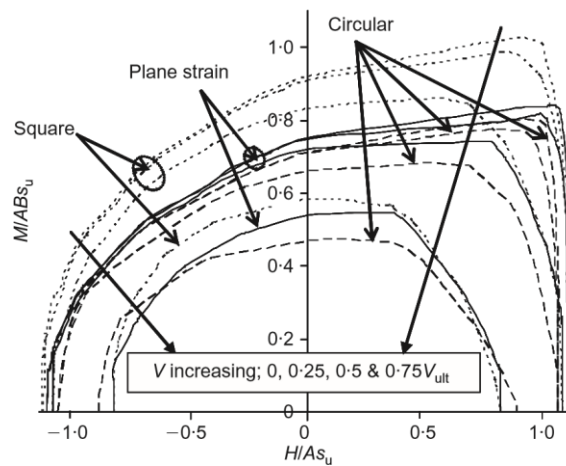


Figure 1.3: Effect of foundation shape on undrained *MH* failure envelopes under unlimited-tension interface conditions (Gourvenec, 2007)

The tensile strength for the soil-foundation interface plays an important role in the development of failure envelopes. The extreme cases are unlimited-tension and zero-tension interfaces. An unlimited-tension interface is often assumed for offshore foundations, particularly for the case of skirted foundations, while onshore shallow foundations can uplift and separate from the soil under large overturning moments, because the soil-foundation interface is unable to resist tensile loads. El-Marassi (2011) investigated the undrained VHM failure envelopes of hybrid monopile-footing foundations for both unlimited- and zero-tension interface conditions using finite element analysis. The results show that the vertical resistance does not depend on the soil-foundation interface conditions, while the lateral and rocking capacities are highly affected by the interface conditions. Taiebat and Carter (2010) numerically studied the three-dimensional undrained

VHM failure envelopes for circular foundations under unlimited-tension and zero-tension interface conditions (see Figure 1.4). The primary differences are: (i) an unlimited-tension interface can sustain moment at $V = 0$; and (ii) The $M-H$ cross section for a zero-tension interface is almost symmetric about $H = 0$, while the $M-H$ envelope for an unlimited-tension interface is asymmetric and the apex of the $M-H$ envelope is located in the positive $M-H$ quadrant (i.e. $+M, +H$).

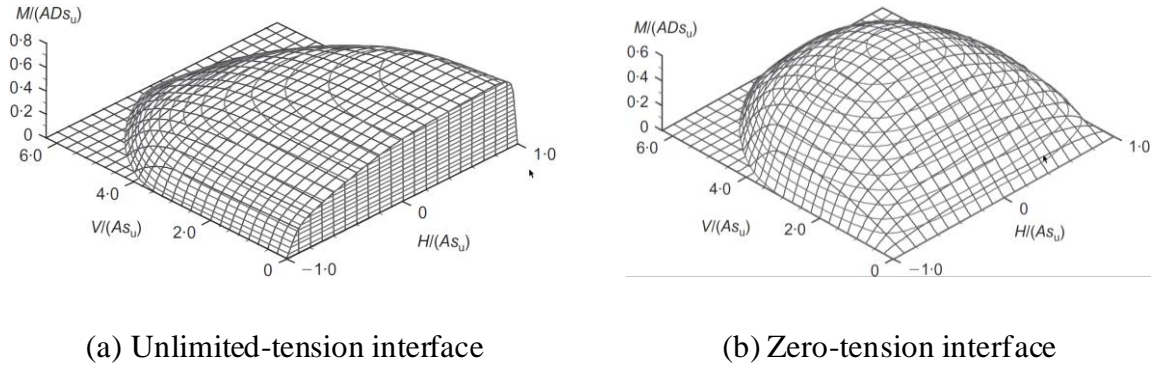


Figure 1.4: Effect of foundation interface conditions on undrained VHM failure envelopes (Taiebat and Carter, 2010): (a) Unlimited-tension interface and (b) Zero-tension interface

Foundation embedment (denoted by foundation embedment ratio, d/D , with d being the foundation embedment depth and D being the diameter of circular foundations) and soil strength heterogeneity (represented by soil strength heterogeneity ratio, $\kappa = kD/s_{u0}$, with k being the strength increase per depth and s_{u0} being the undrained shear strength at foundation level) are also important parameters causing differences in the foundation failure envelopes. The effects of foundation embedment and soil strength heterogeneity can be two-fold. Firstly, they can dramatically increase the bearing capacity of foundations (i.e. the size of the failure envelope), and secondly the shape of the failure envelope can also change with increasing foundation embedment and soil strength heterogeneity. Vulpe et al. (2014) has shown that the undrained failure envelope for circular foundations considerably expands with d/D and κ , and the obliqueness of the $M-H$ failure envelopes increases with d/D and κ due to the cross-coupling between the horizontal and moment loading modes, as shown in Figure 1.5.

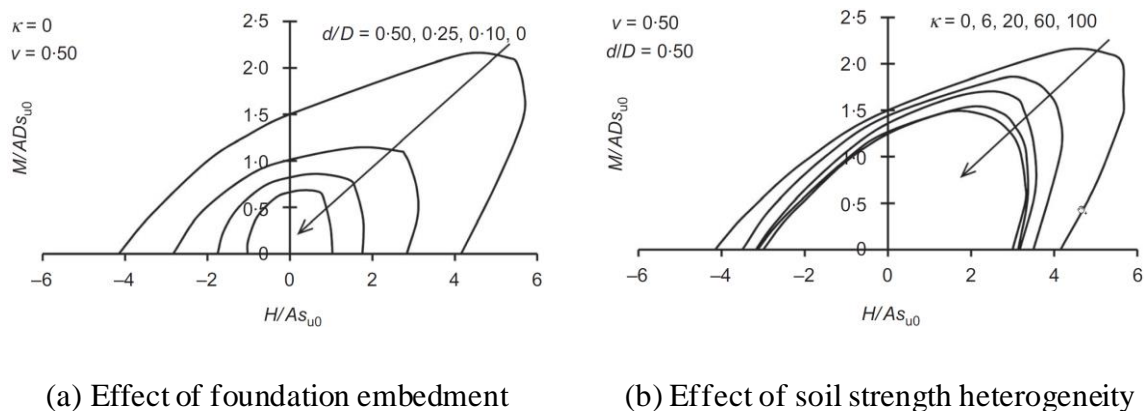


Figure 1.5: Effects of foundation embedment and soil strength heterogeneity on undrained M - H failure envelopes (Vulpe et al., 2014): (a) Effect of foundation embedment and (b) Effect of soil strength heterogeneity

Drained failure envelopes normally consider a zero-tension interface, since tensile stress at the soil-foundation interface is unlikely to be generated due to the drained soil conditions. Butterfield and Gottardi (1994), Martin (1994) and Byrne (2000) experimentally investigated the VHM failure envelope for offshore foundations (e.g. suction caissons and spudcans). The schematic VHM failure envelope is shown in Figure 1.6 (Tapper, 2013). The drained failure envelope has been approximated using parabolic expressions in H - V and M - V loading space, and elliptical equations in M - H loading space. It should also be noted that the elliptical M - H envelope tends to be oblique to the negative ($+M$, $-H$) load combinations (e.g. positive eccentricity), which differs from the undrained failure envelope (see Figure 1.2).

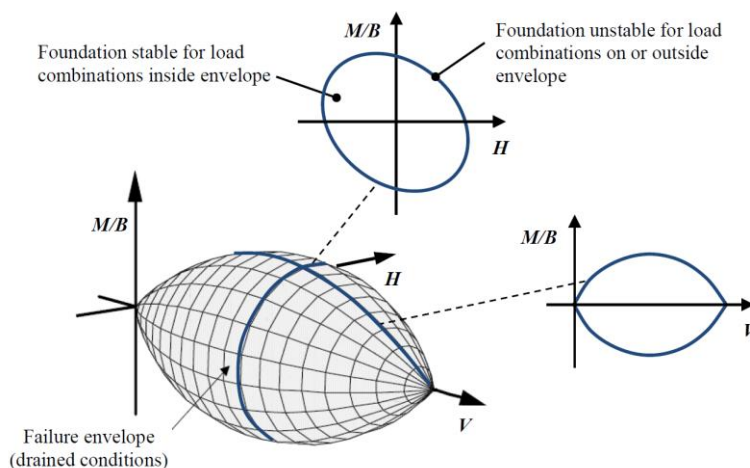


Figure 1.6: Drained VHM failure envelope (Tapper, 2013)

However, numerical analysis of drained failure envelopes is relatively sparse compared with undrained soil conditions. Marassi et al. (2008), Stone et al. (2010) and Marassi et al. (2017) numerically studied the drained VHM failure envelopes for hybrid monopile-footing foundations. However, these failure envelopes are limited to some special cross-sections of the global failure surface and torsional loading was not considered. Hjiatj et al. (2004) evaluated the lower and upper bounds of the bearing capacity for strip foundations on cohesive-frictional soils under non-eccentric inclined loads using numerical limit analysis, while the non-eccentric loading cannot account for the effect of moment loading. Loukidis et al. (2008) undertook finite element analysis to investigate the drained VHM failure envelope for strip foundations on purely frictional sands, and similar oblique elliptical $M-H$ envelopes (see Figure 1.7) have been found. However, the failure envelope concept is not fully adopted and only a combined inclination-eccentricity factor was proposed for the classical bearing capacity theory.

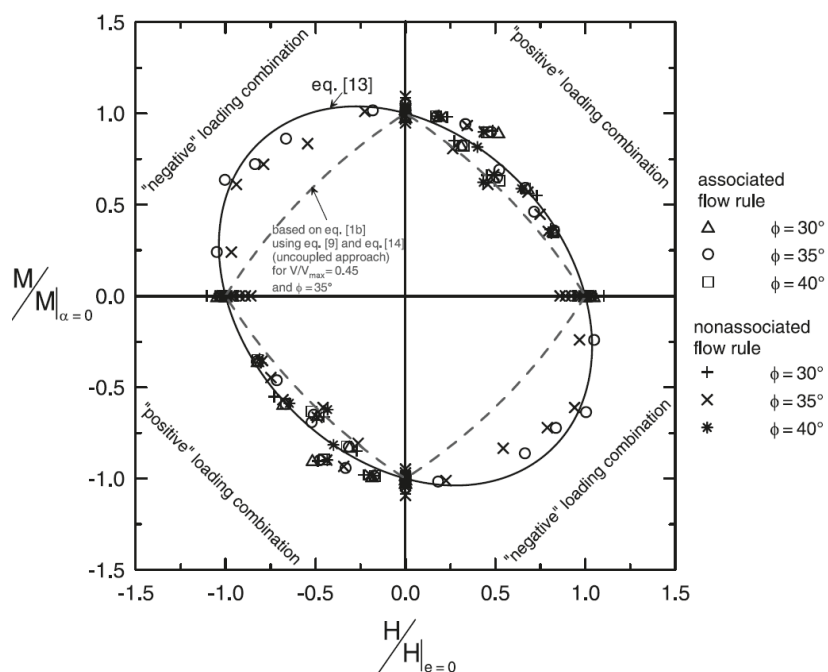
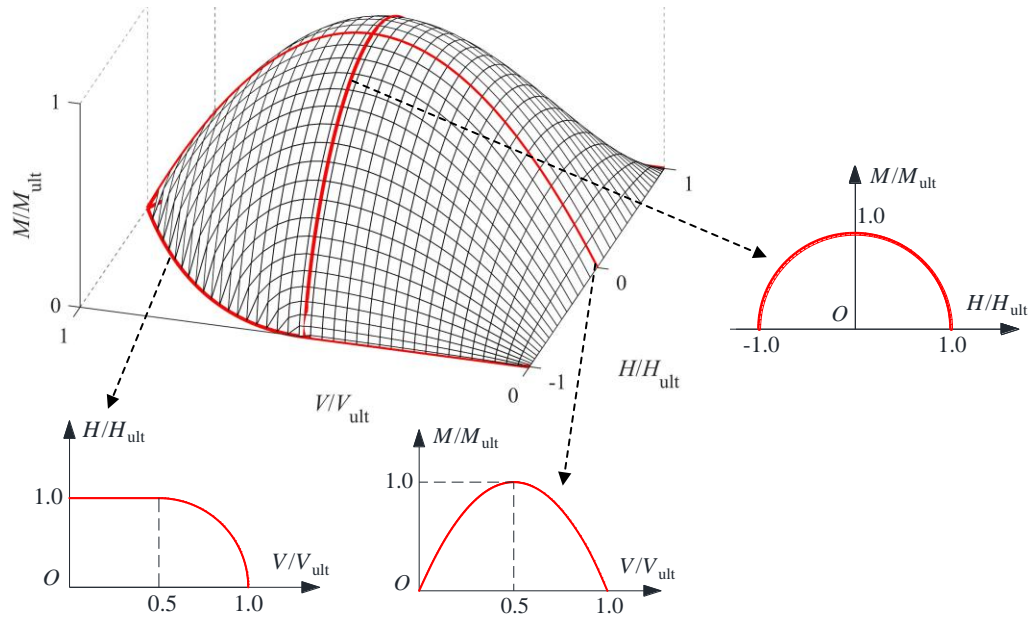
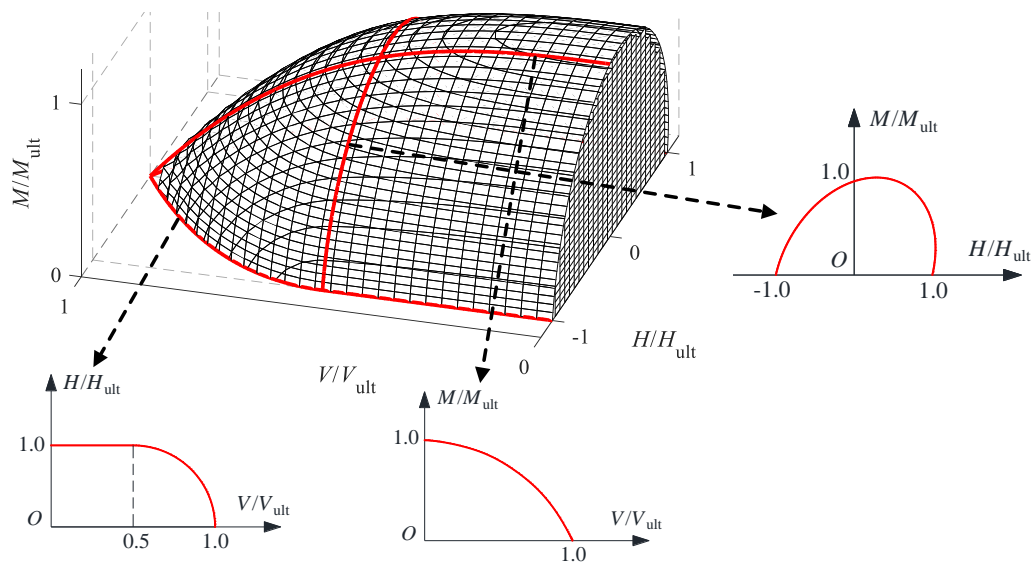


Figure 1.7: Drained $M-H$ failure envelope (Loukidis et al., 2008)

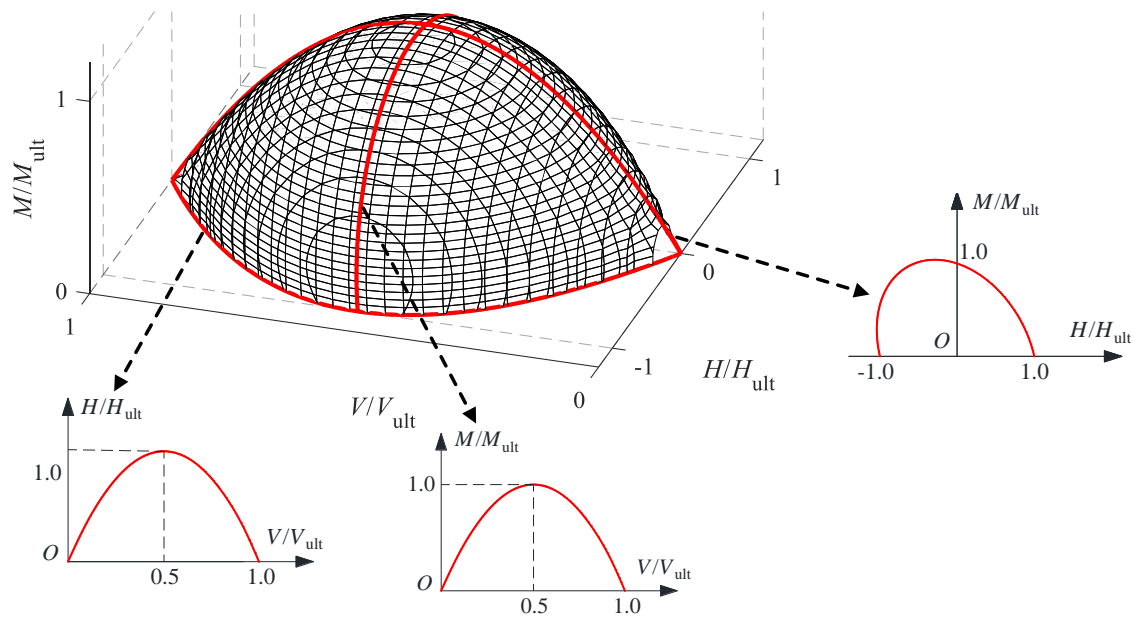
For comparison, the schematics of undrained and drained failure envelopes are compared in Figure 1.8.



(a) Undrained soil conditions & zero-tension interface



(b) Undrained soil conditions & unlimited-tension interface



(c) Drained soil conditions

Figure 1.8: Schematics of failure envelopes: (a) Undrained soil conditions & zero-tension interface; (b) Undrained soil conditions & unlimited-tension interface and (c) Drained soil conditions

Although a number of studies of undrained failure envelopes can be found in the literature, many of them are constrained to unlimited-tension interface conditions for offshore foundations and some scenarios for zero-tension interface conditions that are more suitable for onshore foundations have been ignored, such as circular embedded foundations with zero-tension interfaces. Furthermore, current studies have been primarily limited to a single soil layer with a uniform or linearly increasing undrained shear strength profile. However, onshore clay deposits often have a thin layer of stiff crust with a relatively high undrained shear strength developed from weathering, desiccation and chemical process (Lutenegger, 1995). The effect of a surficial crust on the failure envelope for shallow foundations is still not well investigated.

In contrast to undrained soil conditions, studies of drained failure envelopes are relatively sparse and most of them have been developed using experimental results. Numerical analyses of drained failure envelopes that involve high soil friction angles often converge

rather slowly, particularly for cases using a non-associated flow rule (much slower convergence rate than an associated-flow rule and convergence issues always occur). Numerical studies of drained failure envelopes available in the literature are confined to strip foundations and purely frictional sands in the absence of soil cohesion. However, the drained failure envelope for cohesive-frictional soils, such as over-consolidated clays, has not been addressed.

In addition, current studies of the failure envelope focus primarily on load combinations of vertical (V), horizontal (H) and moment (M) loads. However, environmental loads on structures are often not co-planar, and transverse loads can also induce torsional effects on the foundation (Bienen et al., 2007). Thus, the influence of torsional loads (T) should not be ignored for failure envelopes of shallow foundations. Although the torsional loading effects were investigated by some workers previously (e.g. Abyaneh et al., 2015; Feng et al., 2017; Shen et al., 2017), those studies are limited to rectangular foundations under undrained soil conditions using unlimited-tension interfaces.

1.1.2 Elastic behavior of shallow foundations

Estimation of the serviceability limit state of shallow foundations under working loads can also be of great significance, particularly for large onshore and offshore structures, such as wind turbines and oil and gas platforms. For example, the rocking stiffness of wind turbine foundations in particular is considered to be a critical design parameter, since it controls the location of the center of gravity with respect to the foundation of the turbine (Lang, 2012). As mentioned above, these shallow foundations are generally subjected to combined VHMT loads induced by environmental and structural effects.

A variety of analytical solutions for elastic foundation stiffnesses (Reissner and Sagoci, 1944; Spence, 1968; Gerrard and Harrison, 1970; Poulos and Davies, 1974) have been derived based on theories that assume homogeneous elastic half-spaces subjected to uniaxial vertical, horizontal, moment and torsional loads, as shown by Eq. (1.5).

$$K_V = \frac{4}{1 - \mu} \left(1 + \frac{d}{D} \right) \quad (1.5)$$

$$K_{HH} = \frac{8}{2 - \mu} \left(1 + \frac{4d}{3D} \right)$$

$$K_{MM} = \frac{8}{3(1 - \mu)} \left(1 + \frac{4d}{D} \right)$$

$$K_T = \frac{16}{3} \left(1 + \frac{16d}{3D} \right)$$

where K_V , K_{HH} , K_{MM} and K_T are the vertical, horizontal, moment and torsional foundation stiffness coefficients, respectively; μ is the Poisson's ratio of soil; d is the foundation embedment depth; and D is the foundation diameter.

Bell (1991) demonstrated with finite element analysis that the cross-coupling effects between the vertical, horizontal and rocking behavior can be expressed in a matrix form (Eq. (1.6)). The sign conventions for the loads and deformations are shown in Figure 1.9.

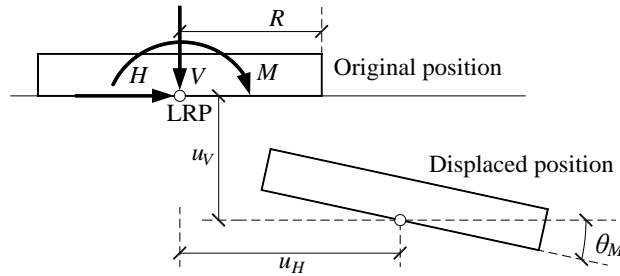


Figure 1.9: Sign conventions for loads and deformations (Osman et al., 2007)

$$\begin{bmatrix} \frac{V}{GR^2} \\ \frac{H}{GR^2} \\ \frac{M}{GR^3} \end{bmatrix} = \begin{bmatrix} K_V & 0 & 0 \\ 0 & K_{HH} & K_{HM} \\ 0 & K_{MH} & K_{MM} \end{bmatrix} \cdot \begin{bmatrix} \frac{u_V}{R} \\ \frac{u_H}{R} \\ \theta_M \end{bmatrix} \quad (1.6)$$

where u_V , u_H and θ_M are the vertical, horizontal and rotational deformations, respectively; and R is the foundation radius. K_{MH} and K_{HM} are equal, and represent the cross-coupling effects between the horizontal and rotational degrees of freedom. The stiffness coefficients are nonlinear functions of the foundation embedment ratio (i.e. d/D), soil Poisson's ratio,

foundation embedment conditions and foundation geometry (Doherty and Deeks, 2003). Despite the availability of these coupled solutions (e.g. Gazetas, 1983; Gazetas, 1991), uncoupled foundation stiffness methods still predominate in most guidelines used for shallow wind turbine foundation design, such as DNV (2016), API (2011) and ISO (2016).

Although many studies of the uncoupled and coupled foundation stiffness are available in the literature, the soil is always treated as an idealized isotropic material. However, many natural soils have been known to be anisotropic or at least transversely isotropic (cross-anisotropic) due to their deposition and complex stress history (Bishop and Hight, 1977). Graham and Houlsby (1983) and Yang et al. (2008) demonstrated that both granular soils and clays at small strains exhibit stiffness anisotropy that can be satisfactorily described with cross-anisotropic elasticity. Given the ubiquity of high-quality site investigation data, the effects of soil stiffness anisotropy on the foundation stiffnesses for shallow foundations may also be evaluated. In addition, studies of torsional foundation stiffness are relatively sparse, since it is often considered as a constant regardless of soil Poisson's ratio. Given that this is included as a load combination case in some of the design guidelines, more accurate estimation of the torsional foundation stiffness, accounting for foundation embedment, soil stiffness heterogeneity and anisotropy, would also be a useful analytical tool for industry.

The abovementioned methods for estimating the foundation bearing capacity and deformation are all for static load cases. It should be noted that wind turbine foundations are primarily subjected to cyclic loading induced by wind and the foundation of a wind turbine will experience millions of load cycles. Cyclic loading can lead to the reduction in soil strength and foundation stiffness and may cause resonant vibration (Gazetas, 1991; El Naggar, 2001), therefore, these cyclic loading effects should also be included for the design of this type of foundations.

1.2 Objectives of the research

The overall aim of this work was to create appropriate ultimate limit and serviceability limit state design tools for large onshore shallow foundations of wind turbines. The specific objectives can be summarized as follows:

- To investigate the general coupled VHMT load failure envelope of circular foundations subject to a zero-tension interface for undrained soil conditions, and to examine the effects of soil strength heterogeneity and foundation embedment on the VHMT load failure envelope.
- To evaluate the effects of a surficial crust layer of the soil on the undrained VHMT load failure envelope for circular surface foundations.
- To study the drained VHMT load failure envelope for circular surface foundations on cohesive-frictional soils.
- To assess the coupled elastic stiffness coefficients for circular surface and embedded foundations resting on cross-anisotropic soils with linearly increasing stiffness with depth under combined VHMT loads.

1.3 Thesis outline

In line with the aforementioned research aims, this thesis has been divided into six chapters. Except for the introductory and concluding chapters, each chapter has its own introduction, literature review and list of references due to the integrated-article format. This thesis has been organized as follows:

- **Chapter 1:** Provides an overview of the methods for bearing capacity and deformation assessments of large shallow wind turbine foundations. The classical bearing capacity method and the failure envelope approach are separately reviewed. The foundation stiffness method available in the literature is summarized and the background on the cross-anisotropic elastic soil is provided. A rationale for the research conducted is provided. The objectives and structure of the thesis are also included in this chapter.
- **Chapter 2:** Investigates the full VHMT failure envelope of circular foundations under a zero-tension interface for undrained soil conditions. The effects of soil strength heterogeneity and foundation embedment on the VHMT failure envelope have been separately studied. A full 4-D VHMT failure envelope is estimated using the finite element method.

- **Chapter 3:** Evaluates the effects of a surficial crust layer (thickness and strength) on the undrained VHMT failure envelope for circular surface foundations. Undrained conditions have been considered for both the crustal layer and the underlying soil. The general expression of the 4-D VHMT failure envelope is derived.
- **Chapter 4:** Presents the drained VHMT failure envelope for circular surface foundations on cohesive-frictional soils under a zero-tension interface. The effects of the soil friction angle and soil self-weight on the VHMT failure envelope have been studied. Analytical equations for the drained 4-D VHMT failure envelope are estimated.
- **Chapter 5:** Obtains the coupled elastic foundation stiffness coefficients for circular foundations resting on cross-anisotropic soils under combined VHMT loads. A three-parameter cross-anisotropic model has been used to model the elastic soil behavior. Foundation stiffnesses accounting for the effects of foundation embedment, soil stiffness non-homogeneity and anisotropy have been estimated using finite element analysis.
- **Chapter 6:** Provides an example of the application of the failure envelope and foundation stiffness approaches for a shallow foundation of a typical Canadian wind turbine. The main findings of this research, along with recommendations for further related studies, are also summarized.

1.4 References

- Abyaneh, S. D., Ojo, A., Maconochie, A., and Haghghi, A. (2015). The undrained bearing capacity of shallow foundations subjected to three-dimensional loading including torsion. *In Proceedings of the 25th International Ocean and Polar Engineering Conference*, Kona, Hawaii, 21-26 June 2015. International Society of Offshore and Polar Engineers, Cupertino, pp. 668-674.
- Allotey, N., and El Naggar, M. H. (2003). Analytical moment–rotation curves for rigid foundations based on a Winkler model. *Soil Dynamics and Earthquake Engineering*, 23(5), 367-381.
- Allotey, N., and El Naggar, M. H. (2008a). An investigation into the Winkler modeling of the cyclic response of rigid footings. *Soil Dynamics and Earthquake Engineering*, 28(1), 44-57.

- Allotey, N., and El Naggar, M. H. (2008b). Generalized dynamic Winkler model for nonlinear soil–structure interaction analysis. *Canadian Geotechnical Journal*, 45(4), 560-573.
- API (American Petroleum Institute) (2011). API Recommended Practice, Geotechnical and Foundation Design Considerations. American Petroleum Institute, Washington, D.C.
- Bell, R. W. (1991). The analysis of offshore foundations subjected to combined loading. Master's dissertation, University of Oxford, Oxford, UK.
- Bienen, B., Byrne, B. W., Houlsby, G. T., and Cassidy, M. J. (2006). Investigating six-degree-of-freedom loading of shallow foundations on sand. *Géotechnique*, 56(6), 367-379.
- Bienen, B., Gaudin, C., and Cassidy, M. J. (2007). Centrifuge tests of shallow footing behaviour on sand under combined vertical-torsional loading. *International Journal of Physical Modelling in Geotechnics*, 7(2), 01-21.
- Bishop, A. W., and Hight, D. W. (1977). The value of Poisson's ratio in saturated soils and rocks stressed under undrained conditions. *Géotechnique*, 27(3), 369-384.
- Butterfield, R., and Gottardi, G. (1994). A complete three-dimensional failure envelope for shallow footings on sand. *Géotechnique*, 44(1), 181-184.
- Byrne, B. W. (2000). Investigations of suction caissons in dense sand. Doctoral dissertation, University of Oxford, Oxford, UK.
- Cassidy, M. J. (1999). Non-linear analysis of jack-up structures subjected to random waves. Doctoral dissertation, University of Oxford, Oxford, UK.
- Cerato, A. B., and Lutenegro, A. J. (2007). Scale effects of shallow foundation bearing capacity on granular material. *Journal of Geotechnical and Geoenvironmental Engineering*, 133(10), 1192-1202.
- Chen, W. F. (2013). Limit analysis and soil plasticity. Elsevier, Amsterdam, Netherlands.
- Conte, E., Donato, A., and Troncone, A. (2013). Progressive failure analysis of shallow foundations on soils with strain-softening behaviour. *Computers and Geotechnics*, 54, 117-124.
- Cremer, C., Pecker, A., and Davenne, L. (2001). Cyclic macro - element for soil - structure interaction: material and geometrical non - linearities. *International Journal for Numerical and Analytical Methods in Geomechanics*, 25(13), 1257-1284.
- DNV GL (Det Norske Veritas GL) (2016). DNVGL-ST-0126: Support structures for wind turbines. DNV GL Group, Høvik, Norway.
- Doherty, J. P., and Deeks, A. J. (2003). Elastic response of circular footings embedded in a non-homogeneous half-space. *Géotechnique*, 53(8), 703-714.
- EI Naggar M. H. (2001). Dynamics of Foundations. In: Rowe R. K. Geotechnical and Geoenvironmental Engineering Handbook. Springer, Boston, M.A.

- El-Marassi, M. (2011). Investigation of hybrid monopile-footing foundation systems subjected to combined loading. Doctoral dissertation. The University of Western Ontario, London, Ont.
- El-Marassi, M., Newson, T., El-Naggar, M. H., and Stone, K. (2008). Numerical modeling of the performance of a hybrid monopiled-footing foundation. *In Proceedings of the 61st Canadian Geotechnical Conference*, Edmonton, Canada, 21-24 September 2008. Canadian Geotechnical Society, pp. 97-104.
- Feng, X, Randolph, MF, Gourvenec, S, and Wallerand, R (2014). Design approach for rectangular mudmats under fully three-dimensional loading. *Géotechnique*, 64(1), 51-63.
- Feng, X., Randolph, M. F., and Gourvenec, S. (2017). An analytical solution for the undrained horizontal–torsional resistance of mudmats. *Géotechnique*, 67(4), 325-337.
- Gazetas, G. (1983). Analysis of machine foundation vibrations: state of the art. *International Journal of Soil Dynamics and Earthquake Engineering*, 2(1), 2-42.
- Gazetas, G. (1991). Formulas and charts for impedances of surface and embedded foundations. *Journal of geotechnical engineering*, 117(9): 1363-1381.
- Gerrard, C.M., and Harrison, W.J. (1970). Circular loads applied to a cross-anisotropic half space. C.S.I.R.O. *Australian Division Applied Geomechanics*, Technical Paper No. 8.
- Gourvenec, S (2007). Shape effects on the capacity of rectangular footings under general loading. *Géotechnique*, 57(8), 637-646.
- Gourvenec, S, and Randolph, M (2003). Effect of strength non-homogeneity on the shape of failure envelopes for combined loading of strip and circular foundations on clay. *Géotechnique*, 53(6), 575-586.
- Graham, J., and Houlsby, G. T. (1983). Anisotropic elasticity of a natural clay. *Géotechnique*, 33(2), 165-180.
- Hansen, J. B. (1970). A revised and extended formula for bearing capacity. Bulletin No. 28, Danish Geotechnical Institute, Copenhagen, Denmark. 5-11.
- Hjiaj, M., Lyamin, A. V., and Sloan, S. W. (2004). Bearing capacity of a cohesive-frictional soil under non-eccentric inclined loading. *Computers and Geotechnics*, 31(6), 491-516.
- Houlsby, G. T., and Cassidy, M. J. (2002). A plasticity model for the behaviour of footings on sand under combined loading. *Géotechnique*, 52(2), 117-129.
- ISO (International Standards Organization). (2016). ISO 19901-4: Petroleum and natural gas industries specific requirements for offshore structures – part 4: geotechnical and foundation design considerations, 2nd edition. International Standards Organization, Geneva, Switzerland.
- Kumar, J., and Khatri, V. N. (2008). Effect of footing width on N_c . *Canadian Geotechnical Journal*, 45(12), 1673-1684.

- Lang, P. J. (2012). Sensitivity of shallow wind turbine foundation design and soil response to geotechnical variance with construction cost implications. W.I.: Master's thesis Report, University of Wisconsin-Madison, Madison, W.I.
- Loukidis, D., and Salgado, R. (2011). Effect of relative density and stress level on the bearing capacity of footings on sand. *Géotechnique*, 61(2), 107-119.
- Loukidis, D., Chakraborty, T., and Salgado, R. (2008). Bearing capacity of strip footings on purely frictional soil under eccentric and inclined loads. *Canadian Geotechnical Journal*, 45(6), 768-787.
- Lutenegger, A.J. (1995). Geotechnical behavior of overconsolidated surficial clay crusts. Transportation research record No. 1479, National Academy, Washington, D.C., 61-74.
- Martin, C. M. (1994). Physical and numerical modelling of offshore foundations under combined loads. Doctoral dissertation, Oxford University, Oxford, UK.
- Meyerhof, G. G. (1963). Some recent research on the bearing capacity of foundations. *Canadian Geotechnical Journal*, 1(1), 16-26.
- Nova, R., and Montrasio, L. (1991). Settlements of shallow foundations on sand. *Géotechnique*, 41(2), 243-256.
- Osman, A. S., White, D. J., Britto, A. M., and Bolton, M. D. (2007). Simple prediction of the undrained displacement of a circular surface foundation on non-linear soil. *Géotechnique*, 57(9), 729-737.
- Perkins, S. W., and Madson, C. R. (2000). Bearing capacity of shallow foundations on sand: A relative density approach. *Journal of Geotechnical and Geoenvironmental Engineering*, 126(6), 521-530.
- Poulos, H. G., and Davis, E. H. (1974). Elastic solutions for soil and rock mechanics, John Wiley, New York, N.Y.
- Prandtl, L. (1920). Über die Häete plastischer Körper. *Nachr. Ges. Wissensch, Göttingen, math.-hys. Klasse*, 74-85.
- Reissner, E., and Sagoci, H. F. (1944). Forced torsional oscillations of an elastic half-space. I. *Journal of Applied Physics*, 15(9), 652-654.
- Reissner, H. (1924). Zum Erddruckproblem. In *Proceedings of the 1st International Congress for Applied Mechanics*. Delft, Netherlands, 22–26 April 1924. Technische Boekhandel en Drukkerij J.Waltman Jr., Delft, 295-311.
- Shen, Z, Feng, X, and Gourvenec, S (2016). Undrained capacity of surface foundations with zero-tension interface under planar VHM loading. *Computers and Geotechnics*, 73, 47-57.
- Shen, Z., Feng, X., and Gourvenec, S. (2017). Effect of interface condition on the undrained capacity of subsea mudmats under six-degree-of-freedom loading. *Géotechnique*, 67(4), 338-349.

- Spence, D. A. (1968). Self similar solutions to adhesive contact problems with incremental loading. *In Proceedings of the Royal Society of London. Series A. Mathematical and Physical Sciences*, 305(1480), pp. 55-80.
- Stone, K. J. L., Newson, T., and El-Marassi, M. (2010). An investigation of the performance of a monopiled-footing foundation. *In Proceedings of the 7th International Conference on Physical Modelling in Geotechnics*, Zurich, Switzerland, 28 June - 1 July 2010. pp. 829-833.
- Taiebat, H. A., and Carter, J. P. (2002). Bearing capacity of strip and circular foundations on undrained clay subjected to eccentric loads. *Géotechnique*, 52(1), 61-64.
- Taiebat, H. A., and Carter, J. P. (2010). A failure surface for circular footings on cohesive soils. *Géotechnique*, 60(4), 265-273.
- Tapper, L. (2013). Bearing capacity of perforated offshore foundations under combined loading. Doctoral dissertation, Oxford University, Oxford, UK.
- Terzaghi, K. (1951). Theoretical soil mechanics. Chapman & Hall, London, UK.
- Vulpe, C., Gourvenec, S., and Power, M. (2014). A generalised failure envelope for undrained capacity of circular shallow foundations under general loading. *Géotechnique Letters*, 4(3), 187-196.
- Yang, Z. X., Li, X. S., and Yang, J. (2008). Quantifying and modelling fabric anisotropy of granular soils. *Géotechnique*, 58(4), 237-248.
- Zadroga, B. (1994). Bearing capacity of shallow foundations on noncohesive soils. *Journal of geotechnical engineering*, 120(11), 1991-2008.

2 Undrained capacity of circular shallow foundations under combined VHMT loading

2.1 Introduction

Shallow foundations have been extensively used to support large onshore and offshore structures, such as wind turbines, oil and gas platforms, transmission towers and masts. For many of these structures, the load-bearing capacity of their foundations under combined loadings is particularly important due to the complex environmental loads. For example, the horizontal loads on a wind turbine caused by combined wind, waves and current can be substantial and a large tower height can lead to significant moment loading on the foundation. Traditional analytical methods for these types of structure are based on classical solutions for the uniaxial vertical bearing capacity of shallow foundations. To account for the effect of load inclination and eccentricity, the load inclination factor and the effective foundation area are introduced to the conventional method, as recommended by some geotechnical design guidelines (e.g. DNV, 2016). However, these simple, traditional methods may not be accurate enough in some cases, because the load inclination and eccentricity effects are separately considered (Gourvenec, 2007). In general, this approach can be conservative for combined V - H - M loading cases (Taiebat and Carter, 2002), while it has been shown to be non-conservative for strip foundations on soils with shear strength increasing with depth (Ukritchon et al., 1998).

A more recent design approach is the failure envelope method, which explicitly incorporates the load interaction effects of the various load components (Shen et al., 2017). This method has been recommended as an alternative to conventional theory in API (2011) and ISO (2016). Failure envelopes under undrained conditions for different types of foundations (e.g. strip (Bransby and Randolph, 1998), rectangular (Gourvenec and Randolph, 2003) and circular (Shen et al., 2016) foundations), homogeneous (Taiebat and Carter, 2010) or non-homogeneous (Feng et al., 2014) soils, and zero-tension (Shen et al., 2016) or unlimited-tension (Gourvenec and Randolph, 2003) interface conditions have been previously studied. These studies focus primarily on load combinations of vertical (V), horizontal (H) and moment (M) loads. However, environmental loads on the structure

are often not co-planar, and transverse loads can also induce torsional effects on the foundation (Bienen et al., 2007). Thus, the influence of torsional loads should not be ignored for failure envelopes of shallow foundations. Although the torsional loading effects were investigated by some workers previously (e.g. Shen et al., 2017; Abyaneh et al., 2015; Feng et al., 2017), those studies are limited to rectangular foundations using an unlimited-tension interface. This form of interface is often assumed for offshore structures, particularly for the case of skirted foundations. However, the reliability of under-base suction in offshore environments can be conditional (Sheng et al., 2016). Moreover, onshore shallow foundations can uplift and separate from the soil under large overturning moments, because the soil-foundation interface is unable to resist tensile loads. Since many of the aforementioned studies have concentrated on offshore cases with unlimited-tension interfaces, this interface condition has been generally ignored.

To address these omissions in the literature, the object of this study is to investigate the full VHMT failure envelope of circular foundations under a zero-tension interface for undrained soil conditions. The effects of soil strength heterogeneity and foundation embedment on the VHMT failure envelope have been separately studied. A full 4-D VHMT failure envelope is estimated using the finite element (FE) method.

2.2 Method – finite element analysis

In this paper, the effects of soil strength heterogeneity and foundation embedment have been separately studied using: (i) surface foundations on heterogeneous soils and (ii) embedded foundations in homogeneous soils.

2.2.1 Material models and interface conditions

A linear elastic perfectly plastic constitutive relationship with a Mohr-Coulomb (M-C) failure criterion was used to model the soil behavior. The M-C criterion devolves to the Tresca criterion under undrained soil conditions, which is defined by three soil parameters: the undrained Young's modulus, E_u , Poisson's ratio, μ , and the undrained shear strength, s_u . To study the effect of the soil strength heterogeneity, the undrained soil shear strength was considered to linearly increase with depth from the ground surface (see Figure 2.1):

$$s_u = s_{u0} + kz \quad (2.1)$$

where s_{u0} is the undrained shear strength at foundation level; k is the strength increase per depth. For the analyses, s_{u0} was held constant at 100 kPa and the Poisson's ratio of the undrained soil was taken as 0.495. The dimensionless soil strength heterogeneity ratio defined by $\kappa = kD/s_{u0}$ (Gourvenec and Randolph, 2003) was taken as 0 (homogeneous), 2, 6 and 10. A sufficiently large E_u/s_{u0} ratio of 10000 was selected to minimize mesh distortion (Abyaneh et al., 2015). The foundation was assumed to act as a rigid body. A load reference point (LRP) attached to the center of the base of foundation was utilized to apply prescribed displacements or loads, as shown in Figure 2.1.

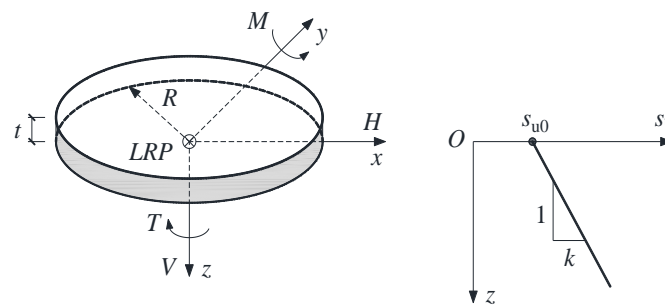


Figure 2.1: Sign conventions and soil strength profile

Similar to Shen et al. (2016), the FE analyses considered a zero-tension rough base that allows separation of the foundation from the soil. The zero-tension rough base can be modelled using a Coulomb friction with a friction coefficient of 20 (Shen et al., 2016). For embedded foundations, a reduced interface shear strength (i.e. intermediate roughness) for side and top interfaces is always recommended due to installation or in-service loading processes (Gourvenec et al., 2011; Deshpande, 2016). In this analysis, smooth side and top conditions (i.e. an interface adhesion factor $\alpha = 0$ and the shear strength on the interface $\alpha s_u = 0$) for the embedded foundations were considered to provide more conservative estimations. The same consideration was also made by Gourvenec and Mana (2011).

2.2.2 Geometry and mesh

The FE analysis was conducted using the software ABAQUS (Dassault Systèmes, 2016). The diameter (D) and thickness (t) of the circular foundation used in this paper are 19 m

and 3 m, representing typical dimensions for current onshore wind turbines used in North America. The embedment depth ratio, d/D (d is the foundation embedment depth), was taken as 0, 0.16, 0.30 and 0.50 to span cases of practical interest. To avoid the effects of the model boundaries on the development of failure mechanisms, the mesh length, L , and mesh height, H , were taken as 120 m and 50 m, following the recommendations of Deshpande (2016).

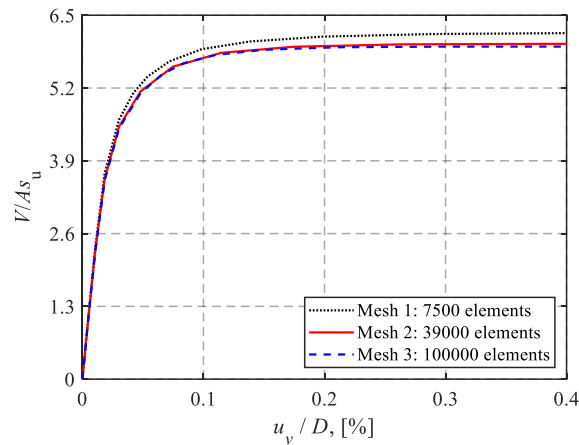
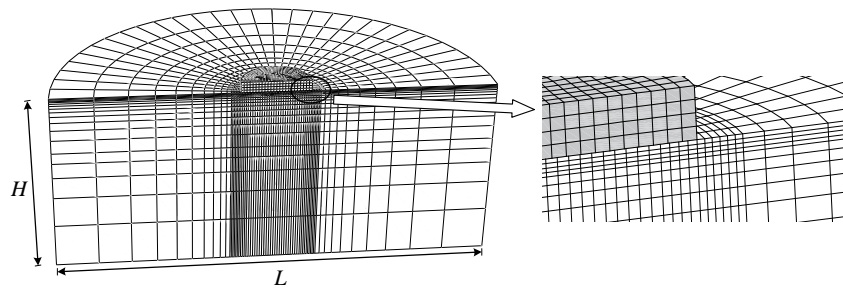
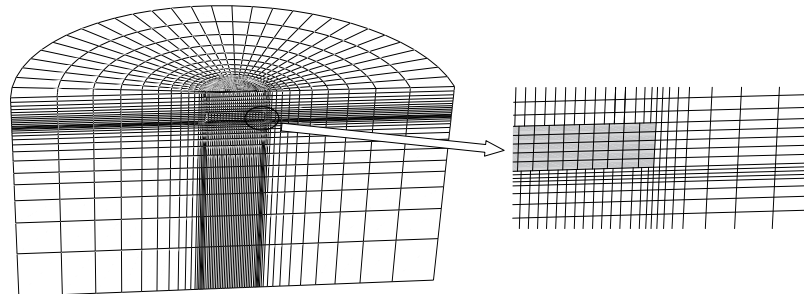


Figure 2.2: Mesh convergence study for a homogeneous soil



(a) Surface foundation



(b) Embedded foundation ($d/D = 0.50$)

Figure 2.3: Half-view of the FE mesh: (a) Surface foundation and (b) Embedded foundation ($d/D = 0.50$)

A mesh convergence study was carried out for a number of cases and a typical result is shown in Figure 2.2. The difference between the ultimate vertical loads using Mesh 2 (39000 elements) and 3 (100000 elements) is about 2%. However, the model solution with Mesh 3 takes about 6 times longer than that using Mesh 2. Therefore, Mesh 2 was adopted in the analysis. Figure 2.3 shows the three-dimensional half model using Mesh 2. The mesh was composed of around 39000 brick elements (i.e. first-order, 8-noded brick element with reduced integration and hourglass control). To capture the intense stress concentration close to the foundation edge and the large plastic shear strains at the interface, the soil regions in the vicinity of the foundation edge and the horizontal thin soil layer close to the interface were carefully refined (Gourvenec and Randolph, 2003). The cylindrical circumference of the soil was constrained to prevent out-of-plane translations, and the bottom of the soil domain was fixed in the three orthogonal directions.

2.2.3 Sign conventions and loading paths

The sign conventions for the loads are also shown in Figure 2.1. In the analyses, the horizontal and moment loads were considered to be in the same plane.

Probe tests and swipe tests were employed to detect the failure envelopes under various load conditions. In a probe analysis, a fixed-ratio of displacement is imposed to the foundation to track the failure point on the failure envelope (for $M-H$, $H-T$ and $M-T$ failure envelopes, a vertical load is first applied at the LRP of the foundation). A probe test can only obtain a single point on a failure envelope.

The swipe test brings the foundation to a collapse state in coordinate direction 1 first (displacement-controlled), followed by a displacement applied in coordinate direction 2, during which the increment of the displacement in coordinate direction 1 remains zero (Gourvenec and Randolph, 2003). For some cases the swipe test cannot capture the entire failure envelope due to convergence issues, hence additional probe tests were carried out to facilitate the analysis. Three typical failure envelopes obtained using both swipe and probe tests are shown in Figure 2.4. However, swipe tests can considerably underestimate the failure envelopes for embedded foundations (Gourvenec and Randolph, 2003).

Therefore, swipe tests were performed only for surface foundations and probe tests were utilized for embedded foundations.

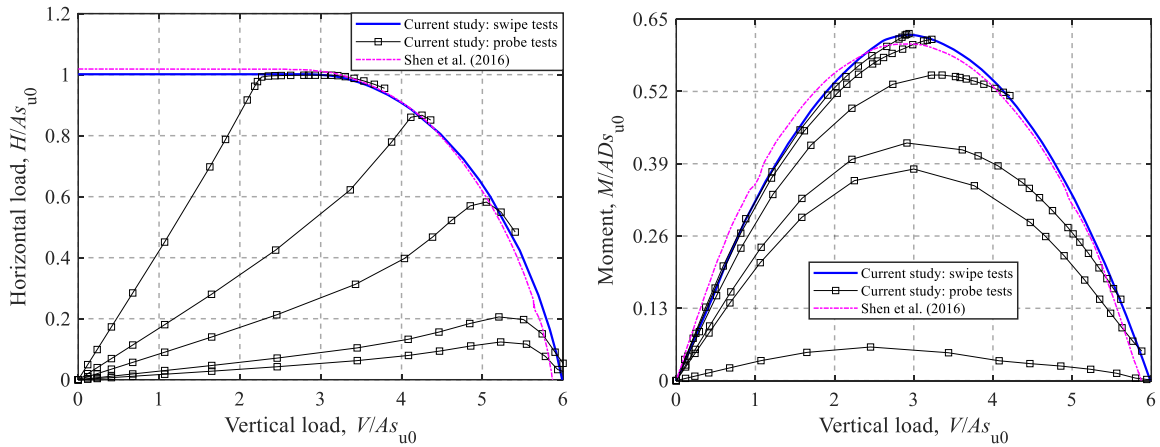
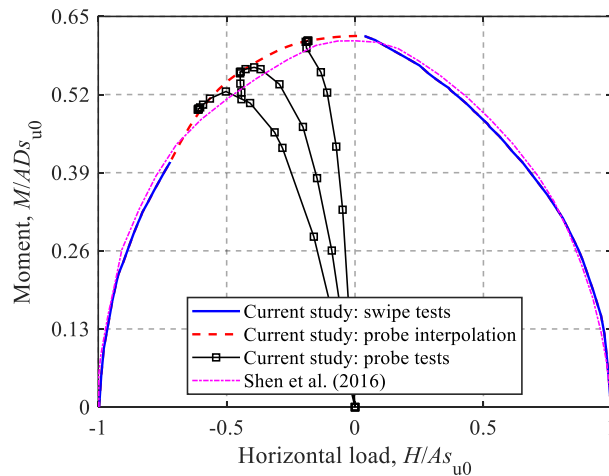
(a) H - V (b) M - V (c) M - H at $V/V_{ult} = 0.50$

Figure 2.4: VHM failure envelopes of a surface foundation for $\kappa = 0$: (a) H - V ; (b) M - V and (c) M - H at $V/V_{ult} = 0.50$

2.3 Surface foundations on non-homogeneous soils

For VHM loading, Shen et al. (2016) has numerically studied the failure envelopes for circular *surface* foundations on non-homogeneous soils under a zero-tension interface. These envelopes have been confirmed during the current study and for reasons of brevity

only a few cases are shown in Figure 2.4. There is an excellent match between the two sets of envelopes and this also provides validation of the methods used herein. In this section, the effects of torsion on the more general VHMT failure envelopes are assessed and discussed. The FE results and the corresponding closed-form equations for torsion-vertical (T - V), horizontal-torsion (H - T) and moment-torsion (M - T) envelopes are presented.

2.3.1 Pure uniaxial capacity

The ultimate loads for vertical, horizontal and torsional modes are referred to as the corresponding uniaxial load-carrying capacities in the absence of other loading modes. As the foundation with a zero-tension interface cannot resist moment loading without vertical loads, the ultimate moment capacity is referred to as the maximum moment load under vertical loading (Shen et al., 2016). The uniaxial bearing capacity factors are defined as:

$$\begin{aligned} v_0 &= V_{\text{ult}}/(As_{u0}) \\ h_0 &= H_{\text{ult}}/(As_{u0}) \\ m_0 &= M_{\text{ult}}/(ADs_{u0}) \\ t_0 &= T_{\text{ult}}/(ADs_{u0}) \end{aligned} \quad (2.2)$$

where A is the soil-foundation contact area. The estimated values of v_0 , h_0 , m_0 and t_0 for soils with different heterogeneity ratios are summarized in Table 2.1.

Table 2.1: Uniaxial bearing capacity factors for soils with various soil strength heterogeneity ratios

κ	v_0	h_0	m_0	t_0
0	6.00	1.00	0.62	0.33
2	7.51	1.00	0.74	0.33
6	9.59	0.99	0.91	0.33
10	11.29	1.00	1.03	0.34

The values of v_0 , h_0 and m_0 summarized in Table 2.1 generally agree with the results of Shen et al. (2016) (with difference less than 3%). Similar to the horizontal bearing capacity,

the torsional bearing capacity exhibits independence from the heterogeneity ratio (He and Newson, 2019), as the failure state for horizontal and torsional modes is reached only when the shear stress of s_{u0} is fully developed.

2.3.2 Torsion-Vertical loading

The T - V failure envelopes for soils with different soil heterogeneity ratios are shown in Figure 2.5. Figure 2.5(b) indicates that the T - V envelopes normalized by the corresponding ultimate capacities collapse into a narrow band regardless of the heterogeneity ratios.

Feng et al. (2014) provided an expression for the normalized T - V failure envelopes for rectangular foundations with an unlimited-tension interface, which was then used by Shen et al. (2017) to apply to a zero-tension interface:

$$T/T_{\text{ult}} = [1 - 4(V/V_{\text{ult}} - 0.5)^2]^{0.4}, V/V_{\text{ult}} > 0.5 \quad (2.3)$$

$$T/T_{\text{ult}} = 1, V/V_{\text{ult}} \leq 0.5$$

Abyaneh et al. (2015) proposed a similar equation for circular foundations under an unlimited-tension interface condition:

$$V/V_{\text{ult}} = 0.5 + 0.5[1 - (T/T_{\text{ult}})^{2.5}]^{0.3}, V/V_{\text{ult}} > 0.5 \quad (2.4)$$

$$T/T_{\text{ult}} = 1, V/V_{\text{ult}} \leq 0.5$$

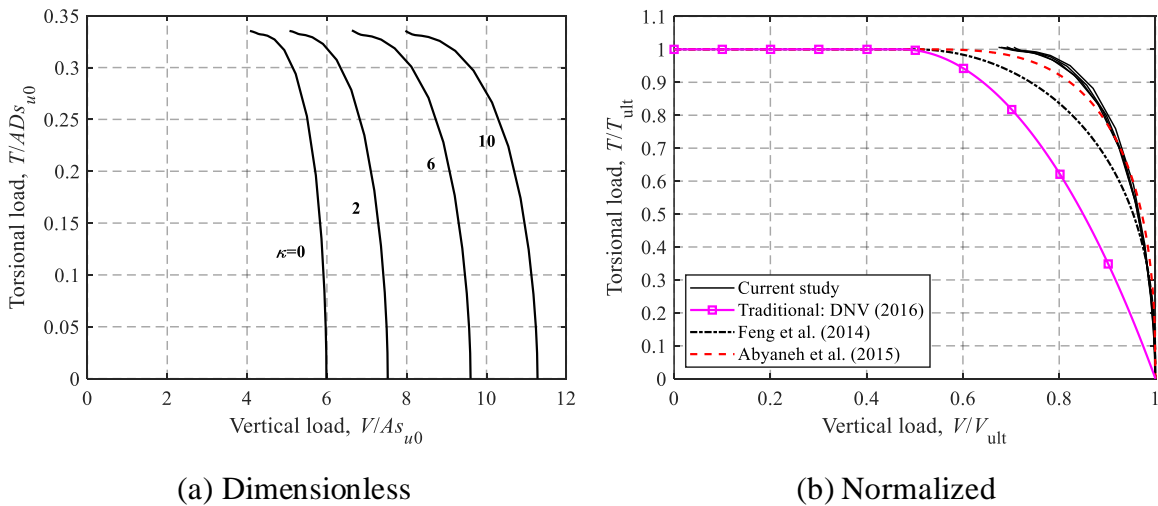


Figure 2.5: T - V failure envelopes: (a) Dimensionless and (b) Normalized

Eqs. (2.3) and (2.4) are presented in Figure 2.5 for comparison. This shows that Eq. (2.4) can provide a reasonable approximation, although it was developed for an unlimited-tension interface. In contrast, Eq. (2.3) gives more conservative results compared with the FE-calculated curves. Traditional methods from DNV (2016) using the concept of the effective foundation area are also compared in Figure 2.5. The results from the traditional methods lies entirely inside the FE-calculated failure envelopes and are more conservative than the two equations.

2.3.3 Horizontal-Torsion loading

Figure 2.6 presents the H - T failure envelopes normalized by the corresponding maximum values for $V/V_{\text{ult}} = 0.25, 0.50$ and 0.75 . It can be seen that the H - T failure envelopes are independent of the soil strength heterogeneity ratio, since the failure mechanisms under horizontal and torsional loading involve only the interface strength. Finnie and Morgan (2004) proposed Eq. (2.5) to model the H - T relationship without moment:

$$(H/H_{\text{max}})^l + (T/T_{\text{max}})^n = 1 \quad (2.5)$$

where H_{max} and T_{max} are the maximum horizontal and torsional loads for a given V/V_{ult} .

As shown before, for $V/V_{\text{ult}} \leq 0.50$, $H_{\text{max}} = H_{\text{ult}}$ and $T_{\text{max}} = T_{\text{ult}}$ (see Eq. (2.3)). For $V/V_{\text{ult}} > 0.50$, T_{max} can be calculated from Eq. (2.3) as:

$$T_{\text{max}} = [1 - (2V/V_{\text{ult}} - 1)^{3.33}]^{0.4} \cdot T_{\text{ult}} \quad (2.6)$$

H_{max} for $V/V_{\text{ult}} > 0.50$ can be evaluated using Green's original solution (Green, 1954; Sheng et al., 2016) as $H_{\text{max}} = [1 - (2V/V_{\text{ult}} - 1)^2] \cdot H_{\text{ult}}$.

The dimensionless powers, l and n in Eq. (2.5), depend on the foundation geometry. Yun et al. (2009) recommended $l = n = 1.75$ based on the FE analysis of circular and square foundations with an unlimited-tension interface.

The curves of the traditional methods (DNV, 2016) and Eq. (2.5) with $l = n = 1.75$ are also presented together with the FE-calculated results in Figure 2.6. It shows that Eq. (2.5) with $l = n = 1.75$ can be considered to be an acceptable choice to fit the H - T failure envelopes,

although it provides relatively reduced results than the current study under the condition of $V/V_{ult} = 0.75$. In contrast, for all the levels of vertical load mobilizations, the traditional method results in more conservative failure envelopes. The failure curves for $V/V_{ult} = 0.50$ and 0.25 are almost the same due to the fact that the maximum horizontal or torsional forces that can be mobilized for a surface foundation under undrained conditions depend only on the interface resistance under a condition of $V/V_{ult} \leq 0.50$.

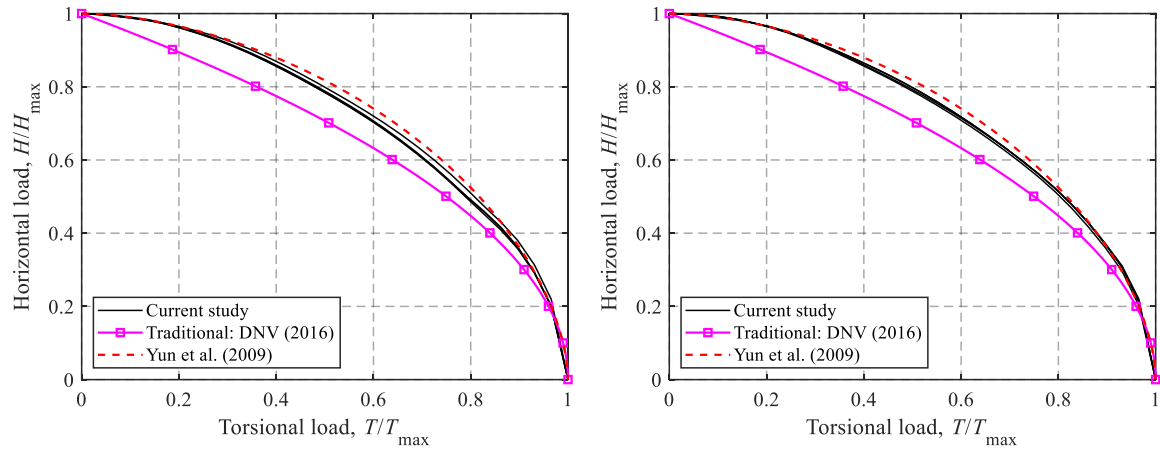
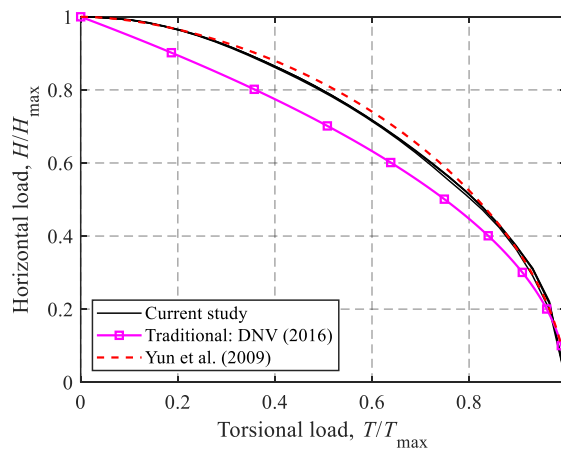
(a) $V/V_{ult} = 0.75$ (b) $V/V_{ult} = 0.50$ (c) $V/V_{ult} = 0.25$

Figure 2.6: H - T failure envelopes: (a) $V/V_{ult} = 0.75$; (b) $V/V_{ult} = 0.50$ and (c) $V/V_{ult} = 0.25$

2.3.4 Moment-Torsion loading

The ultimate load-carrying capacity under combined moment and torsional loading at $V/V_{\text{ult}} = 0.25, 0.50$ and 0.75 for the four soil strength heterogeneity ratios is compared in Figure 2.7. The dimensionless failure envelopes in Figure 2.7(a) shows the expansion of curves with the soil strength heterogeneity ratio. It can be seen that the M - T failure envelopes normalized by the corresponding maximum loads (see Figure 2.7(b) ~ (d)) fall into a tight band for all the levels of vertical load mobilizations, which eliminates their dependence on the soil heterogeneity ratio.

Shen et al. (2017) proposed a M - T relationship for rectangular foundations under a zero-tension interface condition:

$$(M/M_{\text{max}})^p + (T/T_{\text{max}})^q = 1, \text{ for } V/V_{\text{ult}} \leq 0.5 \text{ and } 0 \leq \kappa \leq 10 \quad (2.7)$$

where p and q are dimensionless parameters. Shen et al. (2017) suggested $p = 1.5$ and $q = 2.0$. Based on the results of rectangular foundations with an unlimited-tension interface, Feng et al. (2014) obtained two different powers: $p = 6.0$ and $q = 2.0$.

The calculation of T_{max} also follows Eq. (2.3). M_{max} for different vertical load mobilizations can be evaluated based on the relationship proposed by Gourvenec (2007):

$$M/M_{\text{ult}} = 4[V/V_{\text{ult}} - (V/V_{\text{ult}})^2] \quad (2.8)$$

The analytical relationship (i.e. Eq. (2.7)) and the results from the conventional methods are also shown in Figure 2.7 against the FE-calculated failure envelopes. It can be seen that the curves produced with $p = 1.5$ and $q = 2.0$ (i.e. Shen et al., 2017) always lie inside the failure envelopes, while the case of $p = 6.0$ and $q = 2.0$ (i.e. Feng et al., 2014) predicts envelopes that go significantly beyond the FE-calculated results. To gain better predictions of the current study, p and q of Eq. (2.7) can be adjusted. As shown in Figure 2.7, the case of $p = 2.5$ and $q = 2.0$ can provide more satisfactory predictions. In contrast, the failure envelopes derived from DNV (2016) appear to be approximately linear relationships between T/T_{ult} and M/M_{ult} and lie entirely inside the FE-calculated failure envelopes for various vertical load levels.

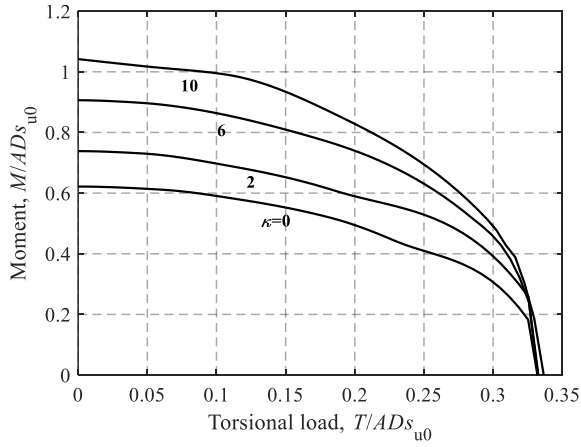
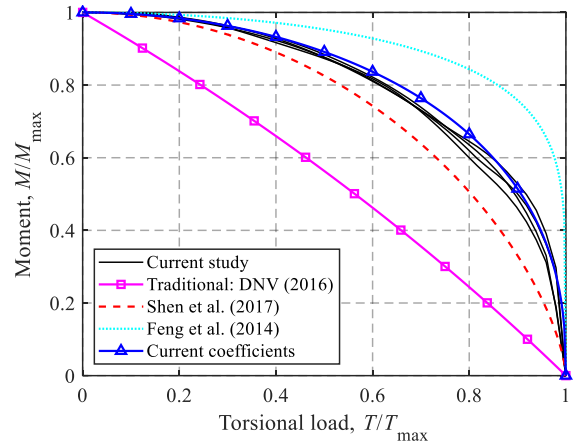
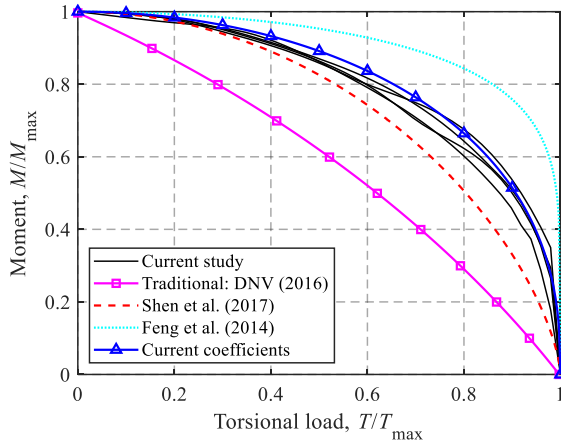
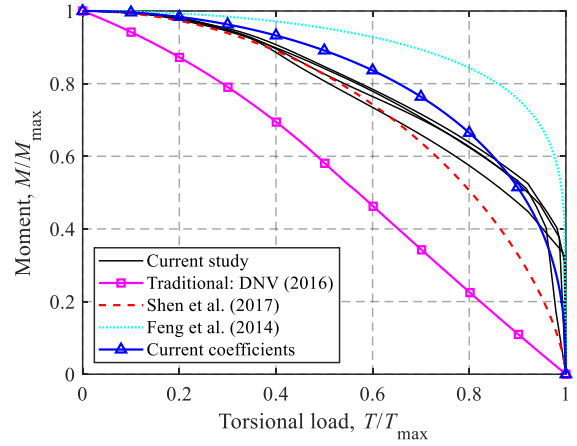
(a) Dimensionless, $V/V_{ult} = 0.50$ (b) Normalized, $V/V_{ult} = 0.75$ (c) Normalized, $V/V_{ult} = 0.50$ (d) Normalized, $V/V_{ult} = 0.25$

Figure 2.7: M - T failure envelopes: (a) Dimensionless, $V/V_{ult} = 0.50$; (b) Normalized, $V/V_{ult} = 0.75$; (c) Normalized, $V/V_{ult} = 0.50$ and (d) Normalized, $V/V_{ult} = 0.25$

2.4 Embedded foundations in a homogeneous soil

2.4.1 Pure uniaxial capacity

The depth correction factor, d_c , is defined as the ratio of the dimensionless capacity for embedded foundations (i.e. $d/D > 0$) to that for surface foundations (i.e. $d/D = 0$), i.e.

$$d_c = \frac{N_{d/D}}{N_{d/D=0}} \quad (2.9)$$

where $N_{d/D} = \frac{V_{ult}}{A \cdot s_u}$ for the vertical capacity, $N_{d/D} = \frac{H_{ult}}{A \cdot s_u}$ for the horizontal capacity and $N_{d/D} = \frac{M_{ult}}{A \cdot D \cdot s_u}$ for the moment capacity. For embedded foundations, the torsional capacity is related only to the base interface (side and top interfaces are smooth), therefore, the embedment ratio does not affect the torsional capacity.

The relationships between the depth factors and embedment depth ratios are shown in Figure 2.8 along with results from design guidelines and previous results. Since the capacity factors for surface foundations are used for normalization, the depth factors always start from 1 at $d/D = 0$. Since DNV (2016) does not provide the embedment factor for the traditional method, the embedment factors recommended in DNV (2017) and ISO (2016) are applied. The FE results of Gourvenec (2008) for an embedded strip foundation with unlimited-tension interfaces are also compared in Figure 2.8 to show the difference between unlimited-tension and zero-tension interface conditions. Compared with the current FE results, DNV (2017) provides considerably conservative results with differences of about 22% and 47% for the vertical and moment depth factors, respectively. Comparable results can be seen for the vertical capacity, while the current depth factors for horizontal and moment capacities are relatively smaller than those of Gourvenec (2008) due to the assumption of unlimited tension interfaces. Since DNV (2017) does not consider the embedment effect for horizontal capacity, ISO (2016) is used for comparison. The total horizontal capacity given by ISO (2016) is equal to the base friction (i.e. $A_{base} \times s_u$) plus the additional side resistance due to the difference between active and passive resistance which is related to the vertical projected area of the foundation in the direction of sliding (i.e. foundation diameter \times thickness). Therefore, the horizontal capacity estimated by ISO (2016) remains constant when the foundation is fully embedded in the soil (i.e. embedment depth = foundation thickness), as shown in Figure 2.8(b). Thus, this calculation is more conservative for embedded foundations. However, due to the possible side gap between foundation and soil caused by installation disturbance and possible cyclic loading process, this approach appears to be reasonable in practice.

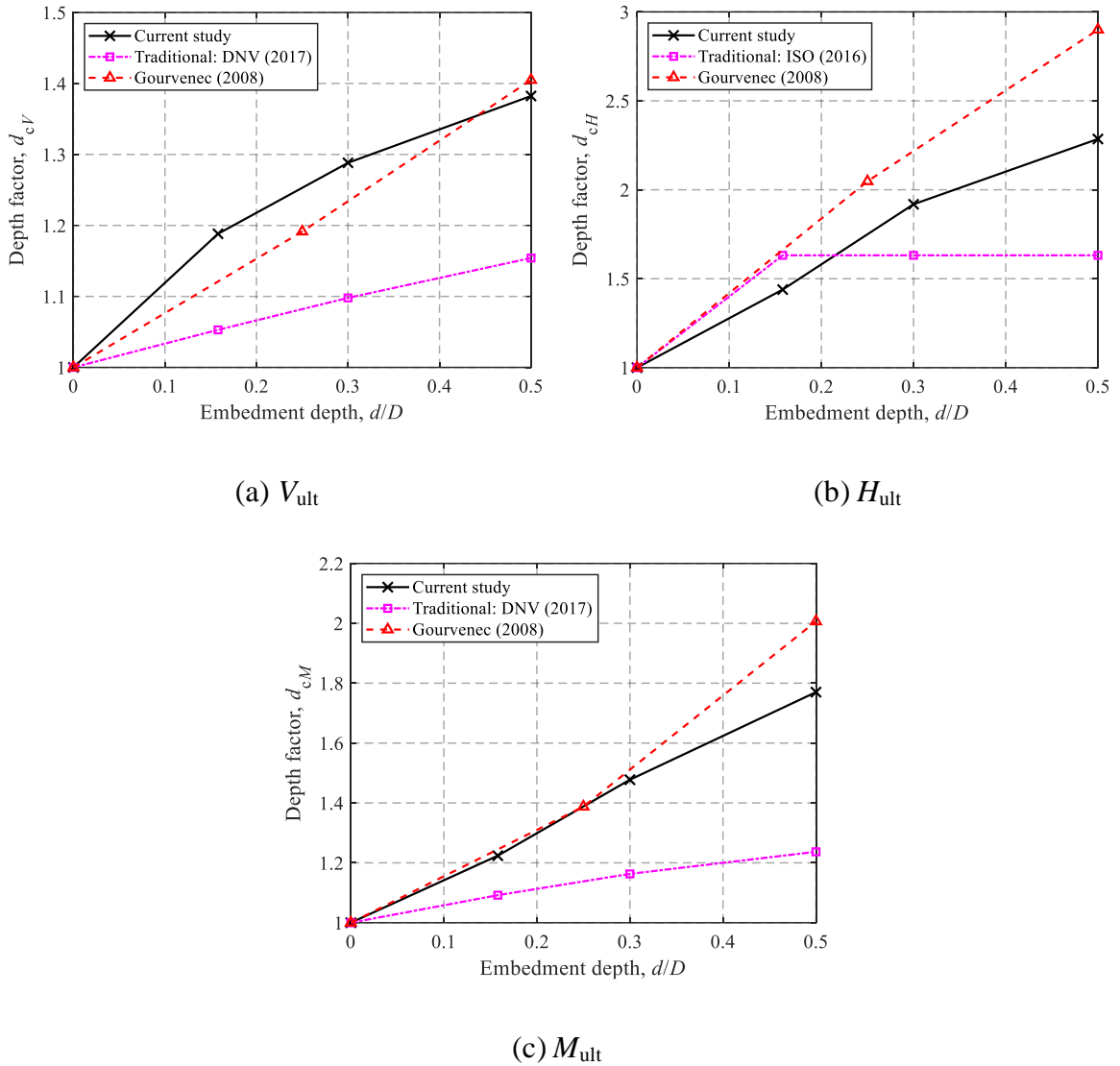


Figure 2.8: Depth correction factors of uniaxial capacities for embedded foundations: (a) V_{ult} ; (b) H_{ult} and (c) M_{ult}

2.4.2 Horizontal-Vertical loading

Figure 2.9 shows the H - V failure envelopes for each embedment ratio considered. Dimensionless loads shown in Figure 2.9(a) represent the absolute size of the failure envelopes and normalized failure envelopes shown in Figure 2.9(b) are more appropriate for developing analytical equations.

As shown in Figure 2.9(a), the failure envelope expands with the increase of the embedment ratio. Compared with the failure envelopes for a strip foundation with an

unlimited-tension interface developed by Gourvenec (2008) (see Figure 2.9(a)), a circular foundation with a zero-tension interface has relatively larger vertical capacities but smaller horizontal capacities due to the friction on the foundation top surface and the developed tension stresses on the side of the foundation for an unlimited-tension interface. As can be seen from Figure 2.9(b), the failure envelopes normalized by their corresponding ultimate capacities fall into a tighter band than those of Gourvenec (2008), whilst DNV (2017) lies slightly inside the current envelopes. A curve fit using Green's solution, which is widely used to describe H - V envelopes (see Eq. (2.10)), can also provide a satisfactory simulation for the current FE results, as shown in Figure 2.9(b).

$$V/V_{ult} = 0.5 + 0.5\sqrt{1 - H/H_{ult}} \quad (2.10)$$

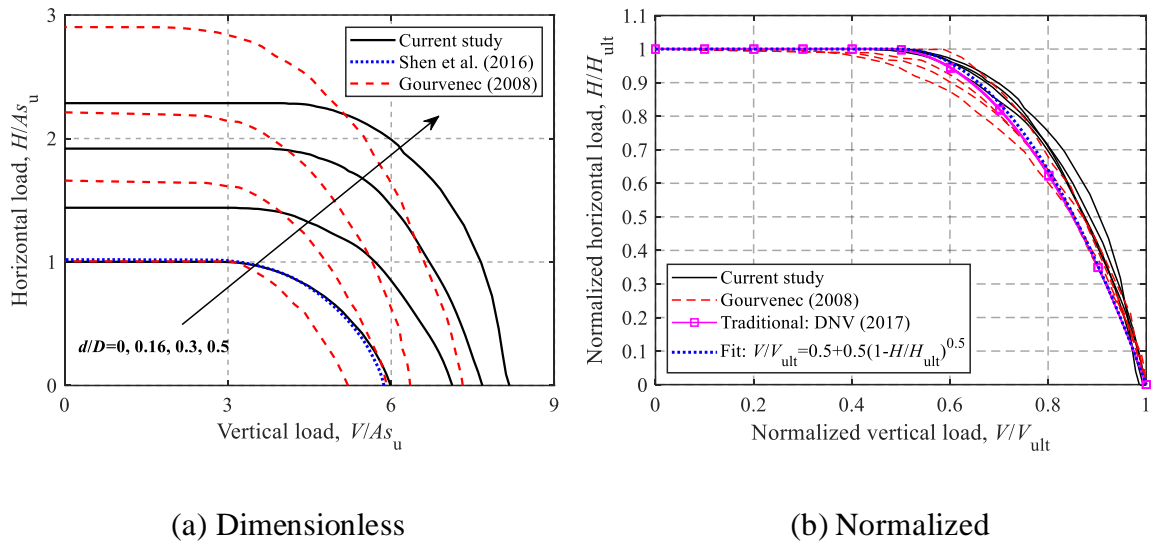


Figure 2.9: H - V failure envelopes: (a) Dimensionless and (b) Normalized

2.4.3 Moment-Vertical loading

Figure 2.10(a) and (b) show the dimensionless and normalized failure envelopes of embedded foundations under combined moment and vertical load (no horizontal load). However, the current study shows different patterns of M - V envelopes compared with those obtained by Gourvenec (2008). This is because the unlimited-tension interface used by Gourvenec (2008) can result in consistently increasing moment capacity with the decrease of vertical load, while the reduction of moment occurs for a no-tension interface owing to

the separation of foundation from the soil under relatively small vertical loads. Figure 2.10(b) shows that DNV (2017) just provides M - V failure envelopes that resemble the current failure envelope for a surface foundation irrespective of embedment ratios. In contrast, the FE results show that embedded foundations can sustain increasing moments with depth at zero vertical load. This is because the side and top soil (i.e. soil above the foundation base) can provide additional resistance even in the absence of vertical loads. As shown Figure 2.10(b), due to the non-zero intercepts with the moment axis (i.e. at $V/V_{\text{ult}} = 0$), the fitted equation for a circular surface foundation under a no-tension interface (see Eq. (2.11)) cannot be directly extended to the embedded cases, therefore, a more generalized form of equation should be developed to account for the embedment effect.

$$M/M_{\text{ult}} = 4[V/V_{\text{ult}} - (V/V_{\text{ult}})^2] \quad (2.11)$$

Figure 2.10(b) shows that the M - V failure envelopes for embedded foundations appear to still follow parabolic forms (e.g. Eq. (2.11)), although they are not complete curves. To transform these incomplete envelopes into the same form to create a complete surface that passes through the origin, the failure envelopes shown in Figure 2.10(a) can be shifted to the right along the x axis (see in Figure 2.10(c)), which is equivalent to:

$$V' = V + \Delta V \text{ and } V'_{\text{ult}} = V_{\text{ult}} + \Delta V \quad (2.12)$$

where ΔV represents the amount of offset and can be defined as $\Delta V = V_{\text{ult}} \cdot f(d/D)$, where $f(d/D)$ is a function of the embedment ratio. Curve fitting shows that $f(d/D) = 0.74(d/D)^2 + 0.12 d/D$ can be a satisfactory prediction. New normalized failure envelopes (i.e. $M/M_{\text{ult}} \sim V'/V'_{\text{ult}}$) can then be obtained based on the modified failure envelopes, as shown in Figure 2.10(d). The figure also shows that Eq. (2.11) can still be used to model the modified curves.

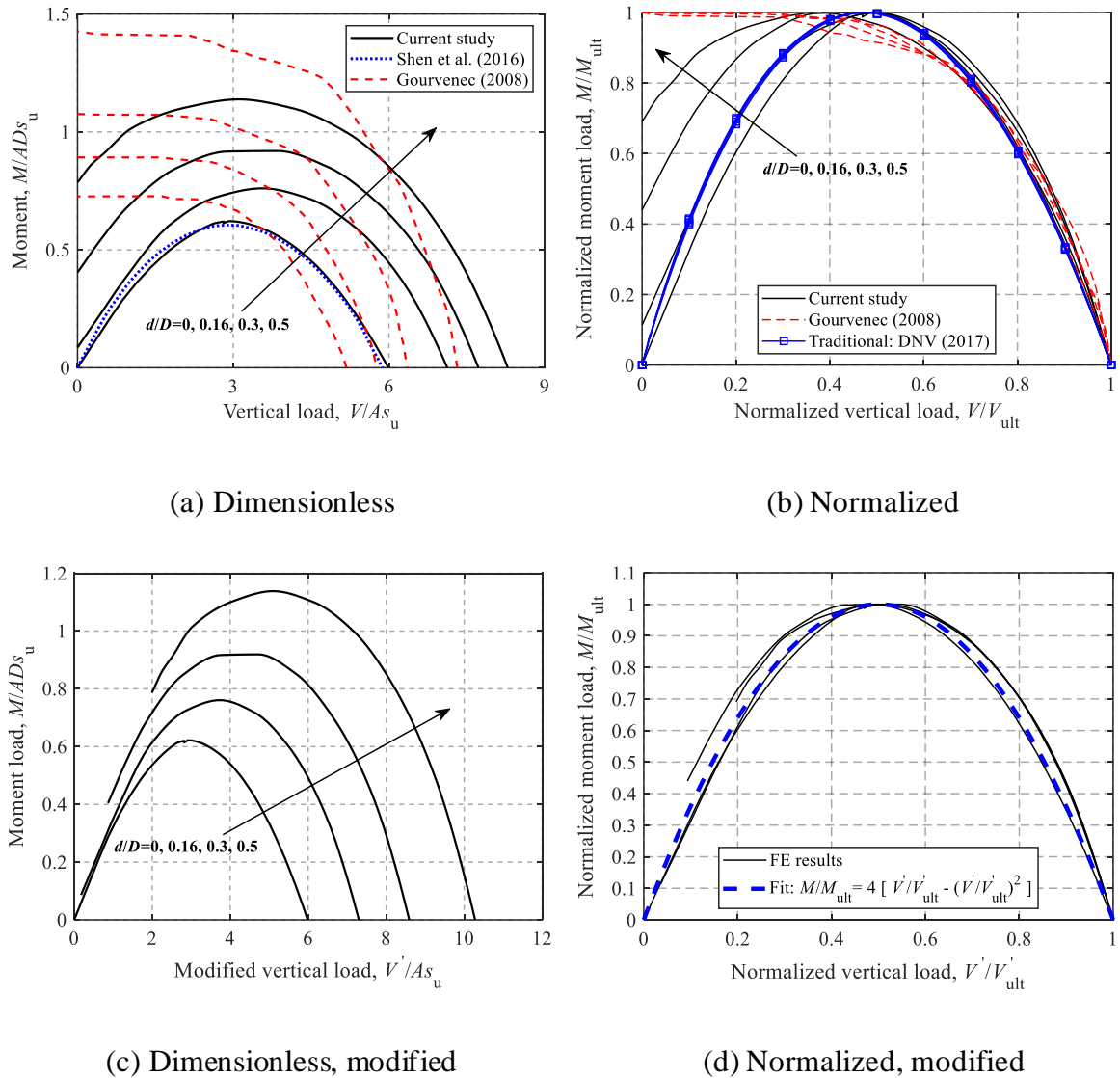


Figure 2.10: M - V failure envelopes: (a) Dimensionless; (b) Normalized; (c) Dimensionless, modified and (d) Normalized, modified

2.4.4 Torsion-Vertical loading

Figure 2.11 shows the dimensionless and normalized T - V failure results for embedded circular foundations. Similar shapes of the failure envelopes can be observed from Figure 2.11(a). Normalized failure envelopes in Figure 2.11(b) show that DNV (2017) significantly underestimates the torsional bearing capacity under the condition of $V/V_{ult} > 0.50$. The analytical equation (see Eq. (2.4)) for a circular foundation under an unlimited-tension interface condition proposed by Abyaneh et al. (2015) is also compared in Figure

2.11(b). Although slight discrepancies between the equation and FE results can be observed, this equation can still provide reasonable and conservative predictions regardless of the embedment ratios.

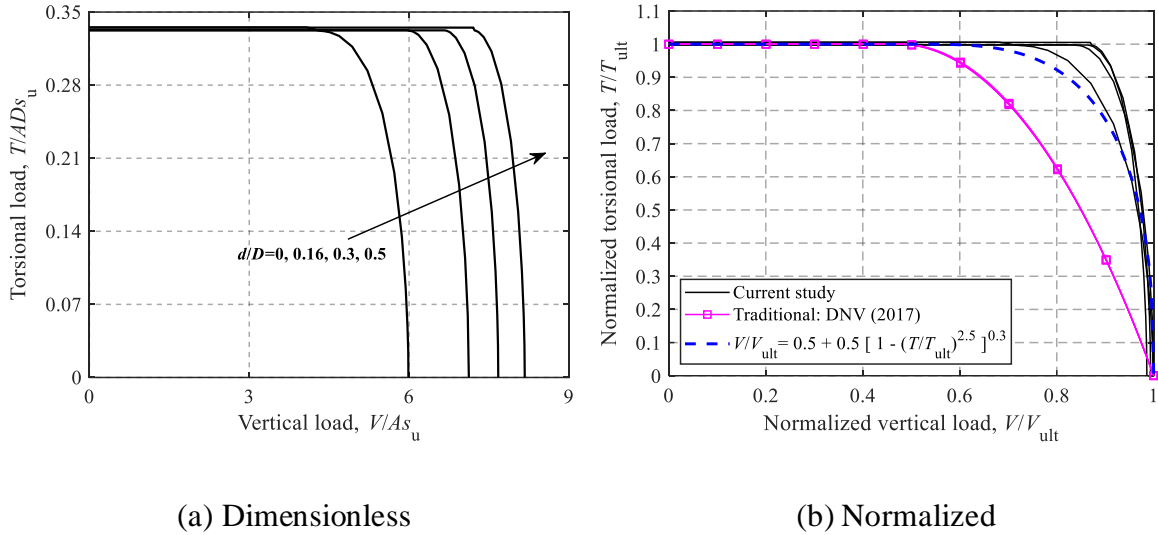


Figure 2.11: T - V failure envelopes: (a) Dimensionless and (b) Normalized

2.4.5 Moment-Horizontal loading

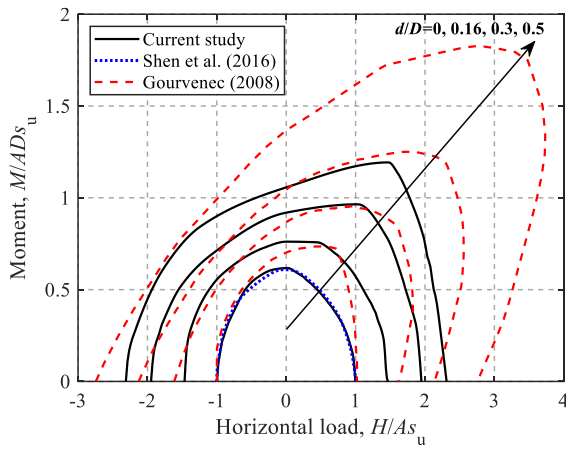
Figure 2.12 shows the dimensionless and normalized M - H failure envelopes at $V/V_{ult} = 0.25, 0.50$ and 0.75 for embedded foundations. Only dimensionless envelopes at $V/V_{ult} = 0.50$ are presented (see Figure 2.12(a)) to show the evolution of the absolute size of the envelopes. As shown in Figure 2.12(a), the failure envelopes for a strip foundation with an unlimited-tension interface obtained by Gourvenec (2008) are consistently larger than the current FE results and the difference gradually increases with the embedment ratio due to different foundation geometries and interface conditions. It should also be noted that the failure envelope for a surface foundation is almost symmetric about $H = 0$, however, the foundation embedment gradually increases the degree of asymmetry (i.e. obliquity of the failure envelope), which means that the M - H capacity in the $(+M, +H)$ region is larger than that in the $(+M, -H)$ region. This phenomenon is due to the cross-coupling effect between horizontal loads and moments. In practice, $(+M, +H)$ is always the case for onshore and offshore structures, therefore, embedded foundations appear to be a better option for

structures subjected to large lateral loads and moments, such as wind turbines and transmission towers.

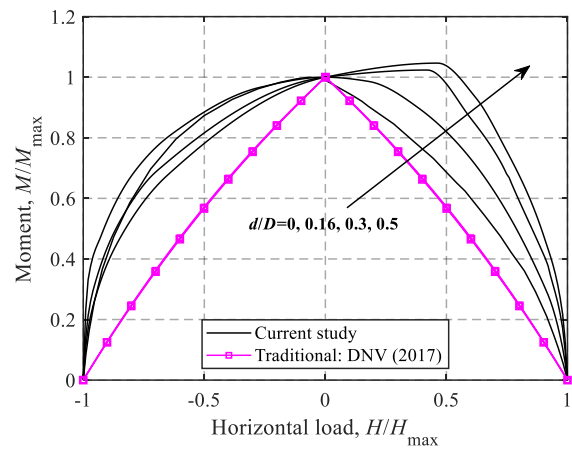
Figure 2.12(b) ~ (d) shows the M - H failure envelopes normalized by the corresponding maximum horizontal load and moment (i.e. intersections of the failure envelopes with the horizontal load and moment axes) along with the failure envelopes provided by DNV (2017). The failure envelopes given by DNV (2017) are more conservative and symmetric about the moment axis regardless of embedment ratios, indicating that no coupling effects are taken into consideration in DNV (2017). The form of equation for M - H failure envelopes accounting for the effect of foundation embedment can be expressed as:

$$(H/H_{\max})^2 + (M/M_{\max})^2[1 - h(H/H_{\max})] = 1 \quad (2.13)$$

where h is a function of d/D , i.e. $h(d/D) = 1.46(d/D) - 0.14$. The comparison between the calculated and estimated M/M_{\max} shown in Figure 2.13 indicates a good fit.



(a) Dimensionless, $V/V_{\text{ult}} = 0.50$



(b) Normalized, $V/V_{\text{ult}} = 0.75$

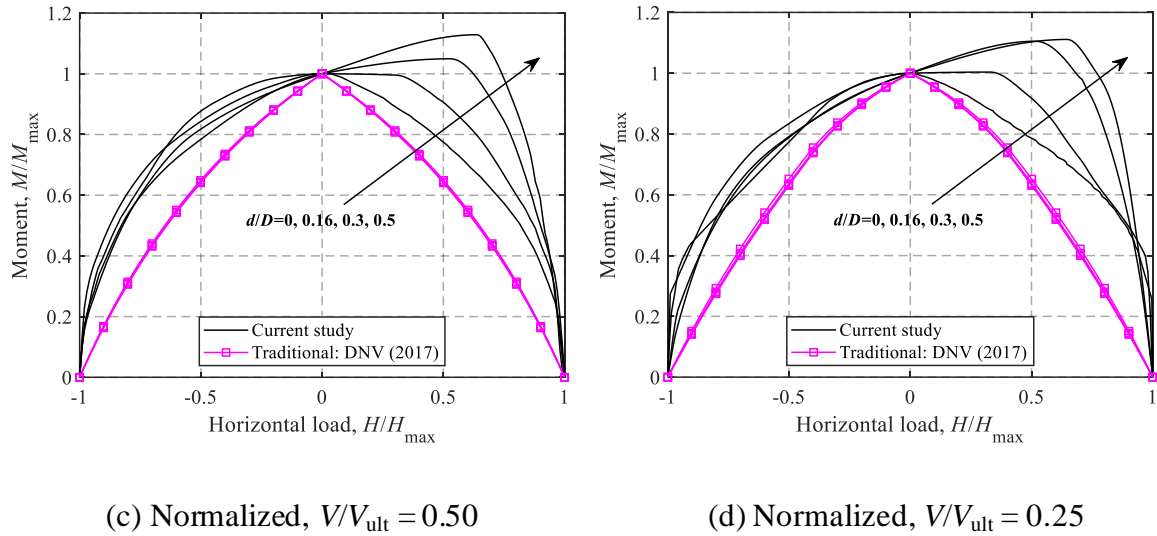


Figure 2.12: M - H failure envelopes: (a) Dimensionless, $V/V_{ult} = 0.50$; (b) Normalized, $V/V_{ult} = 0.75$; (c) Normalized, $V/V_{ult} = 0.50$ and (d) Normalized, $V/V_{ult} = 0.25$

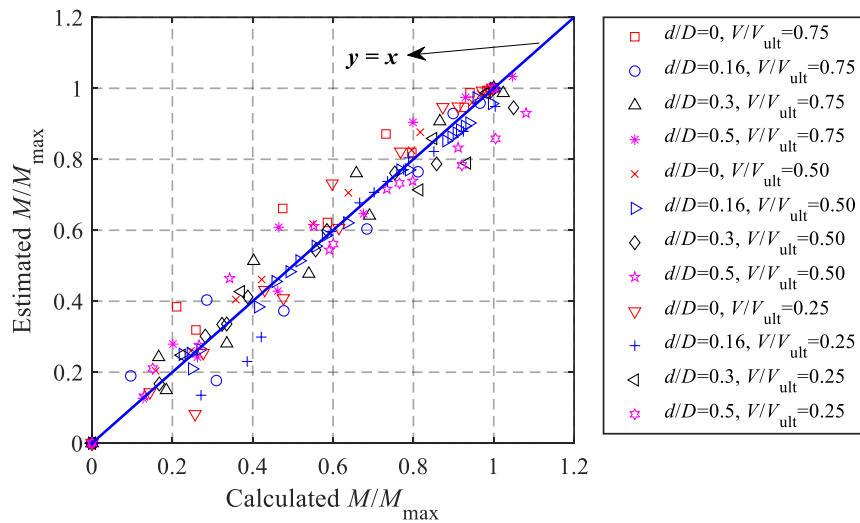


Figure 2.13: Fitting of the probe values of M - H failure envelopes

2.4.6 Horizontal-Torsional loading

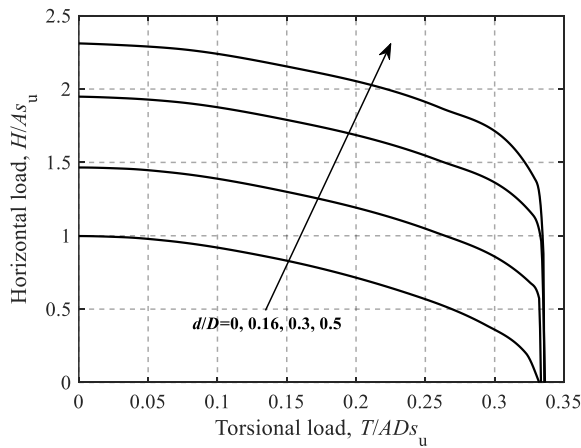
Figure 2.14 shows the dimensionless and normalized failure envelopes under horizontal and torsional loads (zero moment). Figure 2.14(a) exhibits the expansion of the absolute size of the H - T failure envelopes with the foundation embedment ratio. To describe these curves using a unique expression irrespective of vertical load levels and foundation embedment ratios, the corresponding maximum horizontal and torsional loads are adopted

for normalization, as shown in Figure 2.14(b) ~ (d). The comparison shows that the traditional approach consistently leads to more conservative H - T failure envelopes and the embedment effect has no influence on the traditional H - T failure envelope after normalization. In contrast, the FE result shows that the embedment of foundations considerably affects the H - T failure envelope even after normalization although this effect gradually decreases with the foundation embedment ratio.

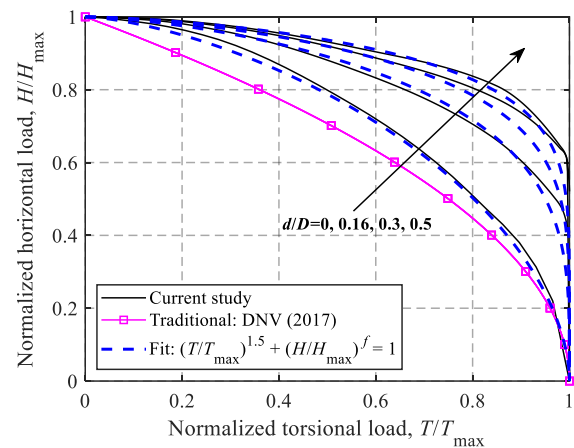
Due to the dispersion of the normalized curves caused by foundation embedment, the embedment effect needs to be taken into consideration in developing analytical expressions. The general form of formula for H - T failure envelopes can be taken as:

$$(T/T_{\max})^{1.5} + (H/H_{\max})^f = 1 \quad (2.14)$$

where f is a function of the embedment ratio. Curve-fitting shows that $f(d/D) = -7.74(d/D)^2 + 13.5 d/D + 1.83$ is a good approximation. The analytical curves of Eq. (2.14) are also compared in Figure 2.14, where reasonable predictions can be observed apart from slight overestimations for embedded foundations at $V/V_{\text{ult}} = 0.25$.



(a) Dimensionless, $V/V_{\text{ult}} = 0.50$



(b) Normalized, $V/V_{\text{ult}} = 0.75$

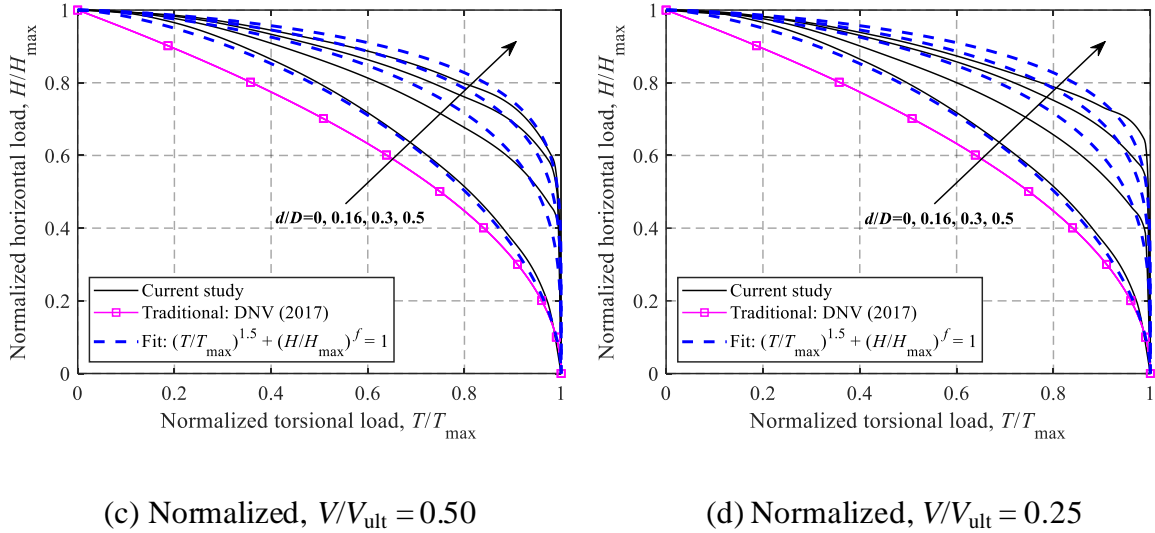


Figure 2.14: H - T failure envelopes: (a) Dimensionless, $V/V_{ult} = 0.50$; (b) Normalized, $V/V_{ult} = 0.75$; (c) Normalized, $V/V_{ult} = 0.50$ and (d) Normalized, $V/V_{ult} = 0.25$

2.4.7 Moment-Torsional loading

The dimensionless and normalized failure envelopes for M - H loading are shown Figure 2.15. Similar to the H - T failure envelopes in Section 2.4.6, a significant expansion of the size of the curves with the embedment ratio can be found from Figure 2.15(a). The failure envelopes obtained by the conventional approach (DNV, 2017) lie significantly inside those derived by FE analysis, as shown in Figure 2.15(b) ~ (d). Foundation embedment also affects the normalized M - T failure envelope, however, unlike H - T failure envelopes, M - T failure envelopes for different embedment ratios mix together and no consistent trend with the embedment ratio can be observed. This feature does not easily lend itself to any simple form of expression that can account for the embedment effect. As a first approximation, a unique equation, which follows the overall trend of the failure envelopes, is also recommended:

$$(T/T_{max})^{1.5} + (M/M_{max})^{3.55} = 1 \quad (2.15)$$

As compared in Figure 2.15, this expression can provide relatively reasonable fits although it is slightly unconservative for a surface foundation under the condition of $V/V_{ult} > 0.40$.

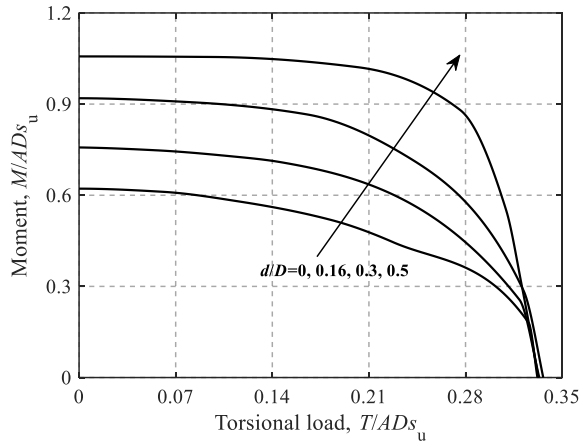
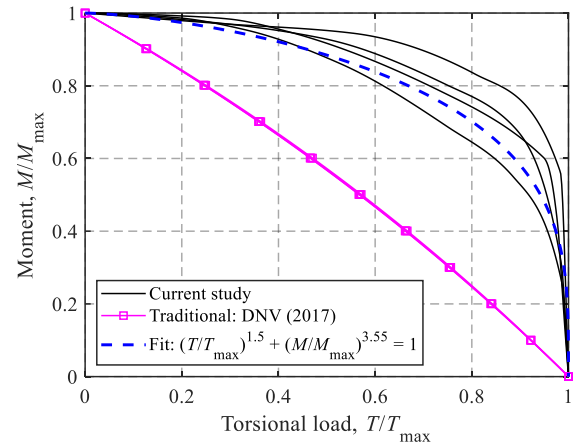
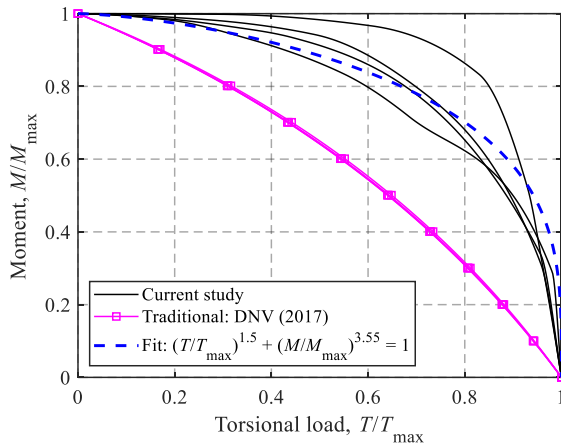
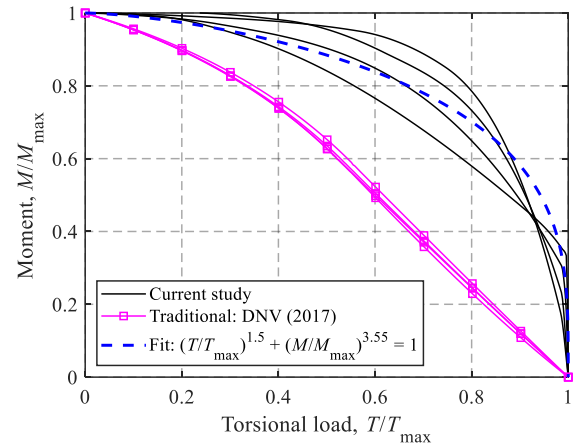
(a) Dimensionless, $V/V_{\text{ult}} = 0.50$ (b) Normalized, $V/V_{\text{ult}} = 0.75$ (c) Normalized, $V/V_{\text{ult}} = 0.50$ (d) Normalized, $V/V_{\text{ult}} = 0.25$

Figure 2.15: M - T failure envelopes: (a) Dimensionless, $V/V_{\text{ult}} = 0.50$; (b) Normalized, $V/V_{\text{ult}} = 0.75$; (c) Normalized, $V/V_{\text{ult}} = 0.50$ and (d) Normalized, $V/V_{\text{ult}} = 0.25$

2.5 Full 4-D failure envelope in VHMT loading space

This section derives the analytical 4-D expression for the failure envelope in VHMT loading space. Three sets of notation are defined: (1) $V_{\text{ult}}, H_{\text{ult}}, M_{\text{ult}}, T_{\text{ult}}$ – uniaxial ultimate capacity; (2) $H_{\text{max}}, M_{\text{max}}, T_{\text{max}}$ – maximum capacity at a given level of the vertical load without other load components; (3) $H'_{\text{max}}, M'_{\text{max}}$ – reduced maximum capacity at a given level of the vertical load with a non-zero torsional load ($T \neq 0$).

Based on the above notations and the patterns of equations used in the previous sections, the general forms of all the equations are summarized in Table 2.2. Specific expressions of these failure envelopes for different soil and foundation conditions can be found in the previous sections.

Table 2.2: Summary of FE-calculated failure envelopes

Failure envelope	Conditions	Analytical form
$H-V$	$M = 0 \ \& \ T = 0$	$\frac{H_{\max}}{H_{\text{ult}}} = f_h \left(\frac{V}{V_{\text{ult}}} \right)$ (2.16)
$M-V$	$H = 0 \ \& \ T = 0$	$\frac{M_{\max}}{M_{\text{ult}}} = f_m \left(\frac{V}{V_{\text{ult}}} \right)$ (2.17)
$T-V$	$M = 0 \ \& \ H = 0$	$\frac{T_{\max}}{T_{\text{ult}}} = f_t \left(\frac{V}{V_{\text{ult}}} \right)$ (2.18)
$M-H$	$V \neq 0 \ \& \ T = 0$	$f_{mh} \left(\frac{H}{H_{\max}}, \frac{M}{M_{\max}} \right) = 1$ (2.19)
$H-T$	$V \neq 0 \ \& \ M = 0$	$\left(\frac{H'_{\max}}{H_{\max}} \right)^c + \left(\frac{T}{T_{\max}} \right)^d = 1$ (2.20)
$M-T$	$V \neq 0 \ \& \ H = 0$	$\left(\frac{M'_{\max}}{M_{\max}} \right)^e + \left(\frac{T}{T_{\max}} \right)^f = 1$ (2.21)

Eq. (2.19) for the $M-H$ failure envelope in Table 2.2 is taken as the basic function. Due to the very similar shape of the $M-H$ failure envelope (only the sizes are different), it is reasonable to assume that Eq. (2.19) is still applicable for the $M-H$ failure envelope under the condition of $T \neq 0$ when normalized by the corresponding maximum values, H'_{\max} and M'_{\max} (these reduce to H_{\max} and M_{\max} in Eq. (2.19) if $T = 0$). An example of the $M-H$ envelope at non-zero torsional loading is shown in Figure 2.16, indicating a good fitting. Therefore, Eq. (2.19) can be replaced by a more generalized form:

$$f_{mh} \left(\frac{H}{H'_{\max}}, \frac{M}{M'_{\max}} \right) = 1 \quad (2.22)$$

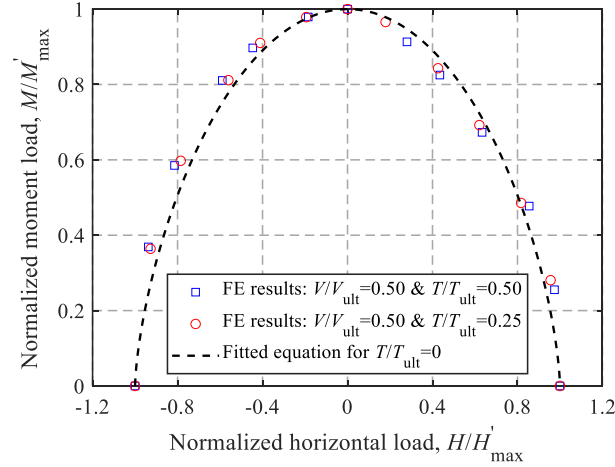


Figure 2.16: M - H envelope for a circular surface foundation on a homogeneous soil at $V/V_{\text{ult}} = 0.50$ for $T \neq 0$

Mathematical manipulations allow the formulation of an analytical 4-D expression for the failure envelope in VHMT loading space in terms of V/V_{ult} , H/H_{ult} , M/M_{ult} , and T/T_{ult} :

$$f_{mh} \left(\frac{H/H_{\text{ult}}}{\left[1 - \left(\frac{T/T_{\text{ult}}}{f_t(V/V_{\text{ult}})} \right)^d \right]^{\frac{1}{c}} \cdot f_h(V/V_{\text{ult}})}, \frac{M/M_{\text{ult}}}{\left[1 - \left(\frac{T/T_{\text{ult}}}{f_t(V/V_{\text{ult}})} \right)^f \right]^{\frac{1}{e}} \cdot f_m(V/V_{\text{ult}})} \right) = 1 \quad (2.23)$$

In practical design, the design loads (factored loads and materials), VHMT, can be directly substituted into the left-hand side of Eq. (20); values less than 1 represent a sufficient ultimate limit design and vice versa. For embedded foundations, it should be noted that the design vertical load, V , should be reduced by $\gamma d \cdot A$ to account for the additional surcharge caused by the soil above foundation base.

As an example, the full 4-D expression of the failure envelope for a surface foundation on non-homogeneous soils (Section 2.3) is shown. The equations for the H - V , M - V and M - H failure envelopes have been given by Shen et al. (2016) and the expressions for the T - V , H - T and M - T failure envelopes can be found in Section 2.3, as summarized in Table 2.3.

Table 2.3: Failure envelopes for a surface foundation on non-homogeneous soils

Failure envelope	Conditions	Analytical equation
H - V	$M = 0$ & $T = 0$	$\frac{V}{V_{\text{ult}}} = 0.5 + 0.5 \sqrt{1 - \frac{H_{\text{max}}}{H_{\text{ult}}}}$ for $\frac{V}{V_{\text{ult}}} > 0.5$
		$\frac{H_{\text{max}}}{H_{\text{ult}}} = 1$ for $\frac{V}{V_{\text{ult}}} \leq 0.5$
M - V	$H = 0$ & $T = 0$	$\frac{M_{\text{max}}}{M_{\text{ult}}} = 4 \left[\frac{V}{V_{\text{ult}}} - \left(\frac{V}{V_{\text{ult}}} \right)^2 \right]$
T - V	$M = 0$ & $H = 0$	$\frac{V}{V_{\text{ult}}} = 0.5 + 0.5 \left[1 - \left(\frac{T_{\text{max}}}{T_{\text{ult}}} \right)^{2.5} \right]^{0.3}$ for $\frac{V}{V_{\text{ult}}} > 0.5$
		$\frac{T_{\text{max}}}{T_{\text{ult}}} = 1$ for $\frac{V}{V_{\text{ult}}} \leq 0.5$
M - H	$V \neq 0$ & $T = 0$	$\left(\frac{H}{H_{\text{max}}} \right)^2 + \left(\frac{M}{M_{\text{max}}} \right)^{1.5} = 1$
H - T	$V \neq 0$ & $M = 0$	$\left(\frac{H'_{\text{max}}}{H_{\text{max}}} \right)^{1.75} + \left(\frac{T}{T_{\text{max}}} \right)^{1.75} = 1$
M - T	$V \neq 0$ & $H = 0$	$\left(\frac{M'_{\text{max}}}{M_{\text{max}}} \right)^{2.5} + \left(\frac{T}{T_{\text{max}}} \right)^2 = 1$

To visualize the shape of the full 4-D failure surface, three special 3-D failure surfaces in terms of V/V_{ult} , H/H_{ult} , M/M_{ult} , and T/T_{ult} (i.e. VHM failure surface at $T = 0$, VHT failure surface at $M = 0$ and VMT failure surface at $H = 0$) are presented in Figure 2.17. The

specific curves listed in Table 2.3 are also shown for comparison. The shape of the 3-D VHM failure surface (for $T=0$) that is shown in Figure 2.17(a) is similar to that obtained by Taiebat and Carter (2010) using a semi-analytical FE approach. For the VHT and VMT failure surfaces, the portion of $T < 0$ is also incorporated due to the symmetry about the plane of $T=0$.

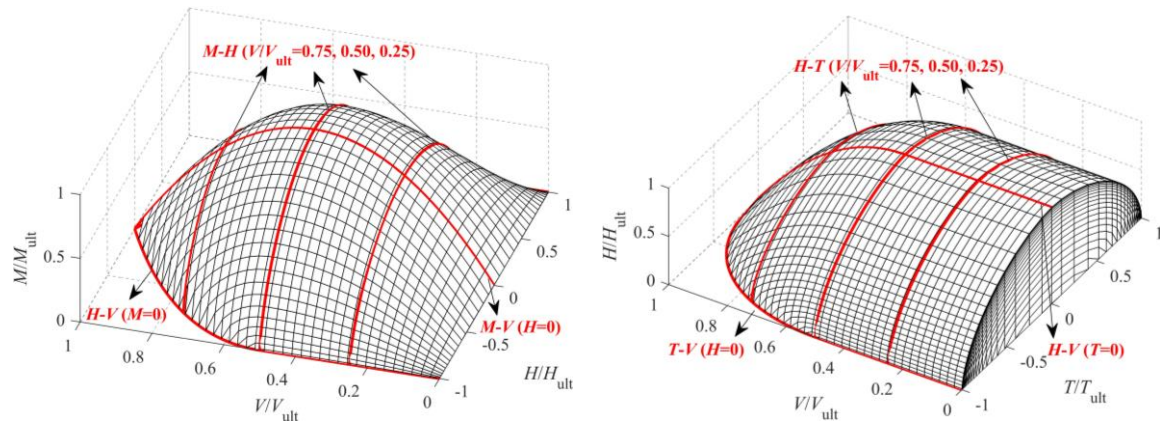
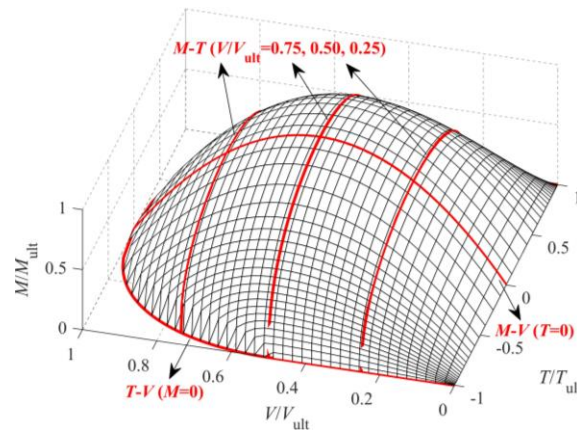
(a) VHM at $T = 0$ (b) VHT at $M = 0$ (c) VMT at $H = 0$

Figure 2.17: 3-D failure surfaces for a circular surface foundation on non-homogeneous soils: (a) VHM at $T = 0$; (b) VHT at $M = 0$ and (c) VMT at $H = 0$

2.6 Conclusions

The general VHMT failure envelopes of circular foundations under a zero-tension interface for undrained soils have been studied using FE analysis. For surface foundations on a non-homogeneous soil, the analytical $V-T$ and $H-T$ and $M-T$ failure envelopes have been provided considering four soil strength heterogeneity ratios. The results indicate that torsional loads can reduce the VHM capacity of circular foundations. The cases of embedded foundations in a homogeneous soil with four embedment depths were also taken into consideration. The effect of foundation embedment on the VHMT failure envelopes was studied and analytical formulas have been proposed. As expected, foundation embedment can significantly increase the capacity of circular foundations under combined VHMT loading. To facilitate the design application of the failure envelope method, a full 4-D analytical expression for the VHMT failure envelope was derived based on the six calculated VHMT failure envelopes (i.e. $V-H$, $V-M$, $V-T$, $V-M-H$, $V-H-T$ and $V-M-T$). These approaches should aid the assessment of the ultimate limit states of shallow circular foundations under combined VHMT loading conditions.

2.7 References

- Abyaneh, S. D., Ojo, A., Maconochie, A., and Haghghi, A. (2015). The undrained bearing capacity of shallow foundations subjected to three-dimensional loading including torsion. *In Proceedings of the 25th International Ocean and Polar Engineering Conference*, Kona, Hawaii, 21-26 June 2015. International Society of Offshore and Polar Engineers, Cupertino, pp. 668-674.
- API (American Petroleum Institute) (2011). API Recommended Practice, Geotechnical and Foundation Design Considerations. American Petroleum Institute, Washington, D.C.
- Bienen, B., Gaudin, C., and Cassidy, M. J. (2007). Centrifuge tests of shallow footing behaviour on sand under combined vertical-torsional loading. *International Journal of Physical Modelling in Geotechnics*, 7(2), 01-21.
- Bransby, M. F., and Randolph, M. F. (1998). Combined loading of skirted foundations. *Géotechnique*, 48(5), 637-655.
- Dassault Systèmes (2016). Abaqus analysis user's manual. Simulia Corp., Providence, R.I.
- Deshpande, V. M. (2016). Numerical modelling of wind turbine foundations subjected to combined loading. Master's thesis, The University of Western Ontario, London, Ont.

- DNV GL (Det Norske Veritas GL) (2017) DNVGL-RP-C212: Offshore soil mechanics and geotechnical engineering. DNV GL Group, Høvik, Norway.
- DNV GL (Det Norske Veritas GL) (2016). DNVGL-ST-0126: Support structures for wind turbines. DNV GL Group, Høvik, Norway.
- Feng, X., Randolph, M. F., and Gourvenec, S. (2017). An analytical solution for the undrained horizontal-torsional resistance of mudmats. *Géotechnique*, 67(4), 325-337.
- Feng, X., Randolph, M. F., Gourvenec, S., and Wallerand, R. (2014). Design approach for rectangular mudmats under fully three-dimensional loading. *Géotechnique*, 64(1), 51-63.
- Finnie, I. M. S., and Morgan, N. (2004). Torsional loading of subsea structures. *In Proceedings of the 14th International Offshore and Polar Engineering Conference*. Toulon, France, 23-28 May 2004. International Society of Offshore and Polar Engineers, Mountain View, pp. 326-333.
- Gourvenec, S. (2007). Shape effects on the capacity of rectangular footings under general loading. *Géotechnique*, 57(8), 637-646.
- Gourvenec, S. (2008). Effect of embedment on the undrained capacity of shallow foundations under general loading. *Géotechnique*, 58(3), 177-186.
- Gourvenec, S. M., and Mana, D. S. K. (2011). Undrained vertical bearing capacity factors for shallow foundations. *Géotechnique Letters*, 1(4), 101-108.
- Gourvenec, S., and Randolph, M. (2003). Effect of strength non-homogeneity on the shape of failure envelopes for combined loading of strip and circular foundations on clay. *Géotechnique*, 53(6), 575-586.
- Green, A. P. (1954). The plastic yielding of metal junctions due to combined shear and pressure. *Journal of the Mechanics and Physics of Solids*, 2(3), 197-211.
- He, P., and Newson, T. (2019). Undrained capacity of circular foundations under combined horizontal and torsional loads. *Géotechnique Letters*, 10(2), 186-190.
- ISO (International Standards Organization). (2016). ISO 19901-4: Petroleum and natural gas industries specific requirements for offshore structures – part 4: geotechnical and foundation design considerations, 2nd edition. International Standards Organization, Geneva, Switzerland.
- Shen, Z., Feng, X., and Gourvenec, S. (2016). Undrained capacity of surface foundations with zero-tension interface under planar VHM loading. *Computers and Geotechnics*, 73, 47-57.
- Shen, Z., Feng, X., and Gourvenec, S. (2017). Effect of interface condition on the undrained capacity of subsea mudmats under six-degree-of-freedom loading. *Géotechnique*, 67(4), 338-349.
- Taiebat, H. A., and Carter, J. P. (2002). Bearing capacity of strip and circular foundations on undrained clay subjected to eccentric loads. *Géotechnique*, 52(1), 61-64.

- Taiebat, H. A., and Carter, J. P. (2010). A failure surface for circular footings on cohesive soils. *Géotechnique*, 60(4), 265-273.
- Ukritchon, B., Whittle, A. J., and Sloan, S. W. (1998). Undrained limit analyses for combined loading of strip footings on clay. *Journal of Geotechnical and Geoenvironmental Engineering*, 124(3), 265-276.
- Yun, G. J., Maconochie, A., Oliphant, J., and Bransby, F. (2009). Undrained capacity of surface footings subjected to combined VHT loading. *In Proceedings of the 19th International Offshore and Polar Engineering Conference*. Osaka, Japan, 21-26 June 2009. International Society of Offshore and Polar Engineers, Mountain View, pp. 9-14.

3 Undrained capacity of circular surface foundations on two-layer clays under combined VHMT loading

3.1 Introduction

Estimation of the bearing capacity of shallow foundations under combined loadings can be of great significance. This is particularly important for large onshore structures, such as wind turbines, transmission towers and masts, due to their complex environmental loading. The majority of offshore foundations are circular or close to circular in form. Apart from the vertical load due to the self-weight of the superstructure, horizontal loads of an onshore wind turbine caused by wind can also be substantial and a large structural height can further lead to significant moment loading of the foundation. Moreover, environmental loads on the structure are often not co-planar and transverse loads can therefore induce torsional effects on the foundation (Bienen et al., 2007).

Traditionally, this type of design is based on classical solutions for the uniaxial vertical bearing capacity of shallow strip foundations using the superposition principle (Terzaghi, 1951). The effects of load inclination and eccentricity are taken into consideration by introducing the load inclination factor and the effective foundation area (e.g. DNV, 2016). Since load inclination and eccentricity effects are separately considered, this semi-empirical modification of the conventional theory may sometimes be insufficiently accurate for practical design (Gourvenec, 2007) and it has also been shown that this simple approach is non-conservative for strip foundations on soils with shear strength increasing with depth (Ukritchon, 1998). This approach is still common for onshore shallow wind turbine foundation design.

The failure envelope method has been recommended as an alternative to conventional theories in some geotechnical design guidelines (particularly those focused on offshore geotechnics), such as API(2011) and ISO (2016), due to the load interaction effect between various load components (i.e. combined vertical, horizontal, moment and torsional loads) being explicitly incorporated (Shen et al., 2017). Failure envelopes for different types of foundations (e.g. strip (Bransby and Randolph, 1998), rectangular (Gourvenec and

Randolph, 2003) and circular (Shen et al., 2016) foundations), homogeneous (Taiebat and Carter, 2010) or non-homogeneous (Feng et al., 2014) soils, and zero-tension (Shen et al., 2016) or unlimited-tension (Gourvenec and Randolph, 2003) interface conditions have been previously investigated under undrained conditions. These studies of the failure envelope method have been primarily confined to a single layer soil with a uniform or linearly increasing undrained shear strength profile. However, onshore clay deposits often have a thin layer of stiff crust with a relatively high undrained shear strength developed from weathering, desiccation and chemical process (Lutenegger, 1995). The shear strength of the upper crustal layer can be more than 10 times that of the underlying clay (Lee and Park, 1999). Nakase et al. (1978) and Sagaseta and Arroyo (1982) have demonstrated that the undrained shear strength profile of the crust strongly affects stability analysis of shallow foundations and embankments because a substantial portion of the failure surface under the structure can be located within the crust. Understanding the effect of a surficial crust on the bearing capacity of shallow foundations is therefore important for optimal design. However, existing design standards (e.g. DNV, 2016) predict the bearing capacity of shallow foundations under idealized soil conditions without considering the existence of the surficial crust. Moreover, the effects of torsional loads are not explicitly taken into consideration (DNV, 2016).

Studies available in the literature that account for the effect of high strength surficial layers on bearing capacity are still sparse. Merifield et al. (1999) evaluated the undrained bearing capacity of a centrally, vertically loaded surface strip foundation on a two-layer clay deposit using numerical upper and lower bound analysis. The values of a modified bearing capacity factor N_c^* were calculated for various thickness ratios (H/B = thickness of upper layer / foundation width) and undrained shear strength ratios (s_{u1}/s_{u2} = undrained shear strength of upper layer / undrained shear strength of bottom layer). Both strong-over-soft (i.e. $s_{u1}/s_{u2} > 1$) and soft-over-strong (i.e. $s_{u1}/s_{u2} < 1$) cases were accounted for. Recently, the same cases for square and circular foundations were further investigated by Merifield and Nguyen (2006) using finite element (FE) analysis. However, this considers only vertical bearing capacity in the absence of horizontal, moment and torsional loads. Park et al. (2010) determined the bearing capacity factor N_c of strip and circular foundations resting on a non-homogeneous crust overlying a uniform soil, but the failure envelope under

combined loadings was not addressed. Feng et al. (2015) studied the failure envelope of a rectangular foundation founded on a crustal layer overlying a normally consolidated clay using an unlimited-tension soil-foundation interface. However, unlike skirted shallow foundations of offshore structures, onshore shallow foundations can uplift and separate from the soil under a large overturning moment because the soil-foundation interface cannot provide tensile resistance (i.e. zero-tension interface).

The object of this paper is to investigate the VHMT failure envelope for circular foundations founded on a surficial crust underlain by a uniform soil under a zero-tension interface condition using finite element analysis. Undrained conditions have been considered for both the crustal layer and the underlying soil. The effects of this surficial crust on the VHMT failure envelope have been studied. A full 4-D VHMT failure envelope expression is also derived in this paper.

3.2 Method – finite element analysis

3.2.1 Material models and interface conditions

A linear elastic perfectly plastic constitutive relationship with a Mohr-Coulomb (M-C) failure criterion was used to model the soil behavior. For undrained conditions, the M-C criterion degenerates to the Tresca criterion, which can be defined by three soil parameters: the undrained Young's modulus, E_u , Poisson's ratio, μ , and undrained shear strength, s_u .

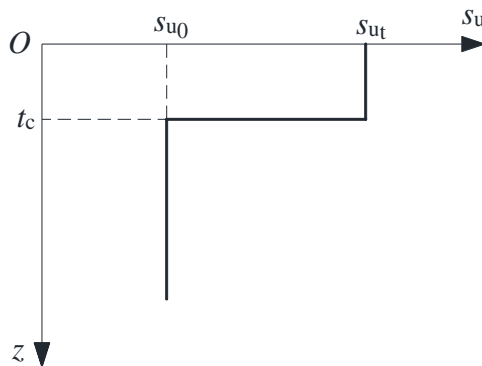


Figure 3.1: Soil profile with a surficial crust

As shown in Figure 3.1, two fundamental parameters may affect the bearing capacity of a surface foundation on a crusted soil: the averaged undrained shear strength of the surficial

crust layer, s_{ut} , and the crust thickness, t_c . As suggested by Lee and Park (1999), in some cases the average shear strength of the upper crust layer can be more than 10 times that of the underlying clay. In this paper, the ratio, s_{u0}/s_{ut} (s_{u0} refers to the undrained shear strength of the underlying soil), has been varied from 0.2 to 1.0 (i.e. 0.2, 0.4, 0.6, 0.8 and 1.0), to represent a typical range of soil profiles. This approach also addresses cases of strong-over-soft clays adopted by Merifield et al. (1999). The special case of $s_{u0}/s_{ut} = 1$ relates a homogeneous soil. As shown by Bjerrum (1973), the thickness of a crust layer will usually range from 1 to 8 m depending on the hydrogeology (i.e. well-drained versus poorly drained). In eastern Canada, the thickness of the upper crust is generally 1 to 5 m and is often of the order of 3 m (Lefebvre et al., 1987). Typically, the diameter (D) of an onshore wind turbine foundation is very large (> 15 m), and these foundations are getting larger with increases of power output and tower height. The diameter of the shallow foundation used in this paper is 19 m, representing the typical dimension for current wind turbines in North America. Therefore, this study has considered models with t_c/D ranging from 0.1 to 0.3 (i.e. 0.1, 0.2 and 0.3) to span most cases of practical interest. This range also covers that used by Feng et al. (2015). The designed FE cases are summarized in Table 3.1 below.

Table 3.1: FE cases for crusted soils under undrained conditions

s_{u0}/s_{ut} t_c/D	0.2	0.4	0.6	0.8	1.0 (Homogeneous)
0.1	(C11)	(C12)	(C13)	(C14)	(C15)
0.2	(C21)	(C22)	(C23)	(C24)	(C25)
0.3	(C31)	(C32)	(C33)	(C34)	(C35)

In the analysis, s_{u0} was held constant at 100 kPa and the Poisson's ratio of the undrained soils was taken to be 0.495. A sufficiently large E_u/s_{u0} ratio equal to 10000 was selected to minimize mesh distortion (Abyaneh et al., 2015). The foundation was assumed to be a rigid body. A load reference point (LRP) was used to apply prescribed displacements or loads, located at the bottom center of the foundation.

Similar to Shen et al. (2016), the FE analyses considered a zero-tension, rough base that allows separation of the foundation from the soil. The zero-tension rough base can be modelled using a Coulomb model with a friction coefficient of 20 (Shen et al., 2016).

3.2.2 Geometry and mesh

The analysis in this paper was conducted using the finite element software ABAQUS (Dassault Systèmes, 2016). To avoid the effects of the model boundaries on the development of failure mechanisms, the mesh length, L , and mesh height, H , were taken as 120 m and 50 m, following the recommendations of Deshpande (2016).

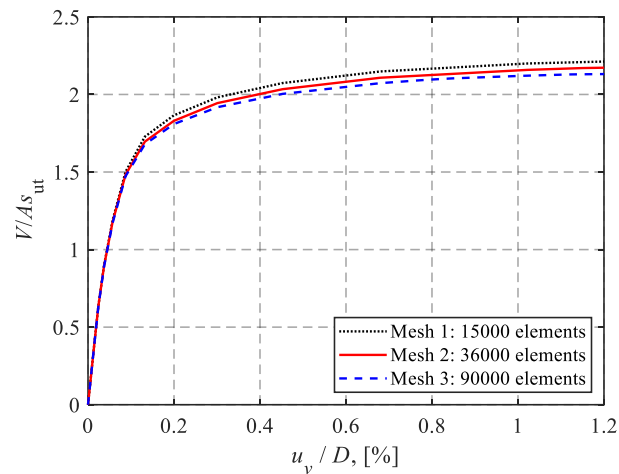


Figure 3.2: Mesh convergence study of Case C31

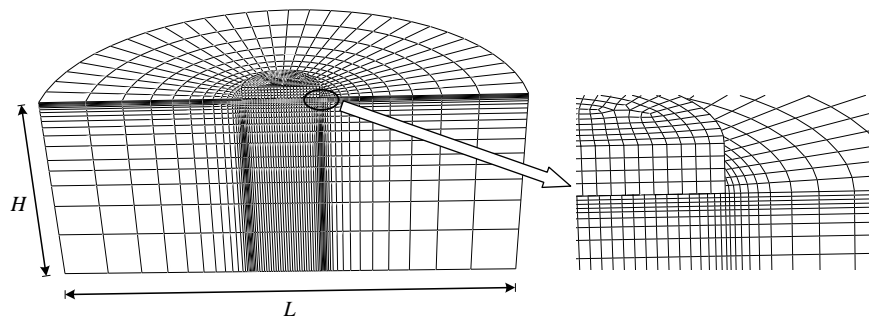


Figure 3.3: Half-view of the FE mesh

A mesh convergence study was carried out for a number of cases. A typical outcome is shown in Figure 3.2. The difference between the ultimate vertical loads using Meshes 2 and 3 is around 2%. However, the model solution with Mesh 3 takes about 6 times longer

than that using Mesh 2. Thus, Mesh 2 was adopted in the analysis. Figure 2.3 shows the half-model of the three-dimensional model using Mesh 2. This mesh was composed of approximately 36000 8-noded brick elements (i.e. first-order, ABAQUS C3D8R). To capture the intense stress concentration close to the foundation edge and the large plastic shear strains at the interface, the soil regions in the vicinity of the foundation edge and the horizontal thin soil layer close to the interface were carefully refined (Gourvenec and Randolph, 2003). The cylindrical circumference of the soil was constrained to prevent out-of-plane translations and the bottom of the soil was fixed in the three orthogonal directions.

3.2.3 Sign conventions and loading paths

The sign conventions for the loads are shown in Figure 2.1. The horizontal and moment loads were considered to be in the same plane.

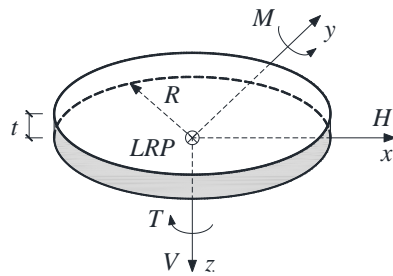


Figure 3.4: Sign conventions

Probe tests and swipe tests were employed to detect the failure envelopes under various load conditions. For a displacement probe analysis, a vertical load is first applied at the LRP of the foundation and remains constant. A fixed-ratio of displacement is then imposed to the foundation to track the failure point on the failure envelope (Gourvenec and Randolph, 2003). One probe test can only provide a single point on a failure envelope. The swipe test, which was introduced by Tan (1990), brings the foundation to a collapse state in coordinate direction 1 first (displacement-controlled), followed by a displacement applied in coordinate direction 2, during which the increment of the displacement in coordinate direction 1 remains zero (Gourvenec and Randolph, 2003). Two typical failure envelopes obtained using the swipe and probe tests are shown in Figure 3.5.

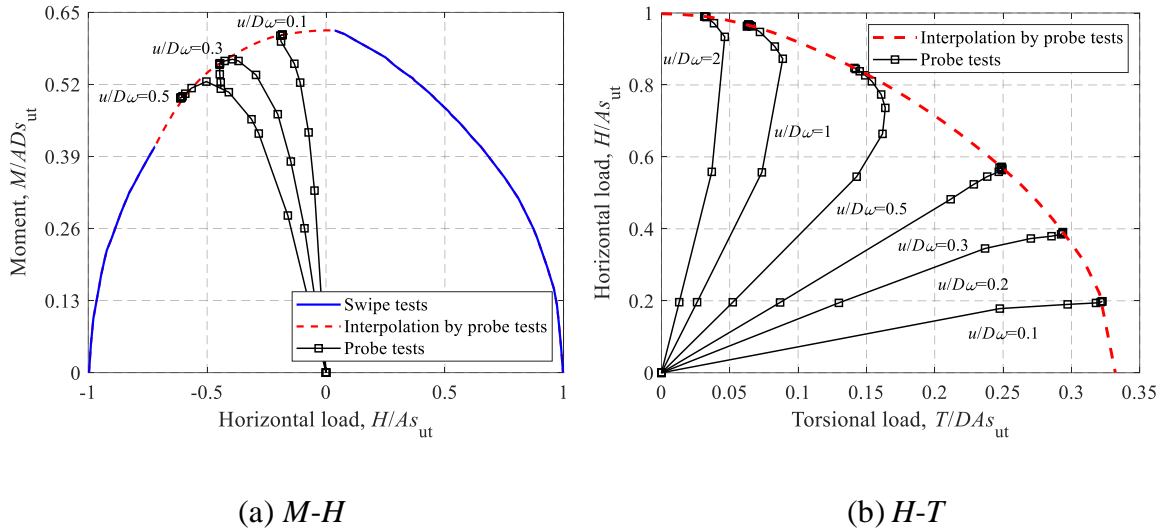


Figure 3.5: $M-H$ and $H-T$ failure envelopes for a uniform soil at $V/V_{ult} = 0.50$: (a) $M-H$ and (b) $H-T$

3.3 Finite element results

The overall strategy for assessing the undrained bearing capacity of a shallow foundation under combined VHMT loads using the FE method can be decomposed into three steps: (i) determining uniaxial ultimate capacities, e.g. V_{ult} , H_{ult} , M_{ult} and T_{ult} (Section 3.3.1); (ii) normalizing $H-V$, $M-V$ and $T-V$ failure envelopes with the corresponding uniaxial ultimate capacities (Sections 3.3.2 ~ 3.3.4); and (iii) normalizing $M-H$, $H-T$ and $M-T$ failure envelopes with the corresponding maximum values (Sections 3.3.5 ~ 3.3.7). Using the results of these different steps, a full 4-D VHMT failure envelope can be derived.

3.3.1 Pure uniaxial capacities

The ultimate loads for vertical, horizontal and torsional modes are referred to as the corresponding uniaxial load-carrying capacities in the absence of the other loading modes. As a foundation with a zero-tension interface cannot resist any moment loading without vertical loads, the ultimate moment capacity is represented by the maximum moment load under vertical loading only. Since horizontal and torsional capacities of a surface foundation are purely related to the undrained shear strength of the surface soil (i.e. s_{ut}), only the vertical and moment capacities have been investigated in this section.

The crust correction factor, s_{cr} , defined as the ratio of the dimensionless capacity for a crusted soil (i.e. $s_{u0}/s_{ut} \neq 1$) to that of a uniform soil (i.e. $s_{u0}/s_{ut} = 1$), is introduced to characterize the effect of a surficial crust:

$$s_{cr} = \frac{N_{s_{u0}/s_{ut}}}{N_{s_{u0}/s_{ut}=1}} \quad (3.1)$$

where $N_{s_{u0}/s_{ut}}^v = \frac{V_{ult}}{A \cdot s_{ut}}$ for the vertical capacity and $N_{s_{u0}/s_{ut}}^m = \frac{M_{ult}}{A \cdot D \cdot s_{ut}}$ for the moment capacity.

The variations of s_{crv} and s_{crm} with regard to s_{u0}/s_{ut} and t_c/D are shown in Figure 3.6. The vertical and moment factors significantly increase with s_{u0}/s_{ut} and gradually converge to unity as s_{u0}/s_{ut} approaches unity. A quadratic polynomial equation with respect to s_{u0}/s_{ut} is proposed to estimate the relationships:

$$s_{cr} = f \cdot \left(\frac{s_{u0}}{s_{ut}}\right)^2 + 1.3 \left(\frac{s_{u0}}{s_{ut}}\right) - [f + 0.3] \quad (3.2)$$

The coefficient, f , is a function of t_c/D , defined as $f(t_c/D) = -0.97 t_c/D - 0.27$ for the vertical capacity and $f(t_c/D) = \frac{-1.18 t_c/D}{t_c/D + 0.18}$ for the moment capacity. As seen in Figure 3.6, the curve fitting is in close agreement with the FE results.

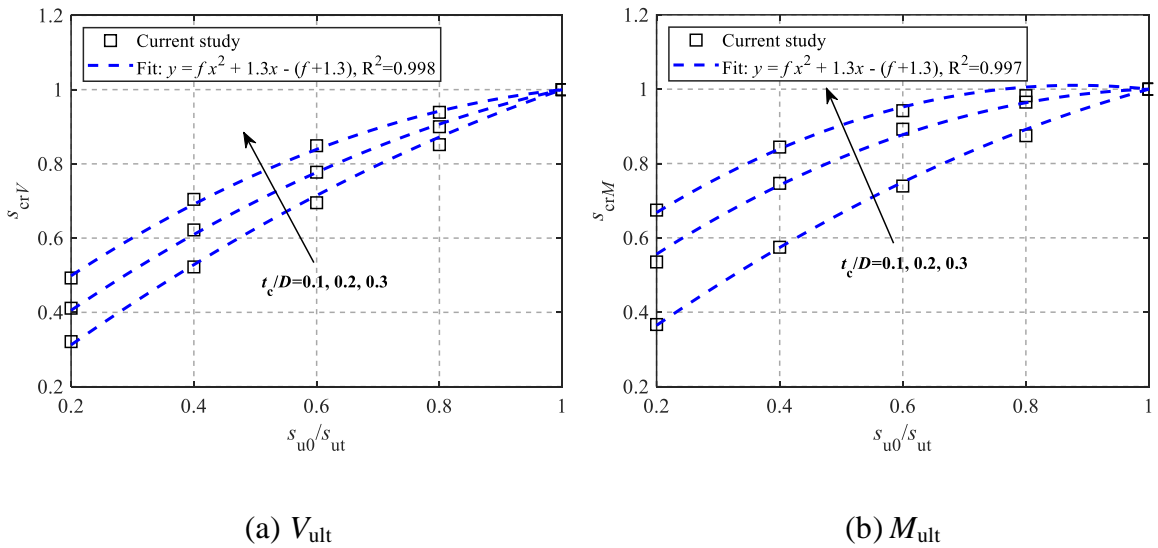


Figure 3.6: Crust correction factors of uniaxial capacities: (a) V_{ult} and (b) M_{ult}

To better understand the effects of s_{u0}/s_{ut} and t_c/D on the collapse mechanism under purely vertical loads, the contours of the maximum plastic shear strain increment are illustrated in Figure 3.7. The geometry of the collapse mechanism can be effectively visualized using the maximum plastic shear strain increment (Loukidis et al., 2008):

$$\begin{aligned} \Delta\gamma_{\max}^p &= \sqrt{(\Delta\varepsilon_{xx}^p - \Delta\varepsilon_{yy}^p)^2 + (\Delta\varepsilon_{xx}^p - \Delta\varepsilon_{zz}^p)^2 + (\Delta\varepsilon_{yy}^p - \Delta\varepsilon_{zz}^p)^2 + (\Delta\gamma_{xy}^p)^2 + (\Delta\gamma_{xz}^p)^2 + (\Delta\gamma_{yz}^p)^2} \quad (3.3) \end{aligned}$$

where $\Delta\varepsilon_{xx}^p$, $\Delta\varepsilon_{yy}^p$, $\Delta\varepsilon_{zz}^p$, $\Delta\gamma_{xy}^p$, $\Delta\gamma_{xz}^p$ and $\Delta\gamma_{yz}^p$ are the plastic normal and shear strain increments in Cartesian coordinates.

As shown in Figure 3.7(a), the failure mechanism for a uniform soil compares well with that of general shear failure (white dashed lines) found from the method of characteristics (Martin, 2003). The comparison between the three cases in Figure 3.7 shows that the depth of the active triangular zone (just beneath the foundation) remains almost the same, although the active triangular zone for Case C21 is slightly curved. However, the shear fan zone for Case C21 extends to a depth of $1D$, but ends at the base of the crust. In addition, Case C21 has no passive zone close to the ground surface, indicating a local shear failure mode. This is because the relatively strong top crust acts as rigid column that restricts both upward and lateral deformations within the crustal layer, while this restriction in turn increases the depth of the failure zone within the bottom layer. A partial shear failure mechanism also appears to be initiating in the lower layer for the two crusted cases. This phenomenon was also observed for both square and circular foundations by Merifield and Nguyen (2006). Figure 3.7(c) shows that the failure mechanism for Case C33 lies in between Figure 3.7(a) and (b), since Case C33 has a moderately strong surficial crust.

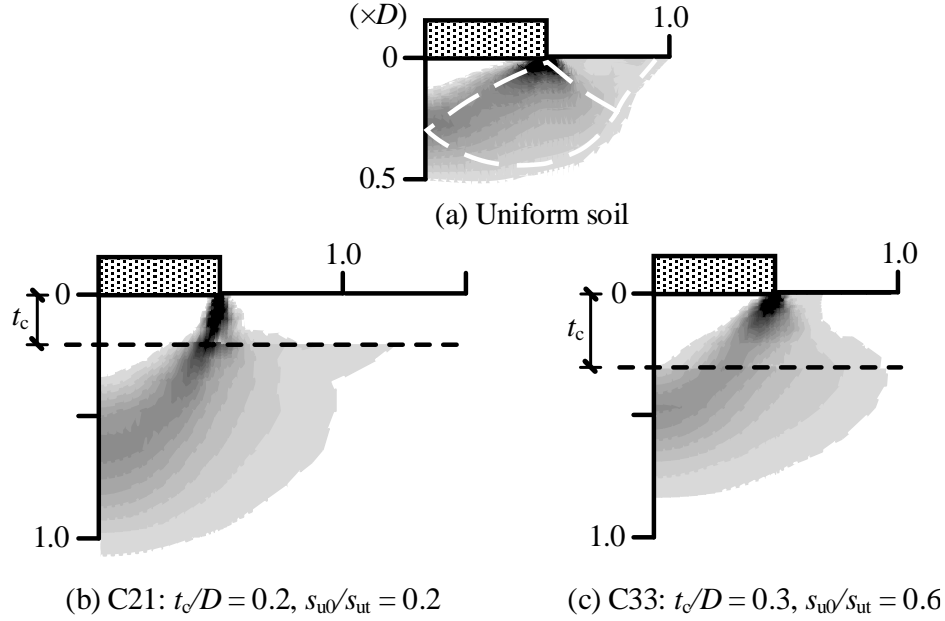


Figure 3.7: Collapse mechanisms under purely vertical loads

3.3.2 Horizontal-Vertical loading

Figure 3.8 shows the effects of s_{u0}/s_{ut} on the dimensionless and normalized H - V failure envelopes using the cases of $s_{u0}/s_{ut} = 0.2 \sim 1.0$ and $t_c/D = 0.2$ (i.e. Cases C21~ C25). The dimensionless failure envelopes shown in Figure 3.8(a) exhibit an expansion of the curves with increasing s_{u0}/s_{ut} . It should also be noted that a stiffer H - V failure envelope can be observed for a smaller value of s_{u0}/s_{ut} (i.e. a greater shear strength difference between the two soil layers), i.e. a lower s_{u0}/s_{ut} ratio corresponds to a larger normalized H - V failure envelope, as shown in Figure 3.8(b). For rectangular foundations on a soil with a crust under an unlimited-tension interface, Feng et al. (2015) proposed an analytical equation (see Eq. (3.4)), that is a function of the loading angle, θ . The curves with $\theta = 0$ and 90° are compared in Figure 3.8(b). A curve fit using Green's solution (see Eq. (3.5)) is also widely used to describe H - V envelopes. It can be seen that Eq. (3.4) with $\theta = 0$ and Eq. (3.5) can provide conservative predictions of the FE results. For simplicity, Eq. (3.5) can be considered to model the H - V failure envelopes ignoring the slight dependence on s_{u0}/s_{ut} .

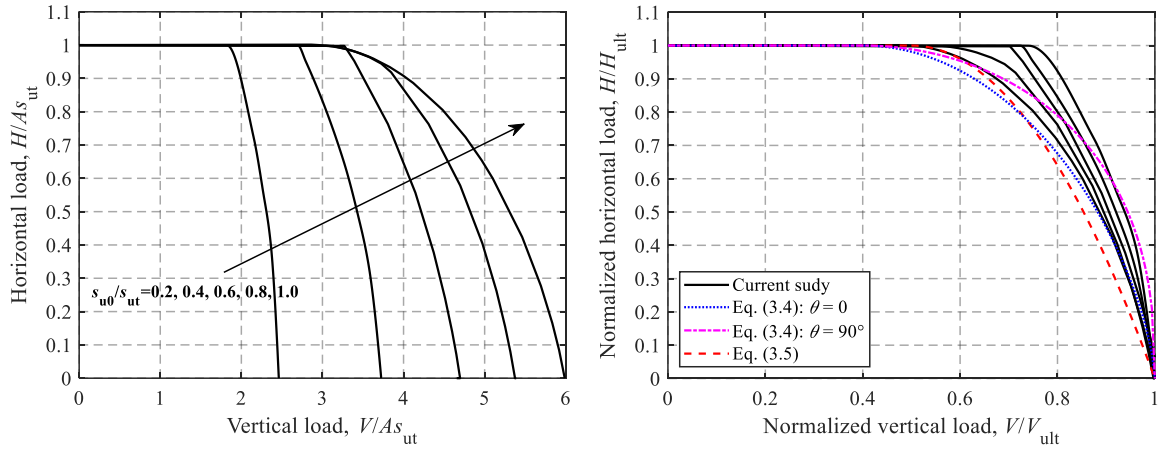
$$V/V_{ult} = 0.4 + 0.6 \sqrt{1 - (H/H_{ult})^{2.5 - \cos^2 \theta}}, \quad \text{for } V/V_{ult} \geq 0.40 \quad (3.4)$$

$$H/H_{ult} = 1, \quad \text{for } V/V_{ult} < 0.40$$

$$V/V_{ult} = 0.5 + 0.5\sqrt{1 - H/H_{ult}}, \quad \text{for } V/V_{ult} \geq 0.50$$

(3.5)

$$H/H_{ult} = 1, \quad \text{for } V/V_{ult} < 0.50$$



(a) Dimensionless

(b) Normalized

Figure 3.8: H - V failure envelopes for $s_{u0}/s_{ut} = 0.2 \sim 1.0$ & $t_c/D = 0.2$: (a) Dimensionless and (b) Normalized

The cases of $s_{u0}/s_{ut} = 0.6$ and $t_c/D = 0.1 \sim 0.3$ (i.e. Cases C13 ~ C33) are presented in Figure 3.9 to show the effect of normalized crust thickness t_c/D on the H - V failure envelopes. As shown in Figure 3.9(a), the size of the H - V failure envelope also increases with t_c/D , but the rate of increase appears to gradually decrease. For the normalized curves shown in Figure 3.9(b), the case of $t_c/D = 0.1$ is close to the case with a uniform soil and the cases of $t_c/D = 0.2$ and 0.3 are almost the same. It can also be seen that Eq. (3.5) can also provide a relatively conservative evaluation of the normalized H - V curves, although dispersion of the curves caused by t_c/D can be observed.

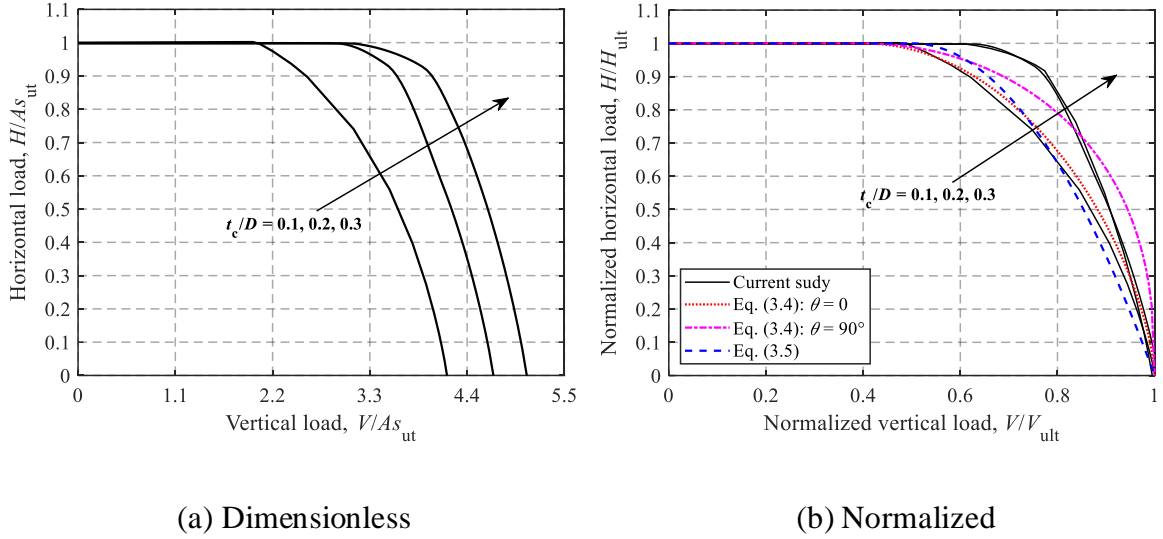


Figure 3.9: H - V failure envelopes for $s_{u0}/s_{ut} = 0.6$ & $t_c/D = 0.1 \sim 0.3$: (a) Dimensionless and (b) Normalized

3.3.3 Moment-Vertical loading

Figure 3.10 shows the effects of s_{u0}/s_{ut} and t_c/D on the failure envelopes under combined vertical and moment loading in terms of dimensionless and normalized loads. Significant expansion of the failure loci in vertical : moment space with increasing s_{u0}/s_{ut} and t_c/D (see Figure 3.10(a) and (c)) is observed, although the rate of expansion gradually decreases with greater s_{u0}/s_{ut} . The failure envelopes in terms of loads normalized by their ultimate values in Figure 3.10(b) and (d) fall in a very tight band, with the shape following the parabolic function given by Eq. (3.6).

$$M/M_{ult} = 4[V/V_{ult} - (V/V_{ult})^2] \quad (3.6)$$

The equation proposed by Feng et al. (2015) for rectangular foundations on a soil with a crust under an unlimited-tension interface is also compared in the figure, however, this is quite different from the current FE results due to the unlimited-tension interface used.

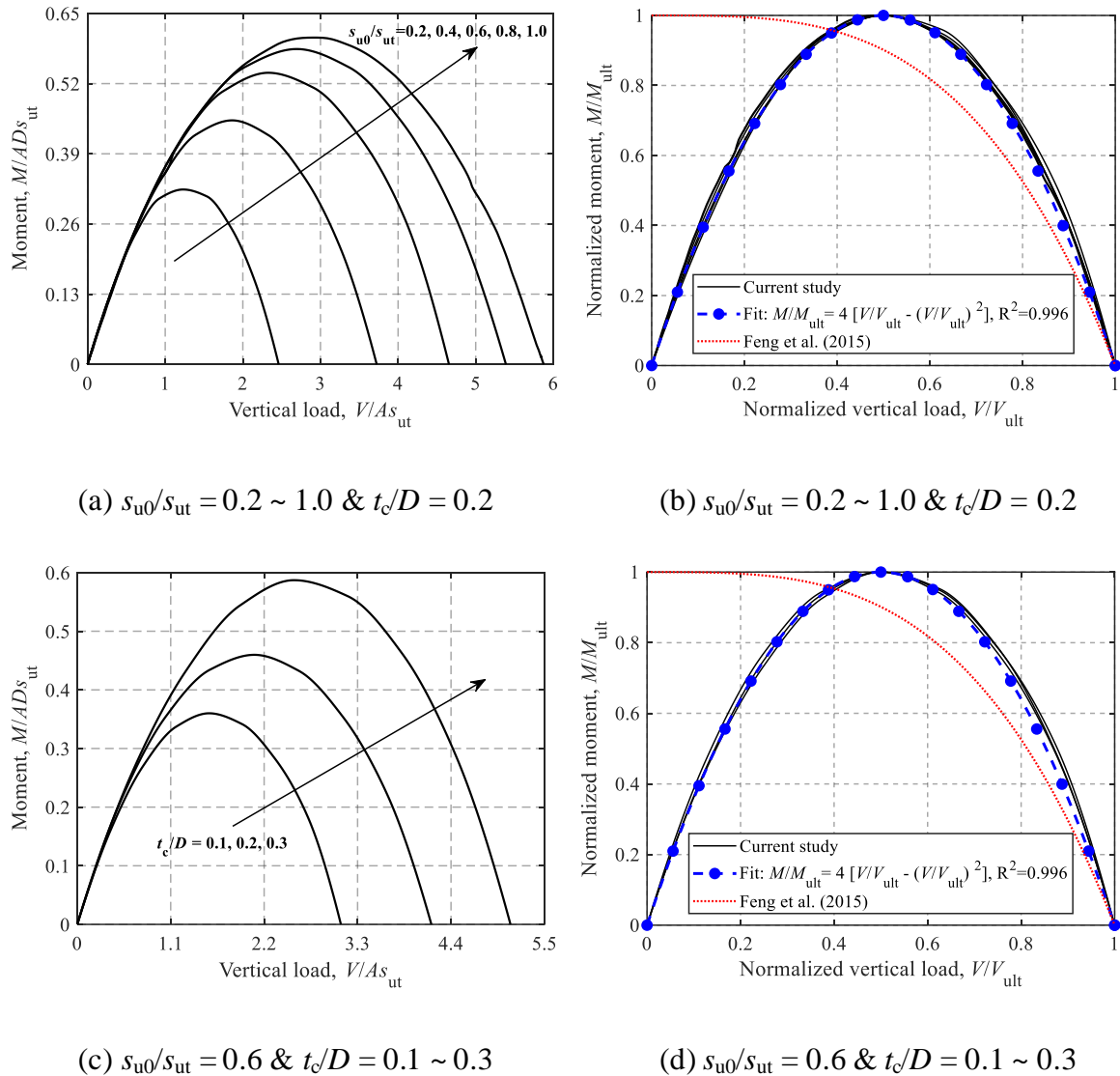


Figure 3.10: M - V failure envelopes: (a) Dimensionless, $s_{u0}/s_{ut} = 0.2 \sim 1.0$ & $t_c/D = 0.2$; (b) Normalized, $s_{u0}/s_{ut} = 0.2 \sim 1.0$ & $t_c/D = 0.2$; (c) Dimensionless, $s_{u0}/s_{ut} = 0.6$ & $t_c/D = 0.1 \sim 0.3$ and (d) Normalized, $s_{u0}/s_{ut} = 0.6$ & $t_c/D = 0.1 \sim 0.3$

Figure 3.11 shows the collapse mechanisms at M_{ult} ($V/V_{ult} = 0.50$) for a uniform soil, and Cases C21 and C33. For the uniform soil, a combined scoop-wedge mechanism is observed (similar to that found by Bransby and Randolph, 1998). Compared with the uniform soil case, the failure zone for Case C21 is primarily confined to the underlying layer and the crust behaves as a rigid column due to the relatively high strength. A wedge mechanism still exists on the right handside of the foundation, but the scoop seems to have been suppressed. Moreover, the depth of failure zone for Case C21 is about two times that for

the uniform soil and the failure pattern for Case C33 lies in between those of the uniform soil and Case C21. Therefore, the main effect of a crustal layer on the collapse zone is suppression of the surface failure and the scoopportion of the mechanisms, and an increase of the depth of the failure zone within the underlying layer.

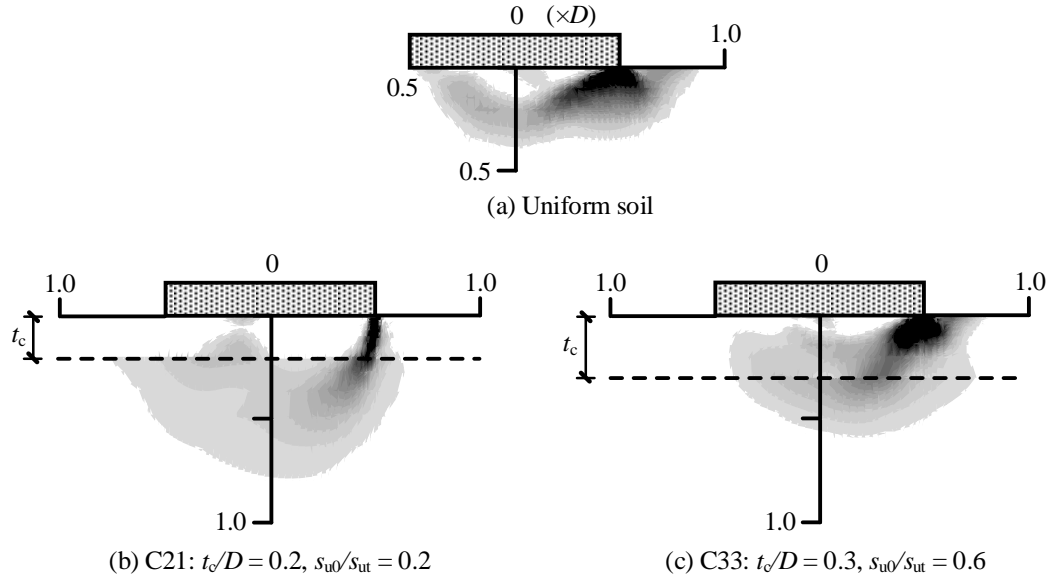


Figure 3.11: Collapse mechanisms at M_{ult}

3.3.4 Torsion-Vertical loading

Figure 3.12 shows the effects of s_{u0}/s_{ut} and t_c/D on the dimensionless and normalized T - V failure envelopes. Similar to the horizontal capacity, the torsional capacity is also determined only by the surface soil strength, therefore, the T - V envelopes share similar features with increasing s_{u0}/s_{ut} and t_c/D to the H - V failure envelopes shown in Figure 3.8. Generally, the T - V failure envelope shows stiffer variations than the H - V failure envelope under the same conditions. The analytical equations proposed by Feng et al. (2014) (see Eq. (3.7)), Abyaneh et al. (2015) (see Eq. (3.8)) and Feng et al. (2015) (see Eq. (3.9)) are compared with the FE result in Figure 3.12(b) and (d). It can be seen that the formula of Abyaneh et al. (2015) gives reasonable and conservative predictions for the T - V envelopes.

$$T/T_{ult} = [1 - 4(V/V_{ult} - 0.5)^2]^{0.4}, V/V_{ult} > 0.50 \quad (3.7)$$

$$T/T_{ult} = 1, V/V_{ult} \leq 0.50$$

$$V/V_{ult} = 0.5 + 0.5[1 - (T/T_{ult})^{2.5}]^{0.3}, V/V_{ult} > 0.50 \quad (3.8)$$

$$T/T_{ult} = 1, V/V_{ult} \leq 0.50$$

$$V/V_{ult} = 0.4 + 0.6\sqrt{1 - (T/T_{ult})^{3.5}}, V/V_{ult} > 0.40 \quad (3.9)$$

$$T/T_{ult} = 1, V/V_{ult} \leq 0.40$$

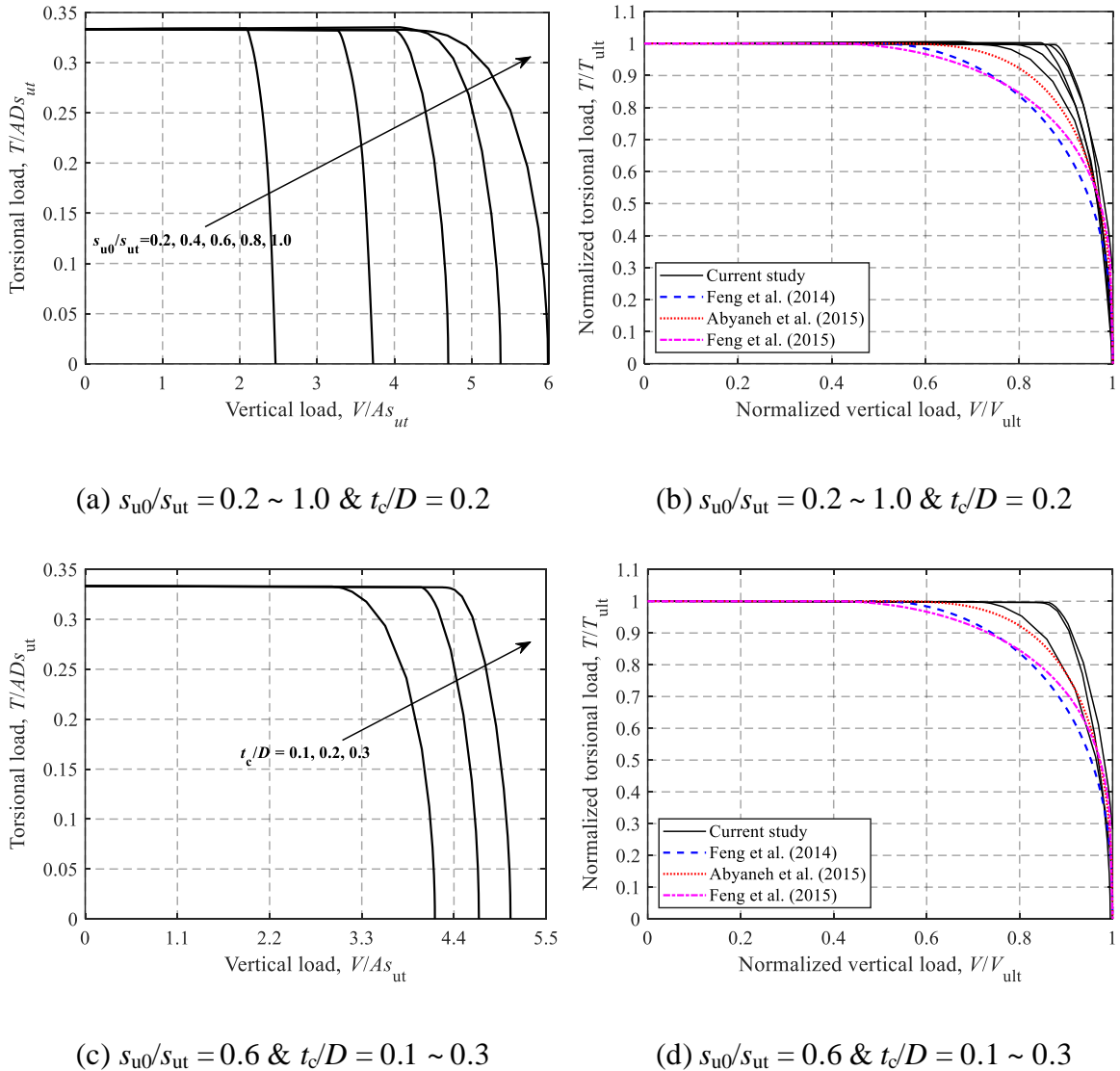


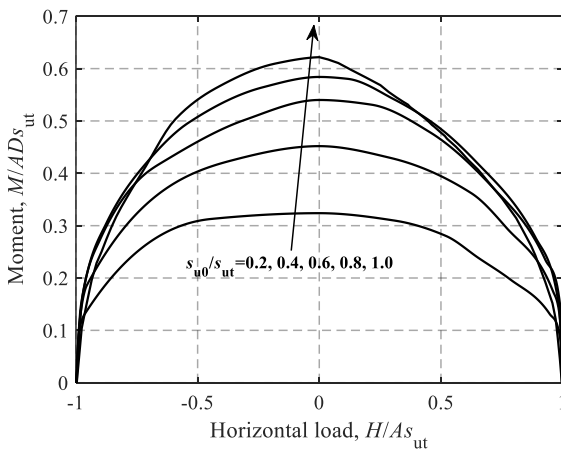
Figure 3.12: T - V failure envelopes: (a) Dimensionless, $s_{u0}/s_{ut} = 0.2 \sim 1.0$ & $t_c/D = 0.2$; (b) Normalized, $s_{u0}/s_{ut} = 0.2 \sim 1.0$ & $t_c/D = 0.2$; (c) Dimensionless, $s_{u0}/s_{ut} = 0.6$ & $t_c/D = 0.1 \sim 0.3$ and (d) Normalized, $s_{u0}/s_{ut} = 0.6$ & $t_c/D = 0.1 \sim 0.3$

3.3.5 Moment-Horizontal loading

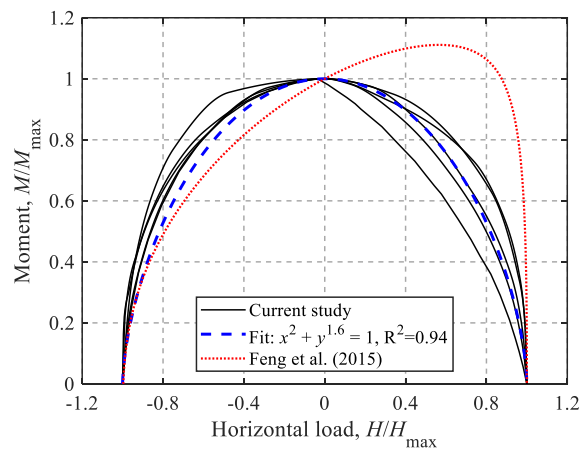
The effects of s_{u0}/s_{ut} and t_c/D on the failure envelopes for $M : H$ loading at $V/V_{ult} = 0.25$, 0.50 and 0.75 are shown in Figure 3.13 and Figure 3.14, respectively. The equation proposed by Feng et al. (2015) for rectangular foundations on a soil with a crust under a unlimited-tension interface is also compared in the figures. Figure 3.13(a) and Figure 3.14(a) shows the dimensionless failure envelopes under the vertical load level of $V/V_{ult} = 0.50$. With the increase of s_{u0}/s_{ut} and t_c/D , expansion of the failure envelopes can be observed, but a similar shape of the curves is expressed. This feature may assist in eliminating the dependence on s_{u0}/s_{ut} , t_c/D and V/V_{ult} levels by normalizing the failure envelopes by their corresponding maximum values, as shown in Figure 3.13(b) ~ (d) and Figure 3.14(b) ~ (d). Moreover, the current $M-H$ curves are almost symmetrical about $H=0$, while the curve proposed by Feng et al. (2015) is oblique due to the effect of the unlimited-tension interface. A unique equation, expressed as:

$$(H/H_{max})^2 + (M/M_{max})^{1.6} = 1 \quad (3.10)$$

can be used to simulate the normalized FE results. As shown in Figure 3.13(b) ~ (d) and Figure 3.14(b) ~ (d), this simple expression gives reasonable fits for various s_{u0}/s_{ut} , t_c/D and V/V_{ult} levels, although a small over-prediction can be observed in the region of $H/H_{max} = 0 \sim 0.60$ for the vertical load level of $V/V_{ult} = 0.25$.



(a) Dimensionless, $V/V_{ult} = 0.50$



(b) Normalized, $V/V_{ult} = 0.75$

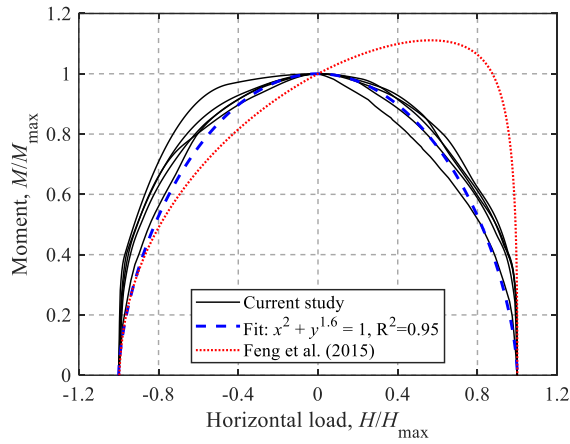
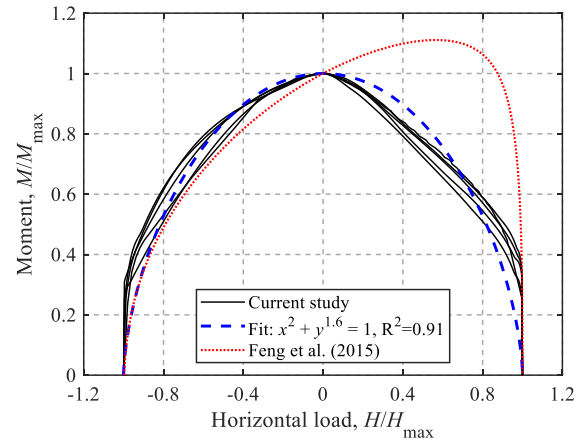
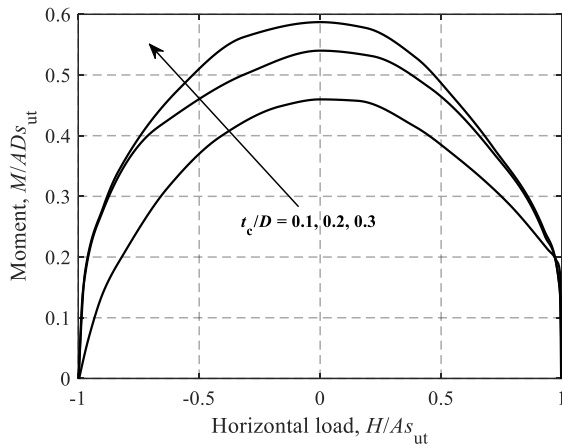
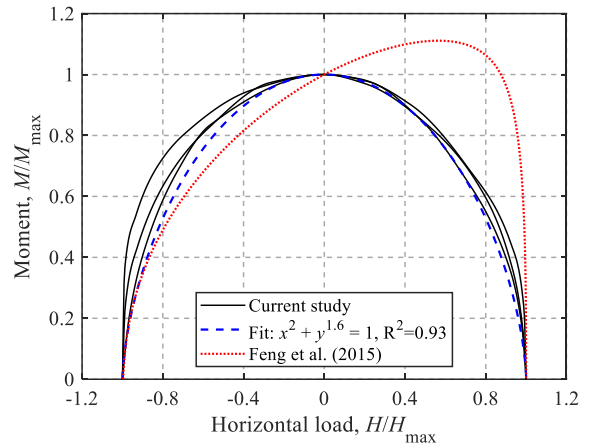
(c) Normalized, $V/V_{ult} = 0.50$ (d) Normalized, $V/V_{ult} = 0.25$

Figure 3.13: M - H failure envelopes for $s_{u0}/s_{ut} = 0.3 \sim 1.0$ & $t_c/D = 0.2$: (a) Dimensionless, $V/V_{ult} = 0.50$; (b) Normalized, $V/V_{ult} = 0.75$; (c) Normalized, $V/V_{ult} = 0.50$ and (d) Normalized, $V/V_{ult} = 0.25$

(a) Dimensionless, $V/V_{ult} = 0.50$ (b) Normalized, $V/V_{ult} = 0.75$

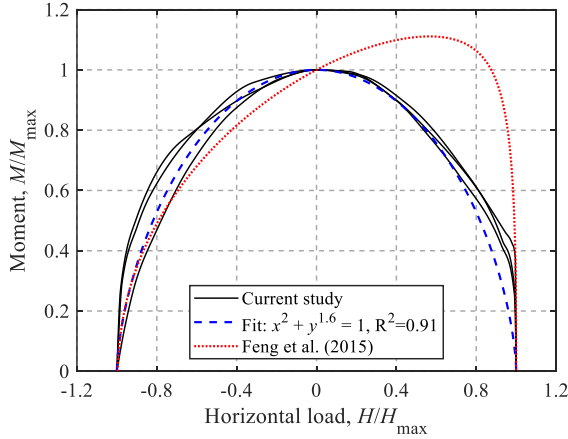
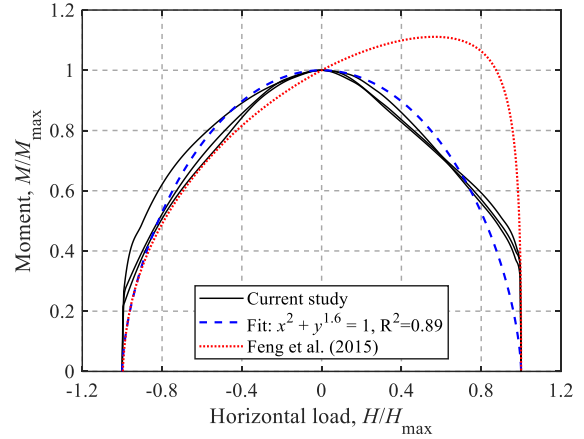
(c) Normalized, $V/V_{ult} = 0.50$ (d) Normalized, $V/V_{ult} = 0.25$

Figure 3.14: M - H failure envelopes for $s_{u0}/s_{ut} = 0.6$ & $t_c/D = 0.1 \sim 0.3$: (a) Dimensionless, $V/V_{ult} = 0.50$; (b) Normalized, $V/V_{ult} = 0.75$; (c) Normalized, $V/V_{ult} = 0.50$ and (d) Normalized, $V/V_{ult} = 0.25$

3.3.6 Horizontal-Torsional loading

Figure 3.15 and Figure 3.16 show the effects of s_{u0}/s_{ut} and t_c/D on the dimensionless and normalized failure envelopes in the H - T loading space (zero moment) at $V/V_{ult} = 0.25, 0.50$ and 0.75 . The dimensionless H - T failure envelopes at $V/V_{ult} = 0.50$ shown in Figure 3.15(a) and Figure 3.16(a) exhibit a high similarity regardless of the values of s_{u0}/s_{ut} and t_c/D . As shown in Figure 3.15(b) ~ (d) and Figure 3.16(b) ~ (d), the equation proposed by Feng et al. (2015) lies slightly inside the normalized FE results. Eq. (3.11) proposed by Finnie and Morgan (2004) can also be considered to fit the H - T failure envelopes for crusted soils. The dimensionless powers, $l = 1.5$ and $n = 1.95$, in Eq. (3.11) yield satisfactory fits, as compared in Figure 3.15(b) ~ (d) and Figure 3.16(b) ~ (d).

$$(H/H_{max})^l + (T/T_{max})^n = 1 \quad (3.11)$$

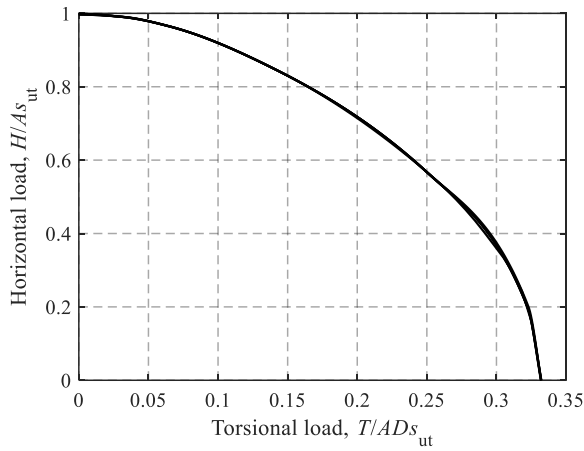
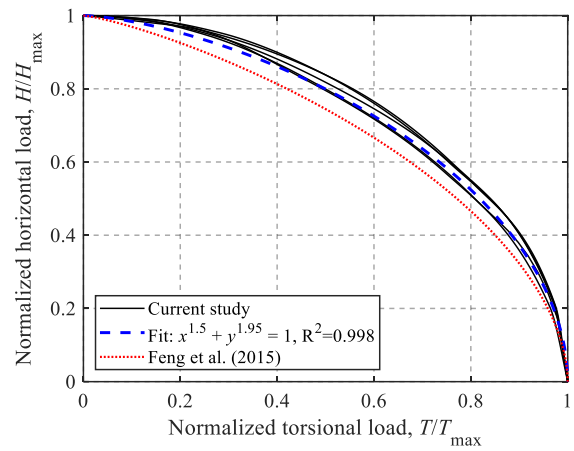
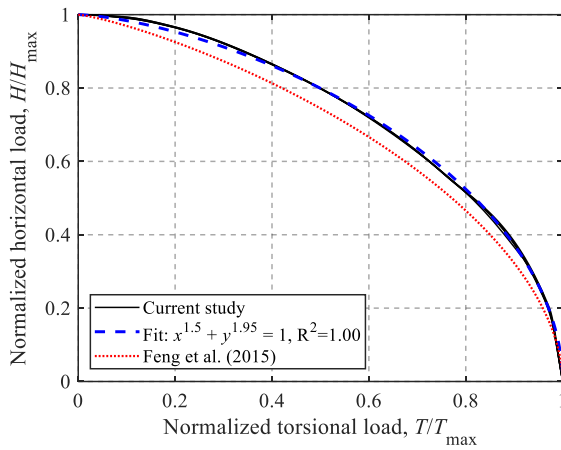
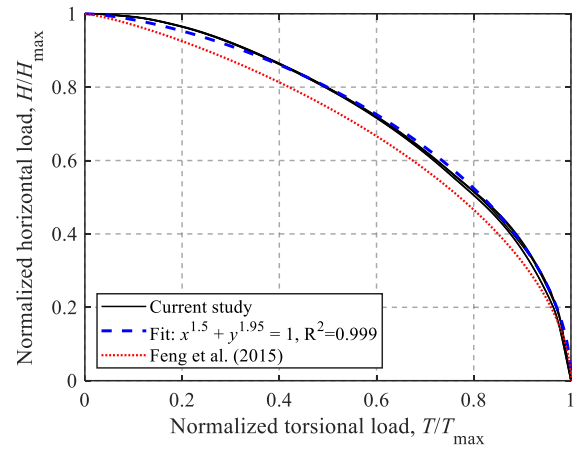
(a) Dimensionless, $V/V_{ult} = 0.50$ (b) Normalized, $V/V_{ult} = 0.75$ (c) Normalized, $V/V_{ult} = 0.50$ (d) Normalized, $V/V_{ult} = 0.25$

Figure 3.15: H - T failure envelopes for $s_{u0}/s_{ut} = 0.2 \sim 1.0$ & $t_c/D = 0.2$: (a) Dimensionless, $V/V_{ult} = 0.50$; (b) Normalized, $V/V_{ult} = 0.75$; (c) Normalized, $V/V_{ult} = 0.50$ and (d) Normalized, $V/V_{ult} = 0.25$

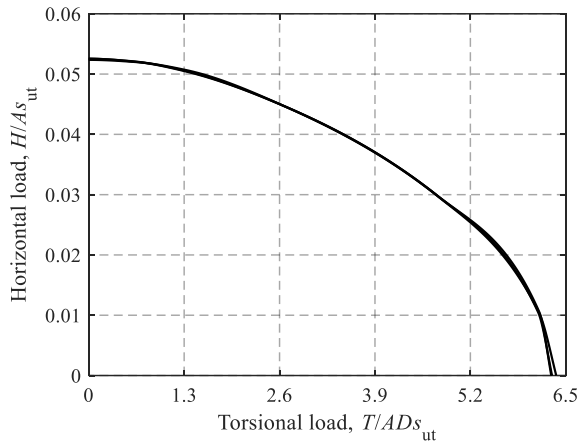
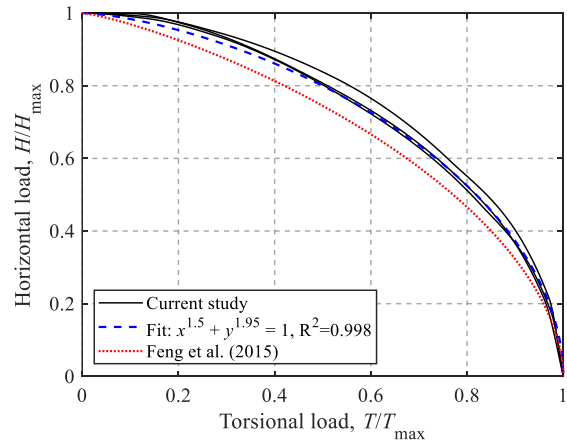
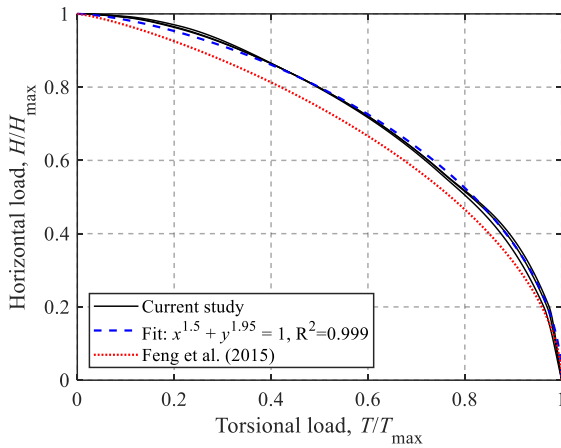
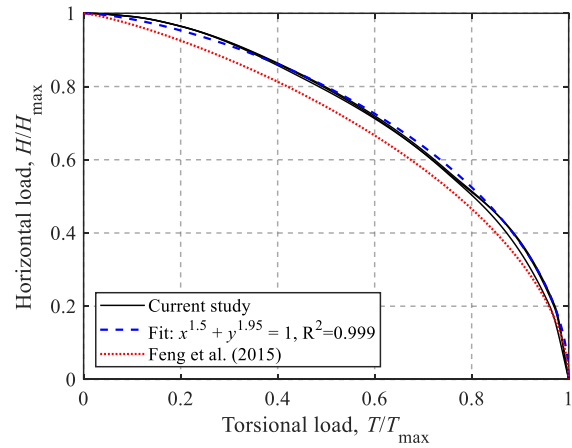
(a) Dimensionless, $V/V_{ult} = 0.50$ (b) Normalized, $V/V_{ult} = 0.75$ (c) Normalized, $V/V_{ult} = 0.50$ (d) Normalized, $V/V_{ult} = 0.25$

Figure 3.16: H - T failure envelopes for $s_{u0}/s_{ut} = 0.6$ & $t_c/D = 0.1 \sim 0.3$: (a) Dimensionless, $V/V_{ult} = 0.50$; (b) Normalized, $V/V_{ult} = 0.75$; (c) Normalized, $V/V_{ult} = 0.50$ and (d) Normalized, $V/V_{ult} = 0.25$

3.3.7 Moment-Torsional loading

The effects of s_{u0}/s_{ut} and t_c/D on the ultimate load-carrying capacity under moment and torsional loading at $V/V_{ult} = 0.25, 0.50$ and 0.75 are shown in Figure 3.17 and Figure 3.18. As shown in Figure 3.17(a) and Figure 3.18(a), unlike the H - T failure envelope at $V/V_{ult} = 0.50$ (see Figure 3.15(a) and Figure 3.16(a)), the absolute size of the dimensionless failure envelopes at $V/V_{ult} = 0.50$ expands with increasing s_{u0}/s_{ut} due to the increase of the

maximum moment. Normalization by the corresponding maximum values of moments and torsional loads can also make these curves to fall into a relatively narrow band. The expression given by Feng et al. (2015) seems to be unconservative for $V/V_{ult} = 0.50$ and 0.25. Similar to Eq. (3.11), the analytical relationship of Eq. (3.12) with the two dimensionless parameters equal to 2 (i.e. a unit circle) is also compared with the FE result in Figure 3.17(b) ~ (d) and Figure 3.18(b) ~ (d). Favorable predictions can be observed apart from slight over-predictions in the region of $T/T_{ult} = 0.40 \sim 0.80$ at $V/V_{ult} = 0.25$.

$$(M/M_{max})^\alpha + (T/T_{max})^\beta = 1 \quad (3.12)$$

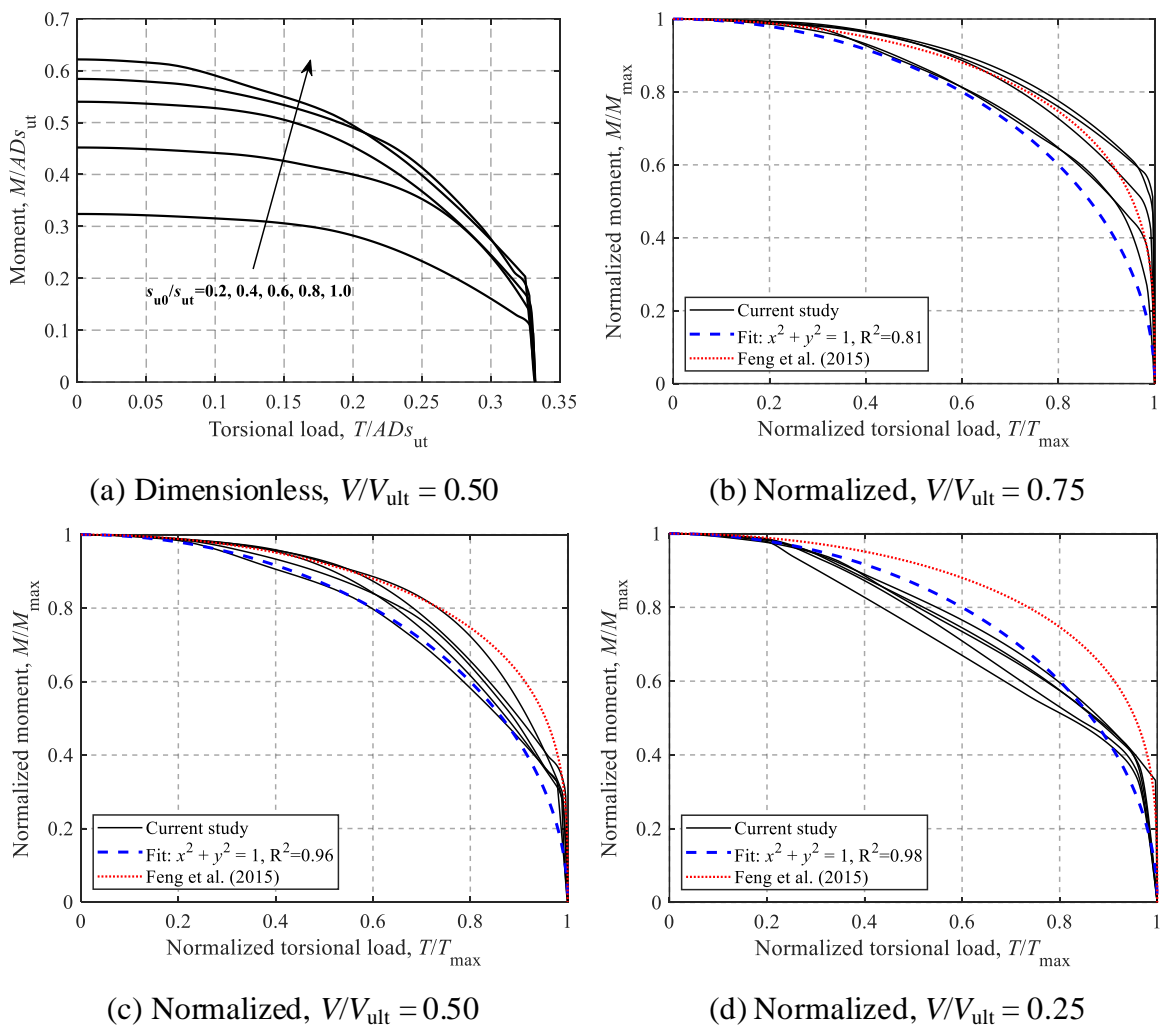


Figure 3.17: M - T failure envelopes for $s_{u0}/s_{ut} = 0.2 \sim 1.0$ & $t_c/D = 0.2$: (a)

Dimensionless, $V/V_{ult} = 0.50$; (b) Normalized, $V/V_{ult} = 0.75$; (c) Normalized, $V/V_{ult} = 0.50$ and (d) Normalized, $V/V_{ult} = 0.25$

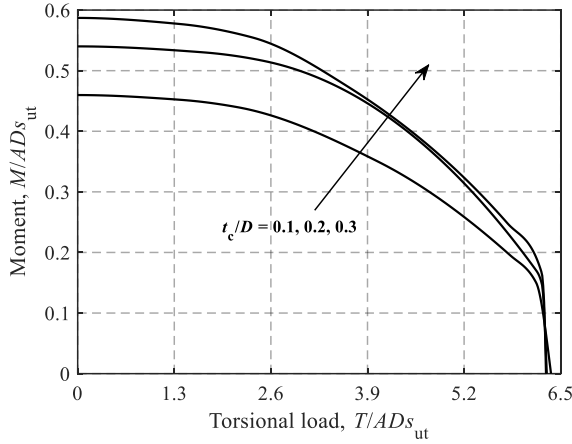
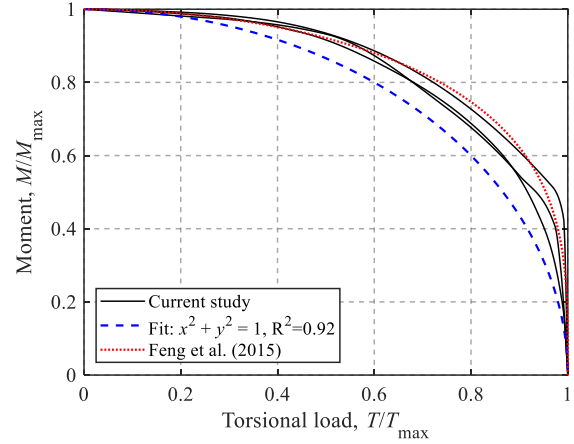
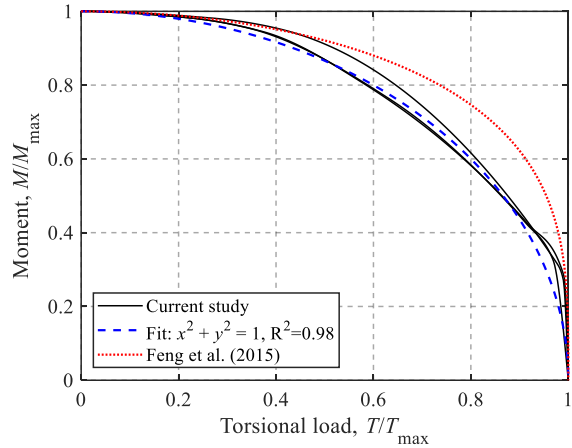
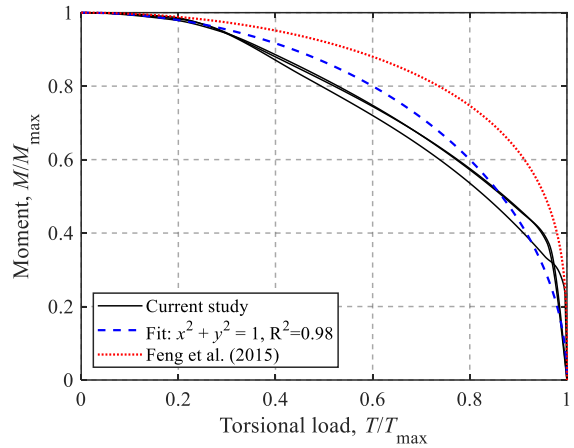
(a) Dimensionless, $V/V_{ult} = 0.50$ (b) Normalized, $V/V_{ult} = 0.75$ (c) Normalized, $V/V_{ult} = 0.50$ (d) Normalized, $V/V_{ult} = 0.25$

Figure 3.18: M - T failure envelopes for $s_{u0}/s_{ut} = 0.6$ & $t_c/D = 0.1 \sim 0.3$: (a) Dimensionless, $V/V_{ult} = 0.50$; (b) Normalized, $V/V_{ult} = 0.75$; (c) Normalized, $V/V_{ult} = 0.50$ and (d) Normalized, $V/V_{ult} = 0.25$

3.4 Full 4-D failure envelope in VHMT loading space

This section derives a 4-D expression for the failure envelope in VHMT loading space. Three sets of notation are defined: (1) V_{ult} , H_{ult} , M_{ult} , T_{ult} – uniaxial ultimate capacity defined in Section 3.3.1; (2) H_{max} , M_{max} , T_{max} – maximum capacity at a given level of the vertical load without other load components; (3) H'_{max} , M'_{max} – reduced maximum capacity at a given level of the vertical load with a non-zero torsional load ($T \neq 0$).

Based on the above notation and the forms of equation used in the previous sections, the general forms of all of the equations are summarized in Table 3.2. f_h, f_m , and f_t are functions of the vertical load level. Specific expressions for these failure envelopes can be found in the previous sections.

Table 3.2: Summary of FE-calculated failure envelopes

Failure envelope	Conditions	Analytical form
$H-V$	$M = 0 \ \& \ T = 0$	$\frac{H_{\max}}{H_{\text{ult}}} = f_h \left(\frac{V}{V_{\text{ult}}} \right)$ (3.13)
$M-V$	$H = 0 \ \& \ T = 0$	$\frac{M_{\max}}{M_{\text{ult}}} = f_m \left(\frac{V}{V_{\text{ult}}} \right)$ (3.14)
$T-V$	$M = 0 \ \& \ H = 0$	$\frac{T_{\max}}{T_{\text{ult}}} = f_t \left(\frac{V}{V_{\text{ult}}} \right)$ (3.15)
$M-H$	$V \neq 0 \ \& \ T = 0$	$\left(\frac{H}{H_{\max}} \right)^a + \left(\frac{M}{M_{\max}} \right)^b = 1$ (3.16)
$H-T$	$V \neq 0 \ \& \ M = 0$	$\left(\frac{H'_{\max}}{H_{\max}} \right)^c + \left(\frac{T}{T_{\max}} \right)^d = 1$ (3.17)
$M-T$	$V \neq 0 \ \& \ H = 0$	$\left(\frac{M'_{\max}}{M_{\max}} \right)^e + \left(\frac{T}{T_{\max}} \right)^f = 1$ (3.18)

Eq. (3.16), which describes the $M-H$ failure envelope under the condition of $T = 0$, is taken as the basic function. However, a more generalized equation for the $M-H$ failure envelope under the condition of $T \neq 0$ is required for deriving the final 4-D expression. Due to the very similar shape of the $M-H$ failure envelope (only the sizes are different), it is reasonable to assume that under the condition of $T \neq 0$, Eq. (3.16) is still applicable for the $M-H$ failure envelope normalized by the corresponding maximum values, H'_{\max} and M'_{\max} (reduce to H_{\max} and M_{\max} in Eq. (3.16) if $T = 0$). Therefore, Eq. (3.16) can be replaced by a more generalized form:

$$\left(\frac{H}{H'_{\max}}\right)^a + \left(\frac{M}{M'_{\max}}\right)^b = 1 \quad (3.19)$$

Mathematical manipulations of Eqs. (3.13), (3.14), (3.15), (3.17), (3.18) and (3.19) allow the formulation of an analytical 4-D expression for the failure envelope in VHMT loading space in terms of V/V_{ult} , H/H_{ult} , M/M_{ult} , and T/T_{ult} , as shown in Eq. (3.20).

$$\begin{aligned} f\left(\frac{V}{V_{\text{ult}}}, \frac{H}{H_{\text{ult}}}, \frac{M}{M_{\text{ult}}}, \frac{T}{T_{\text{ult}}}\right) &= \left(\frac{H/H_{\text{ult}}}{\left[1 - \left(\frac{T/T_{\text{ult}}}{f_t(V/V_{\text{ult}})}\right)^d\right]^{\frac{1}{c}} \cdot f_h(V/V_{\text{ult}})} \right)^a \\ &+ \left(\frac{M/M_{\text{ult}}}{\left[1 - \left(\frac{T/T_{\text{ult}}}{f_t(V/V_{\text{ult}})}\right)^f\right]^{\frac{1}{e}} \cdot f_m(V/V_{\text{ult}})} \right)^b = 1 \end{aligned} \quad (3.20)$$

In practical design, the design loads (factored loads and materials), VHMT, can be directly substituted into the left-hand side of Eq. (3.20); values less than 1 represent a sufficient ultimate limit design and vice versa.

As an example, the full 4-D expression of the failure envelope for Case C24 (i.e. $s_{u0}/s_{ut} = 0.6$ and $t_c/D = 0.2$) is presented. To visualize the shape of the full 4-D failure surface, three 3-D failure surfaces in terms of V/V_{ult} , H/H_{ult} , M/M_{ult} , and T/T_{ult} (i.e. VHM failure surface at $T = 0$, VHT failure surface at $M = 0$ and VMT failure surface at $H = 0$) are presented in Figure 3.19. The specific curves obtained from the FE results in the previous sections are also incorporated for comparison. For the VHT and VMT failure surfaces, the portion of $T < 0$ is also incorporated due to the symmetry about the plane of $T = 0$.

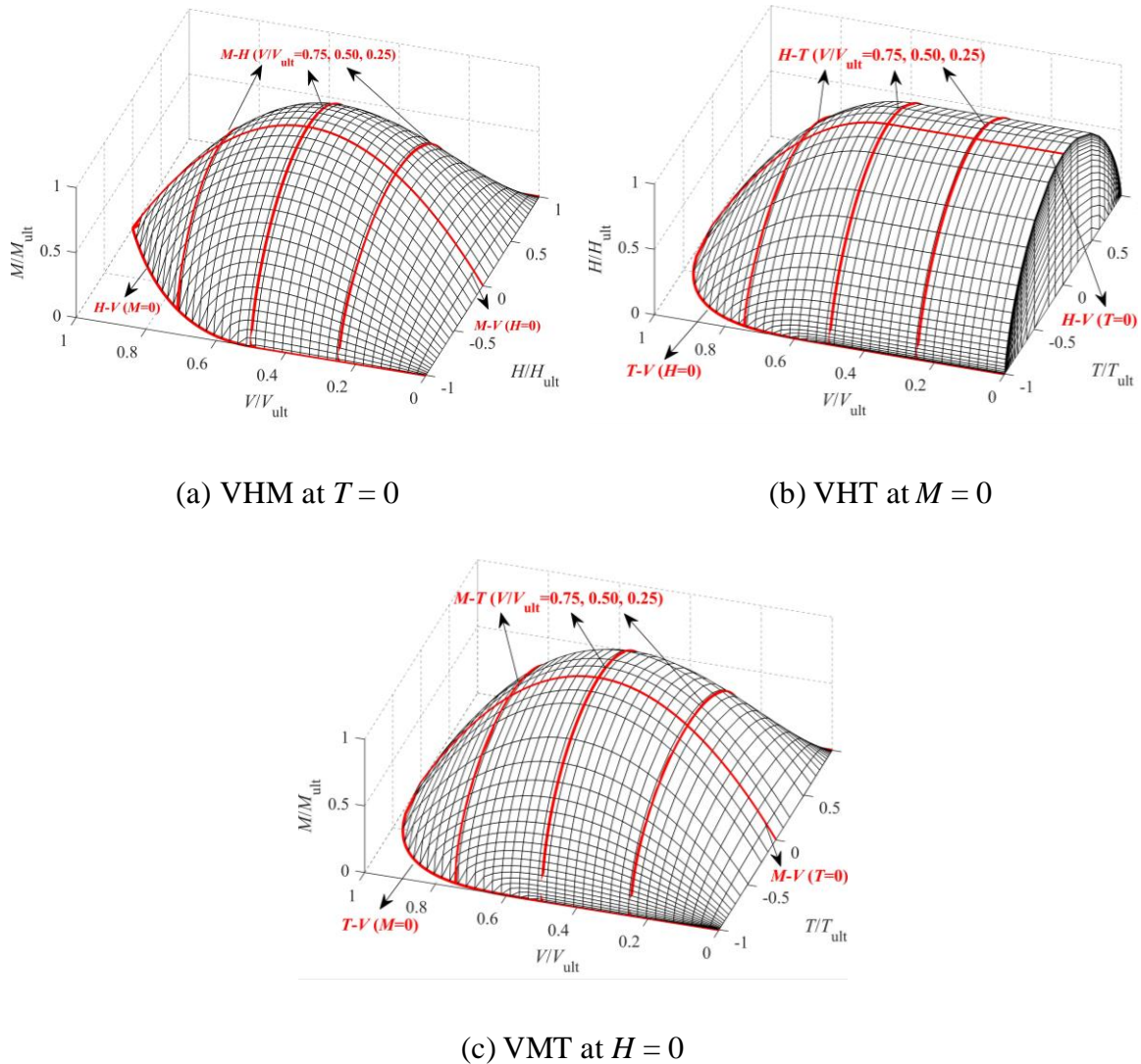


Figure 3.19: 3-D failure surfaces for Case C24 (i.e. $s_{u0}/s_{ut} = 0.6$ and $t_c/D = 0.2$): (a) VHM at $T = 0$; (b) VHT at $M = 0$ and (c) VMT at $H = 0$

3.5 Conclusions

The VHMT failure envelopes of circular foundations resting on a stiff crust which overlies the main soil deposit under undrained conditions have been studied using FE analysis. A zero-tension interface condition was considered. Cases with five values of s_{u0}/s_{ut} and three values of t_c/D have been utilized to investigate the effects of s_{u0}/s_{ut} and t_c/D on the failure envelopes of shallow foundation. For the uniaxial vertical and moment capacities, crust correction factors have been introduced to account for the effects of s_{u0}/s_{ut} and t_c/D . Analytical equations of the crust correction factors, which are functions of s_{u0}/s_{ut} and t_c/D ,

were also proposed. s_{u0}/s_{ut} exhibits a significant influence on the normalized H - V failure envelopes. The same forms of equation that are used for uniform soils, but with different parameters can provide good fits for the VHMT failure envelopes for a soil with a surficial crust. To facilitate the application of the failure envelope method in practical foundation design, a full 4-D analytical expression for the VHMT failure envelope was derived based on the calculated VHMT failure envelopes.

3.6 References

- Abyaneh, S.D., Ojo, A., Maconochie, A., and Haghghi, A. (2015). The undrained bearing capacity of shallow foundations subjected to three-dimensional loading including torsion. *In Proceedings of the 25th International Ocean and Polar Engineering Conference*, Kona, Hawaii, 21-26 June 2015. International Society of Offshore and Polar Engineers, Cupertino, pp. 668-674.
- API (American Petroleum Institute) (2011). API Recommended Practice, Geotechnical and Foundation Design Considerations. American Petroleum Institute, Washington, D.C.
- Bienen, B., Gaudin, C., and Cassidy, M. J. (2007). Centrifuge tests of shallow footing behaviour on sand under combined vertical-torsional loading. *International Journal of Physical Modelling in Geotechnics*, 7(2), 01-21.
- Bjerrum, L. (1973). Problems of soil mechanics and construction on soft clays and structurally unstable soils (collapsible, expansive and others). *In Proceedings of the 8th International Conference in Soil Mechanics and Foundation Engineering*, Moscow, 3, pp. 111-159.
- Bransby, M. F., and Randolph, M. F. (1998). Combined loading of skirted foundations. *Géotechnique*, 48(5), 637-655.
- DassaultSystèmes (2016). Abaqus analysis user's manual. Simulia Corp., Providence, R.I.
- Deshpande, V. M. (2016). Numerical modelling of wind turbine foundations subjected to combined loading. Master's thesis, The University of Western Ontario, London, Ont.
- DNV GL (Det Norske Veritas GL) (2016). DNVGL-ST-0126: Support structures for wind turbines. DNV GL Group, Høvik, Norway.
- Feng, X., Gourvenec, S., Randolph, M. F., Wallerand, R., and Dimmock, P. (2015). Effect of a surficial crust on mudmat capacity under fully three-dimensional loading. *Géotechnique*, 65(7), 590-603.
- Feng, X., Randolph, M. F., Gourvenec, S., and Wallerand, R. (2014). Design approach for rectangular mudmats under fully three-dimensional loading. *Géotechnique*, 64(1), 51-63.

- Finnie, I. M. S., and Morgan, N. (2004). Torsional loading of subsea structures. *In Proceedings of the 14th International Offshore and Polar Engineering Conference*. Toulon, France, 23-28 May 2004. International Society of Offshore and Polar Engineers, Mountain View, pp. 326-333.
- Gourvenec, S. (2007). Shape effects on the capacity of rectangular footings under general loading. *Géotechnique*, 57(8), 637-646.
- Gourvenec, S., and Randolph, M. (2003). Effect of strength non-homogeneity on the shape of failure envelopes for combined loading of strip and circular foundations on clay. *Géotechnique*, 53(6), 575-586.
- International Electrotechnical Commission (2005). IEC 61400-1: Wind turbines – part 1: Design requirements. International Electrotechnical Commission, Geneva, Switzerland.
- ISO (International Standards Organization). (2016). ISO 19901-4: Petroleum and natural gas industries specific requirements for offshore structures – part 4: geotechnical and foundation design considerations, 2nd edition. International Standards Organization, Geneva, Switzerland.
- Lee, Y. N., and Park, B. K. (1999). The Surface Strengthening of Dredged-Clay Fill Layer Deposit in Yulchon Industrial Complex. *In Proceedings of Geotechnical Case Histories in Korea*, pp. 19-27.
- Lefebvre, G., Paré, J. J., and Dascal, O. (1987). Undrained shear strength in the surficial weathered crust. *Canadian Geotechnical Journal*, 24(1), 23-34.
- Lutenegger, A. J. (1995). Geotechnical behavior of overconsolidated surficial clay crusts. *Transportation research record*, 1479, 61.
- Martin C. M. (2003). User guide for ABC – Analysis of Bearing Capacity, Version 1.0. OUEL Report No. 2261/03. University of Oxford, Oxford, UK.
- Merifield, R. S., and Nguyen, V. Q. (2006). Two- and three-dimensional bearing-capacity solutions for footings on two-layered clays. *Geomechanics and Geoengineering: An International Journal*, 1(2), 151-162.
- Merifield, R. S., Sloan, S. W., and Yu, H. S. (1999). Rigorous plasticity solutions for the bearing capacity of two-layered clays. *Géotechnique*, 49(4), 471-490.
- Nakase, A., T. Kimura, K. Saitoh, J. Takemora, and T. Hagiwara. (1978). Behavior of Soft Clay with a Surface Crust. *In Proceedings of the 8th Asian Regional Conference on Soil Mechanics and Foundation Engineering*, Vol. 1, 1978, pp. 410-414.
- Park, H., Lee, S. R., and Jee, S. H. (2010). Bearing capacity of surface footing on soft clay underlying stiff nonhomogeneous desiccated crust. *International Journal of Offshore and Polar Engineering*, 20(03), 224-232.
- Rochelle, P. L., Trak, B., Tavenas, F., and Roy, M. (1974). Failure of a test embankment on a sensitive Champlain clay deposit. *Canadian Geotechnical Journal*, 11(1), 142-164.

- Sagaseta, C., and R. Arroyo. Limit Analysis of Embankments on Soft Clay. *In Proceedings of International Symposium on Numerical Models in Geomechanics*, Zurich, Switzerland, 13-17 September 1982, pp. 618-625.
- Shen, Z., Feng, X., and Gourvenec, S. (2016). Undrained capacity of surface foundations with zero-tension interface under planar VHM loading. *Computers and Geotechnics*, 73, 47-57.
- Shen, Z., Feng, X., and Gourvenec, S. (2017). Effect of interface condition on the undrained capacity of subsea mudmats under six-degree-of-freedom loading. *Géotechnique*, 67(4), 338-349.
- Taiebat, H. A., and Carter, J. P. (2010). A failure surface for circular footings on cohesive soils. *Géotechnique*, 60(4), 265-273.
- Tan, F. S. C. (1990). Centrifuge and theoretical modelling of conical footings on sand. Doctoral dissertation, Cambridge University, Cambridge, UK.
- Terzaghi, K. (1951). *Theoretical soil mechanics*. Chapman & Hall, London, UK.
- Ukritchon, B., Whittle, A. J., and Sloan, S. W. (1998). Undrained limit analyses for combined loading of strip footings on clay. *Journal of Geotechnical and Geoenvironmental Engineering*, 124(3), 265-276.

4 Drained bearing capacity of circular surface foundations under combined VHMT loading

4.1 Introduction

The bearing capacity of shallow foundations under combined loading conditions can be of great significance, particularly for large onshore and offshore structures, such as wind turbines, oil and gas platforms, transmission towers and masts, due to their complex environmental and climate loadings. The majority of large wind turbine shallow foundations are circular or close to circular in form. These wind turbine foundations are generally subjected to combined loadings that includes: vertical loads due to the self-weight of the structure (V), horizontal loads (H) caused by environmental conditions, overturning moments (M) due to the horizontal loading and structural height, and torsional loads (T) induced by wind and structural effects (Bienen et al., 2007).

Traditional analytical methods for these types of structures are based on classical solutions for the uniaxial vertical bearing capacity of strip shallow foundations using the superposition principle (Terzaghi, 1951). The contributions of soil cohesion, soil unit weight and surcharge to the bearing capacity are taken into consideration in an uncoupled manner. The effects of load inclination and eccentricity are accounted for by introducing the load inclination factor and the effective foundation area (e.g. DNV, 2016; API, 2011). For a circular foundation on the surface of a cohesive-frictional soil in the absence of surcharge, the general bearing capacity equation reduces to (Hansen, 1970; DNV, 2016):

$$q_u = c' N_c s_c i_c + \frac{1}{2} \gamma' D' N_\gamma s_\gamma i_\gamma \quad (4.1)$$

where N_c and N_γ are the bearing capacity factors accounting for the cohesion and the self-weight of the soil, respectively; c' is the soil cohesion; γ' is the effective unit weight of the soil; s_c and s_γ are the dimensionless shape factors; i_c and i_γ are the dimensionless inclination factors; and D' is the effective foundation width accounting for the load eccentricity. In general, this approach can be conservative, while it has been shown to be non-conservative for strip foundations on soils with strength increasing with depth (Ukritchon et al., 1998).

The failure envelope method has been recommended as an alternative to more conventional theories in some geotechnical design guidelines (particularly those focused on offshore geotechnics), such as API (2011) and ISO (2016), since this method explicitly accounts for the load interaction effect between the various load components (Shen et al., 2017). Many researchers have studied failure envelopes under undrained soil conditions by considering different foundation shapes (e.g. Bransby and Randolph, 1998; Gourvenec and Randolph, 2003; Shen et al., 2016), soil strength heterogeneity (e.g. Feng et al., 2014) and interface conditions (e.g. Shen et al., 2016; Gourvenec and Randolph, 2003).

Some investigations on failure envelopes for drained soil conditions can also be found in the literature. These studies focus primarily on foundations on sands subjected to centric vertical loads (e.g. Saran et al., 1971), eccentric vertical loads (e.g. Purkayastha and Char, 1977; Zadroga, 1994) and combinations of these two types of loads (e.g. Loukidis et al., 2008; Saran and Agarwal, 1991; Georgiadis and Butterfield, 1988), which can be transformed to $V-H$, $V-M$ and $M-H$ failure envelopes, respectively. These studies also focus mainly on combinations of vertical, horizontal and moment loads. However, environmental loads on structures are often not co-planar, and transverse loads can also induce torsional effects on the foundation (Bienen et al., 2007). Thus, in many cases the influence of torsional loads should not be ignored for failure envelopes of shallow foundations.

However, the aforementioned studies are confined to purely frictional soils in the absence of soil cohesion, ignoring the more general $c-\phi$ problem. Overconsolidated clays and intermediate soils under drained conditions will often exhibit both cohesion and friction angles ranging from 20° to 30° (Soderman and Quigley, 1965). Cox (1962) discussed the pure vertical capacity of circular foundations on cohesive-frictional soils using the theory of axially symmetric plastic deformations. Hjiij et al. (2004) evaluated the lower and upper bounds for the bearing capacity of strip foundations on cohesive-frictional soils under non-eccentric inclined loads using numerical limit analysis; although the failure envelope approach was not adopted and the non-eccentric loading could not account for the effects of moment loading. Moreover, the aforementioned studies on drained failure envelopes are limited to some special cross-sections of the global failure surface, such as the $H-V$ cross-section in the absence of moment and torsional loads, $M-V$ cross-section in the absence of

horizontal and torsional loads, and $M-H$ cross-section under specific vertical load levels in the absence of torsional loading. Therefore, to apply the failure envelope method to practical foundation design, a more general analytical expression of the failure surface in VHMT loading space is required.

To address these omissions in the literature, the object of this study is to investigate the full VHMT failure envelope of circular surface foundations on cohesive-frictional soils under a zero-tension interface for drained soil conditions. The effects of the friction angle and self-weight of the soil on the VHMT failure envelope have been studied. A full 4-D VHMT failure envelope is estimated using the finite element (FE) method.

4.2 Method – finite element analysis

4.2.1 Material models and interface conditions

The constitutive relationship used to model the soil behavior was a linear elastic perfectly plastic model following a Mohr-Coulomb (M-C) failure criterion characterized by cohesion, c' , and friction angle, φ' . The associated flow rule (i.e. the friction angle equal to the dilatancy angle) was considered for the analyses. It is known that the bearing capacity of a circular surface foundation is related not only to the soil properties (i.e. effective unit weight γ' , cohesion c' and friction angle φ'), but also to the foundation dimensions (i.e. diameter D). Cox (1962) and Hjiiaj et al. (2004) showed theoretically that the bearing capacity of a circular surface foundation on a general M-C material without surcharge depends only on two dimensionless numbers involving the aforementioned parameters, i.e. the friction angle φ' and the weight parameter defined by $G = \gamma'D/2c'$.

The effective unit weight of soil was taken as 8.0 kN/m^3 . The diameter (D) and thickness (t) of the shallow circular foundation used in the analyses were 19 m and 3 m, representing typical dimensions for current large wind turbines in North America. Values of $\varphi' = 0, 10^\circ, 20^\circ, 30^\circ, 35^\circ, 40^\circ$ and $G = 0.5, 1.0, 2.0, 3.0$ (corresponding to $c' = 25 \sim 150 \text{ kPa}$) were used to span most soils of practical interest, which is similar to the ranges adopted by Hjiiaj (2004). It has been demonstrated that the Young's modulus, Poisson's ratio and earth pressure coefficient of the soil affect the evolution of load-displacement curves, but have little influence on the collapse loads (Potts et al., 2001; Lee and Salgado, 2005). The

Poisson's ratio (μ') of the soil was taken as 0.35 and a sufficiently large Young's modulus (E') equal to 6×10^6 kPa was chosen to minimize mesh distortion. The foundation was assumed to act as a rigid body. A load reference point (LRP) attached to the center of the base of foundation was utilized to apply prescribed displacements or loads. For drained soil conditions, the FE analyses considered a zero-tension rough base that allows separation of the foundation from the soil.

4.2.2 Geometry and mesh

The FE analyses were conducted using the software ABAQUS (Dassault Systèmes, 2016). To avoid the effects of model boundaries on the development of failure mechanisms, a soil model diameter of $6.5D$ and a depth of the soil of $3.25D$ was adopted, following the model dimensions of Erickson and Drescher (2002) and Achmus et al. (2013). A mesh convergence study was carried out for a number of cases and that for $G = 2$ & $\varphi' = 20^\circ$ is shown in Figure 4.1. Preliminary analyses show that the rate of convergence considerably decreases with increase of φ' and second-order elements (i.e. ABAQUS 20-noded C3D20R elements) can yield faster convergence than first-order elements (i.e. ABAQUS 8-noded C3D8R). In addition, second-order elements can provide higher accuracy and capture stress concentrations more effectively. The difference between the ultimate vertical loads using Mesh 2 (14000 elements) and 3 (20000 elements) is about 1%. However, the model solution with Mesh 3 takes about 3 times longer than that using Mesh 2. Therefore, Mesh 2 was adopted in the analysis. To capture the intense stress concentration close to the foundation edge and the large plastic shear strains at the interface, the soil regions in the vicinity of the foundation edge and the horizontal thin soil layer close to the interface were carefully refined. The cylindrical circumference of the soil domain was constrained to prevent out-of-plane translations, and the bottom of the soil domain was fixed in the three orthogonal directions.

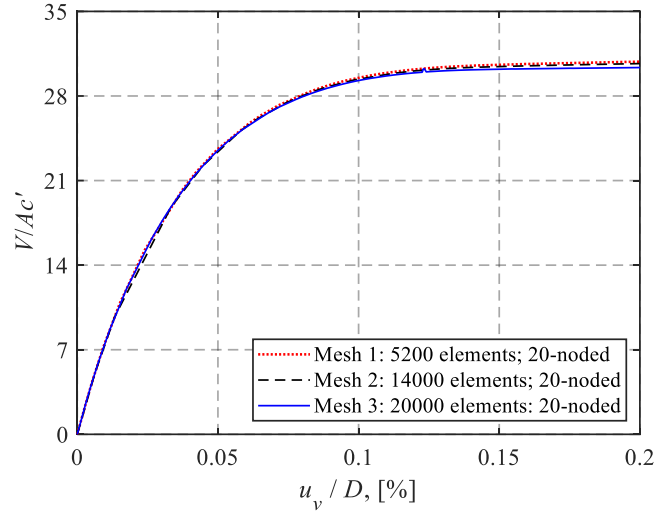


Figure 4.1: Mesh convergence study for the case of $G = 2$ & $\phi' = 20^\circ$

4.2.3 Sign conventions and loading paths

The sign conventions for the loads are shown in Figure 4.2. In the analyses, the horizontal and moment loads were considered to be in the same plane.

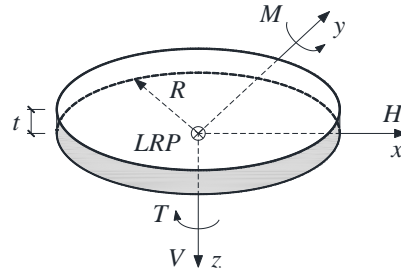


Figure 4.2: Sign conventions

Swipe tests and probe tests were used to detect the failure envelopes under various load conditions. The swipe test brings the foundation to a collapse state in coordinate direction 1 first, followed by a displacement applied in coordinate direction 2, during which the increment of the displacement in coordinate direction 1 remains zero (Gourvenec and Randolph, 2003). In a probe analysis, a vertical load is first applied at the LRP of the foundation and remains constant. A fixed-ratio of displacement is then imposed to the foundation to detect the failure point on the failure envelope. A probe test can only obtain

a single point on a failure envelope. Two typical failure envelopes obtained using both the swipe and probe tests are shown in Figure 4.3.

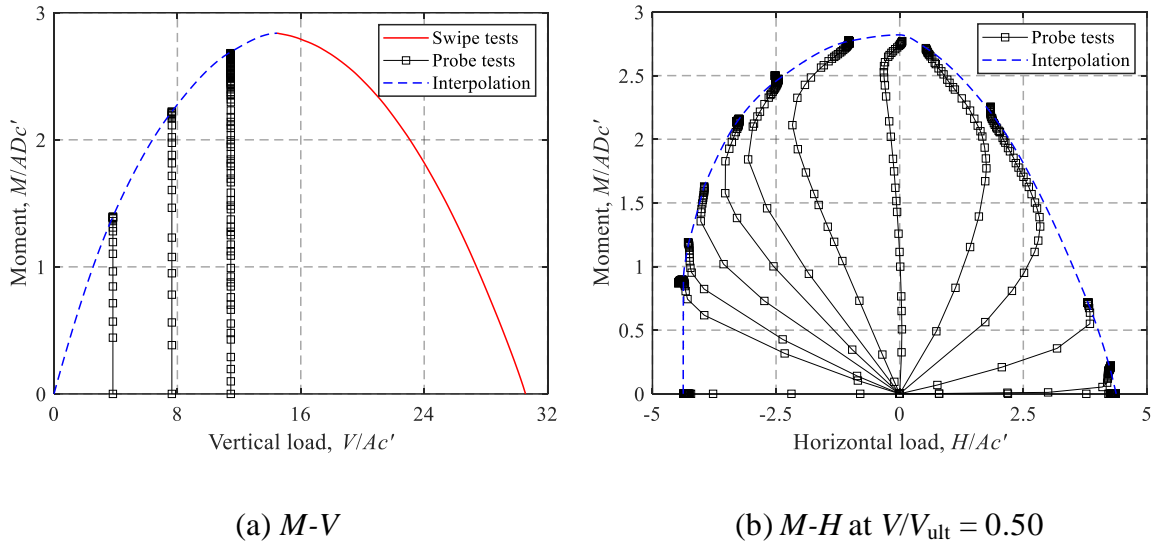


Figure 4.3: $M-V$ and $M-H$ failure envelopes for the case of $G = 2$ & $\phi' = 20^\circ$: (a) $M-V$ and (b) $M-H$ at $V/V_{ult} = 0.50$

4.3 Finite element results

4.3.1 Validation

Following Hjiij et al. (2004), the vertical uniaxial bearing capacity factor can be defined as:

$$v_0 = V_{ult}/(A \cdot c') \quad (4.2)$$

where V_{ult} is the vertical uniaxial bearing capacity and A is the soil-foundation contact area.

Table 4.1 summarizes the values of v_0 for two sets of cases resulting from the present FE analyses and the method of characteristics (MOC). The exact solutions based on the MOC are calculated using the ABC program (Martin, 2003), which has also been validated by other studies (e.g. Smith, 2005; Lyamin et al., 2007). As can be seen from Table 4.1, the present values agree well with the MOC results for various values of ϕ' and G (maximum difference less than 4.82%), supporting the validity of the present FE model.

Table 4.1: Values of ν_0 resulting from FE analyses and the method of characteristics

Cases	$G=2.0$						$\varphi'=20^\circ$			
	$\varphi'=0$	$\varphi'=10^\circ$	$\varphi'=20^\circ$	$\varphi'=30^\circ$	$\varphi'=35^\circ$	$\varphi'=40^\circ$	$G=0.5$	$G=1.0$	$G=2.0$	$G=3.0$
Current study	6.04	12.18	30.60	103.14	218.88	547.21	25.18	27.18	30.60	34.65
Martin (2003)	6.05	12.67	32.15	107.94	228.38	549.09	26.01	28.17	32.15	35.86

4.3.2 Pure uniaxial capacities

Accurate determination of the uniaxial capacities is important for the failure envelope method, since they control the absolute size of the failure surface. For a zero-tension interface under drained soil conditions, the foundation, in the absence of vertical loads, cannot resist moment loading and only small horizontal and torsional loads (contributed by soil cohesion) can be mobilized. Therefore, unlike undrained uniaxial capacities defined by the ultimate loads in the absence of other loading modes (Shen et al., 2016), drained uniaxial capacities for horizontal, moment and torsional modes are referred to as the corresponding maximum loads under vertical loading. Following Eq. (4.2), the uniaxial bearing capacity factors for horizontal, moment and torsional modes are defined as:

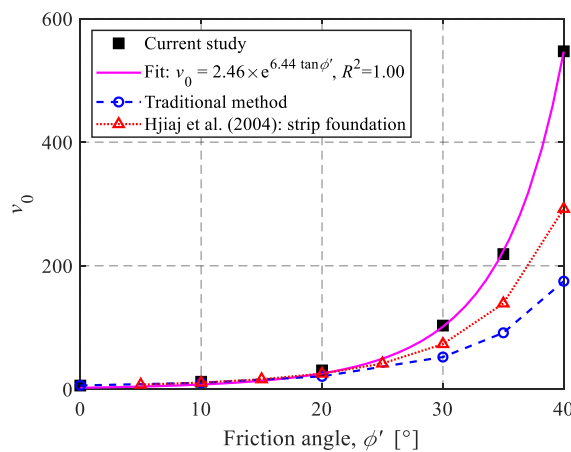
$$\begin{aligned}
 h_0 &= H_{\text{ult}}/(A \cdot c') \\
 m_0 &= M_{\text{ult}}/(A \cdot D \cdot c') \\
 t_0 &= T_{\text{ult}}/(A \cdot D \cdot c')
 \end{aligned} \tag{4.3}$$

where H_{ult} , M_{ult} and T_{ult} are the uniaxial bearing capacities, respectively.

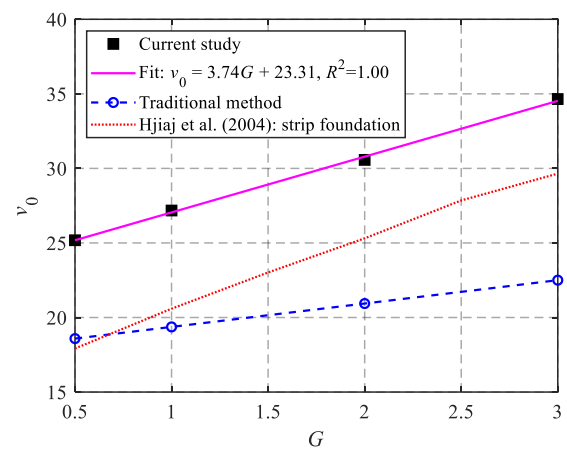
Figure 4.4 shows the values of the bearing capacity factors plotted against G and φ' . The ultimate limit state design for shallow foundations using the traditional method (i.e. DNV, 2016) is also compared in Figure 4.4. Hjjaj et al. (2004) evaluated the lower and upper bounds of the bearing capacity for strip footings on cohesive-frictional soils using numerical limit analysis. Since only non-eccentric inclined loads were investigated by Hjjaj et al. (2004), only these vertical and horizontal modes are compared.

Figure 4.4(a) ~ (d) shows that the bearing capacity factors exponentially increase with ϕ' , which agrees with the overall trends provided by the traditional method and Hjiiaj et al. (2004). However, compared with the FE results, the traditional method considerably underestimates the values for $\phi' > 20^\circ$ and the differences between them significantly increase with ϕ' . Specifically, t_0 at $\phi' = 40^\circ$ calculated by the FE method is around 8 times greater than that predicted by the traditional method. The primary reason for the dramatic discrepancy is the equivalent horizontal load used in the traditional method to account for torsional effects. Figure 4.4(a) and (b) also shows that the results for strip foundations lie in between the FE results and those estimated by the traditional method. Moreover, the current bearing capacity factors are fitted using exponential equations with regard to $\tan\phi'$, as compared in Figure 4.4(a) ~ (d). The comparison shows a satisfactory agreement.

The bearing capacity factors for cases of $G = 0.5 \sim 3$ and $\phi' = 20^\circ$ are shown in Figure 4.4(e) ~ (h) along with the traditional method and Hjiiaj et al. (2004). The figure shows that the bearing capacity factors appear to linearly increase with G . The traditional method consistently provides much more conservative predictions than the FE method. In addition, the slopes of the lines provided by the traditional method are smaller than those predicted by the FE method and Hjiiaj et al. (2004). The results of Hjiiaj et al. (2004) are still smaller than the FE results, but present very similar slopes for v_0 and h_0 , as shown in Figure 4.4(e) and (f). Linear equations with regard to G are used to fit the FE results and favorable predictions can be observed.



(a) V_{ult} ; $G = 2$ & $\phi' = 0 \sim 40^\circ$



(e) V_{ult} ; $G = 0.5 \sim 3$ & $\phi' = 20^\circ$

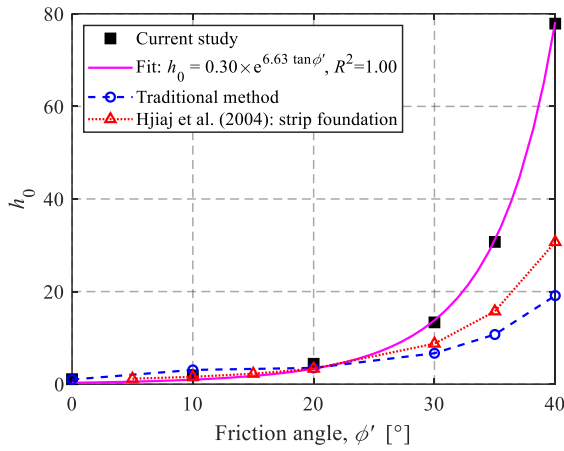
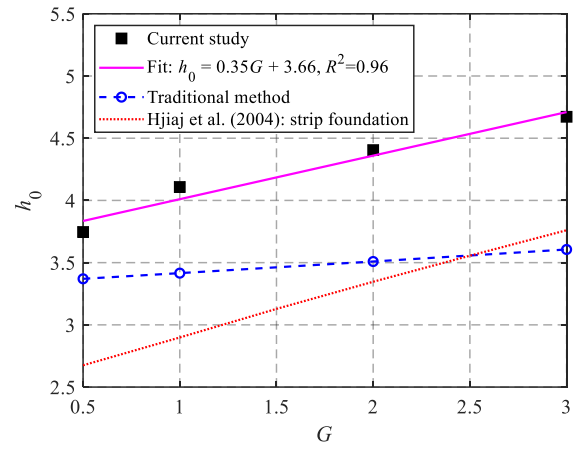
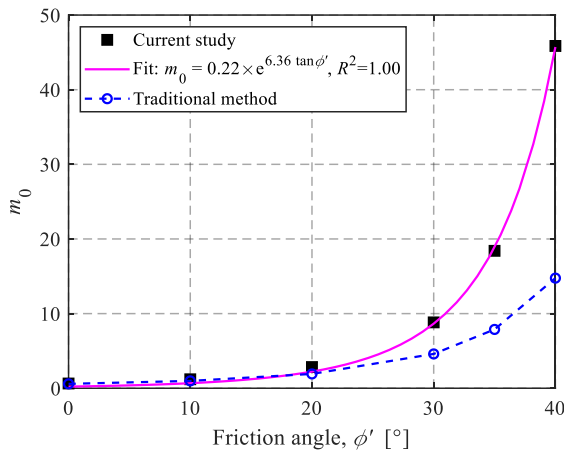
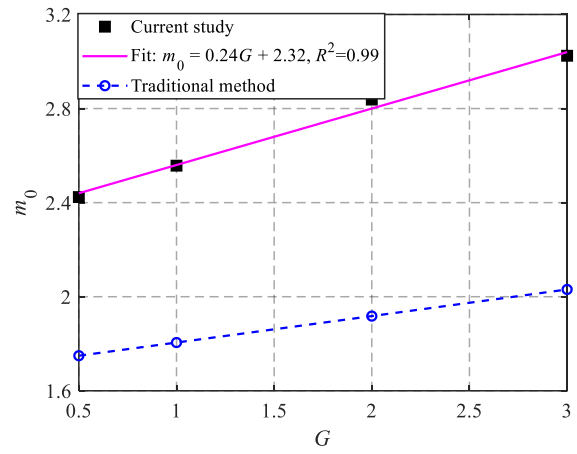
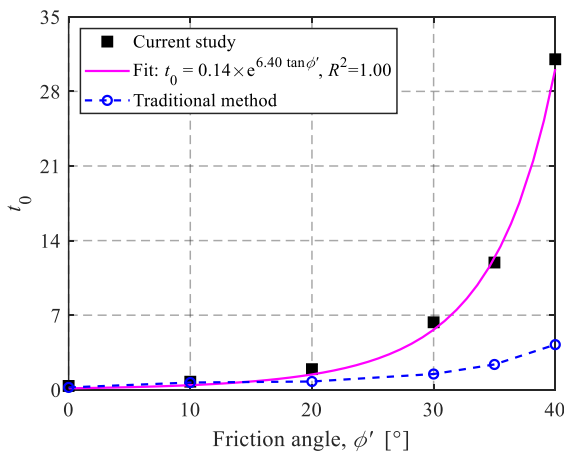
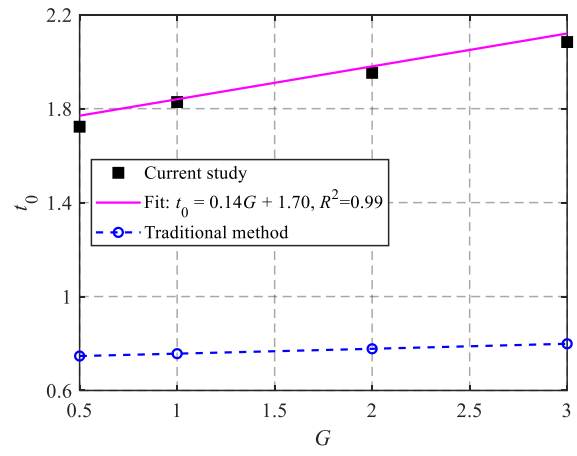
(b) H_{ult} ; $G = 2$ & $\phi' = 0 \sim 40^\circ$ (f) H_{ult} ; $G = 0.5 \sim 3$ & $\phi' = 20^\circ$ (c) M_{ult} ; $G = 2$ & $\phi' = 0 \sim 40^\circ$ (g) M_{ult} ; $G = 0.5 \sim 3$ & $\phi' = 20^\circ$ (d) T_{ult} ; $G = 2$ & $\phi' = 0 \sim 40^\circ$ (h) T_{ult} ; $G = 0.5 \sim 3$ & $\phi' = 20^\circ$

Figure 4.4: Ultimate capacity factors: (a) V_{ult} ; $G = 2$ & $\varphi' = 0 \sim 40^\circ$; (b) H_{ult} ; $G = 2$ & $\varphi' = 0 \sim 40^\circ$; (c) M_{ult} ; $G = 2$ & $\varphi' = 0 \sim 40^\circ$; (d) T_{ult} ; $G = 2$ & $\varphi' = 0 \sim 40^\circ$; (e) V_{ult} ; $G = 0.5 \sim 3$ & $\varphi' = 20^\circ$; (f) H_{ult} ; $G = 0.5 \sim 3$ & $\varphi' = 20^\circ$; (g) M_{ult} ; $G = 0.5 \sim 3$ & $\varphi' = 20^\circ$ and (h) T_{ult} ; $G = 0.5 \sim 3$ & $\varphi' = 20^\circ$

4.3.3 Horizontal-Vertical loading

Figure 4.5 shows the effects of φ' and G on the dimensionless and normalized H - V failure envelopes. Results of Hjiiaj et al. (2004) derived from inclined loads for strip foundations ($\varphi' = 0$ is unavailable) are also compared. For the dimensionless envelopes shown in Figure 4.5(a) and (c), as expected, the initial slopes of the curves (i.e. at $V = 0$) are equal to the corresponding values of $\tan\varphi'$, which can also be confirmed from the curves of Hjiiaj et al. (2004). Specifically, the initial slopes of the failure envelopes in Figure 4.5(c) remain the same due to the same value of φ' . The dimensionless curves also show that the absolute size of the H - V failure envelope gradually increases with G (see Figure 4.5(c)), but dramatically expands with increasing φ' (see Figure 4.5(a)). Moreover, strip foundations exhibit much smaller H - V envelopes than circular foundations and the difference between them increases with φ' , as shown in Figure 4.5(a).

For the normalized envelopes shown in Figure 4.5(b) and (d), the traditional method provides conservative estimations for $V/V_{ult} > 0.50$, while unconservative predictions can be observed for $V/V_{ult} \leq 0.50$. Due to the different initial slopes caused by values of φ' , the normalized curves shown in Figure 4.5(b) do not fall into a narrow band for $V/V_{ult} \leq 0.50$, while this is not the case for curves in Figure 4.5(d) (with the same value of φ'). Since the normalized envelopes for $V/V_{ult} > 0.50$ in Figure 4.5(b) still lie in a relatively narrow band, a piecewise function is proposed to fit the H - V failure envelope. The curves for $V/V_{ult} > 0.50$ can be reasonably well fitted by Eq. (4.4):

$$H/H_{ult} = 4[V/V_{ult} - (V/V_{ult})^2] \quad \text{for } V/V_{ult} > 0.50 \quad (4.4)$$

The curves for $V/V_{ult} \leq 0.50$ can be approximated by a polynomial:

$$H/H_{ult} = a_1(V/V_{ult})^3 + b_1(V/V_{ult})^2 + c_1(V/V_{ult}) + d_1 \quad \text{for } V/V_{ult} \leq 0.50 \quad (4.5)$$

with the coefficients being functions of $\tan \phi'$:

$$\begin{aligned}
 c_1 &= (V_{ult}/H_{ult}) \cdot \tan \phi' \\
 d_1 &= e^{-0.57c_1} \\
 a_1 &= 4 \cdot (c_1 + 4d_1 - 4) \\
 b_1 &= 4 \cdot (-c_1 - 3d_1 + 3)
 \end{aligned}
 \tag{4.6}$$

Reasonable comparisons between the proposed expression and the FE results can be observed in Figure 4.5(b). It can also be seen that the proposed equation with $\phi' = 20^\circ$ shows a good agreement with the failure envelopes in Figure 4.5(d).

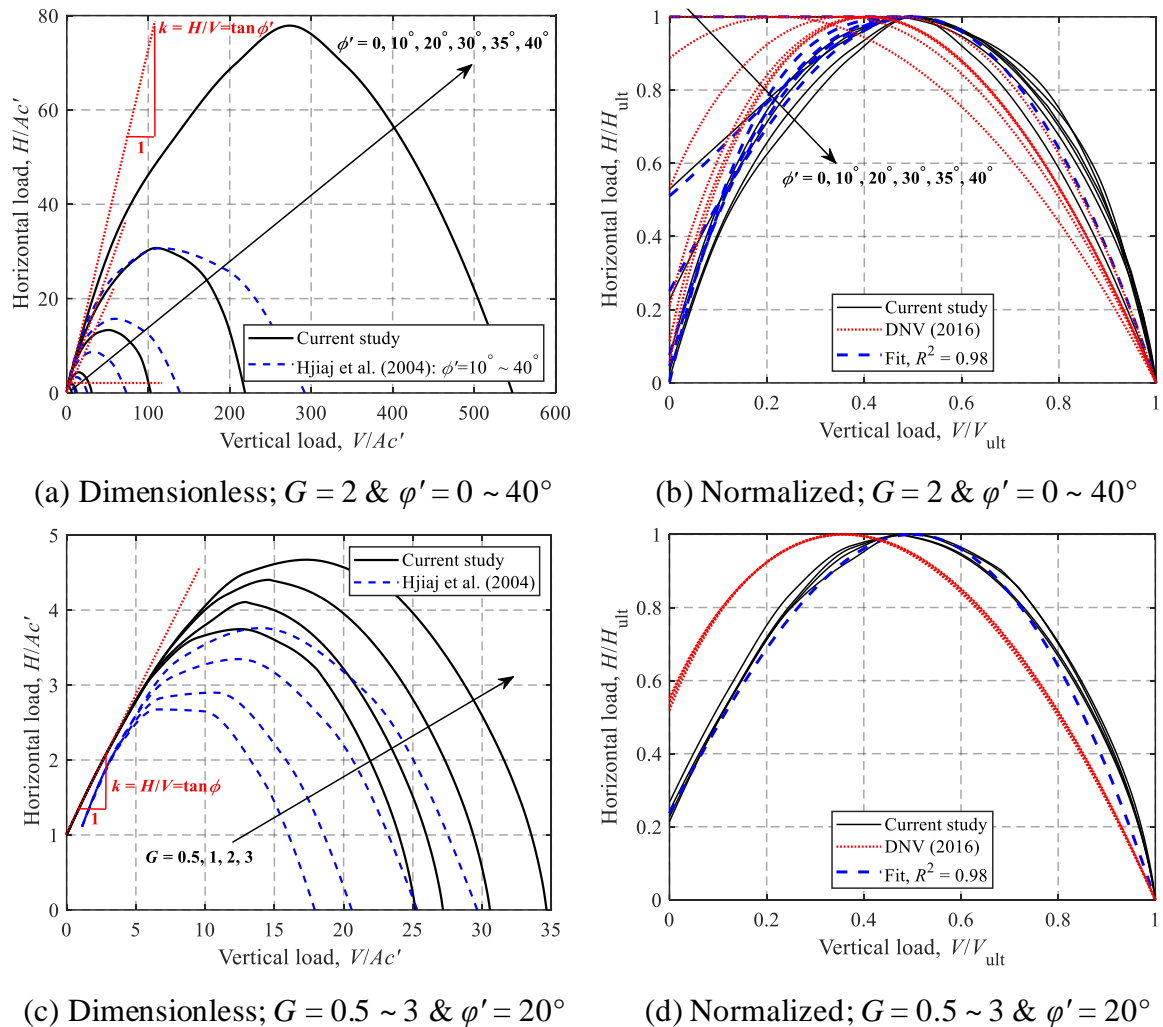
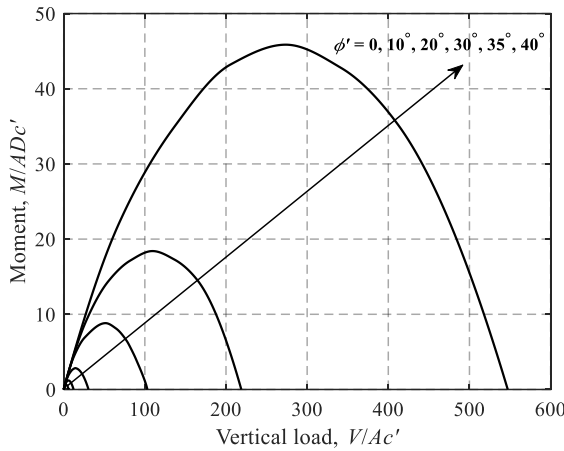


Figure 4.5: H-V failure envelopes: (a) Dimensionless; $G = 2$ & $\phi' = 0 \sim 40^\circ$; (b) Normalized; $G = 2$ & $\phi' = 0 \sim 40^\circ$; (c) Dimensionless; $G = 0.5 \sim 3$ & $\phi' = 20^\circ$ and (d) Normalized; $G = 0.5 \sim 3$ & $\phi' = 20^\circ$

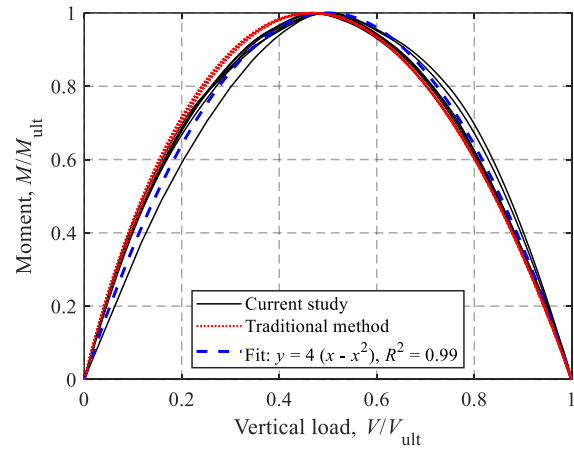
4.3.4 Moment-Vertical loading

Figure 4.6 shows the M - V failure envelopes for cases with various ϕ' and G . Similar to the H - V failure envelopes, the size of the M - V envelopes gradually increases with G , but exponentially expands with ϕ' , as shown in Figure 4.6(a) and (c). Figure 4.6(b) and (d) shows the failure envelopes normalized by their corresponding uniaxial bearing loads. The results estimated with the traditional method satisfactorily compare with the FE results. Furthermore, the normalized curves appear to be independent of ϕ' and G , and can be approximated by a commonly-used envelope equation form used for undrained soil conditions (Shen et al., 2016):

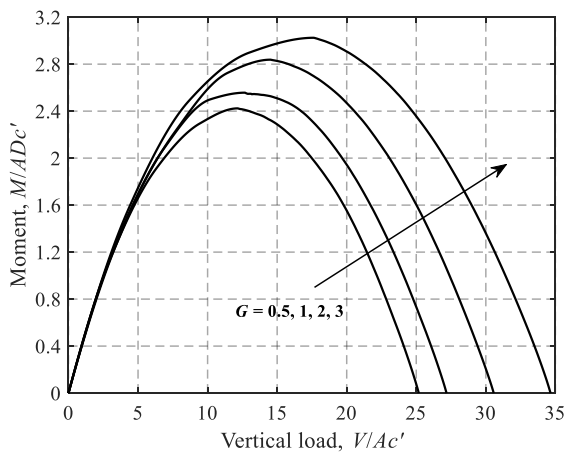
$$M/M_{ult} = 4[V/V_{ult} - (V/V_{ult})^2] \quad (4.7)$$



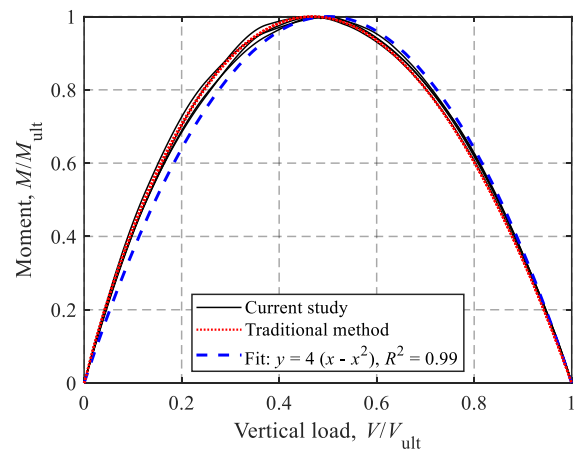
(a) Dimensionless; $G = 2$ & $\phi' = 0 \sim 40^\circ$



(b) Normalized; $G = 2$ & $\phi' = 0 \sim 40^\circ$



(c) Dimensionless; $G = 0.5 \sim 3$ & $\phi' = 20^\circ$



(d) Normalized; $G = 0.5 \sim 3$ & $\phi' = 20^\circ$

Figure 4.6: M - V failure envelopes: (a) Dimensionless; $G = 2$ & $\varphi' = 0 \sim 40^\circ$; (b) Normalized; $G = 2$ & $\varphi' = 0 \sim 40^\circ$; (c) Dimensionless; $G = 0.5 \sim 3$ & $\varphi' = 20^\circ$ and (d) Normalized; $G = 0.5 \sim 3$ & $\varphi' = 20^\circ$

4.3.5 Torsion-Vertical loading

Figure 4.7 shows the effects of φ' and G on the dimensionless and normalized T - V failure envelopes. Since the torsional capacity for surface foundations is related only to the frictional force at the interface, the T - V failure envelopes exhibit similar features to the H - V envelopes. The initial slopes of the T - V envelopes are associated with $\tan \varphi'$ by $k = T/(VD) = \tan \varphi' / 3$, which can be derived by integrating the torsional force at an infinitesimal area (denoted by dA), dT , over the entire base area of the circular foundation, A :

$$T = \iint dT = \iint Vr \left(\frac{dA}{A} \right) \tan \varphi' = \int_0^R \int_0^{2\pi} Vr \left(\frac{rdrd\theta}{\pi R^2} \right) \tan \varphi' = \frac{\tan \varphi'}{3} VD \quad (4.8)$$

As shown in Figure 4.7(b) and (d), the traditional method provides conservative predictions for $V/V_{\text{ult}} > 0.50$ but unconservative results for $V/V_{\text{ult}} \leq 0.50$. Moreover, the normalized curves for $V/V_{\text{ult}} \leq 0.50$ in Figure 4.7(b) are similar to the H - V envelopes due to the φ' -related initial slopes of the curves. Contrary to the normalized H - V curves, the normalized T - V curves for $V/V_{\text{ult}} > 0.50$ show a strong dependence on φ' . However, the normalized curves seem to be independent of G , as shown in Figure 4.7(d). Similar to the H - V envelopes, a piecewise function is also employed to fit the normalized T - V failure envelopes. The normalized curves for $V/V_{\text{ult}} > 0.50$ can be favorably approximated by:

$$T/T_{\text{ult}} = [1 - (2 \cdot V/V_{\text{ult}} - 1)^p]^{0.6} \quad \text{for } V/V_{\text{ult}} > 0.50 \quad (4.9)$$

with the coefficient, p , being a function of $\tan \varphi'$:

$$p = 3.67 \cdot e^{-3 \tan \varphi'} + 1.47 \quad (4.10)$$

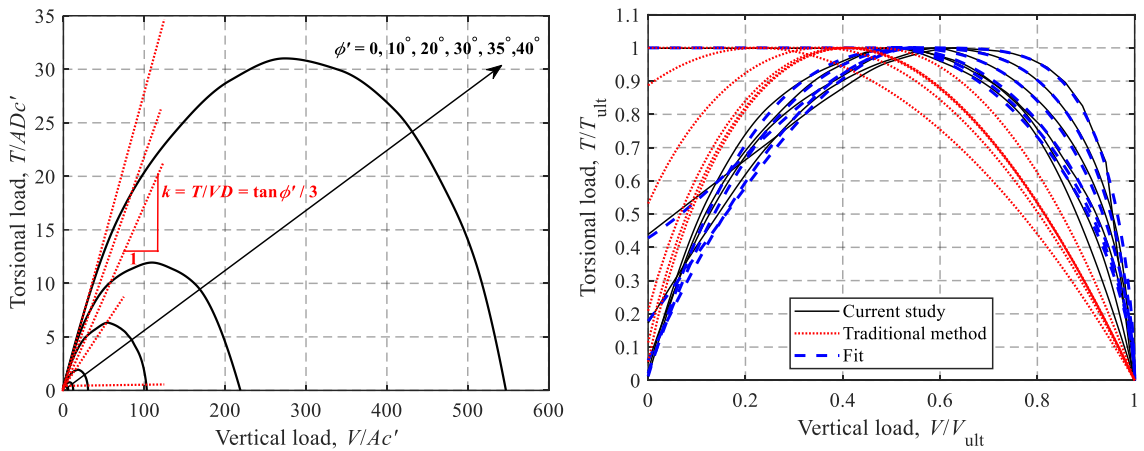
The expression of the curves for $V/V_{\text{ult}} \leq 0.50$ is a polynomial:

$$T/T_{\text{ult}} = a_2(V/V_{\text{ult}})^3 + b_2(V/V_{\text{ult}})^2 + c_2(V/V_{\text{ult}}) + d_2 \quad \text{for } V/V_{\text{ult}} \leq 0.50 \quad (4.11)$$

where a_2 , b_2 , c_2 and d_2 are functions of $\tan \phi'$:

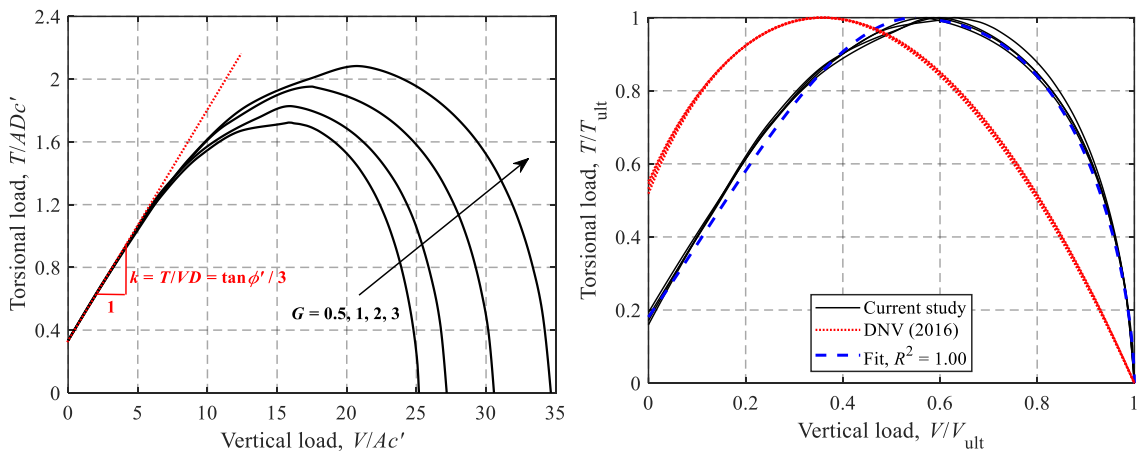
$$\begin{aligned} c_2 &= (V_{ult} D / T_{ult}) \cdot \tan \phi' / 3 \\ d_2 &= e^{-0.90 c_2} \\ a_2 &= (0.55 c_2 + 2 d_2 - 2) / 0.17 \\ b_2 &= (-c_2 - 0.91 a_2) / 1.1 \end{aligned} \quad (4.12)$$

It is evident from Figure 4.7(b) that the proposed expression compares favorably with the FE results and this expression with $\phi' = 20^\circ$ also shows a satisfactory agreement with the envelopes in Figure 4.7(d).



(a) Dimensionless; $G = 2$ & $\phi' = 0 \sim 40^\circ$

(b) Normalized; $G = 2$ & $\phi' = 0 \sim 40^\circ$



(c) Dimensionless; $G = 0.5 \sim 3$ & $\phi' = 20^\circ$

(d) Normalized; $G = 0.5 \sim 3$ & $\phi' = 20^\circ$

Figure 4.7: T - V failure envelopes: (a) Dimensionless; $G = 2$ & $\phi' = 0 \sim 40^\circ$; (b) Normalized; $G = 2$ & $\phi' = 0 \sim 40^\circ$; (c) Dimensionless; $G = 0.5 \sim 3$ & $\phi' = 20^\circ$ and (d) Normalized; $G = 0.5 \sim 3$ & $\phi' = 20^\circ$

4.3.6 Moment-Horizontal loading

Figure 4.8 shows the dimensionless and normalized M - H failure envelopes at $V/V_{ult} = 0.50$ along with the results estimated by the traditional method. A significant size expansion of the dimensionless envelopes with φ' can be observed from Figure 4.8(a). The M - H envelope is approximately symmetric about $H = 0$ for the case of $\varphi' = 0$, while the curves gradually become asymmetric and skewed to the left with increases of φ' . The asymmetry of the M - H envelopes is primarily attributed to the coupling effects between horizontal and moment modes. Figure 4.8(c) shows that M - H envelopes gradually expand with increases of G , but remain the same shape. The traditional method consistently provides conservative predictions. It should also be noted that the curves estimated with the traditional method are symmetric about $H = 0$.

To further eliminate the dependence on the vertical load level ($V/V_{ult} = 0.75, 0.50$ and 0.25 are used), the M - H envelopes are normalized by their corresponding maximum values rather than the uniaxial ultimate loads, as shown in Figure 4.9. The FE data points for $M < 0$ are also incorporated using $f(-M, \pm H) = f(+M, \mp H)$. As adopted by most researchers (e.g. Gottardi and Butterfield, 1993; Loukidis et al., 2008), the equation of an ellipse is used to fit the normalized M - H failure envelopes:

$$\left(\frac{H}{H_{\max}}\right)^2 + \left(\frac{M}{M_{\max}}\right)^2 + C \left(\frac{H}{H_{\max}}\right) \left(\frac{M}{M_{\max}}\right) = 1 \quad (4.13)$$

where H_{\max} and M_{\max} are the maximum horizontal and moment loads under a given value of V/V_{ult} , and can be calculated using the analytical equations for the normalized H - V and M - V envelopes in Sections 4.3.3 and 4.3.4. The best fitted values of the fitting coefficient C are 0.36 and 0.40 for cases of $G = 2$ & $\varphi' = 0 \sim 40^\circ$ and cases of $G = 0.5 \sim 3$ & $\varphi' = 20^\circ$, respectively. For simplification, the average value of $C = 0.38$ is employed, as compared in Figure 4.9.

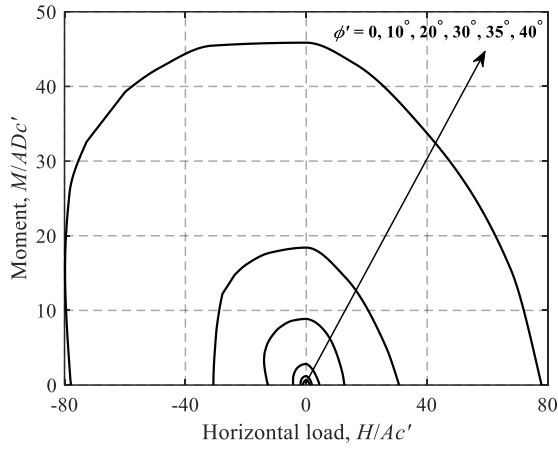
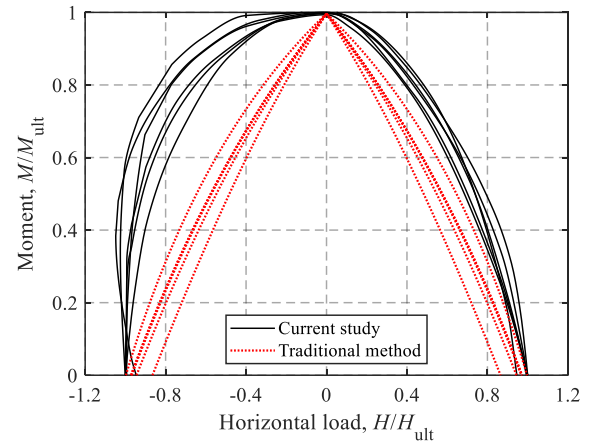
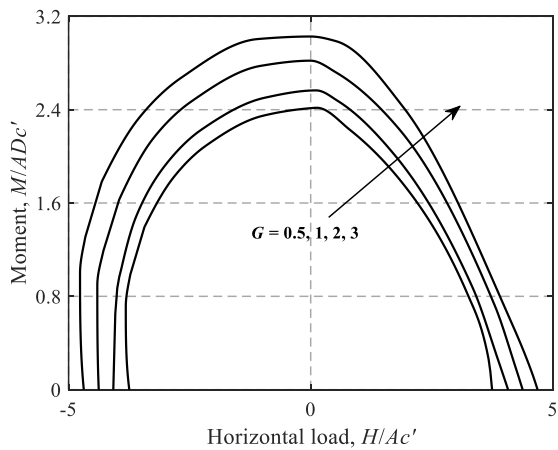
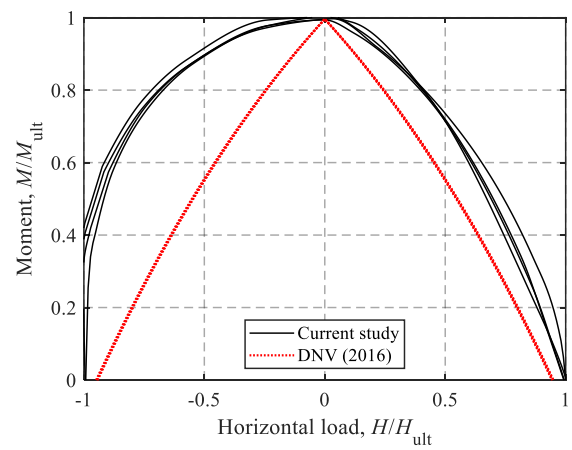
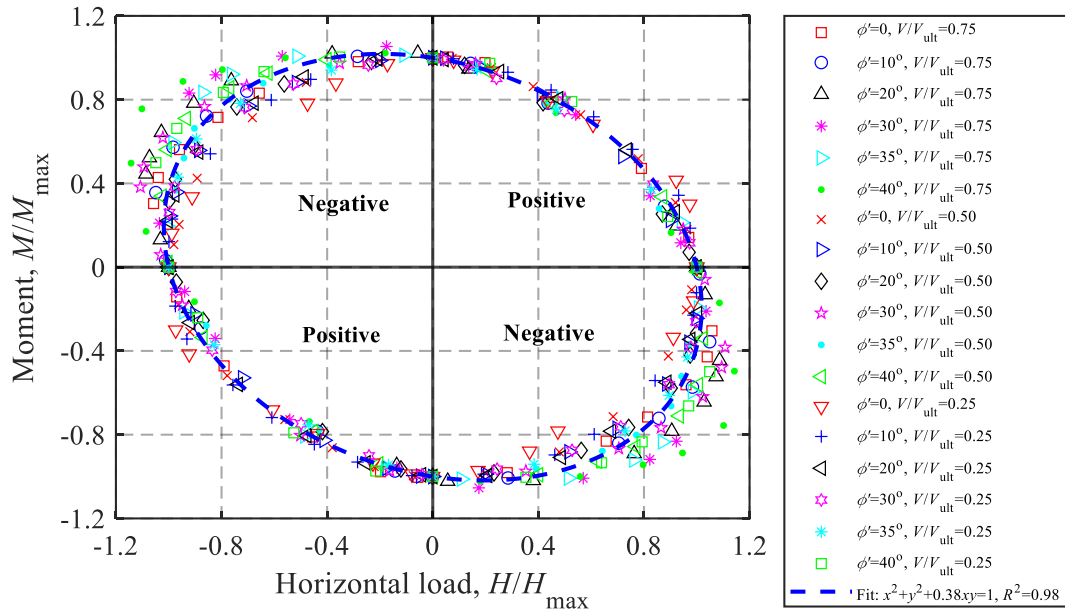
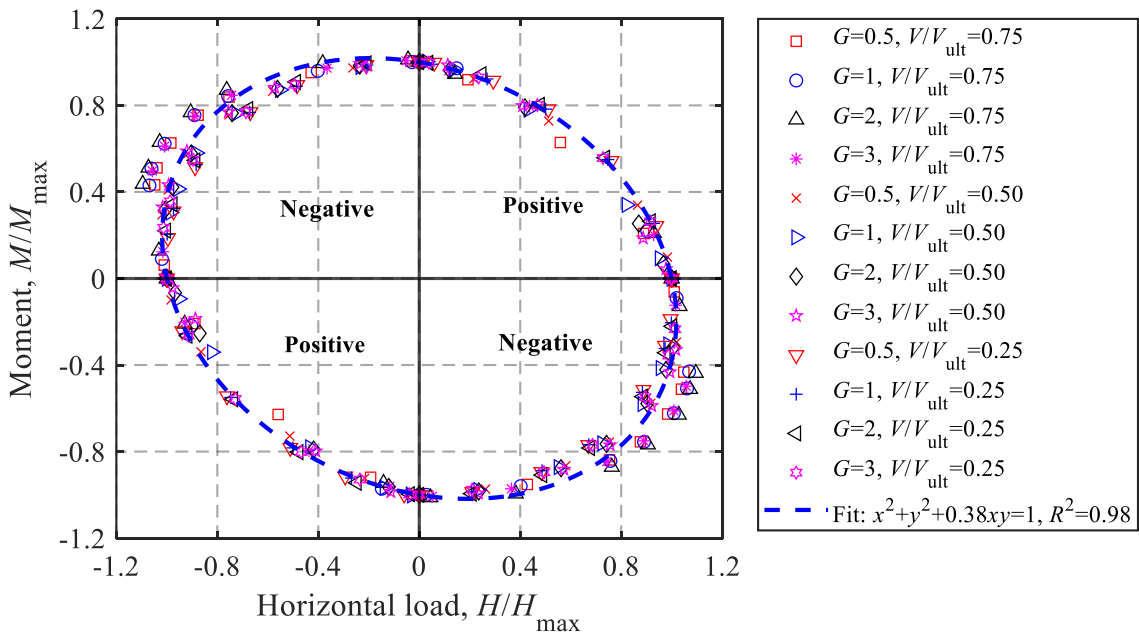
(a) Dimensionless; $G = 2$ & $\varphi' = 0 \sim 40^\circ$ (b) Normalized; $G = 2$ & $\varphi' = 0 \sim 40^\circ$ (c) Dimensionless; $G = 0.5 \sim 3$ & $\varphi' = 20^\circ$ (d) Normalized; $G = 0.5 \sim 3$ & $\varphi' = 20^\circ$

Figure 4.8: M - H failure envelopes at $V/V_{ult} = 0.50$: (a) Dimensionless; $G = 2$ & $\varphi' = 0 \sim 40^\circ$; (b) Normalized; $G = 2$ & $\varphi' = 0 \sim 40^\circ$; (c) Dimensionless; $G = 0.5 \sim 3$ & $\varphi' = 20^\circ$; and (d) Normalized; $G = 0.5 \sim 3$ & $\varphi' = 20^\circ$



(a) $G = 2$ & $\phi' = 0 \sim 40^\circ$



(b) $G = 0.5 \sim 3$ & $\phi' = 20^\circ$

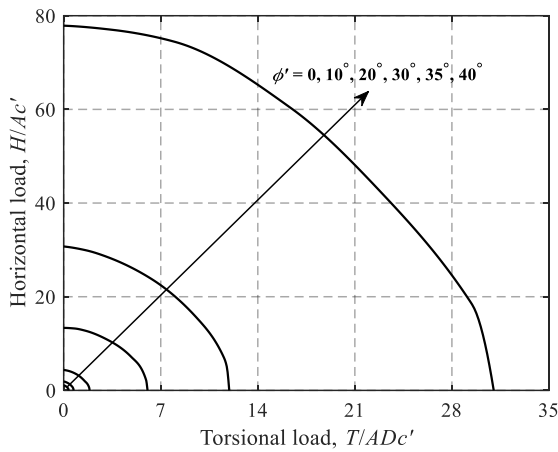
Figure 4.9: Fitting of $M-H$ envelopes: (a) $G = 2$ & $\phi' = 0 \sim 40^\circ$ and (b) $G = 0.5 \sim 3$ & $\phi' = 20^\circ$

4.3.7 Horizontal-Torsional loading

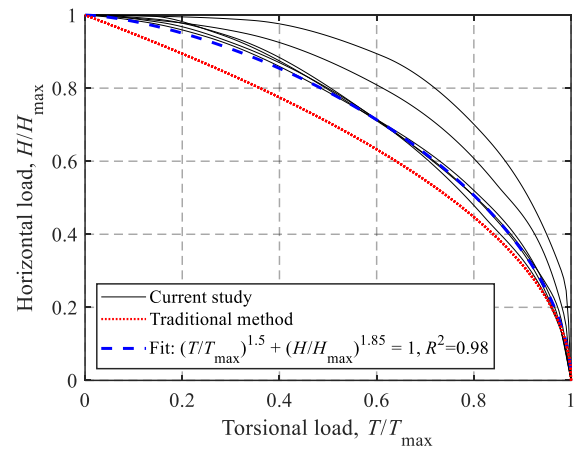
The effects of ϕ' and G on the dimensionless and normalized H - T failure envelopes under $V/V_{\text{ult}} = 0.75, 0.50$ and 0.25 are shown in Figure 4.10 and Figure 4.11, respectively. The dimensionless failure envelopes shown in Figure 4.10(a) and Figure 4.11(a) exhibit a dramatic expansion with ϕ' and a gradual increase with G (with almost the same shape). As shown in Figure 4.10(b) ~ (d) and Figure 4.11(b) ~ (d), the traditional method consistently underestimates the H - T envelopes. Similar to the M - H failure envelopes, the H - T failure envelopes normalized by the corresponding maximum values can enable the elimination of the dependence on ϕ' , G and V/V_{ult} . The normalized H - T failure envelopes can be fitted using the following equation:

$$(H/H_{\text{max}})^c + (T/T_{\text{max}})^d = 1 \quad (4.14)$$

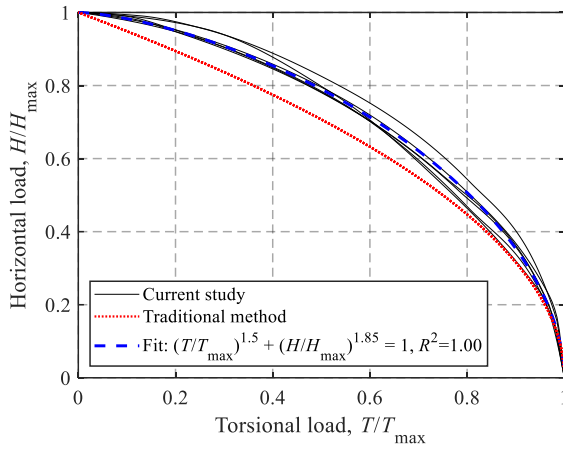
with $c = 1.85$ and $d = 1.5$. This comparison shows a good agreement.



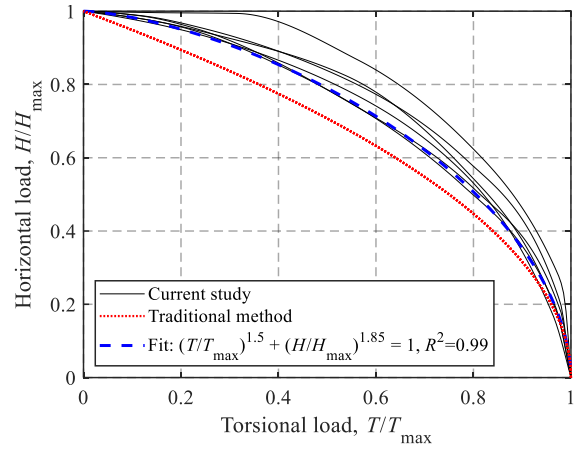
(a) Dimensionless, $V/V_{\text{ult}} = 0.50$



(b) Normalized, $V/V_{\text{ult}} = 0.75$

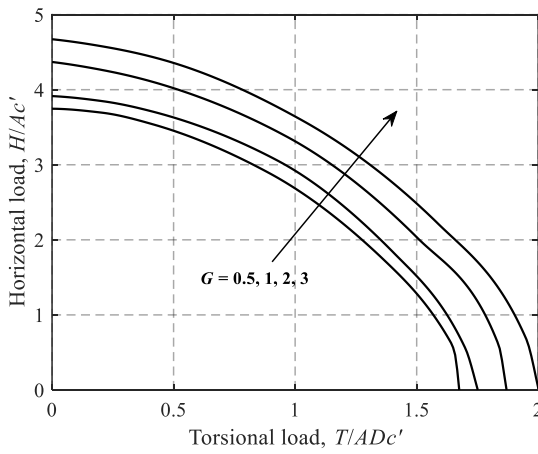


(c) Normalized, $V/V_{ult} = 0.50$

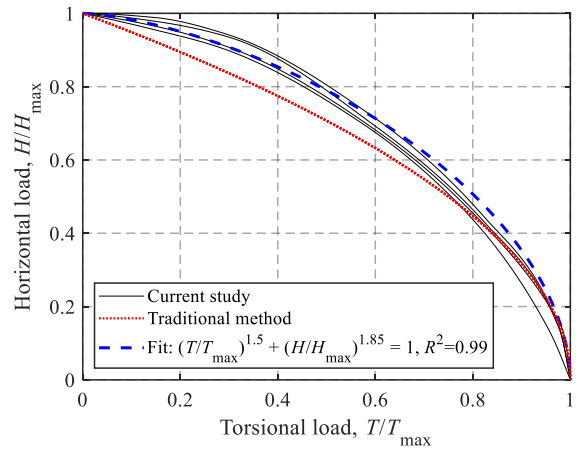


(d) Normalized, $V/V_{ult} = 0.25$

Figure 4.10: H - T failure envelopes for $G = 2$ & $\phi' = 0 \sim 40^\circ$: (a) Dimensionless, $V/V_{ult} = 0.50$; (b) Normalized, $V/V_{ult} = 0.75$; (c) Normalized, $V/V_{ult} = 0.50$ and (d) Normalized, $V/V_{ult} = 0.25$



(a) Dimensionless, $V/V_{ult} = 0.50$



(b) Normalized, $V/V_{ult} = 0.75$

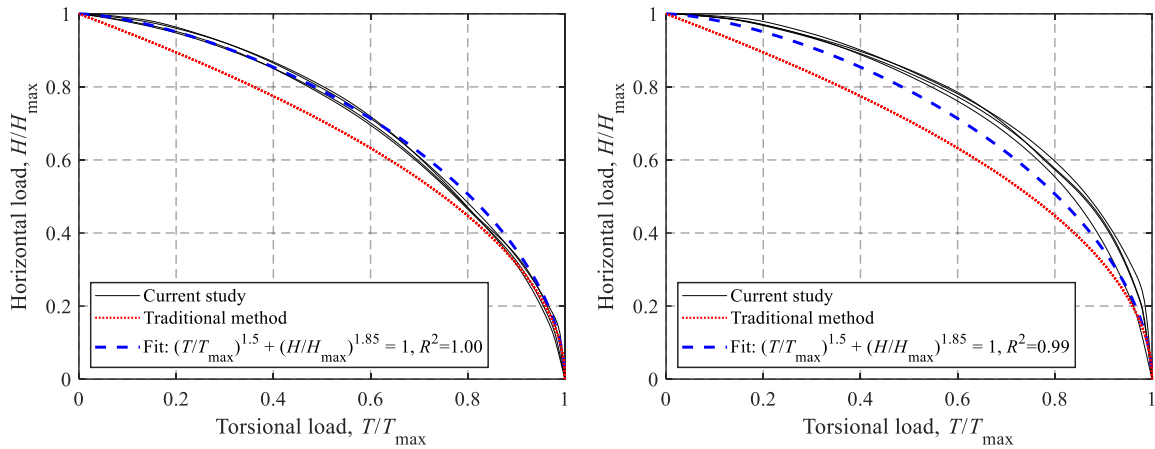
(c) Normalized, $V/V_{ult} = 0.50$ (d) Normalized, $V/V_{ult} = 0.25$

Figure 4.11: H - T failure envelopes for $G = 0.5 \sim 3$ & $\phi' = 20$: (a) Dimensionless, $V/V_{ult} = 0.50$; (b) Normalized, $V/V_{ult} = 0.75$; (c) Normalized, $V/V_{ult} = 0.50$ and (d) Normalized, $V/V_{ult} = 0.25$

4.3.8 Moment-Torsional loading

The effects of ϕ' and G on the dimensionless and normalized M - T failure envelopes under $V/V_{ult} = 0.75, 0.50$ and 0.25 are presented in Figure 4.12 and Figure 4.13. The dimensionless M - T envelopes exhibit similar expansions to the H - T envelopes, as shown in Figure 4.12(a) and Figure 4.13(a). It can also be seen that the curves provided by the traditional method are almost linear and lie significantly inside the FE results. The normalized M - T failure envelopes can be approximated using:

$$(M/M_{max})^e + (T/T_{max})^f = 1 \quad (4.15)$$

with $e = f = 2.0$ (i.e. a unit circle). The comparison indicates favorable predictions.

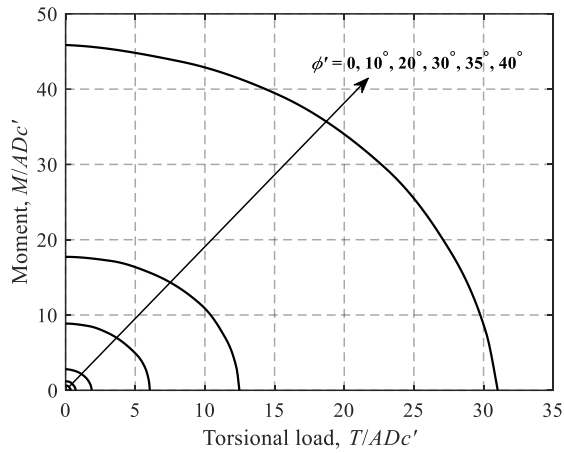
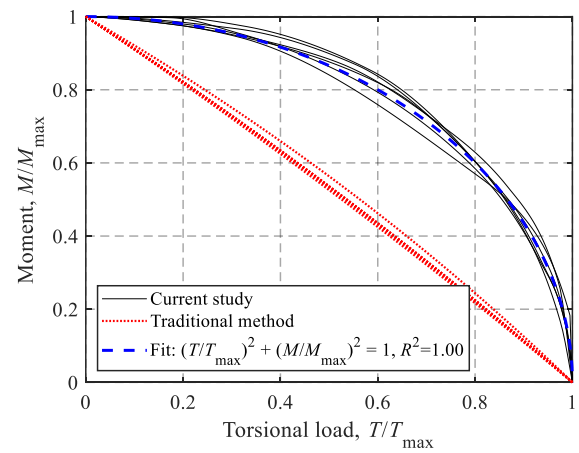
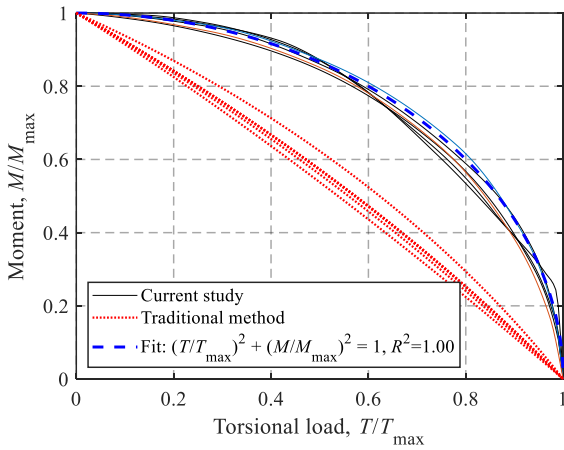
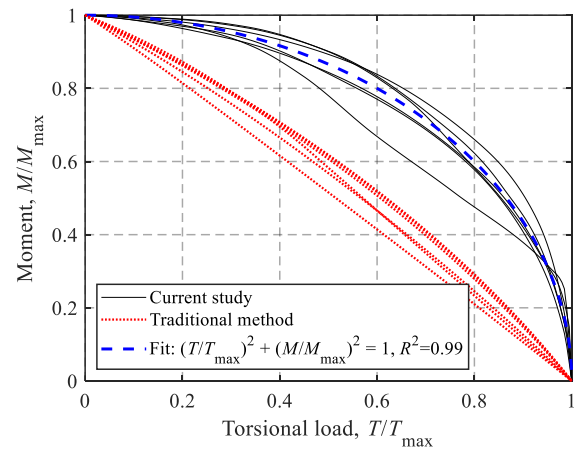
(a) Dimensionless, $V/V_{ult} = 0.50$ (b) Normalized, $V/V_{ult} = 0.75$ (c) Normalized, $V/V_{ult} = 0.50$ (d) Normalized, $V/V_{ult} = 0.25$

Figure 4.12: M - T failure envelopes for $G = 2$ & $\phi' = 0 \sim 40^\circ$: (a) Dimensionless, $V/V_{ult} = 0.50$; (b) Normalized, $V/V_{ult} = 0.75$; (c) Normalized, $V/V_{ult} = 0.50$ and (d) Normalized, $V/V_{ult} = 0.25$

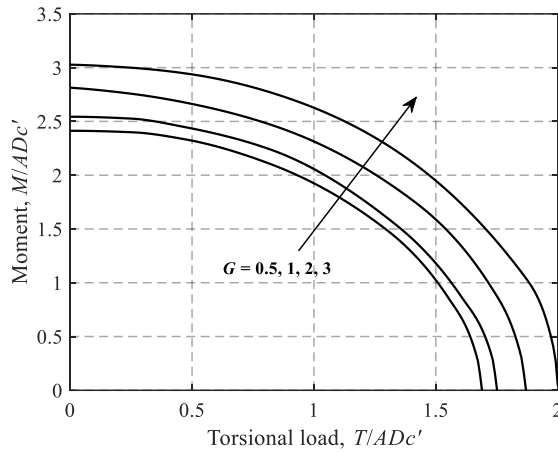
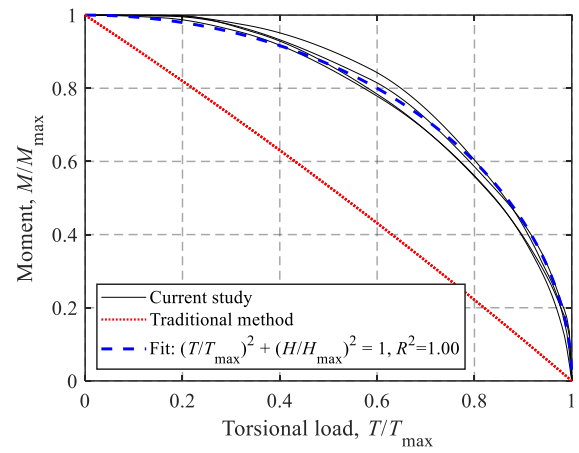
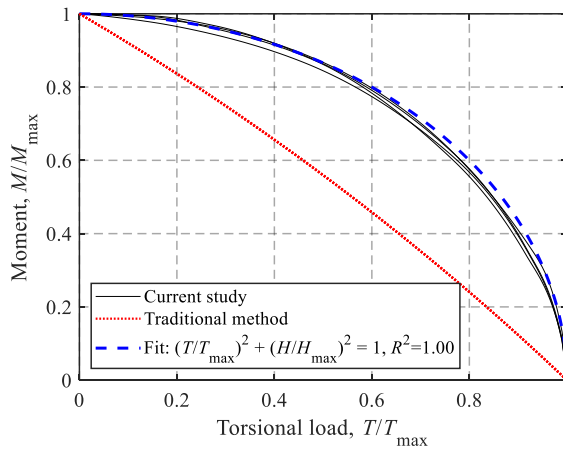
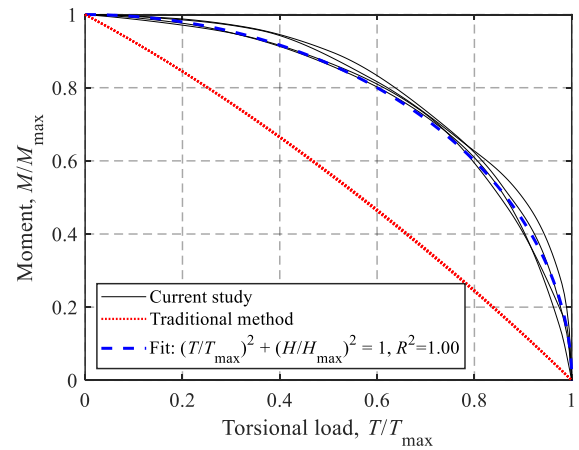
(a) Dimensionless, $V/V_{ult} = 0.50$ (b) Normalized, $V/V_{ult} = 0.75$ (c) Normalized, $V/V_{ult} = 0.50$ (d) Normalized, $V/V_{ult} = 0.25$

Figure 4.13: M - T failure envelopes for $G = 0.5 \sim 3$ & $\varphi' = 20^\circ$: (a) Dimensionless, $V/V_{ult} = 0.50$; (b) Normalized, $V/V_{ult} = 0.75$; (c) Normalized, $V/V_{ult} = 0.50$ and (d) Normalized, $V/V_{ult} = 0.25$

4.4 Full 4-D VHMT failure envelope in VHMT loading space

Three sets of notation are defined: (1) V_{ult} , H_{ult} , M_{ult} , T_{ult} – uniaxial ultimate capacity defined in Section 4.3.2; (2) H_{max} , M_{max} , T_{max} – maximum capacity at a given level of the vertical load without other load components and (3) H'_{max} , M'_{max} – reduced maximum capacity at a given level of the vertical load with a non-zero torsional load ($T \neq 0$).

Using the above notations, the general forms of the FE-calculated failure envelopes are summarized in Table 4.2. f_h , f_m , and f_t are functions of the vertical load level. Specific expressions for these functions can be found in the previous sections.

Table 4.2: Summary of FE-calculated failure envelopes

Plane	Conditions	Analytical form	
$H-V$	$M = 0$ & $T = 0$	$H_{\max}/H_{\text{ult}} = f_h(V/V_{\text{ult}})$	(4.16)
$M-V$	$H = 0$ & $T = 0$	$M_{\max}/M_{\text{ult}} = f_m(V/V_{\text{ult}})$	(4.17)
$T-V$	$M = 0$ & $H = 0$	$T_{\max}/T_{\text{ult}} = f_t(V/V_{\text{ult}})$	(4.18)
$M-H$	$V \neq 0$ & $T = 0$	$(H/H_{\max})^2 + (M/M_{\max})^2 + C(H/H_{\max})(M/M_{\max}) = 1$	(4.19)
$H-T$	$V \neq 0$ & $M = 0$	$(H'_{\max}/H_{\max})^c + (T/T_{\max})^d = 1$	(4.20)
$M-T$	$V \neq 0$ & $H = 0$	$(M'_{\max}/M_{\max})^e + (T/T_{\max})^f = 1$	(4.21)

Eq. (4.19) (i.e. $M-H$ envelope under the condition of $T = 0$) is considered as the basic function. To derive the final 4-D expression, a more generalized equation for the $M-H$ failure envelope under the condition of $T \neq 0$ is needed. Due to the similar shapes of the $M-H$ failure envelopes (only the sizes are different), it is reasonable to assume that under the condition of $T \neq 0$, Eq. (4.19) is still applicable for the $M-H$ envelope normalized by the corresponding maximum values, H'_{\max} and M'_{\max} (which reduce to H_{\max} and M_{\max} in Eq. (4.19) if $T = 0$). Therefore, Eq. (4.19) can be replaced by a more generalized form:

$$(H/H'_{\max})^2 + (M/M'_{\max})^2 + C(H/H'_{\max})(M/M'_{\max}) = 1 \quad (4.22)$$

Mathematical manipulations of Eqs. (4.16), (4.17), (4.18), (4.20), (4.21) and (4.22) allow the formulation of an analytical 4-D expression for the full VHMT envelope in terms of V/V_{ult} , H/H_{ult} , M/M_{ult} , and T/T_{ult} :

$$\begin{aligned}
& f(V/V_{ult}, H/H_{ult}, M/M_{ult}, T/T_{ult}) \\
&= \left(\frac{H/H_{ult}}{\left[1 - \left(\frac{T/T_{ult}}{f_t(V/V_{ult})}\right)^d\right]^{\frac{1}{c}} f_h(V/V_{ult})} \right)^2 + \left(\frac{M/M_{ult}}{\left[1 - \left(\frac{T/T_{ult}}{f_t(V/V_{ult})}\right)^f\right]^{\frac{1}{e}} f_m(V/V_{ult})} \right)^2 \\
&+ C \left(\frac{H/H_{ult}}{\left[1 - \left(\frac{T/T_{ult}}{f_t(V/V_{ult})}\right)^d\right]^{\frac{1}{c}} f_h(V/V_{ult})} \right) \left(\frac{M/M_{ult}}{\left[1 - \left(\frac{T/T_{ult}}{f_t(V/V_{ult})}\right)^f\right]^{\frac{1}{e}} f_m(V/V_{ult})} \right) = 1
\end{aligned} \tag{4.23}$$

For practical design applications, the combined design loads with the appropriate partial factors, VHMT, can be directly substituted into the left-hand side of Eq. (4.23); values less than 1 represent a sufficient ultimate limit design and vice versa.

To visualize the shape of the full 4-D failure surface, three 3-D failure surfaces (i.e. VHM failure surface at $T=0$, VHT at $M=0$ and VMT at $H=0$) for the case of $G=2$ & $\varphi'=20^\circ$ are shown in Figure 4.14. The portion of $T < 0$ for the VHT and VMT surfaces is also incorporated due to the symmetry about the plane of $T=0$. The specific curves obtained from the FE results are also compared.

An associated flow rule (friction angle = the dilation angle) has been used for the soil model in the present study. It should be noted that a non-associated flow rule (friction angle > the dilation angle) can provide more realistic behaviors of certain soils and states. Loukidis et al. (2008) and EI-Marassi (2011) demonstrated that the absolute size of the $V-H$, $V-M$ and $M-H$ envelopes for strip surface foundations increases with the dilation angle, whilst the size and shape of the normalized envelopes appears to be independent of the dilation angle. Therefore, the 4-D analytical expression for the normalized VHMT failure envelope (see Eq. (4.23)) derived using the associated flow rule should also be usable for the non-associated flow case with some appropriate consideration of the soil properties. Since the uniaxial bearing capacities (i.e. V_{ult} , H_{ult} , M_{ult} and T_{ult}) depend on the dilation angle, further numerical analyses using the non-associated flow rule would be required for confirmation, which is beyond the scope of the present study.

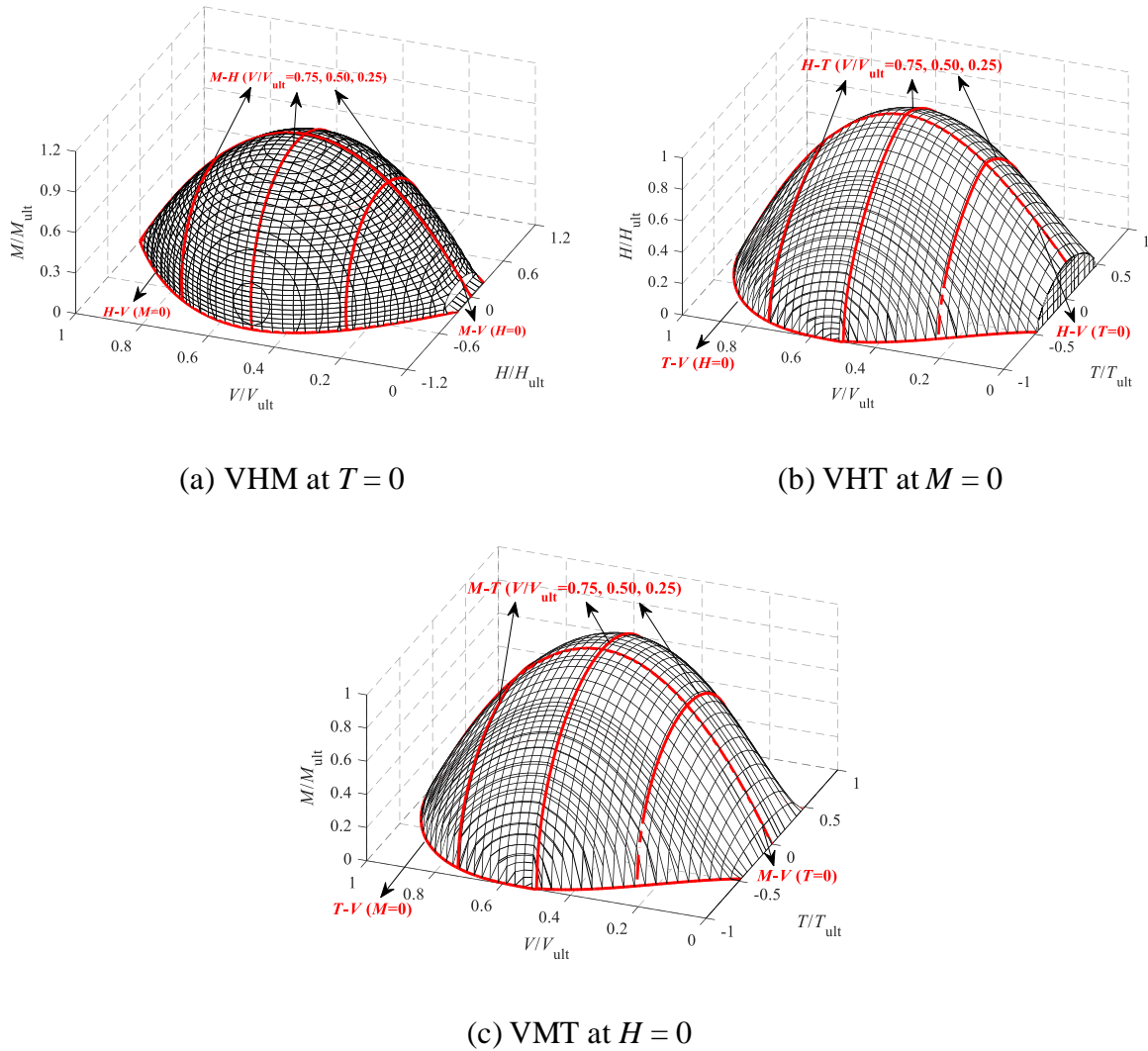


Figure 4.14: 3-D failure surfaces for a circular surface foundation with $G = 2$ & $\phi' = 20^\circ$ under drained soil conditions: (a) VHM at $T = 0$; (b) VHT at $M = 0$ and (c) VMT at $H = 0$

4.5 Conclusions

The general VHMT failure envelopes for circular surface foundations under a zero-tension interface for drained soil conditions have been investigated using finite element analysis. Two dimensionless numbers, the friction angle ϕ' and the weight parameter $G = \gamma'D/2c'$, have been considered for parametric study proposes. The results show that the uniaxial bearing capacities increase with ϕ' exponentially and with G linearly. In addition, the calculated failure envelopes gradually expand with G and exponentially expand with ϕ' .

The traditional method consistently provides conservative predictions of the bearing capacity under combined loads. Analytical expressions have also been proposed to approximate the calculated VHMT failure envelopes. To facilitate the application of the failure envelope method for design, a full 4-D analytical expression for the VHMT failure envelope was derived based on the calculated VHMT failure envelopes.

4.6 References

- Achmus, M., Akdag, C. T., and Thieken, K. (2013). Load-bearing behavior of suction bucket foundations in sand. *Applied Ocean Research*, 43, 157-165.
- API (American Petroleum Institute) (2011). API Recommended Practice, Geotechnical and Foundation Design Considerations. American Petroleum Institute, Washington, D.C.
- Bienen, B., Gaudin, C., and Cassidy, M. J. (2007). Centrifuge tests of shallow footing behaviour on sand under combined vertical-torsional loading. *International Journal of Physical Modelling in Geotechnics*, 7(2), 01-21.
- Bransby, M. F., and Randolph, M. F. (1998). Combined loading of skirted foundations. *Géotechnique*, 48(5), 637-655.
- Cox, A. D. (1962). Axially-symmetric plastic deformation in soils – II. Indentation of ponderable soils. *International Journal of Mechanical Sciences*, 4(5), 371-380.
- Dassault Systèmes (2016). Abaqus analysis user's manual. Simulia Corp., Providence, R.I.
- DNV GL (Det Norske Veritas GL) (2016). DNVGL-ST-0126: Support structures for wind turbines. DNV GL Group, Høvik, Norway.
- El-Marassi, M. (2011). Investigation of hybrid monopile-footing foundation systems subjected to combined loading. Doctoral dissertation, The University of Western Ontario, London, Ont.
- Erickson, H. L., and Drescher, A. (2002). Bearing capacity of circular footings. *Journal of geotechnical and geoenvironmental engineering*, 128(1), 38-43.
- Feng, X., Randolph, M. F., Gourvenec, S., and Wallerand, R. (2014). Design approach for rectangular mudmats under fully three-dimensional loading. *Géotechnique*, 64(1), 51-63.
- Georgiadis, M., and Butterfield, R. (1988). Displacements of footings on sand under eccentric and inclined loads. *Canadian Geotechnical Journal*, 25(2), 199-212.
- Gottardi, G., and Butterfield, R. (1993). On the bearing capacity of surface footings on sand under general planar loads. *Soils and Foundations*, 33(3), 68-79.
- Gourvenec, S., and Randolph, M. (2003). Effect of strength non-homogeneity on the shape of failure envelopes for combined loading of strip and circular foundations on clay. *Géotechnique*, 53(6), 575-586.

- Hansen, J. B. (1970). A revised and extended formula for bearing capacity. Bulletin No. 28, Danish Geotechnical Institute, Copenhagen, Denmark. 5-11.
- Hjiaj, M., Lyamin, A. V., and Sloan, S. W. (2004). Bearing capacity of a cohesive-frictional soil under non-eccentric inclined loading. *Computers and Geotechnics*, 31(6), 491-516.
- ISO (International Standards Organization). (2016). ISO 19901-4: Petroleum and natural gas industries specific requirements for offshore structures – part 4: geotechnical and foundation design considerations, 2nd edition. International Standards Organization, Geneva, Switzerland.
- Lee, J., and Salgado, R. (2005). Estimation of bearing capacity of circular footings on sands based on cone penetration test. *Journal of Geotechnical and Geoenvironmental Engineering*, 131(4), 442-452.
- Loukidis, D., Chakraborty, T., and Salgado, R. (2008). Bearing capacity of strip footings on purely frictional soil under eccentric and inclined loads. *Canadian Geotechnical Journal*, 45(6), 768-787.
- Lyamin, A. V., Salgado, R., Sloan, S. W., and Prezzi, M. (2007). Two- and three-dimensional bearing capacity of footings in sand. *Géotechnique*, 57(8), 647-662.
- Martin C. M. (2003). User guide for ABC – Analysis of Bearing Capacity, Version 1.0. OUEL Report No. 2261/03. Department of Engineering Science, University of Oxford, Oxford, UK.
- Potts, D. M., and Zdravković, L. (2001). Finite element analysis in geotechnical engineering: (Vol. 2) – Application. Thomas Telford Ltd., London, UK.
- Purkayastha, R. D., and Char, A. N. (1977). Stability analysis for eccentrically loaded footings. *Journal of Geotechnical and Geoenvironmental Engineering*, 103 (ASCE 13014 Proceeding).
- Saran, S., and Agarwal, R. K. (1991). Bearing capacity of eccentrically obliquely loaded footing. *Journal of Geotechnical Engineering*, 117(11), 1669-1690.
- Saran, S., Prakash, S., and Murty, A. V. S. R. (1971). Bearing capacity of footings under inclined loads. *Soils and Foundations*, 11(1), 47-52.
- Shen, Z., Feng, X., and Gourvenec, S. (2016). Undrained capacity of surface foundations with zero-tension interface under planar VHM loading. *Computers and Geotechnics*, 73, 47-57.
- Shen, Z., Feng, X., and Gourvenec, S. (2017). Effect of interface condition on the undrained capacity of subsea mudmats under six-degree-of-freedom loading. *Géotechnique*, 67(4), 338-349.
- Smith, C. C. (2005). Complete limiting stress solutions for the bearing capacity of strip footings on a Mohr-Coulomb soil. *Géotechnique*, 55(8), 607-612.
- Soderman, L. G., and Quigley, R. M. (1965). Geotechnical properties of three Ontario clays. *Canadian Geotechnical Journal*, 2(2), 167-189.

- Tan, F. S. C. (1990). Centrifuge and theoretical modelling of conical footings on sand. Doctoral dissertation, Cambridge University, Cambridge, UK.
- Terzaghi, K. (1951). Theoretical soil mechanics. Chapman & Hall, London, UK.
- Ukritchon, B., Whittle, A. J., and Klangvijit, C. (2003). Calculations of bearing capacity factor N_γ using numerical limit analyses. *Journal of Geotechnical and Geoenvironmental Engineering*, 129(5), 468-474.
- Ukritchon, B., Whittle, A. J., and Sloan, S. W. (1998). Undrained limit analyses for combined loading of strip footings on clay. *Journal of Geotechnical and Geoenvironmental Engineering*, 124(3), 265-276.
- Zadroga, B. (1994). Bearing capacity of shallow foundations on noncohesive soils. *Journal of geotechnical engineering*, 120(11), 1991-2008.

5 Effects of soil stiffness anisotropy on elastic solutions of circular foundations under combined VHMT loading

5.1 Introduction

Estimation of the serviceability limit state of shallow foundations under working loads can be of great significance. This is particularly important for large onshore and offshore structures, such as wind turbines (WTs) and oil and gas platforms. The majority of large shallow WT foundations are circular or close to circular in form. These shallow foundations are generally subjected to combined loadings: vertical loads due to the self-weight of the structure (V), horizontal loads (H) caused by environmental conditions, overturning moments (M) due to the horizontal loading and structural height, and torsional loads (T) induced by wind and structural effects. The rocking stiffness of WT foundations in particular is considered to be a critical design parameter, since it controls the location of the center of gravity with respect to the foundation of the turbine (Lang, 2012).

Available analytical solutions for estimating the elastic response of surface-based rigid circular footings are based on theories that assume homogeneous elastic half-spaces subjected to uniaxial vertical, horizontal, moment and torsional loads. Various solutions can be found in the literature, e.g. Spence (1968), Gerrard and Harrison (1970), Poulos and Davies (1974) and Reissner and Sagoci (1944), as shown below:

$$\begin{aligned}
 K_V &= \frac{4 \ln(3 - 4\mu)}{1 - 2\mu} \\
 K_{HH} &= \frac{8}{2 - \mu} \\
 K_{MM} &= \frac{8}{3(1 - \mu)} \\
 K_T &= \frac{16}{3}
 \end{aligned} \tag{5.1}$$

where K_V , K_{HH} , K_{MM} and K_T are vertical, horizontal, moment and torsional elastic stiffness coefficients and μ is the Poisson's ratio of the soil. Kausel et al. (1978) proposed approximate solutions for embedded circular foundations using the direct finite element

(FE) procedures. Extending this concept, Bell (1991) demonstrated with finite element analysis that the cross-coupling effects for structures subjected to simultaneous vertical, horizontal and moment loading can be characterized in a matrix form:

$$\begin{bmatrix} V \\ \frac{GR^2}{H} \\ \frac{GR^2}{M} \\ \frac{M}{GR^3} \end{bmatrix} = \begin{bmatrix} K_V & 0 & 0 \\ 0 & K_{HH} & K_{HM} \\ 0 & K_{MH} & K_{MM} \end{bmatrix} \cdot \begin{bmatrix} u_V/R \\ u_H/R \\ \theta_M \end{bmatrix} \quad (5.2)$$

where u_V , u_H and θ_M are the vertical, horizontal and rotational deformations; and R is the foundation radius. $K_{MH} = K_{HM}$ represent the cross-coupling between the horizontal and rotational degrees of freedom. Note that torsion was not addressed by this study.

Stiffness coefficients have also been found to depend on the foundation embedment ratio, soil Poisson's ratio, foundation embedment conditions and foundation geometry. Doherty and Deeks (2003) further developed coupled VHM foundation stiffness coefficients considering the effects of foundation embedment and soil non-homogeneity (i.e. using a power law variation of shear modulus with depth). However, it should be noted that the solutions of Bell (1991) and Doherty and Deeks (2003) are all for isotropic conditions. In addition, despite the availability of coupled solutions (e.g. Gazetas, 1983; Gazetas, 1991), uncoupled foundation stiffness methods still predominate in most guidelines used for shallow foundation design, such as DNV (2016) and ISO (2016).

Although the aforementioned literature treats the soil as an isotropic material, many natural soils will be anisotropic or at least transversely isotropic (cross-anisotropic) due to their deposition and complex stress history (Bishop and Hight, 1977). Burland et al. (1977), González-Hurtado (2019) and Korobova et al. (2019) have shown that the effects of soil stiffness anisotropy on foundation responses can be significant and should not be ignored. Gazetas (1981) analytically investigated the vertical, horizontal and rocking responses of surface-based rigid strip foundations on cross-anisotropic soils; however, the foundation stiffness cannot be explicitly derived due to analytical complexities. As demonstrated by Yang et al. (2008) and Graham and Houlsby (1983), both granular soils and clays exhibit

stiffness anisotropy that can be satisfactorily described with cross-anisotropic elasticity. The relationship between the increments of effective stress and strain for a cross-anisotropic soil can be described by (Lings et al., 2000):

$$\begin{bmatrix} \delta\varepsilon_{xx} \\ \delta\varepsilon_{yy} \\ \delta\varepsilon_{zz} \\ \delta\gamma_{yz} \\ \delta\gamma_{zx} \\ \delta\gamma_{xy} \end{bmatrix} = \begin{bmatrix} \frac{1}{E_h} & -\frac{\mu_{hh}}{E_h} & -\frac{\mu_{vh}}{E_v} & \cdot & \cdot & \cdot \\ -\frac{\mu_{hh}}{E_h} & \frac{1}{E_h} & -\frac{\mu_{vh}}{E_v} & \cdot & \cdot & \cdot \\ -\frac{\mu_{vh}}{E_v} & -\frac{\mu_{vh}}{E_v} & \frac{1}{E_h} & \cdot & \cdot & \cdot \\ \cdot & \cdot & \cdot & \frac{1}{G_{vh}} & \cdot & \cdot \\ \cdot & \cdot & \cdot & \cdot & \frac{1}{G_{vh}} & \cdot \\ \cdot & \cdot & \cdot & \cdot & \cdot & \frac{1}{G_{hh}} \end{bmatrix} \cdot \begin{bmatrix} \delta\sigma'_{xx} \\ \delta\sigma'_{yy} \\ \delta\sigma'_{zz} \\ \delta\tau'_{yz} \\ \delta\tau'_{zx} \\ \delta\tau'_{xy} \end{bmatrix} \quad (5.3)$$

The subscripts used in Eq. (5.3) follow those adopted by Pickering (1970). The stresses and strains are referred to three Cartesian axes with x and y being horizontal axis and z being the vertical axis of symmetry. Love (2013) showed that only five independent parameters are required to fully describe a cross-anisotropic elastic soil, i.e. Young's modulus in the horizontal direction, E_h ; Young's modulus in the vertical direction, E_v ; Poisson's ratio for horizontal strain due to vertical strain, μ_{vh} ; Poisson's ratio for horizontal strain due to horizontal strain, μ_{hh} and shear modulus in the vertical plane, G_{hv} ($G_{hv} = G_{vh}$). The remaining parameters can be related to these five parameters using:

$$G_{hh} = \frac{E_h}{2(1 + \mu_{hh})} \quad (5.4)$$

$$\frac{\mu_{hv}}{E_h} = \frac{\mu_{vh}}{E_v} \quad (5.5)$$

Eq. (5.4) assumes that the horizontal plane is a plane of isotropy and thermodynamic considerations require Eq. (5.5) to ensure the symmetry of the elastic compliance matrix; Eq. (5.5) has been used in the derivation of Eq. (5.3).

Since thermodynamic considerations require the strain energy of an elastic material is positive, some bounds on the values of the five independent parameters also need to be satisfied. Pickering (1970) demonstrated that E_h , E_v and G_{hv} must always be positive, and inequalities (5.6) and (5.7) should also be satisfied. Raymond (1970) has showed that G_{hv} is confined by inequality (5.8).

$$-1 < \mu_{hh} < 1 \quad (5.6)$$

$$\frac{E_v}{E_h}(1 - \mu_{hh}) - 2\mu_{vh}^2 \geq 0 \quad (5.7)$$

$$G_{hv} \leq \frac{E_v}{2\mu_{vh}(1 + \mu_{hh}) + 2\sqrt{\left(\frac{E_v}{E_h}\right) \cdot (1 - \mu_{hh}^2) \left(1 - \frac{E_h}{E_v} \cdot \mu_{vh}^2\right)}} \quad (5.8)$$

Graham and Houlsby (1983) proposed a simplified cross-anisotropic model consisting of only three independent parameters defined as: (i) modified Young's modulus: $E^* = E_v$; (ii) anisotropy factor: $\alpha = \sqrt{E_h/E_v}$; and modified Poisson's ratio: $\mu^* = \mu_{hh}$.

All of the five cross-anisotropic elastic parameters can therefore be computed using these three independent parameters:

$$\begin{aligned} E_v &= E^*; \quad E_h = \alpha^2 E^* \\ G_{vh} = G_{hv} &= \frac{\alpha E^*}{2(1 + \mu^*)}; \quad G_{hh} = \frac{\alpha^2 E^*}{2(1 + \mu^*)} \\ \mu_{hh} &= \mu^*; \quad \mu_{vh} = \mu^*/\alpha; \quad \mu_{hv} = \alpha\mu^* \end{aligned} \quad (5.9)$$

Substituting Eq. (5.9) into (5.7) yields $-1 < \mu^* = \mu_{hh} \leq 0.5$; therefore, 0.5 is an upper bound of μ_{hh} for this three-parameter model.

As a special case of drained conditions, the undrained condition can be accounted for by mapping the drained parameters to undrained parameters. As given by Ratananikom et al. (2013) and Lings (2001), the undrained Young's modulus and shear modulus of the three-parameter model can be expressed in Eq. (5.10) and other equations shown in Eqs. (5.4) and (5.5) are still applicable.

$$\begin{aligned}
E_v^u &= E^* \cdot \left[\frac{4\alpha\mu^* + 2\mu^* - 2 - \alpha^2}{2(\mu^* + 1)(2\mu^* - 1)} \right] \\
E_h^u &= \alpha^2 E^* \cdot \left[\frac{4\alpha\mu^* + 2\mu^* - 2 - \alpha^2}{2\alpha\mu^*(\mu^* + 1) + (\mu^{*2} - 1)(\alpha^2 + 1)} \right] \\
G_{hh}^u &= G_{hh}; \quad G_{hv}^u = G_{hv}
\end{aligned} \tag{5.10}$$

Following Bell (1991) and Doherty and Deeks (2003), the stiffness of a circular foundation on a cross-anisotropic soil subjected to combined VHMT loads can therefore be expressed in a matrix form as:

$$\begin{bmatrix} V \\ \frac{G_{hv}R^2}{H} \\ \frac{G_{hv}R^2}{M} \\ \frac{G_{hv}R^3}{T} \\ \frac{G_{hv}R^3}{T} \end{bmatrix} = \begin{bmatrix} K_V & 0 & 0 & 0 \\ 0 & K_{HH} & K_{HM} & 0 \\ 0 & K_{MH} & K_{MM} & 0 \\ 0 & 0 & 0 & K_T \end{bmatrix} \cdot \begin{bmatrix} u_V/R \\ u_H/R \\ \theta_M \\ \theta_T \end{bmatrix} \tag{5.11}$$

The objective of this paper is to obtain the coupled elastic stiffness coefficients for circular surface and embedded foundations resting on cross-anisotropic soils with linearly increasing stiffness with depth under combined VHMT loads. The three-parameter cross-anisotropic model has been used to model the elastic soil behavior. Foundation stiffness accounting for the effects of foundation embedment, soil stiffness non-homogeneity and anisotropy have been estimated using finite element analysis.

5.2 Method – finite element analysis

5.2.1 Material models and sign conventions

The soil was modelled as a cross-anisotropic linear elastic material characterized by the three-parameter model (see Eq. (5.9)), with isotropy as a special case (i.e. $\alpha^2 = 1$). As suggested by Lings (2001), Nishimura (2014) and Yimsiri and Soga (2011), the anisotropic ratio α^2 typically ranges from 0 to 2. Therefore, values of $\alpha^2 = 0.2, 0.4, 0.6, 1.0, 1.5$ and 2.0 were used in this study to span most soils of practical interest. Since the typical range of μ^* is $-1 < \mu^* \leq 0.5$ (see Section 5.1), μ^* was taken as $0, 0.1, 0.2, 0.3, 0.4$ and 0.495 .

The diameter (D) and thickness (t) of the foundation used in the analysis were $D = 19$ m and $t = 3$ m, representing typical dimensions for current large WT's in North America. The effect of the foundation embedment (d) was studied by varying the embedment ratios from 0 to 0.16 (i.e. $d/D = 0, 0.03, 0.06, 0.09, 0.12$ and 0.16). Since most natural deep soil deposits exhibit an increase of elastic stiffness with depth (Doherty and Deeks, 2003; Rowe and Booker, 1981), the soil was also modelled as a non-homogeneous layer with linearly increasing elastic modulus with depth (Gibson, 1967). Different gradients (k) for the non-homogeneous soil stiffness increase were considered for β (where $\beta = kD/E_{v0}$ is the normalized Gibson factor, defined by Carrier and Christian (1973)) varying from 0 to 0.40, corresponding to $k = 0, 1.0, 2.0, 3.0, 4.0$ and 5.0 MPa/m. $E_{v0} = 237$ MPa was used in the analysis. Figure 5.1 shows the soil profiles adopted herein. Cases of surface foundations on Gibson soils and embedded foundations in homogeneous soils were separately considered to study the effects of soil stiffness non-homogeneity and foundation embedment. Each case included 36 sub-cases (i.e. six values of $\alpha^2 \times$ six values of μ^*). The foundation was assumed to be a rigid body. A load reference point (LRP) was attached to the center of the base of foundation to apply prescribed displacements or loads.

The base contact between the foundation and the soil was chosen to have a rough condition. For embedded foundations, a reduced friction coefficient (i.e. partially rough interface) for side and top interfaces is always recommended due to installation or in-service loading processes (Gourvenec and Mana, 2011). In this analysis, smooth sides and top of the embedded foundations were considered to provide more conservative estimations. The sign conventions for the loads are shown in Figure 5.1. The horizontal and moment loads were considered to be in the same plane.

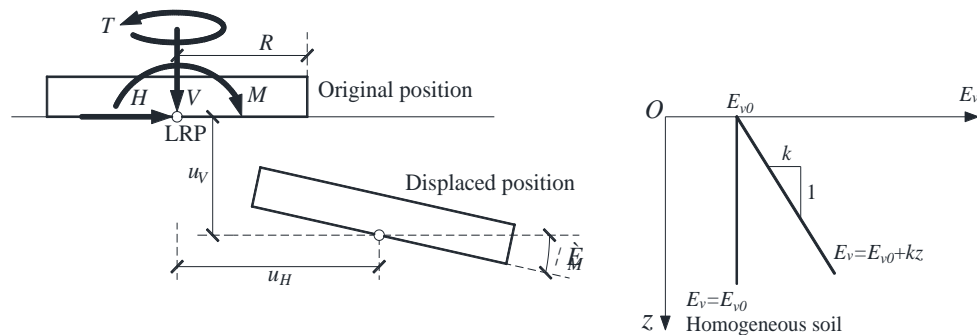


Figure 5.1: Sign conventions & soil profiles (Osman et al., 2007)

5.2.2 Geometry and mesh

A cylinder with finite dimensions was used to simulate the half-space soil. To eliminate potential boundary effects, five model domain widths, L , (i.e. $L = 5D$, $10D$, $20D$, $50D$ and $100D$) were examined. These dimensions represent the horizontal distance from the foundation edge to either side of the domain and the vertical depth of the soil below the foundation. Figure 5.2 shows the effect of model dimensions on K_V and K_{HH} for a surface foundation on a homogeneous isotropic soil and the results of Bell (1991) for the model with a $100D$ mesh size are also compared. The values of K_{MH} , K_{MM} and K_T were also investigated and found to be less sensitive with respect to the domain size. It can be seen that a domain size of $50D \sim 100D$ is therefore sufficiently accurate; thus, a model dimension of $50D$ was adopted for the remaining analyses. The cylindrical circumference of the soil was constrained to prevent out-of-plane translations, and the bottom of the soil was fixed in the three orthogonal coordinate directions.

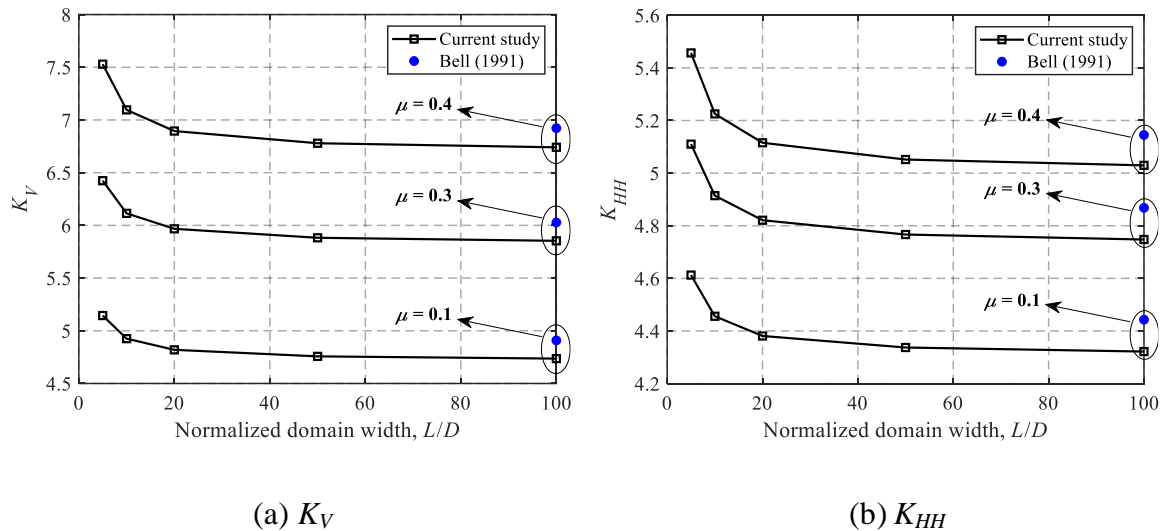


Figure 5.2: Effect of model dimensions on the stiffness coefficients for a surface foundation on a homogeneous isotropic soil: (a) K_V and (b) K_{HH}

A mesh convergence study was carried out for a surface foundation on a homogeneous isotropic soil with $\mu = 0.3$, as summarized in Table 5.1. It can be seen that the foundation stiffnesses calculated using the medium mesh (185000 elements) have very small differences compared with those derived from the dense mesh (367000 elements).

Therefore, the medium mesh was adopted in the analysis. Figure 5.3 shows the plane view of the three-dimensional model using the medium mesh. The mesh was composed of approximately 185000 8-noded brick elements (i.e. first-order, ABAQUS C3D8R). To capture the intense stress concentration close to the foundation edge and the soil -foundation interface, the soil regions in the vicinity of the foundation edge and the horizontal thin soil layer close to the interface were carefully refined.

Table 5.1: Mesh convergence study (surface foundations on a homogeneous soil with $\mu = 0.3$)

Stiffness	Coarse (35000 elements)	Medium (185000 elements)	Dense (367000 elements)
K_V	5.913	5.924	5.924
K_{HH}	4.787	4.792	4.792
K_{MH}	-0.440	-0.446	-0.446
K_{MM}	3.916	3.966	3.966
K_T	5.251	5.213	5.305

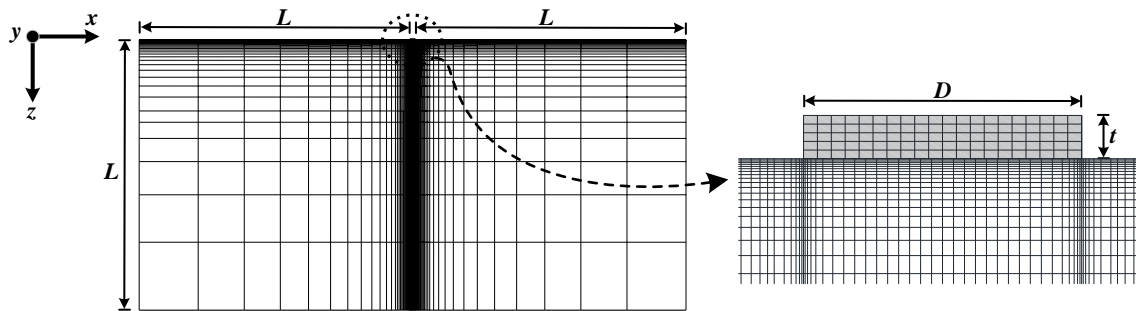


Figure 5.3: Mesh representation

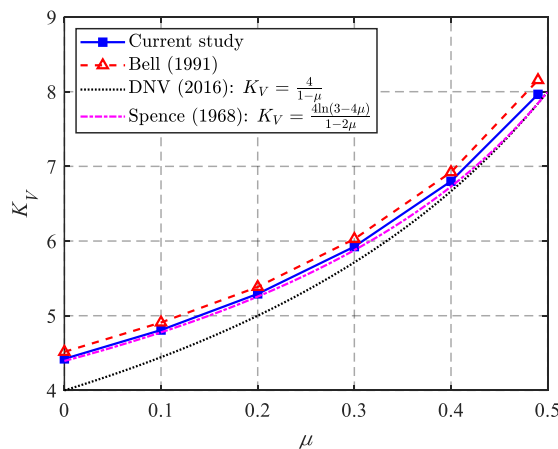
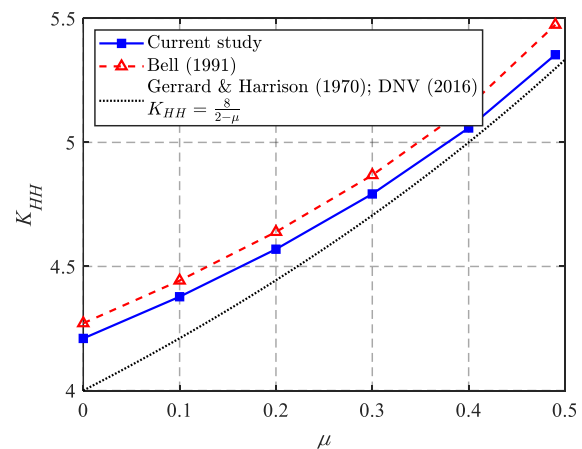
5.3 Finite element results

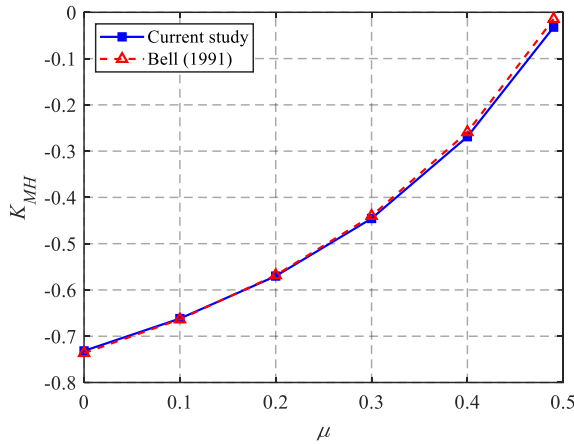
5.3.1 Model calibration

Figure 5.4 shows the comparison between the stiffness coefficients for a surface circular foundation on a homogeneous isotropic soil obtained from the current FE analysis, the Bell

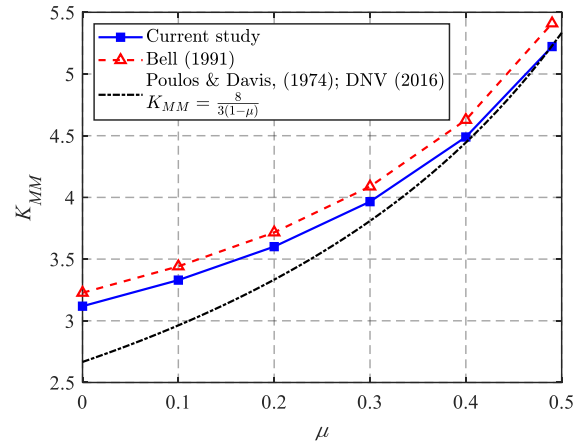
(1991) solutions and the analytical solutions of Spence (1968), Gerrard and Harrison (1970), Poulos and Davis (1974) and DNV (2016).

The figure shows that the current study compares well (with differences less than 5%) with the approximate solutions of K_V , K_{HH} , K_{MH} and K_{MM} from Bell (1991). Both the current study and Bell's (1991) results are a little larger than the analytical solutions. However, the current study lies closer to the analytical solutions than Bell (1991) due to the much finer mesh and improved analytical methods. Moreover, the cross-coupling term obtained from Bell (1991) shown in Figure 5.4(c) exhibits a good agreement with that derived from the FE analysis. It should also be noted that the current FE results have relatively larger K_{HH} and K_{MM} than the analytical solutions, but the difference between them gradually decreases with μ . This is mainly because the analytical solutions of K_{HH} and K_{MM} are uncoupled and the coupling horizontal and rotational behavior gradually decreases with μ , as shown in Figure 5.4(c). Figure 5.4(c) also shows no coupling, when the soil media is incompressible (i.e. undrained case: $\mu = 0.5$), which makes the uncoupled analytical solutions of K_{HH} and K_{MM} approach the current coupled results. As shown in Figure 5.4(e), the torsional stiffness coefficient given by DNV (2016) is invariant with respect to μ , which is slightly larger than the FE results. However, the difference between them is less than 1.5%.

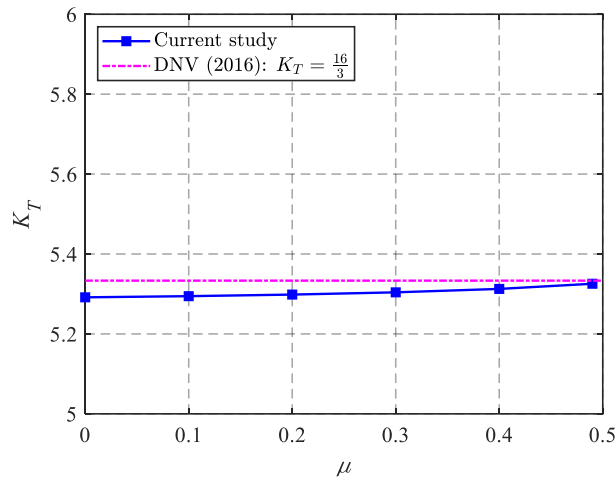
(a) K_V (b) K_{HH}



(c) K_{MH}



(d) K_{MM}



(e) K_T

Figure 5.4: Stiffness coefficients for a surface circular foundation on a homogeneous isotropic soil: (a) K_V ; (b) K_{HH} ; (c) K_{MH} ; (d) K_{MM} and (e) K_T

5.3.2 Stiffness equations for surface foundations on homogeneous soils

The various cases of surface foundations on homogeneous soils can be used to obtain the basic stiffness equations in the absence of the effects of foundation embedment and soil non-homogeneity. Figure 5.5(a) shows the variations of the vertical stiffness coefficient with anisotropy factor for different values of μ^* . In general, K_V gradually increases with the increase of μ^* , but decreases with increasing α^2 . This is because the anisotropy factor is

defined as $\alpha^2 = E_h/E_v$, and K_V relies more on the vertical elastic modulus, E_v . To reduce the variability of the values of K_V caused by μ^* , the term of $K_V(1.1-\mu^*)$ is introduced, as shown in Figure 5.5(b). Figure 5.5(b) shows that the FE results (characterized by the range bars showing the mean, lower and upper bounds) fall into a tight band and a single expression as a function of α^2 is proposed, given by Eq. (5.12) and compared in Figure 5.5(b). Figure 5.5(b) exhibits a good agreement (with $R^2 = 0.997$) between the FE results and the analytical expression below:

$$K_V(1.1 - \mu^*) = \frac{3.20 + 3.14\alpha^2}{0.33 + \alpha^2} \quad (5.12)$$

Eq. (5.12) can be simply manipulated to yield the basic vertical stiffness equation as:

$$K_V = \left(\frac{1}{1.1 - \mu^*} \right) \cdot \left(\frac{3.20 + 3.14\alpha^2}{0.33 + \alpha^2} \right) \quad (5.13)$$

Isotropy (i.e. $\alpha^2 = 1.0$) reduces Eq. (5.13) to the commonly-used isotropic stiffness equation in practical foundation design (e.g. Eq. (5.1)).

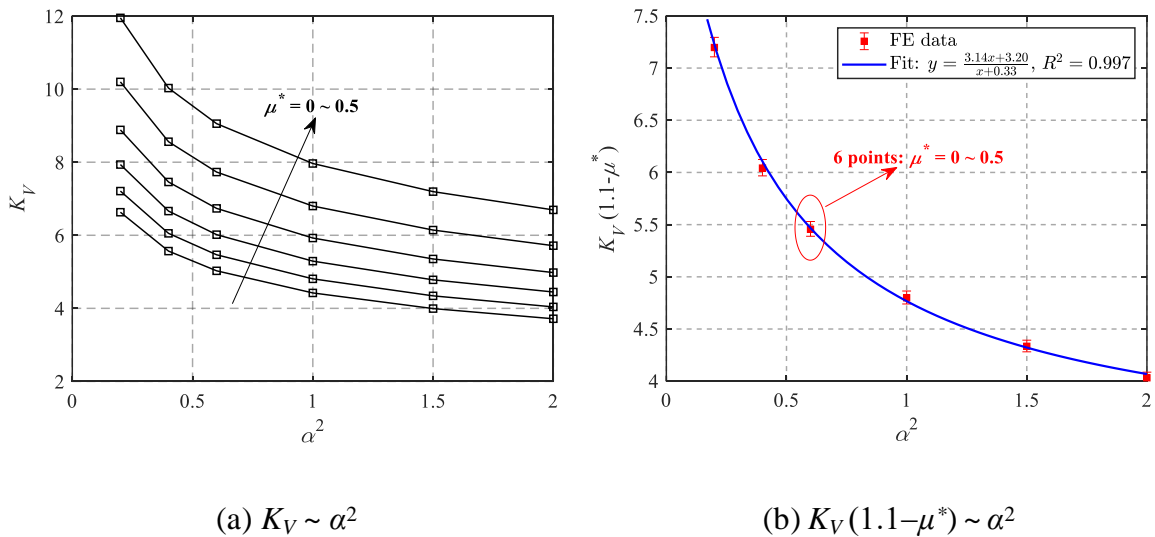


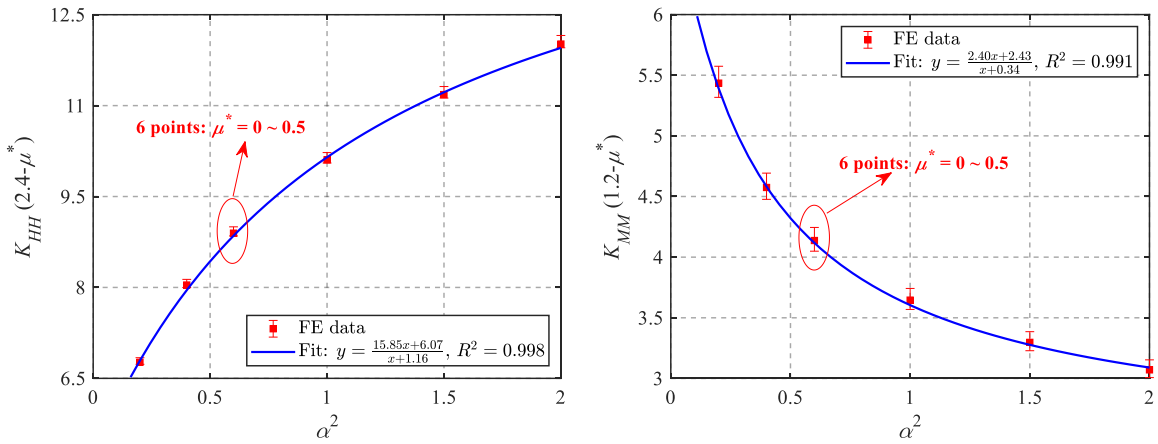
Figure 5.5: Vertical stiffness coefficient for surface foundations on homogeneous soils: (a) $K_V \sim \alpha^2$ and (b) $K_V(1.1 - \mu^*) \sim \alpha^2$

Similar to the vertical stiffness equation, the horizontal and rotational stiffness equations can be derived in the same way, as given by Eqs. (5.14) and (5.15). The comparison shown

in Figure 5.6 also shows satisfactory fits between the FE results and the proposed analytical expressions. It should also be noted that K_{MM} decreases with increase of α^2 , but K_{HH} shows an opposite trend. This is because K_{MM} is dominated by the vertical elastic modulus, while K_{HH} is influenced more by the horizontal elastic modulus.

$$K_{HH} = \left(\frac{1}{2.4 - \mu^*} \right) \cdot \left(\frac{6.07 + 15.85\alpha^2}{1.16 + \alpha^2} \right) \quad (5.14)$$

$$K_{MM} = \left(\frac{1}{1.2 - \mu^*} \right) \cdot \left(\frac{2.43 + 2.40\alpha^2}{0.34 + \alpha^2} \right) \quad (5.15)$$



(a) $K_{HH}(2.4 - \mu^*) \sim \alpha^2$

(b) $K_{MM}(1.2 - \mu^*) \sim \alpha^2$

Figure 5.6: Horizontal and rotational stiffness coefficients for surface foundations on homogeneous soils: (a) $K_{HH}(2.4 - \mu^*) \sim \alpha^2$ and (b) $K_{MM}(1.2 - \mu^*) \sim \alpha^2$

Figure 5.7(a) presents the coupling stiffness coefficients between horizontal and rotational behavior for surface foundations on homogeneous soils. In contrast with K_V , K_{HH} and K_{MM} , K_{MH} appears to be unaffected by the soil anisotropy. Therefore, the coupling stiffness coefficients can be simply expressed as a function of μ^* :

$$K_{MH} = K_{HM} = \frac{-1.28(0.5 - \mu^*)}{0.87 - \mu^*} \quad (5.16)$$

It should also be noted that Eq. (5.16) becomes zero, when μ^* is equal to 0.5, indicating no coupling effect between horizontal and moment responses. This has also been confirmed by Bell (1991).

The relationship between K_T and α^2 is presented in Figure 5.7(b). Contrary to K_{MH} shown in Figure 5.7(a), K_T is affected only by α^2 , and μ^* has no influence on K_T . The relationship can therefore be estimated using Eq. (5.17) and a good agreement can be observed in Figure 5.7(b).

$$K_T = \frac{3.20 + 8.33\alpha^2}{1.16 + \alpha^2} \quad (5.17)$$

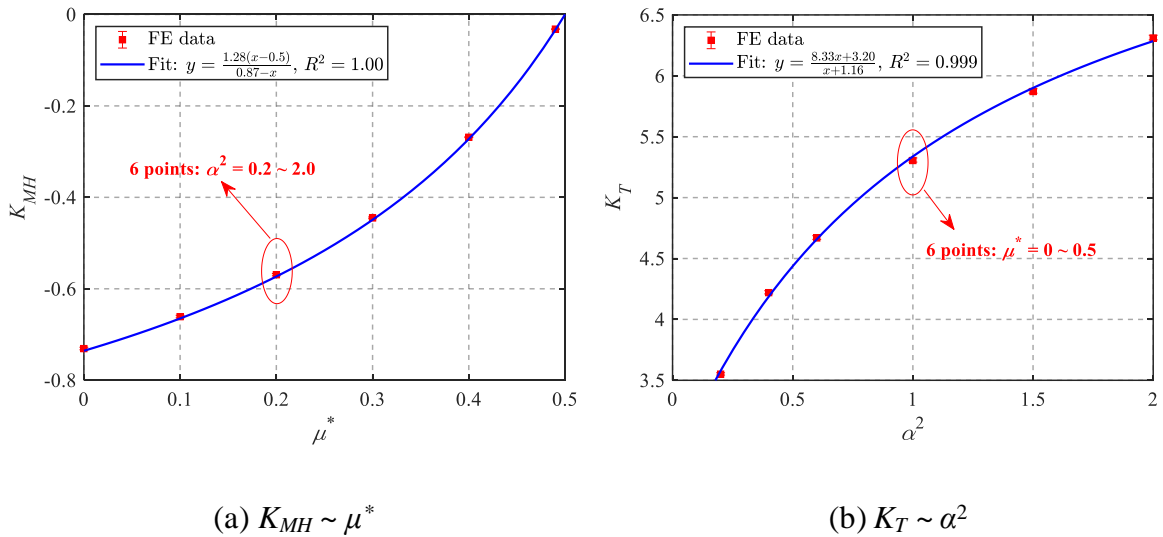


Figure 5.7: Coupling and torsional stiffness coefficients for surface foundations on homogeneous soils: (a) $K_{MH} \sim \mu^*$ and (b) $K_T \sim \alpha^2$

5.3.3 Correction factors for Gibson soils

Analyses of surface foundations on Gibson soils can account for the effects of soil stiffness non-homogeneity (i.e. linearly increasing elastic modulus with depth) on the stiffness of shallow foundations. As shown in Eq. (5.18), the Gibson correction factor for vertical stiffness, defined as the ratio of K_V for a Gibson soil to that for a homogeneous soil, is introduced. $(C_{\beta,V} - 1)$ is adopted to make $(C_{\beta,V} - 1) \sim \beta$ curves start from the origin, as shown in Figure 5.8(a). The data points inside the ellipse shown in Figure 5.8(a) represent

one case with the same stiffness slope, including 36 points (i.e. six values of $\alpha^2 \times$ six values of μ^*). As shown in Figure 5.8(a), generally, $(C_{\beta,V} - 1)$ gradually increases with the increase of β ; however, great variations of the results can be observed due to the dependence of $(C_{\beta,V} - 1)$ on α^2 and μ^* . Thus, $(C_{\beta,V} - 1)$ should be a function of α^2 , μ^* and β , which can be simply assumed to be the product of three independent functions in terms of α^2 , μ^* and β , respectively, as given by Eq. (5.18).

$$C_{\beta,V} = \frac{K_{V,Gibson}}{K_{V,homo}} = 1 + f_{1,V}(\mu^*) \cdot f_{2,V}(\alpha^2) \cdot f_{3,V}(\beta) \quad (5.18)$$

By using

$$f_{1,V}(\mu^*) = \frac{0.23(1 - \mu^*)}{0.77 - \mu^*} \quad (5.19)$$

$$f_{2,V}(\alpha^2) = \frac{0.67 + 0.74\alpha^2}{0.41 + \alpha^2}$$

the relationship between $\frac{C_{\beta,V}-1}{f_{1,V}(\mu^*) \cdot f_{2,V}(\alpha^2)}$ and β is shown in Figure 5.8. It can be seen that the dependence on α^2 and μ^* has been eliminated by dividing $f_{1,V}(\mu^*)$ and $f_{2,V}(\alpha^2)$, and the remaining function, $f_{3,V}(\beta)$, can be satisfactorily fitted using Eq. (5.20), as shown in Figure 5.8(b).

$$f_{3,V}(\beta) = \frac{2.99\beta}{0.81 + \beta} \quad (5.20)$$

Consequently, the Gibson correction factor for vertical stiffness, $C_{\beta,V}$, can be expressed using Eq. (5.21).

$$C_{\beta,V} = 1 + \left(\frac{0.23(1 - \mu^*)}{0.77 - \mu^*} \right) \cdot \left(\frac{0.67 + 0.74\alpha^2}{0.41 + \alpha^2} \right) \cdot \left(\frac{2.99\beta}{0.81 + \beta} \right) \quad (5.21)$$

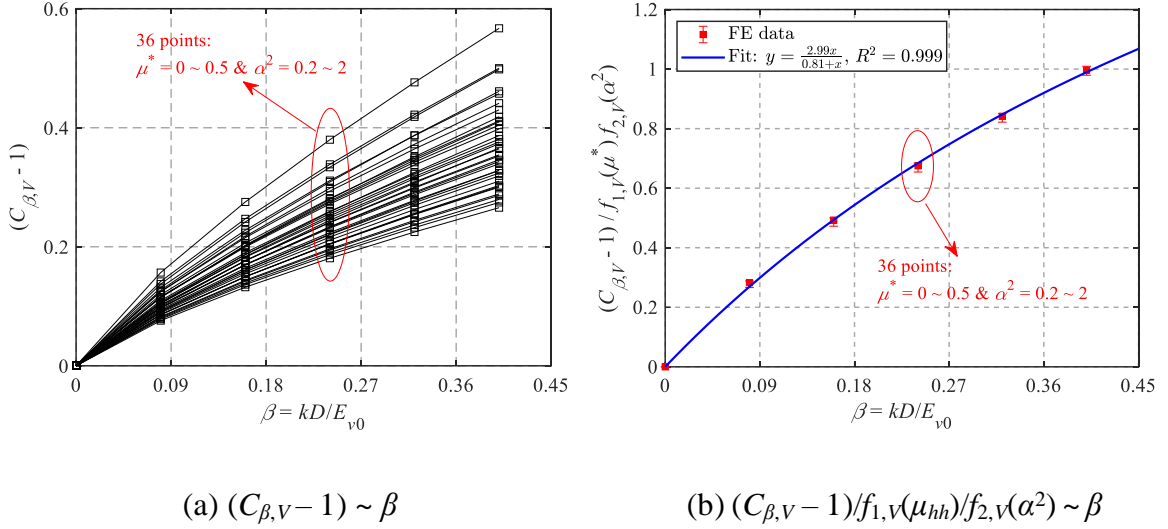


Figure 5.8: Gibson correction factor for vertical stiffness: (a) $(C_{\beta,V} - 1) \sim \beta$ and (b) $(C_{\beta,V} - 1)/f_{1,V}(\mu^*)/f_{2,V}(\alpha^2) \sim \beta$

Following the steps developing the Gibson correction factor for vertical stiffness, the Gibson correction factors for horizontal, rotational and torsional stiffnesses, $C_{\beta,HH}$, $C_{\beta,MM}$ and $C_{\beta,T}$, can be estimated with Eqs. (5.22), (5.23) and (5.24), respectively. The comparison presented in Figure 5.9 shows a good agreement between the FE results and the proposed analytical expressions.

$$C_{\beta,HH} = 1 + (0.17 - 0.013\mu^*) \cdot \left(\frac{0.67 + 0.72\alpha^2}{0.41 + \alpha^2} \right) \cdot \left(\frac{3.30\beta}{0.93 + \beta} \right) \quad (5.22)$$

$$C_{\beta,MM} = 1 + \left(\frac{0.062 - 0.056\mu^*}{0.76 - \mu^*} \right) \cdot \left(\frac{0.68(1 + \alpha^2)}{0.37 + \alpha^2} \right) \cdot \left(\frac{11.10\beta}{4.03 + \beta} \right) \quad (5.23)$$

$$C_{\beta,T} = 1 + \left(\frac{0.030(1 + \alpha^2)}{0.35 + \alpha^2} \right) \cdot (2.54\beta) \quad (5.24)$$

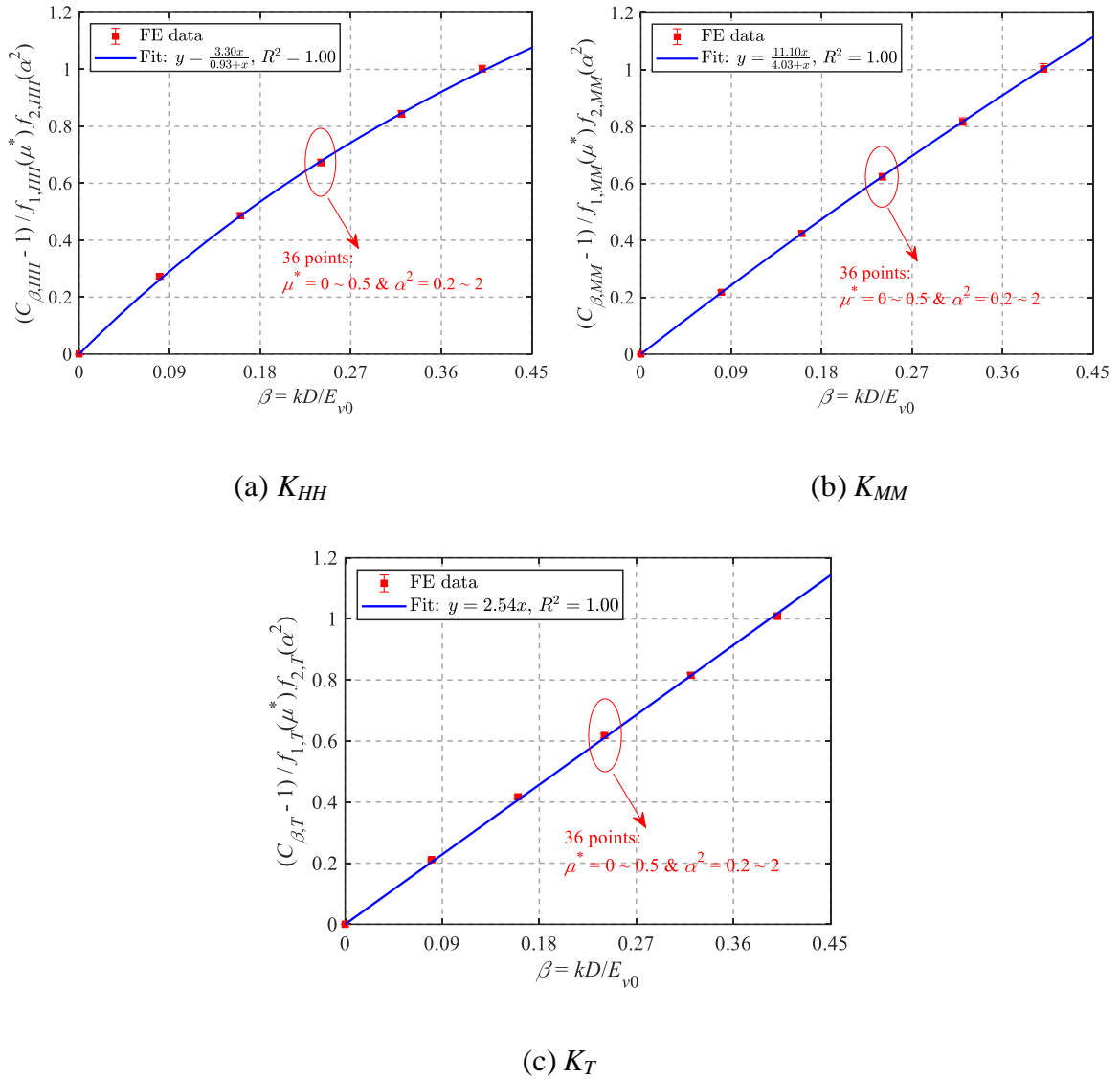


Figure 5.9: Gibson correction factors for horizontal, rotational and torsional stiffness: (a) K_{HH} ; (b) K_{MM} and (c) K_T

In contrast, the coupling stiffness coefficient between horizontal and rotational responses seems to be unaffected by the stiffness non-homogeneity of Gibson soils, as illustrated in Figure 5.10. Therefore, the Gibson correction factor for K_{MH} is equivalent to 1.0, and the basic stiffness equation of K_{MH} for homogeneous soils (see Eq. (5.16)) can still be adopted to evaluate that for Gibson soils, as compared in Figure 5.10. It should be noted that the variation in K_{MH} at $\mu^* = 0.5$ is relatively larger. However, the fitted value of $K_{MH} = 0$ at μ^*

$= 0.5$ is close to the mean value and matches the value for a homogeneous soil (see Eq. (5.16)).

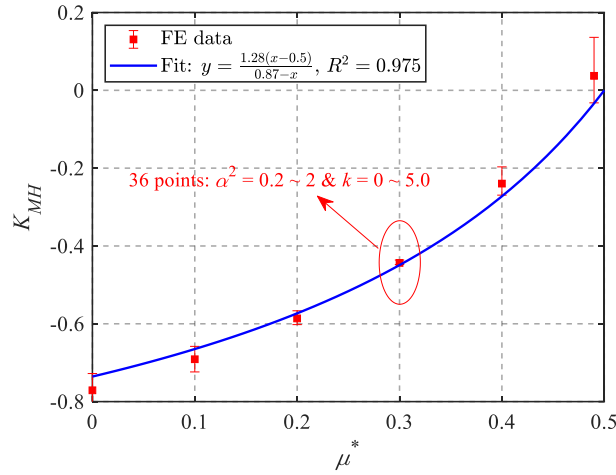


Figure 5.10: Coupling stiffness coefficient for surface foundations on Gibson soils

5.3.4 Correction factors for foundation embedment

The effect of foundation embedment on the stiffness of shallow foundations can be studied using the cases of embedded circular foundations founded in homogeneous soils. In addition to foundation embedment, the thickness of the foundation also exhibits an influence on the foundation stiffness (Doherty and Deeks, 2003). However, its influence is negligible compared with that of the foundation embedment, particularly for $d/D < 0.5$. In this study, the assumed foundation embedment depth does not exceed the thickness of the foundation (i.e. $d \leq t = 3$ m) and the range of the foundation embedment ratio is $d/D \leq 0.16$. Therefore, the effect of the thickness of foundation is ignored and only the effect of foundation embedment is investigated in this section.

Similar to the definition of the Gibson correction factors, the embedment correction factor for vertical stiffness, $C_{d,v}$, defined as the ratio of K_V for an embedded foundation resting on a homogeneous soil to that for a surface foundation founded on a homogeneous soil, is also introduced. Figure 5.11(a) shows the variations of $(C_{d,v} - 1)$ with the embedment ratio, d/D . It can be seen that for a given value of d/D , a significant dispersion of the FE results can be observed due to the dependence on α^2 and μ^* . Similar to the analytical expression for $C_{\beta,v}$ (see Eq. (5.18)), $C_{d,v}$ is assumed to follow the same form of equation:

$$C_{d,V} = \frac{K_{V,emb}}{K_{V,surf}} = 1 + g_{1,V}(\mu^*) \cdot g_{2,V}(\alpha^2) \cdot g_{3,V}(d/D) \quad (5.25)$$

As shown in Figure 5.11(b), the utilization of $g_{1,V}(\mu^*) = \frac{1.28-1.66\mu^*}{7.45+\mu^*}$ and $g_{2,V}(\alpha^2) = \frac{0.59+1.35\alpha^2}{0.94+\alpha^2}$ can result in the FE results lying in a relatively narrow band. The remaining function, $g_{3,V}(d/D)$, can then be evaluated using $g_{3,V}(d/D) = \frac{2.61d/D}{0.26+d/D}$, which yields the embedment correction factor for vertical stiffness to be:

$$C_{d,V} = 1 + \left(\frac{1.28 - 1.66\mu^*}{7.45 + \mu^*} \right) \cdot \left(\frac{0.59 + 1.35\alpha^2}{0.94 + \alpha^2} \right) \cdot \left(\frac{2.61 d/D}{0.26 + d/D} \right) \quad (5.26)$$

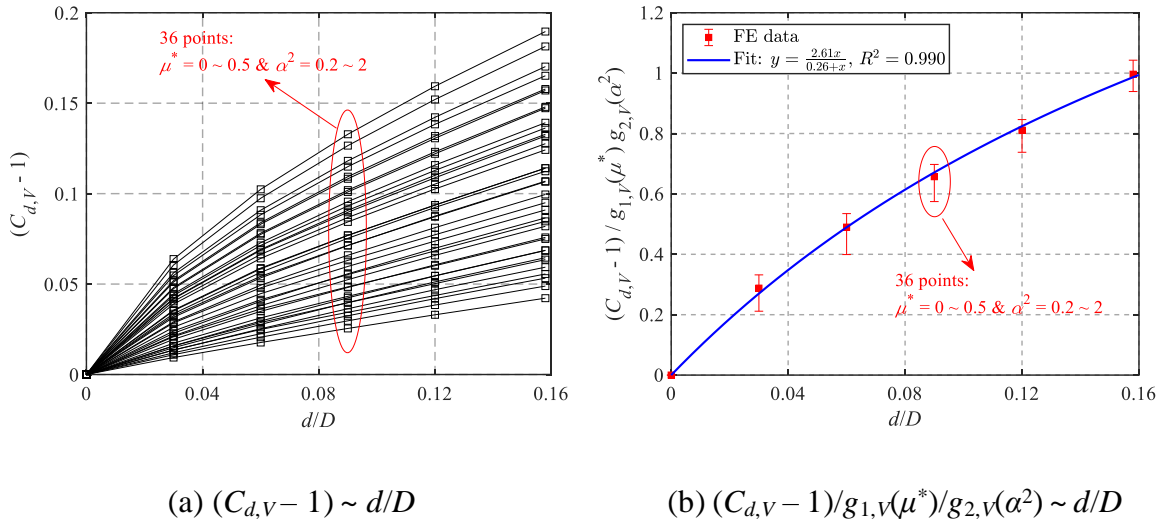


Figure 5.11: Embedment correction factor for vertical stiffness: (a) $(C_{d,V} - 1) \sim d/D$ and (b) $(C_{d,V} - 1) / g_{1,V}(\mu^*) / g_{2,V}(\alpha^2) \sim d/D$

Similar to the embedment correction factor for vertical stiffness, the embedment correction factors for horizontal, rotational and torsional stiffness, $C_{d,HH}$, $C_{d,MM}$ and $C_{d,T}$, can be developed in the same way, as given by Eqs. (5.27), (5.28) and (5.29). Figure 5.12 shows that these expressions can provide reasonable predictions compared with the FE results.

$$C_{d,HH} = 1 + \left(\frac{0.23 - 0.36\mu^*}{0.64 - \mu^*} \right) \cdot \left(\frac{0.60 + 1.37\alpha^2}{1.00 + \alpha^2} \right) \cdot \left(\frac{2.95 d/D}{0.32 + d/D} \right) \quad (5.27)$$

$$C_{d,MM} = 1 + (0.40 - 0.34\mu^*) \cdot \left(\frac{0.71 + 1.60\alpha^2}{1.32 + \alpha^2} \right) \cdot \left(\frac{7.56 d/D}{1.04 + d/D} \right) \quad (5.28)$$

$$C_{d,T} = 1 + \left(\frac{0.20 - 0.27\mu^*}{0.74 - \mu^*} \right) \cdot \left(\frac{0.44 + 1.15\alpha^2}{0.55 + \alpha^2} \right) \cdot \left(\frac{1.42 d/D}{0.068 + d/D} \right) \quad (5.29)$$

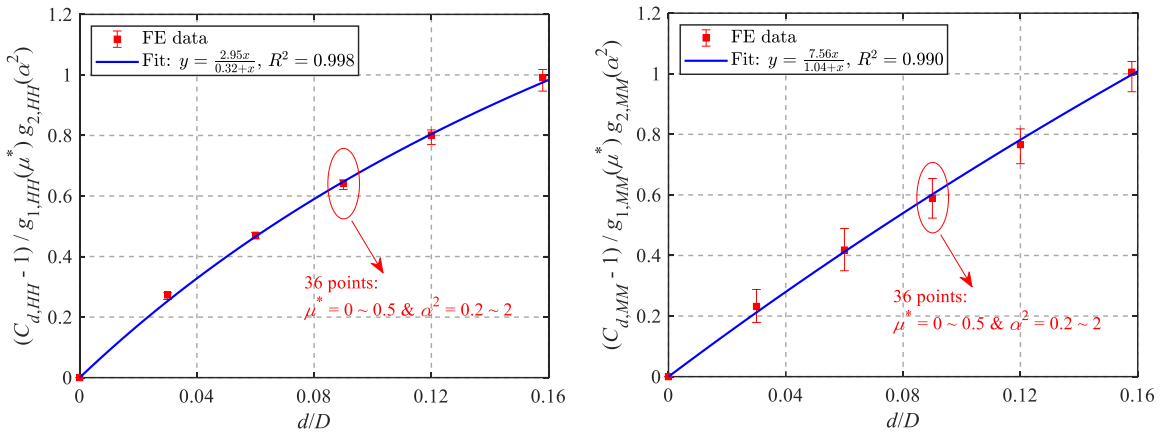
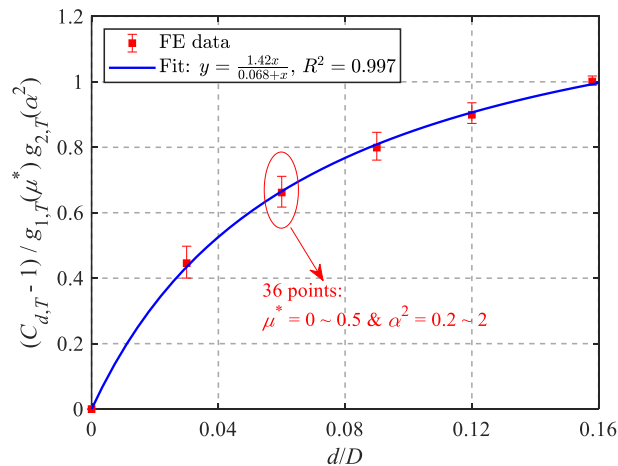
(a) K_{HH} (b) K_{MM} (c) K_T

Figure 5.12: Embedment correction factors for horizontal, rotational and torsional stiffness: (a) K_{HH} ; (b) K_{MM} and (c) K_T

Figure 5.13(a) shows the variations of K_{MH} with d/D . Unlike the effect of Gibson soils discussed in Section 5.3.3, foundation embedment exhibits a significant influence on the coupling stiffness between horizontal and rotational behavior. Generally, the coupling gradually increases with increasing the embedment ratio, which is consistent with the

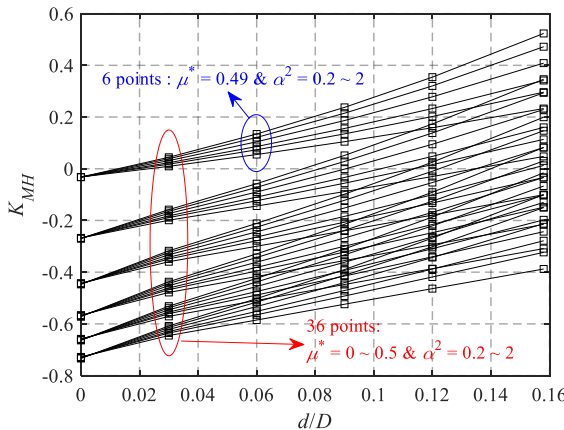
numerical findings by Bell (1991). As can be seen from Figure 5.13(a), six clusters of curves, corresponding to the six values of μ^* , can be clearly observed. It should also be noted that K_{MH} at $d/D = 0$ (i.e. surface foundation) is affected only by μ^* without the influence of α^2 . However, with the increase of d/D , the effect of α^2 on K_{MH} gradually increases and cannot be neglected. Therefore, K_{MH} for embedded foundations should be a function of α^2 , μ^* and β .

Since some values of K_{MH} are close to zero, the vertical, horizontal and rotational embedment correction factors defined by ratios (see Eq. (5.25)) may lead to singularity for K_{MH} . Therefore, the embedment correction factor for K_{MH} is defined using the difference between K_{MH} for an embedded foundation resting on a homogeneous soil and that for a surface foundation on a homogeneous soil. It is also assumed to be the product of three independent functions of α^2 , μ^* and β , respectively, as expressed by Eq. (5.30).

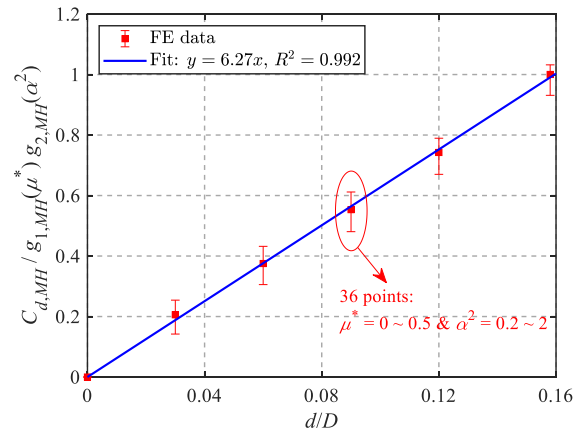
$$C_{d,MH} = C_{d,HM} = K_{MH,emb} - K_{MH,surf} = g_{1,MH}(\mu^*) \cdot g_{2,MH}(\alpha^2) \cdot g_{3,MH}(d/D) \quad (5.30)$$

Using $g_{1,MH}(\mu^*) = \frac{0.63 - 0.85\mu^*}{\mu^{*2} - 1.97\mu^* + 1.21}$ and $g_{2,MH}(\alpha^2) = \frac{0.75 + 1.77\alpha^2}{1.51 + \alpha^2}$, the remaining function, $g_{3,MH}(d/D) = \frac{C_{d,MH}}{g_{1,MH}(\mu^*) \cdot g_{2,MH}(\alpha^2)}$ can be fitted by a linear equation, $g_{3,MH}(d/D) = 6.27 d/D$, as favorably compared in Figure 5.13(b).

$$C_{d,MH} = C_{d,HM} = \left(\frac{0.63 - 0.85\mu^*}{\mu^{*2} - 1.97\mu^* + 1.21} \right) \cdot \left(\frac{0.75 + 1.77\alpha^2}{1.51 + \alpha^2} \right) \cdot (6.27 d/D) \quad (5.31)$$



(a) $K_{MH} \sim d/D$



(b) $C_{e,MH}/g_{1,MH}(\mu^*)/g_{2,MH}(\alpha^2) \sim d/D$

Figure 5.13: Embedment correction factor for coupling stiffness: (a) $K_{MH} \sim d/D$ and (b) $C_{d,MH}/g_{1,MH}(\mu^*)/g_{2,MH}(\alpha^2) \sim d/D$

Based on the above analyses, the complete vertical, horizontal, rotational, coupling and torsional stiffness equations for circular foundations, including both the Gibson and embedment correction factors, are summarized in Eq. (5.32).

$$\begin{aligned}
K_V &= \left[\left(\frac{1}{1.1 - \mu^*} \right) \cdot \left(\frac{3.20 + 3.14\alpha^2}{0.33 + \alpha^2} \right) \right] \\
&\quad \cdot \left[1 + \left(\frac{0.23(1 - \mu^*)}{0.77 - \mu^*} \right) \cdot \left(\frac{0.67 + 0.74\alpha^2}{0.41 + \alpha^2} \right) \cdot \left(\frac{2.99\beta}{0.81 + \beta} \right) \right] \\
&\quad \cdot \left[1 + \left(\frac{1.28 - 1.66\mu^*}{7.45 + \mu^*} \right) \cdot \left(\frac{0.59 + 1.35\alpha^2}{0.94 + \alpha^2} \right) \cdot \left(\frac{2.61 d/D}{0.26 + d/D} \right) \right] \\
K_{HH} &= \left[\left(\frac{1}{2.4 - \mu^*} \right) \cdot \left(\frac{6.07 + 15.85\alpha^2}{1.16 + \alpha^2} \right) \right] \\
&\quad \cdot \left[1 + (0.17 - 0.013\mu^*) \cdot \left(\frac{0.67 + 0.72\alpha^2}{0.41 + \alpha^2} \right) \cdot \left(\frac{3.30\beta}{0.93 + \beta} \right) \right] \\
&\quad \cdot \left[1 + \left(\frac{0.23 - 0.36\mu^*}{0.64 - \mu^*} \right) \cdot \left(\frac{0.60 + 1.37\alpha^2}{1.00 + \alpha^2} \right) \cdot \left(\frac{2.95 d/D}{0.32 + d/D} \right) \right] \quad (5.32) \\
K_{MH} = K_{HM} &= \left[\frac{-1.28(0.5 - \mu^*)}{0.87 - \mu^*} \right] \\
&\quad + \left[\left(\frac{0.63 - 0.85\mu^*}{\mu^{*2} - 1.97\mu^* + 1.21} \right) \cdot \left(\frac{0.75 + 1.77\alpha^2}{1.51 + \alpha^2} \right) \cdot (6.27 d/D) \right] \\
K_{MM} &= \left[\left(\frac{1}{1.2 - \mu^*} \right) \cdot \left(\frac{2.43 + 2.40\alpha^2}{0.34 + \alpha^2} \right) \right] \\
&\quad \cdot \left[1 + \left(\frac{0.062 - 0.056\mu^*}{0.76 - \mu^*} \right) \cdot \left(\frac{0.68(1 + \alpha^2)}{0.37 + \alpha^2} \right) \cdot \left(\frac{11.10\beta}{4.03 + \beta} \right) \right] \\
&\quad \cdot \left[1 + (0.40 - 0.34\mu^*) \cdot \left(\frac{0.71 + 1.60\alpha^2}{1.32 + \alpha^2} \right) \cdot \left(\frac{7.56 d/D}{1.04 + d/D} \right) \right]
\end{aligned}$$

$$K_T = \left[\frac{3.20 + 8.33\alpha^2}{1.16 + \alpha^2} \right] \cdot \left[1 + \left(\frac{0.030(1 + \alpha^2)}{0.35 + \alpha^2} \right) \cdot (2.54\beta) \right] \\ \cdot \left[1 + \left(\frac{0.20 - 0.27\mu^*}{0.74 - \mu^*} \right) \cdot \left(\frac{0.44 + 1.15\alpha^2}{0.55 + \alpha^2} \right) \cdot \left(\frac{1.42 d/D}{0.068 + d/D} \right) \right]$$

5.4 Conclusions

The coupled elastic stiffness of circular foundations founded on cross-anisotropic soils under combined VHMT loading has been studied using finite element analysis. A three-parameter cross-anisotropic soil model was adopted with a range of anisotropic parameters covering typical soils found in practice. The effect of model dimensions was investigated and the results show that a domain width of 50 times the foundation diameter is sufficiently accurate for the FE analysis. The stiffness coefficients for surface foundations resting on a homogeneous isotropic soil favorably compare with reported literature values. The vertical and rocking stiffness decrease with anisotropic parameter α , and the horizontal stiffness shows an increasing trend. However, the coupling stiffness is minimally affected by α . To account for the effects of soil non-homogeneity and foundation embedment, Gibson soils and embedded foundations were also considered. The Gibson and embedment correction factors were derived accordingly. The analysis shows that a higher Gibson modulus (β) can increase the vertical, horizontal and moment stiffness, while it does not affect the coupling between the horizontal and moment responses of a surface foundation.

5.5 References

- Bell, R. W. (1991). The analysis of offshore foundations subjected to combined loading. Master's dissertation, University of Oxford, Oxford, UK.
- Bishop, A. W., and Hight, D. W. (1977). The value of Poisson's ratio in saturated soils and rocks stressed under undrained conditions. *Géotechnique*, 27(3), 369-384.
- Burland, J. B., Broms, B. B., and De Mello, V. F. B. (1977). Behaviour of foundations and structures. In *Proceedings of 9th International Conference on Soil Mechanics and Foundation Engineering*, Tokyo, Japan, 10-15 July 1977. The Japanese Geotechnical Society, Tokyo, Vol. 2, pp. 495-546.
- Carrier, W. D., and Christian, J. T. (1973). Rigid circular plate resting on a non-homogenous elastic half-space. *Géotechnique*, 23(1), 67-84.

- DNV GL (Det Norske Veritas GL) (1992). Foundations, classification notes No. 30.4. DNV GL Group, Høvik, Norway.
- DNV GL (Det Norske Veritas GL) (2016). DNVGL-ST-0126: Support structures for wind turbines. DNV GL Group, Høvik, Norway.
- Doherty, J. P., and Deeks, A. J. (2003). Elastic response of circular footings embedded in a non-homogeneous half-space. *Géotechnique*, 53(8), 703-714.
- Gazetas, G. (1981). Strip foundations on a cross-anisotropic soil layer subjected to dynamic loading. *Géotechnique*, 31(2), 161-179.
- Gazetas, G. (1983). Analysis of machine foundation vibrations: state of the art. *International Journal of Soil Dynamics and Earthquake Engineering*, 2(1), 2-42.
- Gazetas, G. (1991). Formulas and charts for impedances of surface and embedded foundations. *Journal of geotechnical engineering*, 117(9), 1363-1381.
- Gerrard, C. M., and Harrison, W. J. (1970). Circular loads applied to a cross-anisotropic half space. Technical Paper No. 8, CSIRO Australian Division of Applied Geomechanics, Australian Geomechanics Society, St Ives, N.S.W.
- Gibson, R. E. (1967). Some results concerning displacements and stresses in a non-homogeneous elastic half-space. *Géotechnique*, 17(1), 58-67.
- González-Hurtado, J. (2019). The effect of stiffness anisotropy of a glacial clay on the behaviour of a shallow wind turbine foundation. Unpublished Doctoral dissertation, The University of Western Ontario, London, Ont.
- Gourvenec, S. M., and Mana, D. S. K. (2011). Undrained vertical bearing capacity factors for shallow foundations. *Géotechnique Letters*, 1(4), 101-108.
- Graham, J., and Houlsby, G. T. (1983). Anisotropic elasticity of a natural clay. *Géotechnique*, 33(2), 165-180.
- ISO (International Standards Organization). (2016). ISO 19901-4: Petroleum and natural gas industries specific requirements for offshore structures – part 4: geotechnical and foundation design considerations, 2nd edition. International Standards Organization, Geneva, Switzerland.
- Kausel, E., Whitman, R. V., Morray, J. P., and Elsabee, F. (1978). The spring method for embedded foundations. *Nuclear Engineering and design*, 48(2-3), 377-392.
- Korobova, O. A., Maksimenko, L. A., and Solovyanova, I. Y. (2019). Sequence of calculation of anisotropic soil foundations on deformation. *In IOP Conference Series: Materials Science and Engineering*. Vol. 687, No. 4, 044036.
- Lang, P. J. (2012). Sensitivity of shallow wind turbine foundation design and soil response to geotechnical variance with construction cost implications. W.I.: Master's thesis Report, University of Wisconsin-Madison, Madison, W.I.
- Lings, M. L. (2001). Drained and undrained anisotropic elastic stiffness parameters. *Géotechnique*, 51(6), 555-565.
- Lings, M. L., Pennington, D. S., and Nash, D. F. T. (2000). Anisotropic stiffness parameters and their measurement in a stiff natural clay. *Géotechnique*, 50(2), 109-125.

- Love, A. E. H. (2013). A treatise on the mathematical theory of elasticity. Cambridge University Press, Cambridge, UK.
- Martin, C. M. (1994). Physical and numerical modelling of offshore foundations under combined loads. Doctoral dissertation, University of Oxford, Oxford, UK.
- Nishimura, S. (2014). Assessment of anisotropic elastic parameters of saturated clay measured in triaxial apparatus: Appraisal of techniques and derivation procedures. *Soils and Foundations*, 54(3), 364-376.
- Osman, A. S., White, D. J., Britto, A. M., and Bolton, M. D. (2007). Simple prediction of the undrained displacement of a circular surface foundation on non-linear soil. *Géotechnique*, 57(9), 729-737.
- Pickering, D. J. (1970). Anisotropic elastic parameters for soil. *Géotechnique*, 20(3), 271-276.
- Poulos, H. G., and Davis, E. H. (1974). Elastic solutions for soil and rock mechanics, John Wiley, New York, N.Y.
- Ratananikom, W., Likitlersuang, S., and Yimsiri, S. (2013). An investigation of anisotropic elastic parameters of Bangkok Clay from vertical and horizontal cut specimens. *Geomechanics and Geoengineering*, 8(1), 15-27.
- Raymond, G. P. (1970). Stresses and displacements in cross-anisotropic soil. *Géotechnique*, 20(4), 456-458.
- Reissner, E., and Sagoci, H. F. (1944). Forced torsional oscillations of an elastic half-space. I. *Journal of Applied Physics*, 15(9), 652-654.
- Rowe, R. K., and Booker, J. R. (1981). The behaviour of footings resting on a non-homogeneous soil mass with a crust. Part II. Circular footings. *Canadian Geotechnical Journal*, 18(2), 265-279.
- Shrivastava, S., Ghosh, C., and Jonas, J. J. (2012). A comparison of the von Mises and Hencky equivalent strains for use in simple shear experiments. *Philosophical Magazine*, 92(7), 779-786.
- Spence, D. A. (1968). Self similar solutions to adhesive contact problems with incremental loading. *Proceedings of the Royal Society of London A*, 305(1480), 55-80.
- Whitman, R. V. (1976). Soil-platform interaction. In *Proceedings of Conference on Behaviour of Offshore Structures*, Oslo, Norway, 1976. Norwegian Institute of Technology, Trondheim, 1, 817.
- Yang, Z. X., Li, X. S., and Yang, J. (2008). Quantifying and modelling fabric anisotropy of granular soils. *Géotechnique*, 58(4), 237-248.
- Yimsiri, S., and Soga, K. (2011). Cross-anisotropic elastic parameters of two natural stiff clays. *Géotechnique*, 61(9), 809-814.

6 Discussions, conclusions and recommendations

6.1 Discussions

This thesis has investigated the bearing capacity and foundation stiffness for large circular foundations using finite element analysis. Drained and undrained failure envelopes for circular foundations under combined vertical (V), horizontal (H), moment (M) and torsional (T) loads were derived. Solutions for anisotropic, coupled foundation stiffnesses under combined VHMT loadings was also developed. As an example of the application of these methods, the ultimate and serviceability limit state design for a shallow foundation of a typical Canadian wind turbine is estimated using the developed failure envelope and foundation stiffness approaches.

6.1.1 Ultimate limit state design

The diameter of the surface circular foundation is assumed to be 19 m and the undrained shear strength estimated with a cone penetration test (CPT) is shown in Figure 6.1. This shows a typical profile for Ontario with a strong surficial crust. Due to the existence of fissuring and stress-strain compatibility, the high undrained shear strength of this upper crust is unlikely to be fully mobilized at failure (Lefebvre et al., 1987). Rochelle et al. (1974) recommended a comparison between the full (i.e. maximum strength value), mid-depth (i.e. strength value at mid-depth of the crust) and minimum (i.e. strength value just below the crust) strength of the upper crust for limit state analysis. For the s_u profile shown in Figure 6.1, the mid-depth strength is close to the maximum value. Lefebvre et al. (1974) adopted the mean value of the maximum strength of the upper crust and the minimum strength of the underlying soil. In the analysis for this thesis, the estimates for the minimum, maximum and mean undrained shear strength of the crust are compared. The minimum strength case reduces the soil to a single-layer material with a uniform strength with depth. The assumed undrained shear strength profiles (a), (b) and (c) are shown in Figure 6.1. The properties of the soil and the factored ultimate limit state loads from IEC DLC 6.1 (2005) are also summarized in Table 6.1.

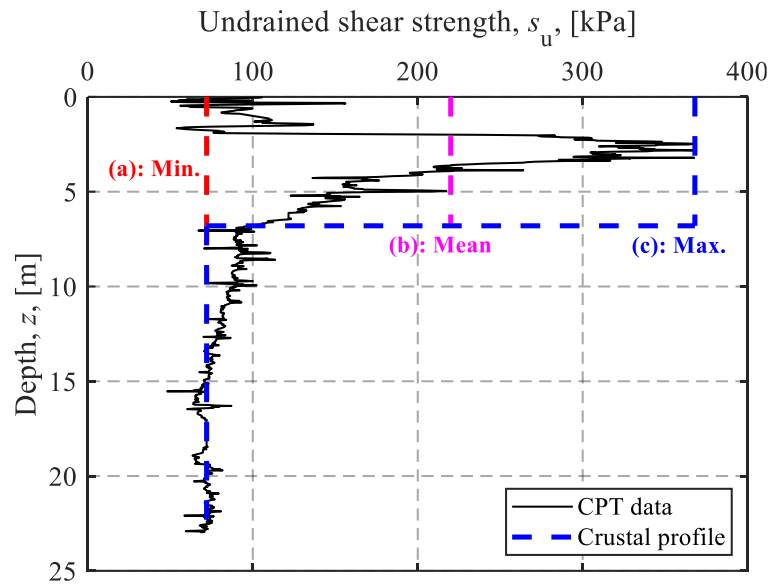


Figure 6.1: Undrained shear strength profile

Table 6.1: Soil parameters and ultimate design loads

Soil	Undrained shear strength of the surficial crust, s_{ut} , [kPa]	(a) Min.: 72 (b) Mean: 220 (c) Max.: 368
	Undrained shear strength of the underlying soil, s_{u0} , [kPa]	72
	Crust thickness, t_c , [m]	6.8
Factored ultimate loads	Vertical load, V , [kN]	21820
	Horizontal load, H , [kN]	1100
	Moment, M , [kN·m]	76200
	Torsion, T , [kN·m]	4400

The corresponding uniaxial bearing capacities are computed based on the factored undrained shear strength (as recommended by DNV (2016), partial safety factor for

materials, $\gamma_m = 1.25$, for total stress analysis), as summarized in Table 6.2. The safety check of ultimate limit state design using the failure envelope methods shows that the three cases all yield acceptable ultimate capacity designs. However, the soil with a surficial crust gains significant extra margins of safety compared with the single-layer assumptions. Figure 6.2 shows the reduced M - H failure envelopes accounting for the design vertical and torsional loads, along with an envelope (d) derived from the traditional approach (DNV, 2016) using the load inclination factor and the effective foundation area (see Eq. (1.2)) for the case of a single-layer material. It can be seen that the traditional approach (d) is more conservative than the other failure envelope methods. In addition, the considerable difference in the absolute sizes of the three failure envelopes indicates that ignoring the contribution of the upper crust may significantly underestimate the bearing capacity and potentially lead to a significant overdesign of the foundation.

Table 6.2: Ultimate limit state design of the foundation

Soil profile case	Ultimate capacity	Normalized load	Safety check
(a) Min. (i.e. single-layer)	$V_{ult} = 95266 \text{ kN}$	$V/V_{ult} = 0.229$	$f\left(\frac{V}{V_{ult}}, \frac{H}{H_{ult}}, \frac{M}{M_{ult}}, \frac{T}{T_{ult}}\right)$ $= 0.420 < 1$ (Safe!)
	$H_{ult} = 15878 \text{ kN}$	$H/H_{ult} = 0.069$	
	$M_{ult} = 187038 \text{ kN}\cdot\text{m}$	$M/M_{ult} = 0.407$	
	$T_{ult} = 99553 \text{ kN}\cdot\text{m}$	$T/T_{ult} = 0.044$	
(b) Mean	$V_{ult} = 200097 \text{ kN}$	$V/V_{ult} = 0.109$	$f\left(\frac{V}{V_{ult}}, \frac{H}{H_{ult}}, \frac{M}{M_{ult}}, \frac{T}{T_{ult}}\right)$ $= 0.238 < 1$ (Safe!)
	$H_{ult} = 49901 \text{ kN}$	$H/H_{ult} = 0.022$	
	$M_{ult} = 481600 \text{ kN}\cdot\text{m}$	$M/M_{ult} = 0.158$	
	$T_{ult} = 312880 \text{ kN}\cdot\text{m}$	$T/T_{ult} = 0.014$	
(c) Max.	$V_{ult} = 271502 \text{ kN}$	$V/V_{ult} = 0.080$	$f\left(\frac{V}{V_{ult}}, \frac{H}{H_{ult}}, \frac{M}{M_{ult}}, \frac{T}{T_{ult}}\right)$
	$H_{ult} = 83471 \text{ kN}$	$H/H_{ult} = 0.013$	

$$M_{\text{ult}} = 692236 \text{ kN}\cdot\text{m} \quad M/M_{\text{ult}} = 0.110 \quad = 0.206 < 1 \text{ (Safe!)}$$

$$T_{\text{ult}} = 523362 \text{ kN}\cdot\text{m} \quad T/T_{\text{ult}} = 0.0084$$

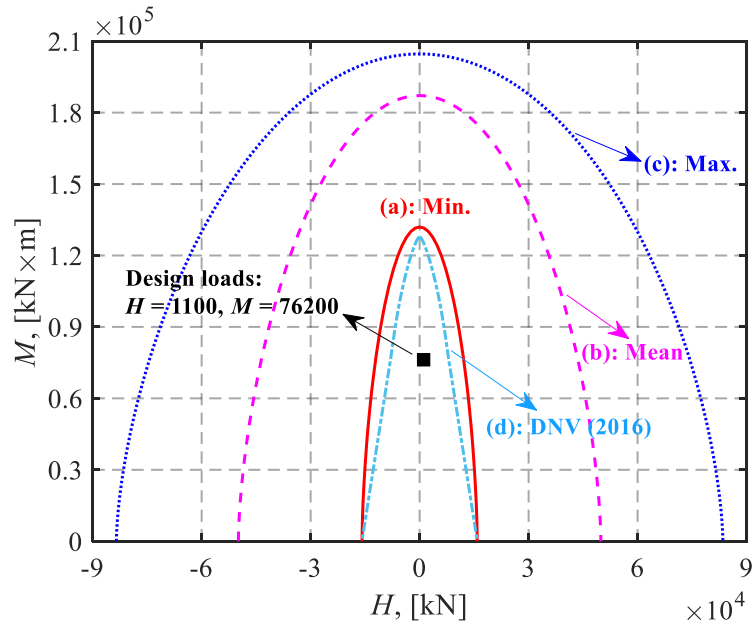


Figure 6.2: Design loads compared with the undrained M - H failure envelopes

For drained soil conditions, the friction angle, cohesion and effective unit weight of the soil are assumed to be $\varphi' = 20^\circ$, $c' = 65 \text{ kPa}$ and $\gamma' = 22.0 - 9.8 = 12.2 \text{ kN/m}^3$. The partial safety factor for materials is taken as $\gamma_m = 1.15$ for effective stress analysis (DNV, 2016). The safety check of ultimate limit state design using drained failure envelopes yields an acceptable ultimate capacity design: $f(V/V_{\text{ult}}, H/H_{\text{ult}}, M/M_{\text{ult}}, T/T_{\text{ult}}) = 0.291 < 1$ (Safe!). The reduced M - H failure envelopes derived from the failure envelope method and the traditional method (DNV, 2016) are compared in Figure 6.3. It can be seen that the traditional approach is more conservative than the failure envelope method, which is similar to the undrained soil condition shown in Figure 6.2.

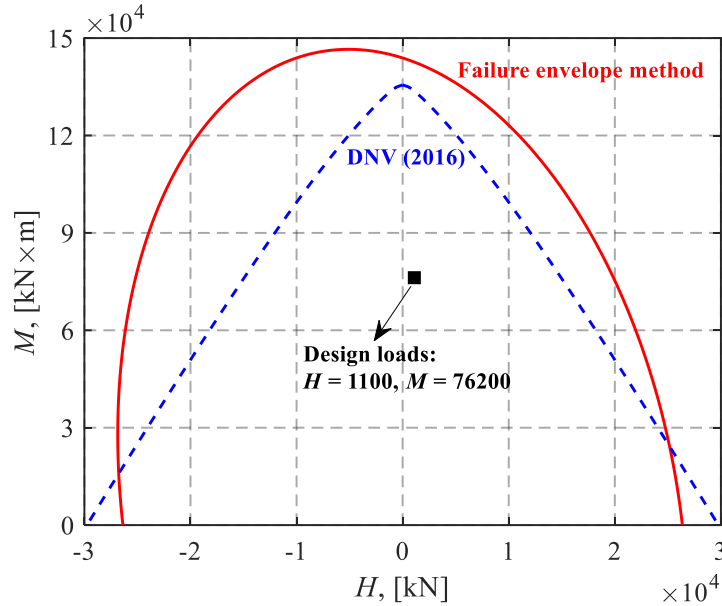


Figure 6.3: Design loads compared with the drained M - H failure envelope

6.1.2 Serviceability limit state design

The foundation responses are also studied based on the stiffness equations from current foundation stiffness approaches: DNV (2016), Bell (1991) and Gazetas (1991). For the coupled stiffness equations provided by Gazetas (1991), K_{HM} is linearly proportional to d/D . For a surface foundation (i.e. $d/D=0$), $K_{HM}=0$ and the relationship of Gazetas (1991) yields the same foundation stiffness as DNV (2016).

The properties of the circular foundation and the cross-anisotropic soil are summarized in Table 6.3. Both surface and embedded foundations have been considered. The factored design loads for the foundation will be assumed to be $V = 21820$ kN, $H = 900$ kN, $M = 60000$ kN·m and $T = 7300$ kN·m. Note that the shear modulus utilized in the analysis (G_R) was taken at a depth equal to the foundation radius (R), following the recommendations of Whitman (1976) and DNV (1992).

Table 6.3: Foundation and soil parameters

α^2	μ_{hh}	$G_{vh} = G_R$, [MPa]	k , [MPa/m]	D , [m]	d/D
1.30	0.24	82.0	2	19	0 & 0.16

In the absence of other information, DNV (2016) suggests working values of shear strain for a wind turbine foundation of 10^{-3} to estimate the reduction in soil stiffness, thus corresponding to approximately $G_R/G_{\max} = 0.3$. In order to more accurately assess the site-specific working value of G , the factored design loads can be applied to the finite element model in this study to iteratively calculate the equivalent shear strain (Shrivastava et al., 2012) and its corresponding value of G_R of the soil at the depth of R using the appropriate shear modulus degradation curve (González-Hurtado, 2019). This procedure provides $G_R/G_{\max} = 0.43$ at a depth of R , thus an assessment for $G_R/G_{\max} = 0.3$ can be assumed to be conservative.

The foundation responses for surface and embedded foundations considering $G_R/G_{\max} = 0.3$ are compiled in Table 6.4. It can be seen that the vertical settlements, u_V , calculated by DNV (2016) and Bell (1991) are considerably larger than that obtained by the current stiffness equations. The horizontal translation, u_H , for the surface foundation considering soil anisotropy is overestimated by Bell (1991), while DNV (2016) and Gazetas (1991) considerably underestimate (around 21% of the current value) the horizontal deformation for the surface foundation due to neglecting the coupling effect between horizontal and rotational responses. For the embedded foundation, DNV (2016) provides considerably larger values of u_H than the current stiffness equations, and Gazetas (1991) considerably underestimates u_H , which is just about 64% of the u_H estimated using the current method. Both the rocking and rotational angles for the surface foundation, estimated with the current study are smaller than those provided by the other methods, but the rocking angle for the embedded foundation is close to those estimated by DNV (2016) and Gazetas (1991). Moreover, foundation embedment can significantly reduce foundation responses.

Table 6.4: Foundation responses for $G_R/G_{\max} = 0.3$

Response	Current study	DNV (2016)	Bell (1991)	Gazetas (1991)
u_V $d/D = 0$	11.113 mm	+59.63%	+49.55%	+59.63%
$d/D = 0.16$	9.928 mm	+54.04%	--	+51.94%

u_H	$d/D = 0$	1.071 mm	-20.89%	+50.70%	-20.89%
	$d/D = 0.16$	0.397 mm	+75.89%	--	-64.08%
θ_M	$d/D = 0$	3.720×10^{-2} deg.	+24.87%	+17.35%	+24.87%
	$d/D = 0.16$	2.713×10^{-2} deg.	+4.40%	--	+4.05%
θ_T	$d/D = 0$	0.299×10^{-2} deg.	+24.36%	--	+24.36%
	$d/D = 0.16$	0.233×10^{-2} deg.	-13.89%	--	-13.94%

For practical design for large shallow wind turbine foundations, three of the most critical limit states are often considered: (i) foundation tilt as a serviceability limit state; (ii) foundation rotational stiffness as a serviceability limit state; and (iii) bearing capacity (drained and undrained) as an ultimate limit state. Ben Hassine (2018) investigated these limit states using a direct reliability-based design (d-RBD) method and found that foundation rotational stiffness is the most critical limit state for shallow wind turbine foundation design. In addition to ultimate and serviceability limit state design, the dynamic behavior of large wind turbine foundations also needs to be assessed. Since current wind turbines are often designed to be slender and flexible structures for cost reduction, the natural frequencies of the overall structures may be close to the low excitation frequencies related to environmental loads from wind and waves (Martins and Mendes, 2016). Static foundation stiffnesses are normally employed to formulate the corresponding dynamic foundation stiffnesses by deriving the dynamic stiffness and damping coefficients. Therefore, further analyses of dynamic foundation stiffnesses for cross-anisotropic soils would be required, which is beyond the scope of the present study.

6.2 Summary and conclusions

This thesis has investigated the ultimate and serviceability limit states for large onshore wind turbine foundations. Compared with the traditional bearing capacity methods, the failure envelope approach developed in this thesis is likely to be more accurate and can be easily and efficiently utilized in practical foundation design. Practitioners just need to

substitute the design loads into the corresponding 4-D analytical VHMT failure envelope expression in a simple spreadsheet or Matlab code and this does not require in-depth knowledge. Moreover, for an onshore wind turbine foundation, since the foundation deformation is often the most critical design factor, the more accurate analytical foundation stiffness equations developed in this thesis are necessary for optimal foundation design and they can be easily implemented for practical foundation design. Assumed reductions in the soil strength and stiffness due to the effects of cyclic loading (dependent on the strain range) can be easily incorporated, as is common practice in offshore engineering currently.

More detailed conclusions of this research drawn from the four linked studies are summarized as follows.

6.2.1 Undrained capacity of circular shallow foundations under combined VHMT loading

Finite element analyses were undertaken to investigate the general VHMT failure envelopes of circular foundations under a zero-tension interface for undrained soil conditions. The $V-T$ and $H-T$ and $M-T$ failure envelopes for surface foundations on non-homogeneous soils were derived to evaluate the effects of torsional loads on the failure envelope for circular foundations. Embedded foundations in a uniform soil with four embedment depths were also taken into consideration to investigate the effects of foundation embedment. A full 4-D analytical expression for the VHMT failure envelope was derived based on the calculated VHMT failure envelopes.

The results showed that torsional loads can reduce the VHM capacity of circular foundations and cannot be ignored for foundation design. For surface foundations on non-homogeneous soils, the normalized $H-T$ and $M-T$ envelopes were predicted with existing analytical equations, but with some modifications. Analyses of embedded foundations indicated that foundation embedment can significantly increase the capacity of circular foundations under combined VHMT loading. In addition, embedded foundations can sustain increasing moments with embedment depth without vertical loads and foundation embedment gradually increases the degree of asymmetry of the $M-H$ failure envelope. It was also found that soil strength heterogeneity affects only the size of the failure envelope

(its effects on the shape of the failure envelope are minimal), while foundation embedment has a significant influence on both the size and shape of the failure envelope.

6.2.2 Undrained capacity of circular surface foundations on two-layer clays under combined VHMT loading

The VHMT failure envelopes for large circular foundations resting on a stiff crust which overlies the main soil deposit were developed using finite element analysis. Undrained conditions were considered for both the crustal layer and the underlying soil. The effects of the undrained shear strength and thickness of the crustal layer on the failure envelopes of circular foundations were investigated. An analytical expression for the VHMT failure envelope was developed.

For the uniaxial vertical and moment capacities, crust correction factors, which are functions of the undrained shear strength and thickness of the crustal layer were proposed. For a surficial crustal layer with high shear strength, the failure mechanisms showed that the relatively strong top crust acts as rigid column that restricts both upward and lateral deformations within the crustal layer, and this restriction in turn increases the depth of the failure zone within the bottom layer. In addition, the strength of the crustal layer exhibits a significant influence on the normalized H - V failure envelopes. Analyses also demonstrated that the same forms of equation that are often used for uniform soils, but with different parameters can provide good fits for the VHMT failure envelopes for a soil with a surficial crust.

6.2.3 Drained bearing capacity of circular surface foundations under combined VHMT loading

Finite element analyses were undertaken to investigate the general failure envelope for large circular surface foundations subjected to combined VHMT loading under drained soil conditions. Two dimensionless numbers, the friction angle ϕ' and the weight parameter $G = \gamma'D/2c'$, have been considered for parametric study proposes. A closed-form equation for the drained VHMT failure envelope was derived based on the calculated failure envelopes.

The finite element results showed that the uniaxial bearing capacities increase with ϕ' exponentially and with G linearly. In addition, the calculated failure envelopes gradually

expand with G and exponentially expand with ϕ' . Analytical expressions were also proposed to approximate the normalized failure envelopes. Compared with the finite element results, the traditional method consistently provides conservative predictions of the bearing capacity under combined loads. Moreover, the equivalent horizontal load accounting for the effects of torsional loading recommended by DNV (2016) significantly underestimates the uniaxial torsional capacity.

6.2.4 Effects of soil stiffness anisotropy on elastic solutions of circular foundations under combined VHMT loading

The coupled elastic stiffnesses for large circular foundations founded on cross-anisotropic soils under combined VHMT loading were investigated using finite element analysis. A three-parameter cross-anisotropic model with a range of anisotropic parameters covering typical soils found in practice was utilized to model the soil behavior. The effect of model domains was examined. Gibson soils and embedded foundations were considered to investigate the effects of soil stiffness heterogeneity and foundation embedment.

It is found that a domain width of 50 times the foundation diameter is sufficiently accurate for the finite element analysis. The results showed that the vertical and rocking stiffness decrease with anisotropic parameter α , and the horizontal stiffness shows an increasing trend. However, the coupling between the horizontal and moment responses of a surface foundation is minimally affected by α . The analyses also indicated that a higher Gibson modulus can increase the vertical, horizontal and moment stiffness, but it does not affect the coupling stiffness. To account for the effects of soil stiffness non-homogeneity and foundation embedment, Gibson and embedment correction factors were also derived.

6.3 Limitations and recommendations for future work

6.3.1 Limitations of current research

This thesis focuses on the static capacity and deformation for large onshore wind turbine shallow foundations. However, it should be noted that the forces acting on these foundations are primarily cyclic loads caused by wind. For the ULS and SLS design of these foundations, cyclic loading effects should be considered for several reasons.

One of the main effects caused by cyclic loading is the degradation of soil strength and stiffness. Over the lifetime of a wind turbine, the foundation will experience millions of load cycles. Cyclic loading builds excess pore water pressure and causes cyclic shear strains to develop with cycling, leading to a loss of soil shear strength and stiffness. Moreover, a decrease in the foundation stiffness could shift the natural frequency of the structure closer to the excitation frequencies of the loading, leading to more significant vibrations (Lombardi et al., 2013). In addition, the dynamic stiffness of shallow foundations highly depends on the loading frequency. For circular foundations, the dynamic foundation stiffness decreases with loading frequency and a considerable reduction may occur for undrained soil conditions (Gazetas, 1991). The inclusion of material damping can further reduce foundation stiffness (EI Nagggar, 2001).

The reduction in soil strength can significantly affect the ULS design for onshore wind turbine foundations. The reduction in soil stiffness and the change of natural frequency can be important factors for foundation SLS design. Therefore, although these cyclic loading effects are not investigated in this research, they should still be incorporated for onshore wind turbine foundation design.

6.3.2 Recommendations for future work

Based on the research presented in this thesis, recommendations for further related research are summarized as follows:

- The numerical analyses performed in this thesis has focused on circular foundations. Recently, a number of onshore and offshore structures (e.g. wind turbines) have been constructed with foundations that have double symmetrical polygon shapes, i.e. octagons (Yilmaz et al., 2014). DNV (2016) recommends design of these foundations as an equivalent inscribed circular foundation to accommodate for the octagonal shape. To date, there has been no verification of this assumption (particularly for the failure envelope method).
- This work is focused on bearing strata extending to infinity. However, in some cases, a thin layer of soil may be underlain by bedrock. This is particularly important for future wind turbines with much larger shallow foundations (in order

to resist the larger loads induced by higher wind turbine towers and longer blades). A larger shallow foundation involves a larger volume of soil (i.e. influence zone) below the foundation base, which may be affected by bedrock. Future work could be undertaken to investigate the VHMT failure envelopes for circular foundations resting on finite soil layers.

- Chapter 3 investigated the VHMT failure envelope for two-layer clays. However, a sand-over-clay or dense-over-loose sand deposit is also a common case for foundation design. For heavy structures that need to be constructed over a weak deposit, replacing a certain depth of the weak deposit by granular materials is a commonly-used ground improvement technique in geotechnical practice. Therefore, the failure envelope for circular foundations on a sand-over-clay and dense-over-loose sand deposit under combined VHMT loading could also be investigated.
- For dense sands, it has been demonstrated that the relative density and stress levels of sands significantly affect the bearing capacity of shallow foundations due to strain softening and progressive failure (e.g. Perkins and Madson, 2000; Cerato and Lutenegeger, 2007; Kumar and Khatri, 2008; Loukidis and Salgado, 2011; Conte et al., 2013). Future research could examine the effects of the relative density and stress levels of sands on the VHMT failure envelope for circular foundations.
- The numerical modelling of the foundation stiffness for embedded foundations was undertaken on cases of relatively shallow depths for current large onshore wind turbines. With the increase of wind turbine towers and blades, wind turbine foundations would be more deeply embedded in order to resist larger moments. Therefore, further work would be useful to investigate the foundation stiffness for foundations with relatively larger embedment depths.

6.4 References

- Bell, R. W. (1991). The analysis of offshore foundations subjected to combined loading. Master's dissertation, University of Oxford, Oxford, UK.
- Ben Hassine, J. (2018). Direct reliability-based design (d-RBD) of shallow wind turbine foundations. Doctoral dissertation, Colorado School of Mines, Golden, Colo.

- Cerato, A. B., and Lutenecker, A. J. (2007). Scale effects of shallow foundation bearing capacity on granular material. *Journal of Geotechnical and Geoenvironmental Engineering*, 133(10), 1192-1202.
- Conte, E., Donato, A., and Troncone, A. (2013). Progressive failure analysis of shallow foundations on soils with strain-softening behaviour. *Computers and Geotechnics*, 54, 117-124.
- DNV GL (Det Norske Veritas GL) (1992). Foundations, classification notes No. 30.4. DNV GL Group, Høvik, Norway.
- DNV GL (Det Norske Veritas GL) (2016). DNVGL-ST-0126: Support structures for wind turbines. DNV GL Group, Høvik, Norway.
- EI Naggar M. H. (2001). Dynamics of Foundations. In: Rowe R. K. *Geotechnical and Geoenvironmental Engineering Handbook*. Springer, Boston, M.A.
- Gazetas, G. (1991). Formulas and charts for impedances of surface and embedded foundations. *Journal of geotechnical engineering*, 117(9): 1363-1381.
- González-Hurtado, J. (2019). The effect of stiffness anisotropy of a glacial clay on the behaviour of a shallow wind turbine foundation. Unpublished Doctoral dissertation. The University of Western Ontario, London, Ont.
- International Electrotechnical Commission (2005). IEC 61400-1: Wind turbines – part 1: Design requirements. International Electrotechnical Commission, Geneva, Switzerland.
- Kumar, J., and Khatri, V. N. (2008). Effect of footing width on N_y . *Canadian Geotechnical Journal*, 45(12), 1673-1684.
- Lefebvre, G., Paré, J. J., and Dascal, O. (1987). Undrained shear strength in the surficial weathered crust. *Canadian Geotechnical Journal*, 24(1): 23-34.
- Lombardi, D., Bhattacharya, S., and Wood, D. M. (2013). Dynamic soil–structure interaction of monopile supported wind turbines in cohesive soil. *Soil Dynamics and Earthquake Engineering*, 49: 165-180.
- Loukidis, D., and Salgado, R. (2011). Effect of relative density and stress level on the bearing capacity of footings on sand. *Géotechnique*, 61(2), 107-119.
- Martins, C. J. and Mendes L. M. M. (2016). Determination of Stiffness for Wind Tower Foundation by Operational Modal Analysis. *International Journal of Mechanics and Applications*, 6(3): 43-48.
- Perkins, S. W., and Madson, C. R. (2000). Bearing capacity of shallow foundations on sand: A relative density approach. *Journal of Geotechnical and Geoenvironmental Engineering*, 126(6), 521-530.
- Rochelle, P. L., Trak, B., Tavenas, F., and Roy, M. (1974). Failure of a test embankment on a sensitive Champlain clay deposit. *Canadian Geotechnical Journal*, 11(1): 142-164.

- Whitman, R. V. (1976). Soil-platform interaction. *In Proceedings of Conference on Behaviour of Offshore Structures*. Oslo, Norway, 2-5 August 1976. Norwegian Institute of Technology, Trondheim, 1, 817.
- Yilmaz, M., Schubert, S., Tinjum, J. M., and Fratta, D. (2014). Foundation soil response to wind turbine generator loading. *In Geo-Congress 2014: Geo-characterization and Modeling for Sustainability*. Atlanta, Georgia, 23-26 February 2014. American Society of Civil Engineers, Reston, pp. 1493-1502.

Curriculum Vitae

Name:	Pengpeng He
Post-secondary Education and Degrees:	China University of Mining and Technology, Xuzhou, Jiangsu, China, 2009-2013 B.Eng.
	China University of Mining and Technology, Xuzhou, Jiangsu, China, 2013-2016 M.Eng.
	Western University, London, Ontario, Canada, 2016-2020 Ph.D.
Honors and Awards:	China Scholarship Council (CSC), 2016-2020
	Western Graduate Research Scholarship, 2016-2020
Related Work Experience	Teaching Assistant, Western University, London, Ontario, Canada, 2016-2020
	Research Assistant, Western University, London, Ontario, Canada, 2016-2020

Publications:

Articles in refereed journals:

[1] He, P., and Newson, T. (2019). Undrained capacity of circular foundations under combined horizontal and torsional loads. *Géotechnique Letters*, 10(2), 186-190.

[2] He, P., González-Hurtado, J., Newson, T., Hong, H., Postman, M., and Molnar, S. (2020). Field monitoring of the ground vibrations adjacent to an onshore wind turbine foundation. *Canadian Geotechnical Journal*. (Accepted on May 2, 2020).

[3] **He, P.**, and Cui, Z. (2015). Dynamic response of a thawing soil around the tunnel under the vibration load of subway. *Environmental Earth Sciences*, 73(5), 2473-2482.

[4] Cui, Z., **He, P.**, and Yang, W. (2014). Mechanical properties of a silty clay subjected to freezing-thawing. *Cold Regions Science and Technology*, 98, 26-34.

Conference papers:

[1] **He, P.**, and Newson T. (2019). Undrained capacity of circular shallow foundations under combined VHMT loading. *In Proceedings of the 16th Pan-American Conference on Soil Mechanics and Geotechnical Engineering*, Cancun, Mexico.

[2] González-Hurtado J., **He, P.**, Newson, T., Hong, H., Postman, M., and Molnar, S. (2017). Field monitoring and analysis of an onshore wind turbine shallow foundation system. *In Proceedings of the 70th Canadian Geotechnical Conference*, Ottawa, Canada.